Simulation of hydrogen diffusion in fcc polycrystals. Effect of deformation and grain boundaries : effect of deformation and grain boundaries

Dmitrii Ilin

université de BORDEAUX

THÈSE

PRÉSENTÉE A

L'UNIVERSITÉ DE BORDEAUX

ÉCOLE DOCTORALE DES SCIENCES PHYSIQUES ET DE L'INGÉNIEUR

POUR OBTENIR LE GRADE DE DOCTEUR

SPÉCIALITÉ : Mécanique et ingénierie

par **Dmitrii ILIN**

Simulation of hydrogen diffusion in fcc polycrystals. Effect of deformation and grain boundaries.

Soutenance le : 14 octobre 2014

Directeur de thèse: Jean-Marc OLIVE

Membres du jury:

Vladyslav Shyvaniuk	Chercheur senior (HDR), NASU, Kiev	Rapporteur
Monique Gaspérini	Professeure, LSPM Université Paris 13	Rapporteur
Döme Tanguy	Chargé de recherche CNRS, Lyon	Examinateur
Jacques Chêne	Directeur de recherche CNRS (HDR), Paris	Examinateur
Jean-Louis Bobet	Professeur, Université de Bordeaux	Examinateur
Jean-Marc Olive	Chargé de recherche CNRS (HDR), Bordeaux	Directeur de thèse
Isabelle Aubert	Maître de conférence, Université de Bordeaux	Examinateur
Nicolas Saintier	Professeur, ENSAM Bordeaux	Examinateur
Thierry Couvant	Ingénieur-chercheur, EDF R&D	Invité

Abstract

In the present work, we establish a one-way coupled crystal plasticity – hydrogen diffusion analysis and use this approach to study the hydrogen transport in artificial polycrystalline aggregates of 316L steel with different grain geometries and crystallographic orientation. The data about stress/strain fields computed at the microstructure scale utilizing the crystal plasticity concept are transferred to the in-house diffusion code which was developed using a new numerical scheme for solving parabolic equations. In the case of initial uniform hydrogen content, the heterogeneity of the mechanical fields is shown to induce a redistribution of hydrogen in the microstructure. The effect of strain rate is clearly revealed. In the second part, hydrogen transport across grain boundaries is investigated considering the specific diffusivity and segregation properties of these interfaces. Using a discrete atomic layer model, the retarding impact of grain boundaries is demonstrated on bicrystals and bamboo type membranes with and without external mechanical loading. To reproduce the effects observed in the atomistic simulations into the crystal plasticity – hydrogen diffusion model, a new physically based multi-scale method is proposed. Using this new approach we study the effect of grain boundary trapping kinetics on hydrogen diffusion and reveal a new grain boundary diffusion regime which has not been reported before.

Keywords: Hydrogen diffusion, fcc polycrystals, crystal plasticity, grain boundary diffusion, segregation, multi-scale model.

Titre: Simulation de diffusion de l'hydrogène dans les polycrystaux cfc. Effet de la déformation et des joints de grains.

Résumé: Une approche couplée prenant en compte l'interaction de la plasticité cristalline et de la diffusion d'hydrogène a été établie et utilisée pour étudier le transport de l'hydrogène dans les agrégats polycristallins synthétiques de l'acier 316L avec des géométries de grains and des orientations cristallographiques différentes. Les champs mécaniques calculés à l'aide du code ZeBuLoN sont transférés dans un code de diffusion développé dans le cadre de ce travail. Une nouvelle formulation associée à un nouveau schéma numérique permet un calcul qui présente une bonne convergence. Les résultats des simulations montrent la redistribution de l'hydrogène dans les polycristaux dû à la présence des hétérogénéités des contraintes hydrostatiques à l'échelle intragranulaire. L'effet de la vitesse de déformation a été quantitativement obtenu. Afin d'enrichir l'approche continue, un intérêt particulier est porté sur le rôle des joints de grains. Des simulations numériques d'un modèle atomique plan par plan ont été développées et appliquées aux bicristaux et aux structures de type "bambou". Les effets de puits ou de barrière induits par la présence des joints de grains sont clairement démontrés dans le cas du nickel pur. Pour reproduire ces effets dans les simulations de diffusion avec le modèle continue, une approche originale de simulation "multi-échelles" de la diffusion au joint de grain a été développée, et un nouveau régime de diffusion au joint de grain a été modélisé.

Mots-clés: Diffusion de l'hydrogène, polycristaux cfc, plasticité cristalline, diffusion aux joints de grains, ségrégation, modèle multi-échelles.

Résumé

Le phénomène de fragilisation par l'hydrogène est connu depuis longtemps mais leur compréhension et leur modélisation restent des domaines de recherche largement ouverts. Les interactions hydrogène-matériau et leurs conséquences sur les risques de rupture prématurée nécessitent la prise en compte de couplages complexes mécanique-diffusion, stimulant le développement et l'application de modèles et d'outils numériques. La simulation de la réponse des matériaux à des configurations variées contribue à la réflexion sur la pertinence des modèles et sur les possibilités de confrontations modélisation-expériences et finalement à la compréhension des mécanismes de fragilisation par l'hydrogène.

Le travail présenté ici porte sur la simulation numérique de la diffusion de l'hydrogène dans des polycristaux cubique face centré (cfc), abordée à différentes échelles, avec une focalisation sur les effets de microstructure et de joints de grains. Le mémoire présenté est organisé en cinq chapitres, précédés d'une brève introduction et suivis de neuf annexes.

Dans le Chapitre1, nous présentons une brève revue bibliographique, dont des compléments spécifiques sont donnés dans les chapitres suivants. Les principaux mécanismes d'interaction hydrogène-matériau (adsorption et absorption, diffusion, piégeage par les défauts) sont d'abord présentés, ainsi que le modèle classique de piégeage, basé sur l'équilibre entre concentrations d'hydrogène diffusif et piégé, et conduisant à un coefficient de diffusion effectif. Différents mécanismes de fragilisation par l'hydrogène sont ensuite évoqués, et illustrés à l'aide de travaux récents basés sur des modélisations discrètes. Les deux derniers paragraphes sont consacrés aux résultats expérimentaux à l'échelle macroscopique relatifs à la fragilisation par l'hydrogène dans deux matériaux cfc, l'acier 316L et le nickel, qui sont considérés dans les simulations présentées dans les chapitres suivantes.

L'hydrogène est connu pour modifier significativement le comportement mécanique des matériaux métalliques. Sous sollicitation mécanique, la diffusion de l'hydrogène dans les métaux n'est pas uniquement pilotée par des processus diffusionels simples. Des couplages forts existent avec les champs mécaniques locaux plus particulièrement avec les gradients de contrainte hydrostatique et de déformation plastique.

Le Chapitre2 présente des simulations par éléments finis de la diffusion d'hydrogène dans des polycristaux virtuels 2D d'acier 316L pour objectif d'étudier et de comprendre l'impact de l'hétérogénéité des champs mécaniques sur la distribution d'hydrogène

à l'échelle de la microstructure. Des calculs de microstructure utilisant une approche couplée mécanique/diffusion sont présentés. Les calculs sont réalisés en utilisant une description explicite de la microstructure et un modèle de plasticité cristalline prenant en compte les écrouissages isotrope et cinématique à l'échelle des systèmes de glissement, ainsi que de l'anisotropie élastique (code de calcul ZeBuLoN).

Un code de diffusion couplée, développé dans le cadre de la thèse, permet d'analyser l'effet de la microstructure (morphologie des grains, phases, texture, joints de grains) sur la distribution d'hydrogène au sein des polycristaux sous différents chargements. Ces calculs mettent en évidence, dans le cas du 316L, un fort effet de la microstructure sur les répartitions (ségrégations) d'hydrogène au sein des agrégats et la forte sensibilité de ces ségrégations à la vitesse de déformation et à la taille de grain.

Les agrégats polycristallins virtuels ont été générés (code GMICRO) avec trois géométries de grains et neuf orientations cristallographiques aléatoires différents. Prechargés dans une enceinte d'hydrogène sous pression jusqu'à une concentration uniforme, les agrégats sont soumis à une traction uni-axiale de 2.2% aux vitesses de déformation de $2.2 \cdot 10^{-5}\ s^{-1}$, $2.2 \cdot 10^{-6}\ s^{-1}$ et $2.2 \cdot 10^{-7}\ s^{-1}$. Les conditions aux limites en hydrogène sont appliquées sur le bord de la chambre et imposent le nul flux normal à la frontière du domaine considéré. Les champs mécaniques obtenus par le code ZeBuLoN sont transférés à chaque pas de calcul à un code-maison développé dans lequel est implémentée l'équation de diffusion couplée. Les résultats des simulations montrent la redistribution de l'hydrogène dans les polycristaux dû à la présence de l'hétérogénéité des champs mécaniques à l'échelle intragranulaire.

La concentration d'hydrogène piégé, corrélée à la déformation plastique, est très faible par rapport à l'hydrogène diffusif. Dans le cas de la vitesse de déformation de $2.2 \cdot 10^{-5}\ s^{-1}$, le degré d'hétérogénéité de la teneur en hydrogène dans l'agrégat est faible et la redistribution est observée au voisinage des joints de grains. Cela est dû au fait que le temps de diffusion est trop court (1000 s) dans le cas des polycristaux cfc dans lesquelles la diffusivité est très faible. Dans les agrégats déformés à la vitesse de $2.2 \cdot 10^{-6}\ s^{-1}$ (le temps de diffusion est 10 000 s), le niveau d'hétérogénéité d'hydrogène est plus élevé et la distribution de l'hydrogène dans les grains est affectée. Dans le cas de la vitesse de déformation de $2.2 \cdot 10^{-7}\ s^{-1}$ (le temps de diffusion est 100 000 s), des groupes distincts de grains saturés et appauvris en moyenne sont observés. L'effet de la vitesse de déformation

obtenu par la modélisation est en accord avec les résultats expérimentaux selon lesquels la fragilisation par l'hydrogène est observée dans les matériaux déformés aux faibles vitesse de déformation.

Dans le Chapitre3, une synthèse bibliographique sur l'approche phénoménologique de la ségrégation, la cinétique de piégeage au joint et l'anisotropie de diffusion au joint de grains est présenté. Pour étudier la diffusion d'hydrogène à travers le joint de grain, le modèle atomistique 1D plan par plan (PPP) pour les calculs de diffusion adopté de la littérature est présenté et implémenté pour des simulations de diffusion d'hydrogène dans des bicristaux ainsi que des structure bambou constituée de joints parallèles dans le cas de nickel pur. Les concentrations homogènes sont supposées par plan atomique parallèle à l'interface. Toute la physique de la diffusion est donnée par les fréquences de saut entre plans. Dans le cas où on néglige les interactions entre les atomes d'hydrogène (champ moyen), les équations qui donnent l'évolution temporelle des concentrations sont simples à résoudre, ce qui permet de traiter plusieurs milliers de plans (système d'1 μm de part et d'autre de l'interface) et de modéliser l'impact local des joints sur l'évolution d'hydrogène globale dans le matériau. Différentes simulations sont réalisées, pour différentes conditions aux limites et tailles de grains, avec ou sans préchargement en hydrogène, et comparées à la diffusion sans présence du joint. Les calculs sont également effectués au cas d'un chargement cyclique de part et d'autre du joint. Les résultats des simulations montrent l'effet retardant des joints de grains sur l'évolution de l'hydrogène dans les agrégats polycristallins.

Cela montre la nécessité de prendre en compte l'impact de joint de grains sur le transport d'hydrogène à travers le joint. Pour reproduire les effets de joint de grains obtenus par les calculs atomistiques dans le cas de diffusion 2D et 3D et enrichir l'approche plasticité cristalline – diffusion, nous avons développé une approche originale de simulation "multi-échelles" de la diffusion au joint de grain qui est présentée dans le chapitre suivant.

Dans le Chapitre 4, une synthèse bibliographique sur la problématique de la diffusion le long des joints de grains est présentée et les modèles de diffusion classiques sont revus. Ensuite, une nouvelle approche qui permet de prendre en compte les propriétés de diffusion spécifiques des joints de grains est proposée. Le joint est traité en différence finie selon un modèle atomique (FDAL) tandis que le grain est maillé en éléments finis (FE), permettant de tenir en compte dans la diffusion les effets de cinétique de piégeage, l'anisotropie et la

dépendance de la diffusivité transverse dans l'évolution de la concentration d'hydrogène.

L'approche (FEFDAL) est appliquée à différentes configurations de diffusion le long du joint ou transversalement et permet d'étudier les effets de puits ou de barrière induits par la présence des joints en 2D. L'effet de court-circuit de diffusion est considéré et comparé aux modèles classiques continus de diffusion (modèle de Fisher et modèle 2D continu). L'impact du piégeage est étudié en considérant une membrane bicristalline dans laquelle l'interface est perpendiculaire à la surface imposée au chargement par l'hydrogène et en supposant que la diffusivité le long du joint est égale à la diffusivité en volume. Les valeurs d'énergie de ségrégation au joint de grains de nickel pur sont adoptées de la littérature.

Les résultats de simulation montre que le piégeage au joint de grains ralenti l'évolution de concentration dans le volume des grains. Ces résultats sont originaux et n'ont pas été rapporté dans la littérature avant. Une étude en fonction des valeurs d'énergie de ségrégation a été effectuée. Les résultats de cette étude paramétrique montrent que la cinétique de piégeage doit être prise en compte dans le cas des joints de grains avec les énergies de ségrégation inférieures à -0.1 eV selon les hypothèses utilisées dans l'approche FEFDAL, et que l'hypothèse d'équilibre locale est valide dans le cas des joints avec les énergies de ségrégation supérieures à -0.1 eV.

En utilisant la méthode FEFDAL, nous avons également modélisé la diffusion dans une jonction triple ainsi que la redistribution d'hydrogène dans un bicristal en présence d'hétérogénéité de contrainte de part et d'autre du joint. L'approche FEFDAL proposée dans ce travail constitue une alternative aux modèles classiques de diffusion basés sur l'équilibre des concentrations d'hydrogène, notamment sur la mise en évidence de l'effet retardant de la ségrégation au joint sur la diffusion de l'hydrogène dans le grain. Elle peut être développée en 3D sur des géométries et chargements plus complexes et permettre d'enrichir le modèle plasticité cristalline – diffusion présenté dans le Chapitre2.

Le Chapitre5 présente le bilan des principaux résultats obtenus en utilisant l'approche plasticité cristalline – diffusion pour les simulation de la diffusion de l'hydrogène dans les polycristaux virtuels, le modèle atomistique 1D pour les calculs de la diffusion à travers les joints de grains dans les bicristaux et les structures bambou, et la nouvelle méthode FEFDAL. Plusieurs perspectives sont proposées pour des développements des modèles présentés dans ce travail et des applications sont discutées.

Acknowledgements

First of all, I would like to express my deepest and sincere gratitude to my advisor, Jean-Marc Olive, who gave me the opportunity to apply my knowledges working upon one of the most interesting subjects in materials science and engineering. I thank him for his scientific guidance and for believing in me, for his great support and encouragement, his jokes, smiles and laugh. Merci beaucoup! I would like to thank Professor Alexander Shuvalov who was the main initiator of my PhD study in France and who put me in contact with Jean-Marc.

I express my appreciations to all our colleagues who contributed to the present dissertation. I am particularly grateful to Professor of Mathematics Rémi Abgrall for his explanations, responses (even on Sunday!) and his assistance in developing the programming tools which I used during the whole period of my PhD study, and to Döme Tanguy for valuable explanations of physical aspects of hydrogen diffusion at grain boundaries, his suggestions and great contribution to this work. I would like to thank Sergiy Teus, Sergiy Stepanyuk, Valentin Gavriljuk, Yoji Mine and David Marechal for their critical viewpoints and advices. A special gratitude goes to Anton Kutsenko for his support, his time for the collaboration and contribution to my PhD work as well as for our long bike trips and his histories.

I would like to thank Isabelle Aubert and Nicolas Saintier for their guidance and advices. In addition, I express a special thanks to them because they found the time to play music with me!

I express sincere gratitude my to my teacher of french language Sabrina Houdaibi, to my colleagues and friends Matthieu Dondt and Djoudi Sidane who helped me a lot at the beginning of my stay in France, to all PhD students, post-doctoral fellows and colleagues in our laboratory for their friendship Julien Jumel, Monique Puiggali, Marie-Benedicte Touzet Cortina, Béatrice Desoudin, Sandrine Guit, Michel Mesnard, Martin Shanahan, Aurore Nicolas, Racine Ly, Mohamed Biskri, Alexis Viel, Benoit Mascaro, Abdoulaye Ba, Karim Saidoun, Emmanuel Siryabe, Benoit Tallon, Julien Chandezon, Romain Legrand, Jérémy Guitard, Pierric Mora, Samuel Rodriguez, Alban Leleux, Feng Xu, Lazhar Homri, Florian Daude, Michal Budzik, Marwene Assel, Alexander Nikitin, Arsenii Chulkov, Roman Zhuravlev, to my family for their support and encouragement. I

would like to mention my grandfather who is not alive but who believed in me and whose hands were the exemplar for me how the man should work.

Contents

Introduction

It is well known that hydrogen can affect mechanical properties of metallic materials, degrade material toughness, strength and enhance crack opening rate (hydrogen-assisted cracking). This effect of hydrogen (so called Hydrogen Embrittlement) was investigated over several decades but is still not well understood.

Hydrogen is the smallest and lightest atom in the universe. As a result, it can diffuse through metals rapidly. The high mobility and low solubility makes it difficult to analyse hydrogen evolution and distribution in metals and alloys. Frequently used surface chemical analysis techniques to measure elemental composition of materials, X-ray Photoelectron Spectroscopy (XPS) and Auger Electron Spectroscopy (AES), cannot detect hydrogen. More sensitive techniques, such as Second Ion Mass Spectrometry, are required. However, the analysis of an exposed surface has to be done at very low temperatures since a hydrogen coverage can change due to the high mobility of solutes. In addition, Elastic Recoil Detection Analysis (ERDA) and Scanning Kelvin Probe Force Microscopy (SKPFM) were demonstrated recently to be able to measure hydrogen concentrations locally at the microscopic scale. All these experimental methods can provide the information about hydrogen distribution only near the surface of a metallic material and the results may be affected by the rapid formation of oxide layer in air conditions. The evolution of hydrogen in the material bulk cannot be observed *in situ* and usually studied indirectly by analysing, for example, tensile properties and fracture surfaces, by performing permeation experiments and using Thermal Desorption Spectroscopy, and also by conducting measurements with radioactive isotopes of hydrogen (deuterium and tritium).

The diffusion rate of hydrogen at grain boundaries, which is important characteristic of hydrogen transport in polycrystalline materials, is difficult to measure as well.

The problems of hydrogen detection makes it important to develop numerical models accounting for physical aspects of hydrogen behaviour in metals and its interaction with defects (vacancies, dislocations, grain boundaries etc.). Studies combining the experimental observations of hydrogen evolution and impacts on mechanical properties of materials with corresponding computer simulation are expected to be a highly promising approach in the future.

The aim of the present work is to make a contribution to the theoretical basis for numerical computations of hydrogen diffusion and to study the effect of microstructure on hydrogen transport in metals with face-centered cubic (fcc) crystal lattice.

Hydrogen diffusion can studied theoretically using atomistic models, such as first principle calculations, molecular dynamics and so on, or utilising the continuum approach. These models can be classified according to the time and length scales which can be considered in the computations (Figure 1). Due to the high computational cost, atomistic approaches are usually used for the simulations of hydrogen diffusion of several picoseconds and systems considered in these simulations contain about several hundreds or several thousands of atoms. A lot of examples of atomistic calculations of hydrogen interaction with microstructural defects can be found in the literature, such as hydrogen diffusion around an edge dislocation, in the vicinity of grain boundaries, near a crack tip or hydrogen-vacancy interaction. The continuum approach was also widely used by several research groups for the analyses of hydrogen transport, for example, near a blunting crack tip by finite element calculations.

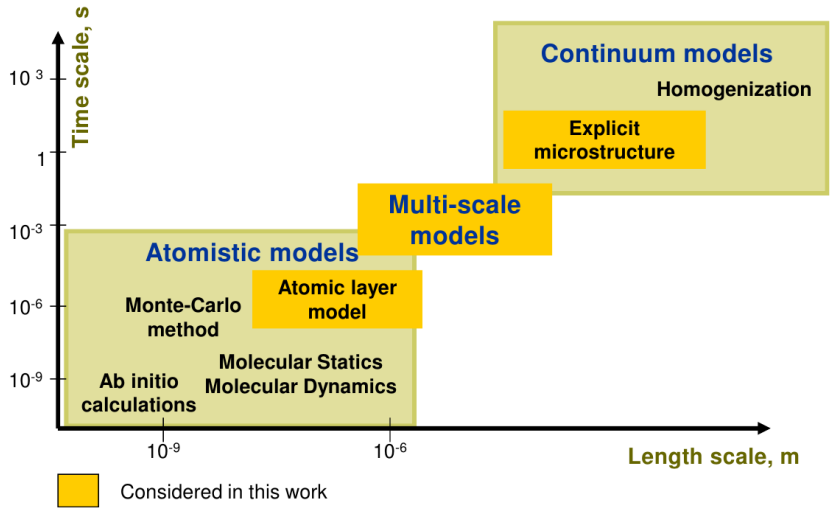

Figure 1: Classification of different approaches for the theoretical study of hydrogen diffusion with respect to the time and length scales.

In the first part of the present dissertation (Chapter 1), physical aspects of hydrogen diffusion (Section 1-2) and interaction with material defects (Section 3) are considered. Then, hydrogen effects on material properties and models of Hydrogen Embrittlement are briefly described (Section 4). In particular, the effects of hydrogen on mechanical

behaviour of austenitic stainless 316L steel (Section 5) and pure nickel (Section 6) are reviewed.

In the following parts, hydrogen diffusion modelling is performed at the scale of a polycrystalline aggregate. The effects of deformation and grain boundaries are investigated. For each problem considered, a review of the literature is presented.

In Chapter 2, we study the effect of microstructure induced stress-strain heterogeneities on hydrogen diffusion in polycrystalline 316L steel. To simulate hydrogen redistribution in pre-charged polycrystalline aggregates loaded at different strain rates, we use the approach in which the crystal plasticity model and classical hydrogen transport equations are coupled.

In the third part (Chapter 3), we focus on the diffusion across grain boundaries and study the dilatory effect of trapping by boundaries on hydrogen transport in nickel bicrystals and bamboo type membranes. In this case, the diffusion problem is one-dimensional (1D), and 1D atomic layer model is utilised.

To reproduce the effects of grain boundaries observed in the simulations using the 1D atomic layer model and investigate the effect of grain boundary trapping in the case of two-dimensional diffusion problem, we develop a new multi-scale model (Chapter 4). Taking into trapping kinetics, we model hydrogen diffusion in nickel bicrystals as well as in the vicinity of a junction of three grains and reveal the retarding impact of grain boundary on hydrogen evolution in the bulk of grains.

Finally, the results of the present dissertation are outlined and tasks for the future work are proposed in Chapter 5.

Chapter 1

Hydrogen in metals

Hydrogen (H) is an element with atomic structure of one proton and one electron. In its natural state, it forms di-atomic molecules of hydrogen gas, H_2. In this molecular state, it is too large to diffuse in most metals, and mono-atomic hydrogen has to be produced from the molecule by dissociation at the surface interface.

1.1 Hydrogen adsorption and absorption

Hydrogen is mostly introduced into metallic materials by gas or cathodic charging. It is worth mentioning that the equivalent hydrogen gas pressure associated with cathodic charging conditions is very high, and, for example, according to Brass and Chêne [1], is about 90 000 bar for charging from 0.1 M NaOH at 100 mA/cm^2 current density and temperature of 95^{o}C in the case of austenitic 316L steel. In the present section, we consider briefly basic processes of adsorption stage. Some details are also given in Appendix.

Two stages are distinguished in the adsorption process of hydrogen molecule: physisorption and chemisorption. The energetic threshold separating the binding energies of physisorption and chemisorption is about 0.5 eV per adsorbed species [2].

Physisorption is caused by the forces of Van der Waals, i.e. without sharing and transport of electrons between adsorbed molecule and solid. The molecule does not dissociate.

After dissociation, the chemisorption stage involves a chemical reaction between the surface and the adsorbate. Chemical bonds are generated at the adsorbent surface due to the interaction of electron clouds and transfer of electrons of adsorbed atom and solid.

In the case of hydrogen adsorption by a metal, the reaction can be described by the

equation:

$$H_2 + 2M \leftrightarrow 2MH_{ads} \tag{1.1}$$

In this equation, it is supposed that H_2-molecule dissociates and H-atom are adsorbed by the surface of metal. The reaction (1.1) is reversible, i.e. two H-atoms adsorbed can recombine to form H_2-molecule (Tafel mechanism).

The quantity of adsorbed gas at constant temperature is represented by the curve known as the isotherm of adsorption. The most frequently used isotherms are described by equations of Temkin, Freundlich or Langmuir which are based on different assumptions about the dependence of the heat of adsorption on surface coverage by the adsorbate (the details are given in Appendix). All mentioned isotherms were used for analysing the mechanisms of hydrogen embrittlement. It was noted that the isotherms of Freundlich and Temkin are more suitable than the adsorption isotherm of Langmuir [2].

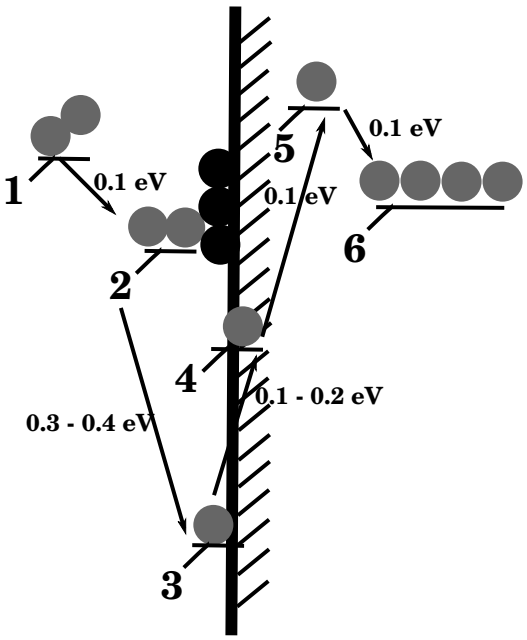

Figure 1.1: Scheme of hydrogen-iron surface interaction: 1 - hydrogen molecule; 2 - adsorbed hydrogen molecule; 3 - adsorbed r-type hydrogen atom; 4 - adsorbed s-type hydrogen atom; 5 - hydrogen atom in the interstitial lattice site; 6 - hydrogen cluster [2].

On the base of quantum mechanics analysis, two different states of hydrogen are distinguished: r- and s-atoms [2]. Hydrogen in r-state is the atom which is not influenced by the electron cloud of metal. The type of binding of H-atom to a surface is analogous to the covalent bond. Atoms in r-state repel each other. S-state is the hydrogen atom

which is dissolved in the metal and dissociated into proton and electron. S-atom is injected into the electron cloud of metal. Hydrogen atom in r- and s-states are shown in Figure 1.1 as well as the initial H_2-molecule and hydrogen in the interstitial lattice site and in clusters [2].

For cathodic charging, hydrogen adsorption is described by the Volmer reaction in the case of acid media:

$$H_3O^+ + e^- + M \rightarrow H_2O + MH_{ads}, \tag{1.2}$$

and for a basic media as follows:

$$H_2O + e^- + M \rightarrow OH^- + MH_{ads}. \tag{1.3}$$

As it is seen from these reactions, there is no stage of the dissociation of H_2-molecule in contrast to the hydrogen gas charging.

The adsorption can be followed by the process of desorption according to the reaction of Heyrovsky:

$$H^+ + e^- + MH_{ads} \rightarrow H_2 + M \tag{1.4}$$

or the reaction of Tafel:

$$H_{ads} + H_{ads} \rightarrow H_2 + 2M \tag{1.5}$$

After the adsorption step, hydrogen atom recombines in the surface-subsurface diffusing into the bulk. This stage is usually called the absorption and described by the following equation:

$$MH_{ads} \rightarrow MH_{abs} \tag{1.6}$$

Finally, the reaction of hydrogen adsorption-absorption by a metal can be described by the equation:

$$H_2 + 2M \leftrightarrow 2MH_{ads} + Q, \tag{1.7}$$

in which the dissociation of H_2-molecule is considered, and $Q < 0$ or $Q > 0$ depending on the endothermic or exothermic behaviour, respectively. In the case of endothermic reaction the solubility at constant temperature can be described by the equation (Sievert's law):

$$c = \beta \sqrt{\frac{p}{p_0}} exp\left(-\frac{\Delta H_S}{kT}\right), \tag{1.8}$$

where β is a constant, $p_0 = 0.1\ MPa$ (atmospheric pressure). This law is used in the second chapter of the present dissertation.

1.2 Hydrogen diffusion in a crystal lattice

After adsorption and absorption by a metal, hydrogen atoms are accommodated in the interstitial sites of crystal lattice. H-solute can occupy octahedral (O-) or tetrahedral (T-) sites (Figure 1.2). According to atomistic calculations [3–7], the preferential sites in face-centered cubic (fcc) structure metals are O-interstitial positions, while in body-centered cubic (bcc) structure metals hydrogen is accommodated in T-sites.

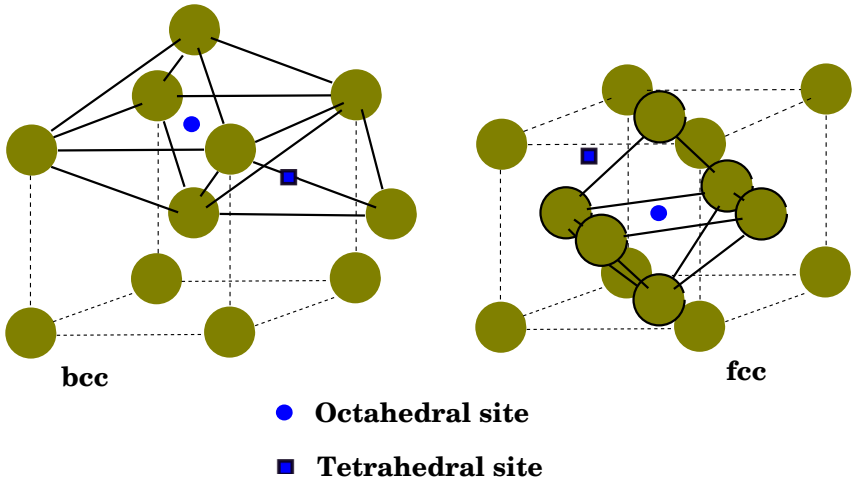

Figure 1.2: Octahedral and tetrahedral interstitial sites in the bcc and fcc crystal lattice.

H-atom located in the interstitial lattice site can move into the neighbouring position. The frequency, with which the hops between the normal interstitial sites occur, varies for different materials. This jump frequency determines the rate of hydrogen transport.

The evolution of the concentration of diffusing particles is usually described by Fick's laws. According to the first Fick's law, a flux of impurities, $\mathbf{J}$, is proportional to the gradient of concentration, $\boldsymbol{\nabla} c$:

$$\mathbf{J} = -\mathbf{D}\boldsymbol{\nabla} c, \tag{1.9}$$

where $\mathbf{D}$ is a diffusivity tensor (or the diffusion coefficient in one-dimensional case), and $c = c(x, y, z, t)$ is a function of coordinates and time. The negative sign in Eq. (1.9) indicates opposite directions of the concentration gradient and diffusion flux. The diffusion process leads to the equilibrium state when $\boldsymbol{\nabla} c = 0$.

For diffusing species which obey the conservation law, one may write:

$$-\boldsymbol{\nabla} \cdot \mathbf{J} = \frac{\partial c}{\partial t}. \tag{1.10}$$

Combining Eqs. (1.9) and (1.10), we obtain the equation of diffusion or the second Fick's law:

$$\frac{\partial c}{\partial t} = \boldsymbol{\nabla}^T \mathbf{D} \boldsymbol{\nabla} c. \tag{1.11}$$

From the mathematical point of view, the second Fick's law is the second-order partial differential equation. It is non-linear if the diffusivity depends on concentration. If the diffusivity is independent of concentration, Eq. (1.11) simplifies to

$$\frac{\partial c}{\partial t} = \mathbf{D} \boldsymbol{\Delta} c. \tag{1.12}$$

The diffusivity tensor, $\mathbf{D}$, is symmetric and can be transformed to its three orthogonal principal axes [8]. It then takes the form:

$$\mathbf{D} = \begin{pmatrix} D_1 & 0 & 0 \\ 0 & D_2 & 0 \\ 0 & 0 & D_3 \end{pmatrix} \tag{1.13}$$

where D_1, D_2 and D_3 are called the principal diffusion coefficients or the principal diffusivities. In the present work, we deal with hydrogen diffusion in cubic structure metals for which [8, 9]:

$$D_1 = D_2 = D_3. \tag{1.14}$$

1.3 Hydrogen trapping

1.3.1 Interaction of hydrogen with defects

Trapping sites are the structural imperfections (vacancies, other solutes, dislocations, voids, grain boundaries) in metals in which the potential energy of hydrogen is less than in normal lattice sites.

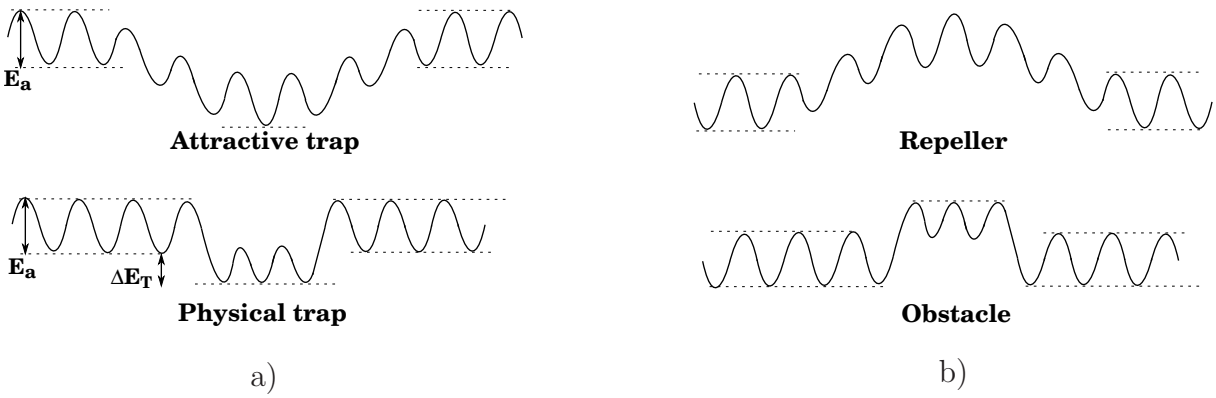

Figure 1.3: Schematic of potential energy profiles in the vicinity of (a) attractive and physical traps; (b) repellers and obstacles are shown for the comparison.

In Figure 1.3a, the characteristic potential energy profiles of two kinds of traps, attractive and physical, are shown according to the classification of Pressouyre [10].

Attractive traps are the regions in a lattice where hydrogen is subjected to attractive forces. These forces are of four types and are due to electrical fields (atoms and other defects introducing electron vacancies will attract hydrogen when it is present as a screened proton), stresses, temperature gradients or to the nonideal part of a chemical potential gradient [10].

Physical traps are due to a physical discontinuity of the metal lattice where it is more energetically favourable for H-atom to stay. Mixed traps where both characters, attractive and physical, can be also distinguished [10].

Traps can be classified with respect to their dimensions. The corresponding classification is presented in Table 1.1.

Table 1.1: Classification of hydrogen traps according to the dimension

Type	Traps
Point defect	Vacancies
Linear	Dislocations Triple junctions
Planar	Interfaces
Volumic	Cracks Voids Particles dissolving hydrogen

In Figure 1.3b, the characteristic energy profiles of repellers and obstacles are presented for the comparison [11]. These defects have the opposite to the segregation effect of trapping sites, i.e. repel hydrogen: inclusion, particles, phases that do not dissolve hydrogen or induce compressive stresses in the surrounding matrix. Interfaces (in particular, grain boundaries) can also act as diffusion barriers/obstacles. This point will be discussed in Chapter 3 and Chapter 4.

a) Reversible trap b) Irreversible trap

Figure 1.4: Schematic of potential energy profiles for reversible and irreversible traps.

Depending on the value of trap binding energy, two types of trap are usually distinguished: irreversible and reversible. The irreversible traps have the strong trapping effect and are characterised, respectively, by a high migration energy barrier for a H-atom to jump into a normal lattice site (Figure 1.4). The reversible trapping sites have a weak trap binding energy. This classification depends on the temperature and time. The prob-

ability for a hydrogen atom to leave a trapping site increases with temperature. For the infinitely large times, all traps can be considered as reversible.

H-solutes interact strongly with a hydrostatic stress field of material imperfections [12]. In the case of edge dislocation, the stress field around the dislocation core is heterogeneous: both dilatation and compression zones are present (Figure 1.5a). Hydrogen segregates in the zone of higher hydrostatic stress and repelled by the compression field (Figure 1.5b).

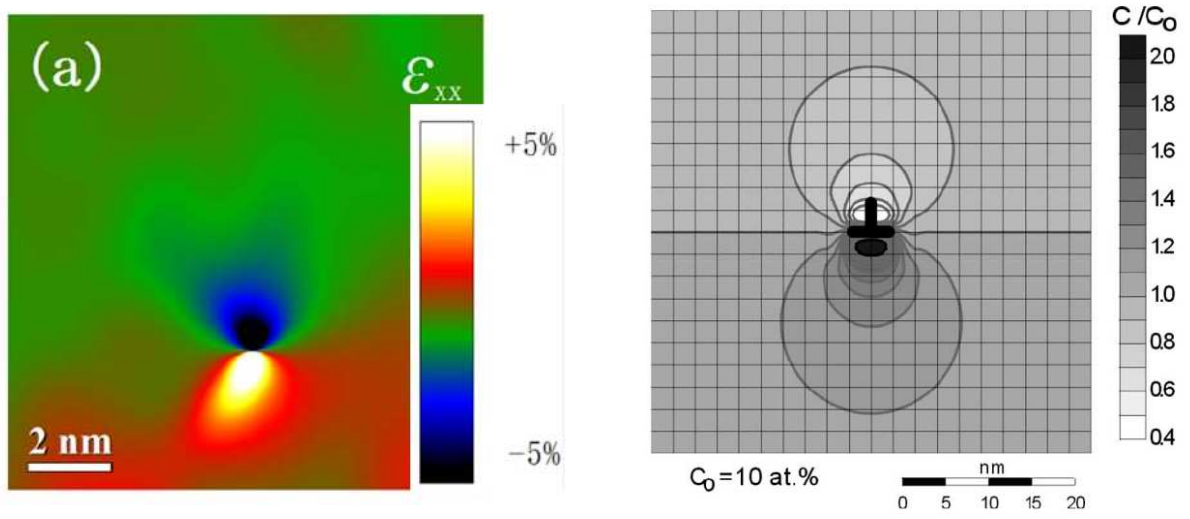

a) b)

Figure 1.5: (a) Strain field in the vicinity of edge dislocation in gold measured by high-resolution transmission electron microscopy [13]; (b) equilibrium hydrogen distribution around a single edge dislocation calculated for 316L austenitic stainless steel [14].

Besides an increase of hydrogen solubility and the retarding of diffusion process in metals, the transport of H-atoms by dislocations can contribute into the evolution of H-content in materials. Suggested first in the work of Bastien et al. [15, 16], the H-transport by dislocations was demonstrated experimentally in several works.

Donovan [17] found that the release rate of tritium from thermally charged iron, nickel, 304L stainless steel, 5086 aluminium alloy and Inconel 718 increases during plastic deformation. The temperature dependence of the release rate corresponds to activation energies that are consistent with the interpretation that the enhanced release during plastic deformation is due to the dislocations which egress from a specimen and carry with them hydrogen [17].

Chêne et al. [18] studied the desorption of tritium in nickel base super-alloy single

crystals. It was shown that the rate of tritium desorption in the domain of plasticity is greater by a factor of five compared to the one under elastic tension, that provides evidence for hydrogen accelerated transport by dislocations.

It was noted that an increase of strain rate results in the reduction of hydrogen desorption from materials. To transfer H-atoms, the dislocation velocity can not to be greater than a critical value, V_{cr}, calculated according to the Einstein-Stokes relation:

$$V_{cr} = M_C F_{cr}, \tag{1.15}$$

where M_C is a mobility of Cottrell atmosphere:

$$M_C = \frac{D}{kT}, \tag{1.16}$$

and F_{cr} is a critical force for keeping H-atom to be trapped by a moving dislocation. This force was estimated by Tien et al. [19] as follows:

$$F_{cr} = \frac{\Delta E_T}{30b}, \tag{1.17}$$

where b is a Burgers vector. According to the estimation of Tien et al., in the expression (1.17), it is assumed that the maximal distance at which a hydrogen atom interacts with a dislocation is greater than the Burgers vector, b, by a factor of 30 [19]. The critical distance was reported to be about 8.5 times greater than b in the paper of Taketomi et al. [20] who studied hydrogen distribution and diffusion around the $\{112\}\langle 111\rangle$ edge dislocation in α-iron by performing the molecular statics simulation (Figure 1.6) and, hence, the critical force can be estimated as follows:

$$F_{cr} = \frac{\Delta E_T}{8.5b}. \tag{1.18}$$

It is also worth to mention that Taketomi et al. found the possibility for hydrogen to be trapped not only by the hydrostatic stress field of edge dislocations. The study of Taketomi et al. revealed that the hydrogen-trap energy is influenced by a shear stress field of edge dislocation and, hence, screw dislocations are capable to affect H-diffusion and H-distribution in metals [20].

The interaction of hydrogen with moving dislocations was studied in the work of Fishgoyt and Kolachev [21]. Figure 1.7 represents schematically the effect of stress gradients around an edge dislocation on the hydrogen redistribution. After the dislocation slip, H-concentration heterogeneities appear which can eliminate with time by the concentration

gradient diffusion or, in the case of the presence of a dislocation source, e.g. Frank-Read type, the slip of one dislocation can be followed by the other increasing/maintaining the H-concentration heterogeneity.

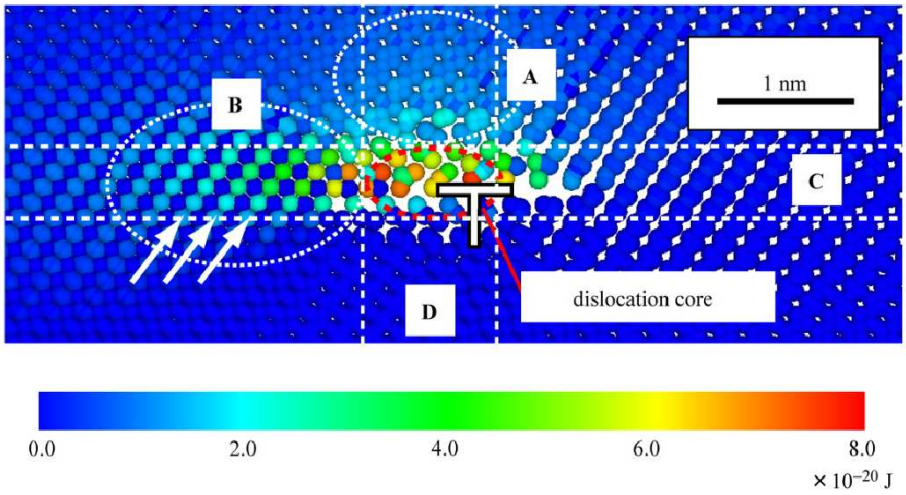

Figure 1.6: Distribution of hydrogen trap energy around the $\{112\}\langle 111\rangle$ edge dislocation in α-iron found from the molecular statics study [20].

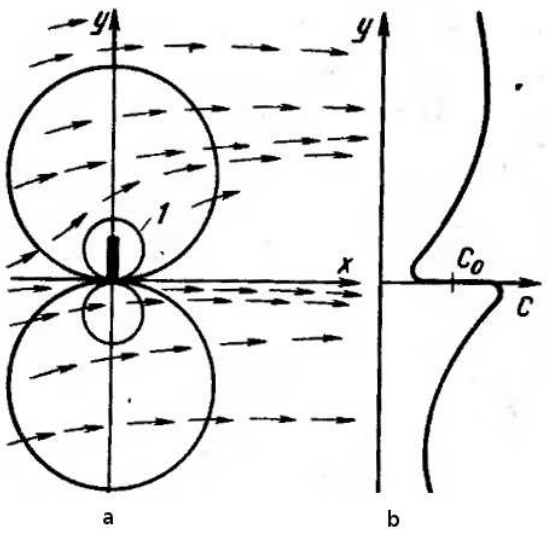

Figure 1.7: (a) Stress field contour and (b) hydrogen distribution in the vicinity of a moving dislocation [2]. The arrows in (a) show schematically the hydrogen flux in the stress field of dislocation.

Being adsorbed and absorbed by a metal, hydrogen can be also accommodated in

vacancies. Ab-initio calculations demonstrate that up to twelve hydrogen atoms can be trapped by a monovacancy in aluminium [22], six in palladium [23], five in bcc iron [24], six in fcc iron [25]. The ab-initio study of hydrogen-vacancy formation presented by Tateyama et al. [24] shows that the major complex in bcc α-iron at ambient conditions is VH_2 and the maximum value of H-atoms that can be trapped by one vacancy is five (see Figure 1.8).

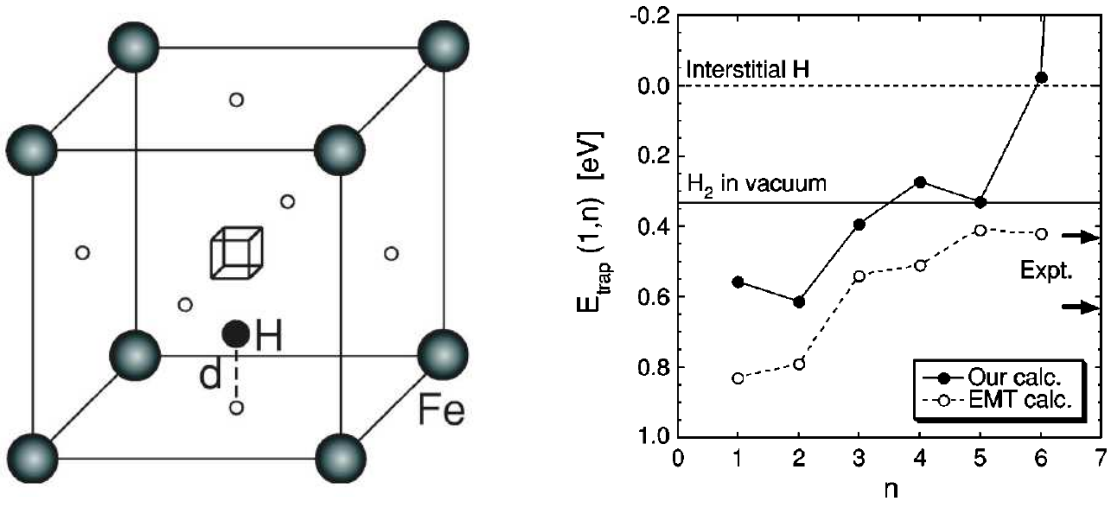

a) b)

Figure 1.8: Hydrogen-vacancy interaction in α-iron. Schematic view of hydrogen-monovacancy complex VH_1 is shown in (a). The transparent cube at the center represents the monovacancy. The gray spheres show the position of Fe-atoms and the black one is hydrogen. Six open circles located at the face centers of the cubic lattice are octahedral sites. Each H-atom is located near the corresponding O-site. In (b), calculated in [24] H-trapping energies in α-iron are shown as filled circles; the open circles and arrows show the results of effective-medium theory calculations [26] and experiments [27], respectively.

The formation of hydrogen-vacancy complexes increases both the concentration of vacancies and hydrogen content in the metal. The results of Nazarov et al. [25] show that a single vacancy in a fcc Fe matrix is a highly effective and capacious trap being able to accommodate up to six H-atoms. Nazarov et al. derived the analytic thermodynamic model that generalizes previous approaches and that treats the various point defects and complexes in a fully grand canonical ensemble. Applying this model, the authors found that the presence of hydrogen can enhance the vacancy concentration by more than seven

orders of magnitude resulting in superabundant vacancies [28]. However, it was noted that despite the huge influence of hydrogen on vacancies, the effect of vacancies on the total H-concentration is negligible except for at high-temperature and extreme H-rich conditions.

Hydrogen interaction with crack tips is considered in Sec. 1.4 in this chapter. Hydrogen trapping by grain boundaries is the subject of studies presented in Chapter 3 and Chapter 4.

1.3.2 Hydrogen trapping models

Darken and Smith [29] were the first who suggested that hydrogen diffusion is retarded by defects in materials. McNabb and Foster [30] developed the formulation to account for the hydrogen trapping phenomenon in metals. Oriani [31] reformulated the equations proposed by McNabb and Foster in the context of the assumption of local equilibrium. Both formulations are presented here.

Let N_T be the number of traps per unit volume, and θ_T is a fraction of occupied trapping sites. Thereby, the number of occupied trapping sites is:

$$C_T = \theta_T N_T \tag{1.19}$$

It is considered that the effect of traps can be described by two parameters - the mean probability that hydrogen will be trapped, k (trapping rate), and the probability for hydrogen atoms to be released by traps, p (untrapping rate).

McNabb and Foster postulated that the number of hydrogen atoms trapped in a unit of time in the volume δV is proportional to the concentration of diffusing atoms, C_L, and to the number of vacant traps, $N_T(1-\theta_T)$, and is equal to $kC_L N_T(1-\theta_T)\delta V$. The number being released in a unit of time is proportional to the number of occupied traps and is given by $pC_T\delta V$. For the small volume δV, the rate of increase of the number of atoms in the trapped population $\partial(C_T\delta V)/\partial t$ is equal to the difference between the rates of capture and release [30]:

$$\frac{\partial(C_T\delta V)}{\partial t} = kC_L N_T(1-\theta_T)\delta V - pC_T\delta V. \tag{1.20}$$

If N_T is a constant with accounting for (1.19) Eq. (1.20) reduces to

$$\frac{\partial\theta_T}{\partial t} = kC_L(1-\theta_T) - p\theta_T. \tag{1.21}$$

In the case of steady state, Eq. (1.21) takes the form:

$$kC_L(1-\theta_T) - p\theta_T = 0, \tag{1.22}$$

and the relation between the parameters k and p can be established:

$$\frac{k}{p} = \frac{\theta_T}{C_L(1-\theta_T)} \tag{1.23}$$

In the Oriani formulation [31], it is assumed that the trapped population of H-atoms, θ_T, is in a local equilibrium with the population of diffusing H-atoms, θ_L. The relation between the two atomic populations is described by the equilibrium constant, $K_T = a_T/a_L$, where a_T and a_L are the activities of the H-atoms upon the trapping sites and upon the normal lattice sites, respectively. Assuming no interaction between occupied sites, each of the two activities are expressed in terms of fractional occupancies as

$$a_i = \frac{\theta_i}{1-\theta_i}. \tag{1.24}$$

Hence, one can write

$$K_T = \frac{\theta_T}{1-\theta_T}\frac{1-\theta_L}{\theta_L}. \tag{1.25}$$

Further, if $\theta_L << 1$, what is usually the case,

$$K_T = \frac{\theta_T}{1-\theta_T}\frac{1}{\theta_L}. \tag{1.26}$$

The constant K_T is iven by

$$K_T = \exp\left(-\frac{\Delta E_T}{kT}\right), \tag{1.27}$$

where ΔE_T is a trap binding energy. If N_L is the number of normal lattice sites per unit volume, the concentration of diffusing atoms, C_L, can be expressed as

$$C_L = \theta_L N_L. \tag{1.28}$$

Relating Eqs. (1.26) and (1.28) with (1.23), we obtain

$$\frac{k}{p} = \frac{K_T}{N_L}. \tag{1.29}$$

Considering the total concentration of hydrogen as the sum of the concentration in normal lattice sites and the concentration in trapping sites:

$$C = C_L + C_T \tag{1.30}$$

and assuming that hydrogen is transported by lattice diffusion, i.e.

$$\mathbf{J} = -D_L \boldsymbol{\nabla} C_L, \tag{1.31}$$

where D_L denotes the lattice diffusivity, one can rewrite the second Fick's law for the hydrogen diffusion with trapping:

$$\frac{\partial C_L}{\partial t} + \frac{\partial C_T}{\partial t} = D_L \boldsymbol{\Delta} C_L, \tag{1.32}$$

Using the Oriani formulation in the form

$$C_T = \frac{C_L N_T K_T}{C_L K_T + N_L}, \tag{1.33}$$

we obtain:

$$\frac{\partial C_L}{\partial t} = D_{eff} \boldsymbol{\Delta} C_L, \tag{1.34}$$

where

$$D_{eff} = D_L / \left(1 + \frac{\partial C_T}{\partial C_L}\right), \tag{1.35}$$

Calculating the derivative $\partial C_T / \partial C_L$ when N_T is constant, we obtain for the effective diffusivity:

$$D_{eff} = D_L / \left(1 + \frac{N_T N_L K_T}{(C_L K_T + N_L)^2}\right). \tag{1.36}$$

Leblond and Dubois [32] obtained general equations for hydrogen diffusion in metals including effects of trapping phenomena, diffusion obstacles, stresses, temperature and non-uniform solubility by using Boltzmann-type statistical transport equations which describe the random jumps of hydrogen atoms from site to site. The authors have shown that the previous models are recovered in some special cases thereby clarifying their application conditions. In particular, McNabb and Foster formulation was derived by Leblond and Dubois assuming only one type of traps, uniform stress and temperature distribution, and homogeneous material (i.e. uniform solubility).

In the present work, we model hydrogen transport in the framework of Oriani theory assuming local equilibrium and uniform constant temperature and solubility (Chapter 2). The model of random jumps of hydrogen atoms from site to site is also used in the simplified one-dimensional case to study hydrogen trapping and diffusion at grain boundaries (Chapter 3 and Chapter 4).

1.4 Hydrogen embrittlement mechanisms

As it was shown in previous sections, hydrogen interaction with metals is complex. Due to the multiplicity of this interaction, the deleterious effect of hydrogen on material behaviour (so called Hydrogen Embrittlement) is still incompletely understood. To describe the effect of hydrogen on mechanical properties of metals, different mechanisms were proposed (hydrogen attack, hydride formation, hydrogen-vacancy interaction, adsorption-induced dislocation emission, hydrogen-enhanced decohesion, hydrogen-enhanced localized plasticity), and they are still under debate. The overall opinion is that no single mechanism is applicable, and their combination is supposed to be responsible for hydrogen degradation of metals. Among these mechanisms, hydrogen-induced deconhesion (HEDE) [33] and hydrogen-enhanced localized plasticity (HELP) [34] are mostly used in models of hydrogen-assisted cracking. These mechanisms are revisited in the thermodynamic framework in a recent paper of Kirchheim [35].

The HEDE mechanism postulates embrittlement due to localized reduction in cohesive strength induced by the segregation of hydrogen to defects such as grain boundaries, microcracks, notches and second phase particles; the embrittlement is attributed to a decrease in the strength of atomic bonding of the host metal in regions of hydrogen accumulation. First principle calculations for Al (111) [36] and bcc Fe (110) surfaces [37] demonstrate a reduction both in surface energy and cohesive strength of the interfaces with increasing hydrogen concentration. It means that hydrogen accumulation ahead of a crack or trapping at internal interfaces in the material, will result in a cleavage along a fracture plane or decohesion of the interfaces at lower loads. However, high local concentrations are required [3,37,38]. Shen et al. [38] calculated approximate segregation energies for $\Sigma 9\{221\}[110]$ symmetric tilt grain boundary by combined semi-empirical and ab-initio calculations and demonstrated that segregation alone is not expected to lead to a significant reduction in cohesive strength for bulk concentrations lower than 1000 ppm. This means that other mechanisms than a simple segregation should be involved also, like H-induced structural changes, to explain experimentally observed failure of the interfaces at low H-concentrations [38].

The HELP mechanism is based on both experimentally [39–42] and numerically [14, 43–45] obtained evidences that hydrogen, which segregates and form a Cottrell atmo-

sphere around dislocation cores, reduces barriers for the dislocation motion and allows the dislocation slip to be activated at lower stress levels. Observations of enhanced dislocation mobility indicate that hydrogen shields elastic fields of dislocations and causes the localization of slip. Molecular dynamics studies of the interaction of a single H-atom with an edge dislocation in α-iron [45] suggest that hydrogen dissolved in tetrahedral sites can reduce the Peierls stress for the dislocation motion.

Numerical simulation of hydrogen-assisted cracking can be performed at different scales considering systems composed of several hundreds or several thousands of atoms and systems corresponding to the scale of laboratory test specimens.

Molecular statics simulations of Telitchev and Vinogradov [46] show that the presence of even one H-atom near the crack tip leads to severe distortion of the α-Fe lattice, decohesion and loss of strength in comparison with H-free sample (Figure 1.9).

In several works [47–50], the models that advocates the synergistic action of both the HELP and decohesion mechanisms for hydrogen-assisted fracture were elaborated. Matsumoto et al. [47] performed molecular dynamics simulation of crack propagation in α-Fe single crystals containing about one million Fe atoms with and without hydrogen. It was demonstrated that H-atoms at dislocation cores reduce the energy barrier for the dislocation motion and increases the dislocation mobility; the separation (decohesion) of a slip plane is caused due to the hydrogen atoms trapped by dislocation, and such separation is connected among pile-up dislocations.

Wen et al. [48] performed molecular dynamics simulation together with the embedded atom method (EAM) on a single crystal of nickel pre-charging to different amounts of hydrogen with various distributions (Figure 1.11). The results of Wen et al. support the hydrogen-enhanced decohesion mechanism with localized deformation and brittle fracture.

Liang and Sofronis [49] presented finite element calculations for the nickel-base alloy 690 (i) postulating that hydrogen reduces the flow stress of the material in a local small volume and this reduction is proportional to the corresponding local hydrogen concentration in the material [51], and (ii) describing the interfacial cohesion in the presence of hydrogen in the form of a traction-separation law. Novak et al. [50] proposed the model of hydrogen-induced intergranular failure in which the decohesion is initiated at grain boundary carbide particles in high-strength AISI 4340 steel; in this approach, the intensity of the failure event depends on the local stress and hydrogen accumulation with

a dislocation pile-up at the matrix-carbide interface.

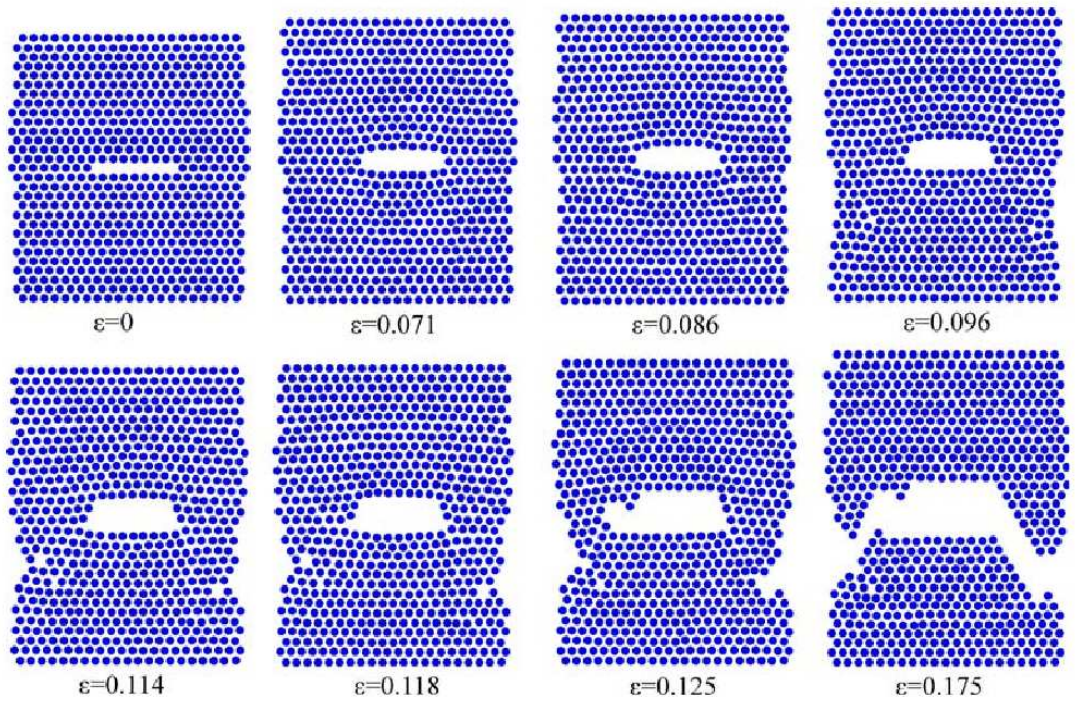

a)

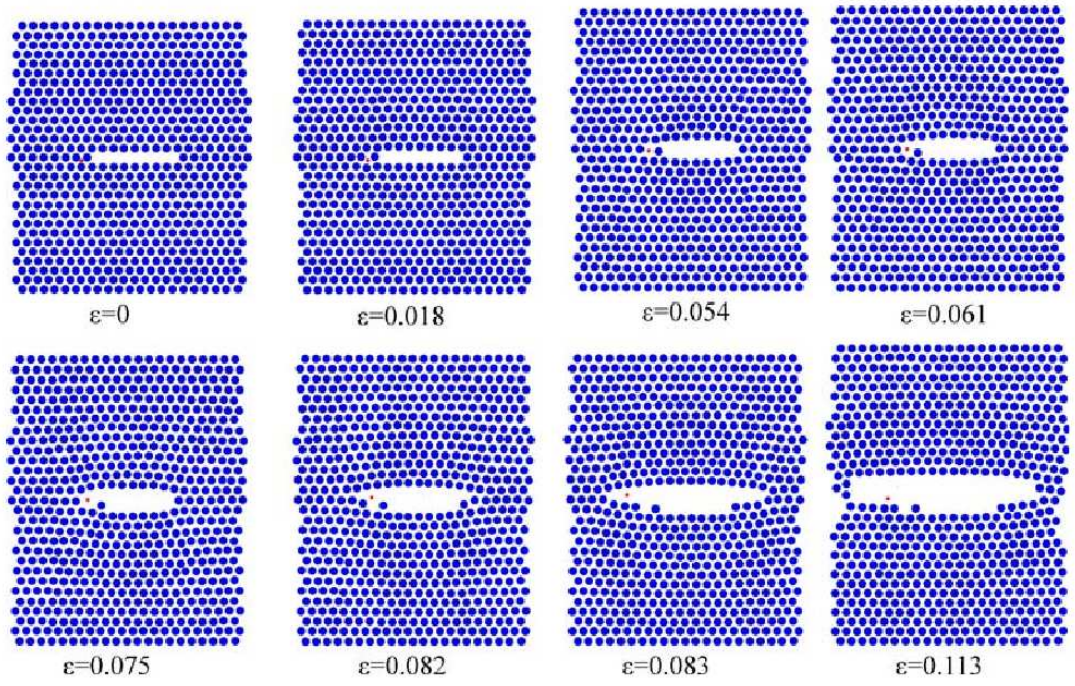

b)

Figure 1.9: Evolution of the α-iron structure (a) without hydrogen and (b) with one hydrogen atom (red) in mode I of crack opening [46].

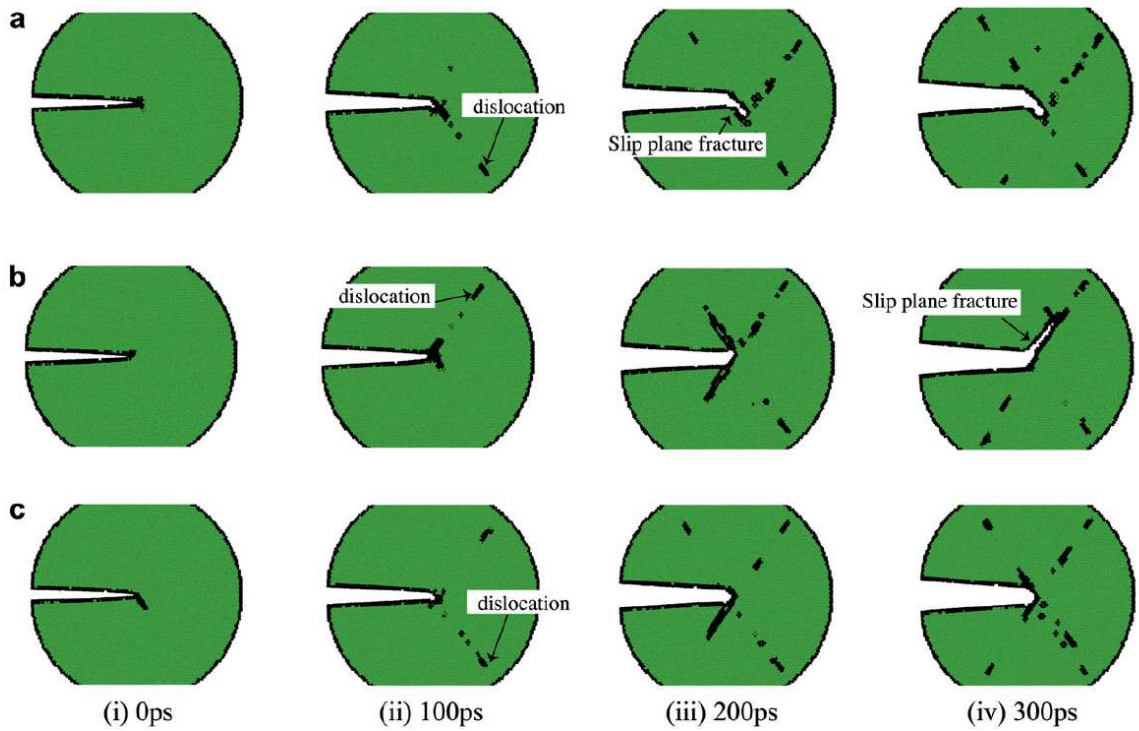

Figure 1.10: Crack propagation in α-Fe single crystal consisting of about 71 000 atoms with hydrogen concentration of (a) $\approx$ 1.8 mass ppm, (b) $\approx$ 5.4 mass ppm and (c) without hydrogen [47].

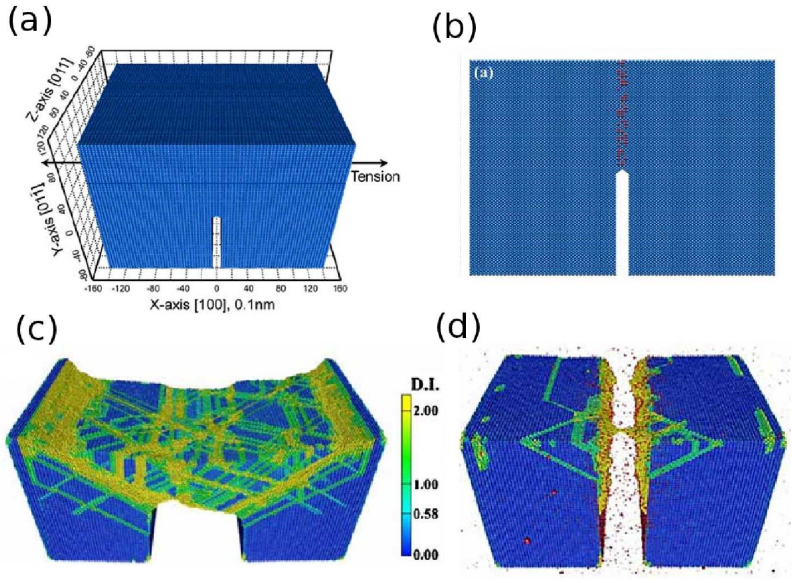

Figure 1.11: Results of molecular dynamics simulations performed on (a) a three dimensional single crystal with a crack tip containing 1 021 563 nickel atoms. Crack propagation is simulated (c) without hydrogen and (d) with hydrogen atoms distributed as shown in (b) [48].

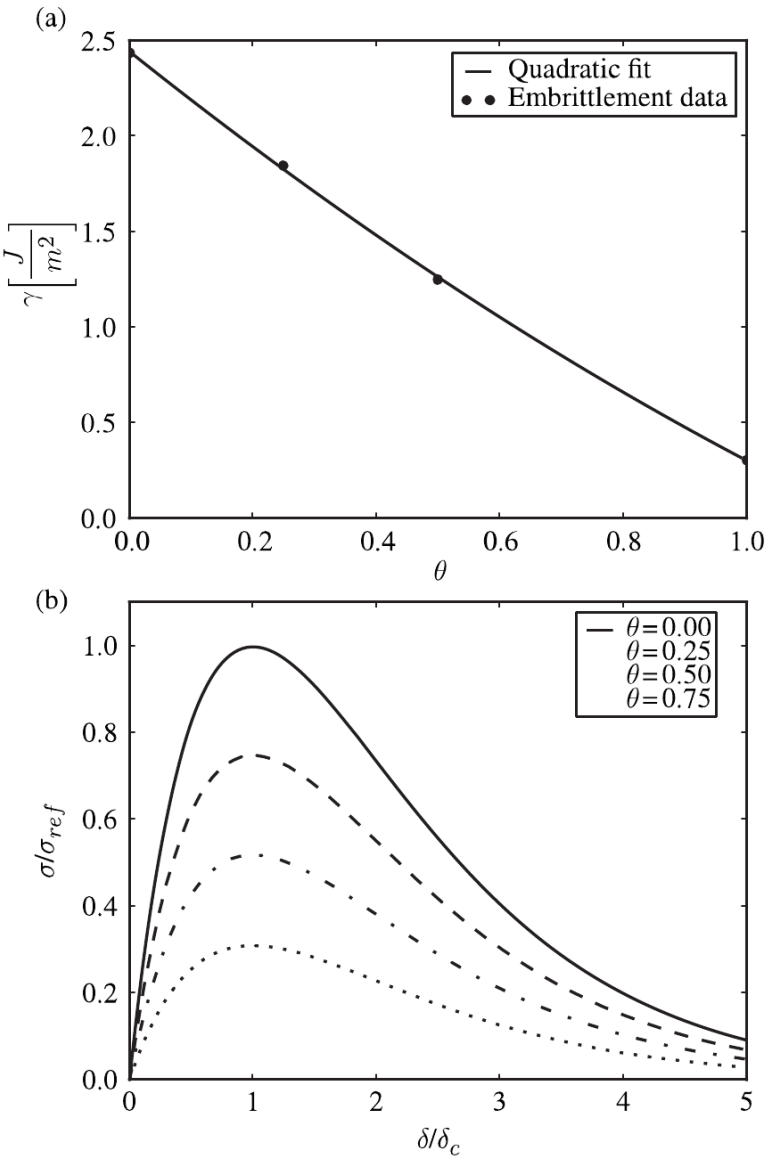

Figure 1.12: (a) Effect of hydrogen on cohesive energy of bcc Fe(110) (first principles computations [37]) and (b) traction-separation law for different values of impurity coverage θ for hydrogen in Fe [53].

In the work of Serebrinsky et al. [52], a continuum model informed by quantum mechanical calculations [37] was constructed for the simulation of hydrogen embrittlement in metals. In the approach used by Serebrinsky et al., the key features include concentration-dependent constitutive relations for cohesive strength derived from first principles quantum mechanics, stress-assisted impurity diffusion, impurity coverage at the incipient crack surfaces determined from the Langmuir relation and continuum finite element modelling including plasticity. It was shown that this approach produces plausible results for inter-

mittent crack propagation in embrittled steels as well as provides qualitative and quantitative predictions of a number of experimental observations, such as crack initiation times and their dependence on applied stress intensity and yield strength. Similar model was used by Rimoli and Ortiz [53] for the modelling of intergranular hydrogen embrittlement (Figure 1.12).

1.5 Effect of hydrogen on mechanical properties of stainless steel 316L

Due to the low hydrogen diffusivity, austenitic stainless steels are thought to be little susceptible to hydrogen embrittlement. The 316L stainless steel is widely used in technologies involving industrial atmospheres or fuels composed of hydrogen. Because of its high resistance to hydrogen influence, the 316L steel as well as other stainless steels (304, 304L, 316) is included in the list of materials recommended for application in H-gas and liquid environments [54]. The steel retains a significant part of its flaw tolerance even in the most severe test conditions. At the same time, the data about tensile behaviour of 316L steel presented in the literature show that this material is susceptible to hydrogen, and it might degrade the admittance of the steel to levels below the required safety margin [55].

The drastic effect of hydrogen on the behaviour of 316L steel was observed in the examination under severe conditions by Valiente et al. [55]: precracked samples were tested under slow mechanical loading (Figure 1.13) and cathodic hydrogen charging (in 1 N H_2SO_4 solution containing 0.25 g 1^{-1} As_2O_3 at current density of 100 mA/cm^2). The 316L steel fails in air by plastic instability, and fracture takes place after plastic collapse and fracture surfaces are typically ductile [55, 56]. The comparison of tensile testing of specimens with and without simultaneous cathodic polarization indicates that hydrogen does not essentially alter the macroscopic failure mode of the specimens if loaded at not extremely low loading rates. The mechanical behaviour of the steel in the presence of hydrogen does not change from ductile to brittle in a macroscopic sense. In hydrogen environment the steel fails by plastic instability as in air conditions, but failure loads are lower and decrease with embrittlement time. It is seen from Figure 1.13 that hydrogen has a primary tendency to cause crack branching at the crack tip in 316L austenitic stainless steel.

Ductile fracture with transition to the brittle on the surface region was observed by Herms et al. [57] in slow strain rate test under cathodic charging conditions (Figure 1.14). The influence of hydrogen on the density, nature and size of microvoids present on dimpled fracture surface was revealed.

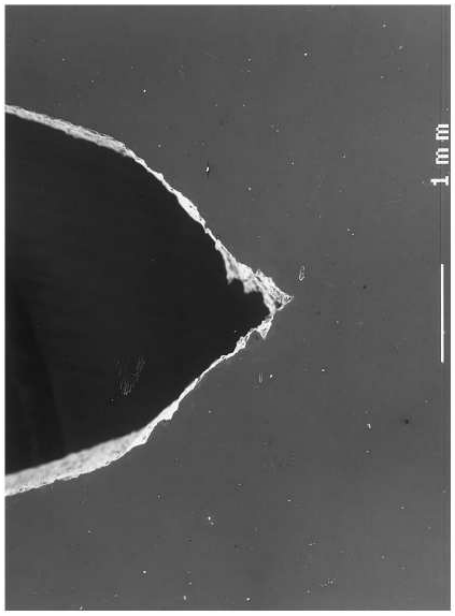

a) hydrogen free test, COD rate: 100 $\mu m/min$

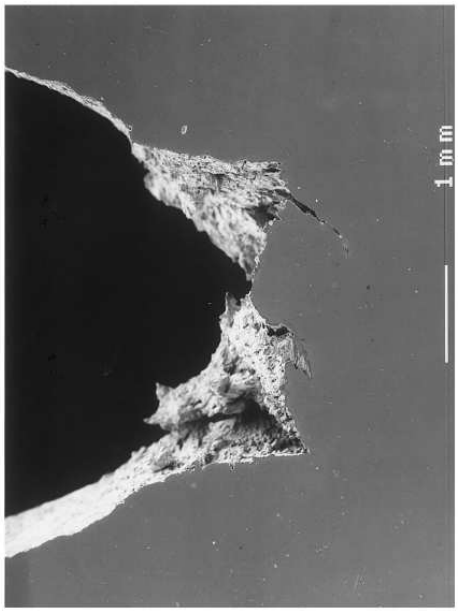

b) under hydrogen charging, COD rate: 10 $\mu m/min$

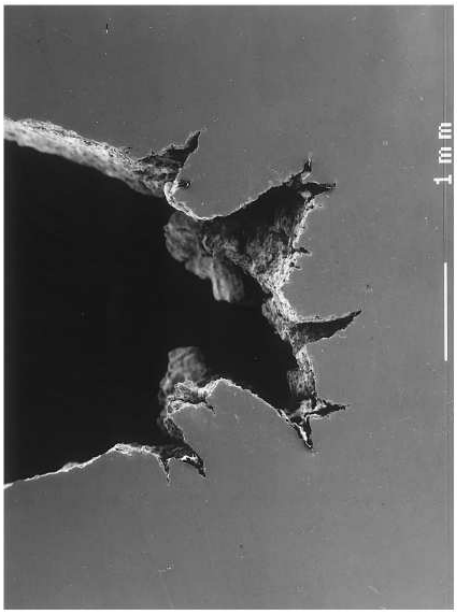

c) under hydrogen charging, COD rate: 1 $\mu m/min$

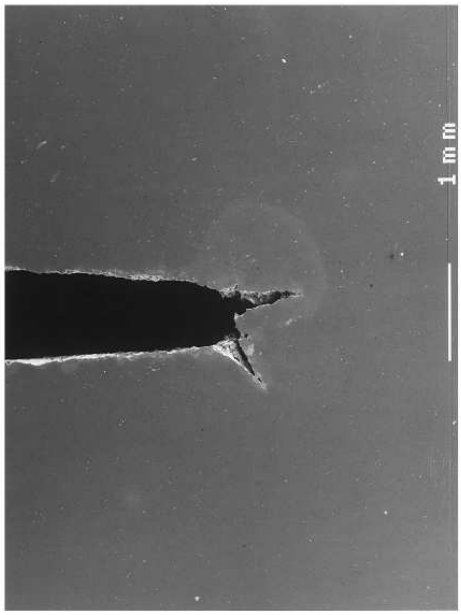

d) under hydrogen charging, COD rate: 0.1 $\mu m/min$

Figure 1.13: Crack profiles observed in pre-cracked samples of 316L stainless steel under mechanical loading with different crack opening displacement (COD) rates for hydrogen free and subjected to cathodic charging (in 1 N H_2SO_4 solution containing 0.25 g 1^{-1} As_2O_3 at current density of 100 mA/cm^2) material [55].

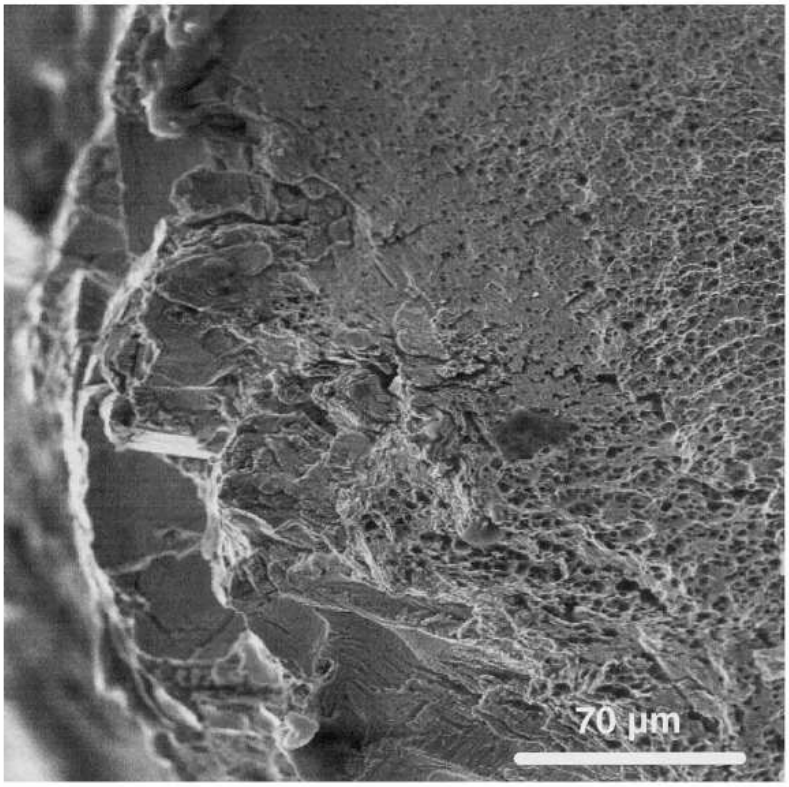

Figure 1.14: Transition between brittle and ductile fracture of 316L steel wire cathodically charged (in 1 N H_2SO_4 solution containing 0.25 g 1^{-1} As_2O_3 at current density of 100 mA/cm^2) during tensile test [57]. Strain rate: $10^{-6}s^{-1}$.

The hydrogen effect on dimple formation on the fracture surface was also studied by Matsuo et al. [58] using hydrogen gas exposure (at 10 MPa pressure and temperature of 250^oC during 192 h) and tensile tests. A reduction of average size of dimples was observed in the H-charged specimens compared to the uncharged ones. These results were found to be consistent with the hydrogen enhanced localization of shear deformation.

The sensitized 316L steel is much more susceptible to hydrogen cracking than the annealed steel [59, 60]. The sensitization of the steel is usually a results of thermal exposure in the 500 to 800^oC temperature range. Thermal aging leads to the precipitation of chromium carbide particles along grain boundaries and to a depletion of chromium around the precipitates. From examinations of fracture surfaces of tested specimens while cathodically charged, Minkovitz and Eliezer [59, 60] found considerable difference between the annealed and sensitized specimens. The fracture in the sensitized samples was predominantly intergranular, while the annealed specimens produce ductile rupture with regions

of microvoid coalescence.

Significant degradation of tensile properties in sensitized type 316L steel was reported by Rosenthal et al. [61]. Namely, ductility losses, flow stress increase, decreased strain-hardening capacity were observed. Hydrogen was also found to increase the amount of strain-induced martensite in sensitized 316L steel.

In the work of Brass and Chêne [1], the macroscopic effects of hydrogen on tensile characteristics at the constant strain rate of $10^{-3}\ s^{-1}$ of a 316L stainless steel were studied as a function of the charging conditions and of the grain size. According to the results of Brass and Chêne, the internal hydrogen affects the tensile behaviour of the 316L steel at room temperature by increasing the yield strength, decreasing the hardening coefficient and a homogeneous elongation. The extent of these effects depends on the grain size. It was found that the influence of hydrogen on the yield strength and on the strain hardening is less pronounced in the large grain material charged by hydrogen (up to 135 wt. ppm) than in the small grain specimens. This suggests that the H-induced changes in mechanical properties are mainly attributed to the dislocation-grain boundary interaction [1].

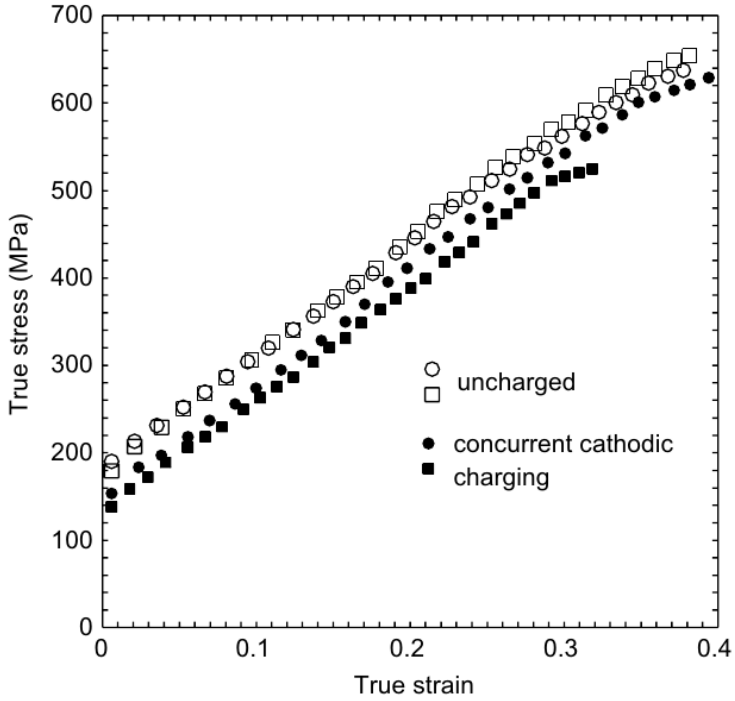

Figure 1.15: Influence of hydrogen on the true stress-strain curves of 316L steel samples ($10^{-3}\ s^{-1}$, 95^{o}C).

In the case of external hydrogen (cathodic charging), tensile straining reveals the softening effect of hydrogen (Figure 1.15) resulting from enhancing the dislocation emission from the surface. Brass and Chêne also obtained the evidence of hydrogen transport by dislocations from the analysis of tritium desorption during plastic deformation of precharged specimens.

In the work of Aubert et al. [62], 316L stainless steel with high nickel content was used to prevent the second phase formation in specimens cathodically charged by hydrogen and subjected subsequently to tensile straining at strain rate of 10^{-3} s^{-1}. The analysis of surface slip morphology was performed using atomic force microscope (AFM) on both charged and uncharged samples, and a significant effect of hydrogen on slip morphology was reported.

The nickel content and its distribution was found to affect significantly the degree of hydrogen influence on the mechanical behaviour of the 316L steel. The combined effect of austenite stabilisation and promotion of cross slip at high Ni content leads to the high resistance to the embrittlement and to macroscopic ductile fracture behaviour [63]. In the work of Michler et al. [64] it is demonstrated that nickel macro segregation and microstructural heterogeneity are the reasons of data scatter for 316L steel in slow strain rate tests.

1.6 Effect of hydrogen on mechanical properties of nickel

The effect of hydrogen on mechanical behaviour and failure occurrence in nickel specimens was reported in numerous works. The data presented in the literature suggest that the embrittlement of nickel by hydrogen is sensitive to strain rate, grain size, test temperature and hydrogen concentration, and the brittle fracture due to hydrogen is intergranular [65–72] (Figure 1.16).

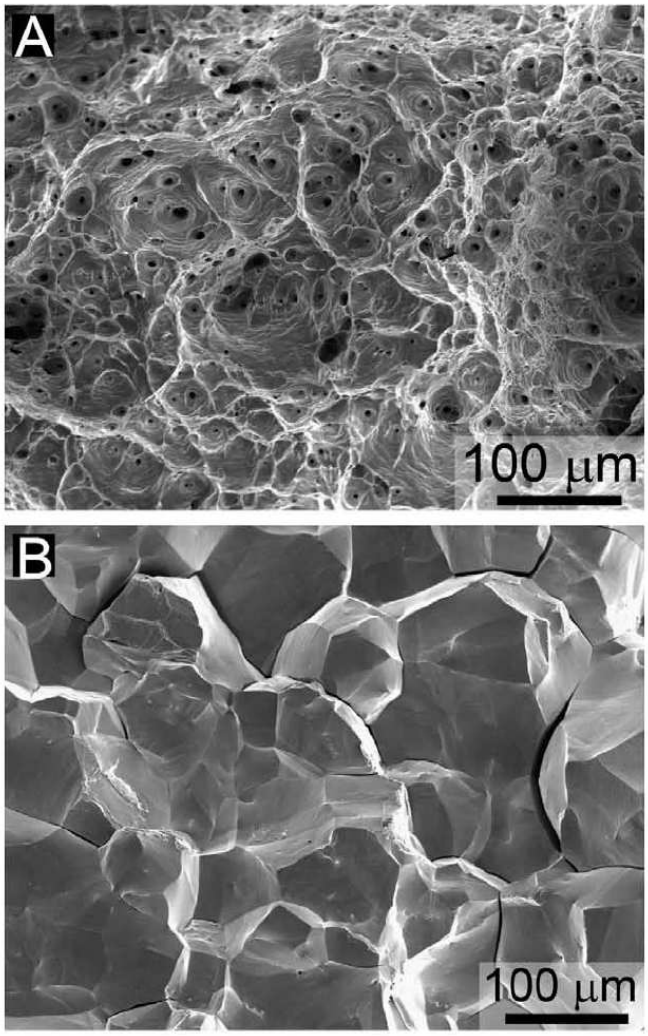

Figure 1.16: Secondary electron micrographs of fracture surfaces after tensile testing of Ni-201 [73]. (A) Fracture surface in the uncharged specimen with microvoid coalescence observed typically in ductile materials. (B) Intergranular fracture in hydrogen embrittled nickel after charging at 3400 appm.

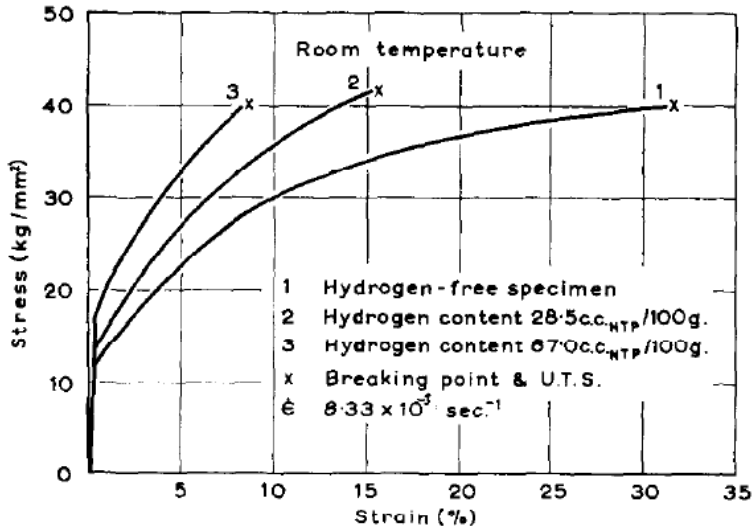

Figure 1.17: Stress-strain curves of nickel for different hydrogen content at room temperature. Strain rate: $8.33 \cdot 10^{-3} s^{-1}$ [65].

It was noted that the embrittlement is more pronounced under test conditions which promote serrated yielding (the Portevin-Le Chatelier effect) [65, 66]. Wilcox and Smith found that all fractures of hydrogen-charged nickel tested at -80^{o}C are completely intercrystalline, the cracks form after 7 to 9% elongation and propagate slowly to fracture which generally occurs after about 15 to 25% elongation. It was suggested by the authors [66] that two conditions are necessary for crack nucleation: (1) a high stress concentrations which are provided by slip bands held up at grain boundaries (GBs) and triple junctions (TPs), and (2) a high concentration of hydrogen in the vicinity of the stress concentrators. It was also proposed by Wilcox and Smith that the excess hydrogen lowers the surface energy thereby facilitating the GB crack nucleation. Smith and co-workers [65,66] emphasized that crack propagation is controlled by the mobility of hydrogen solutes and *the embrittlement appears at temperatures and strain rates at which hydrogen atoms can segregate to moving dislocations.*

Birnbaum and co-workers extensively studied the effect of hydrogen on the fracture mode in polycrystalline nickel pre-charged by hydrogen as well as in specimens charged during deformation.

Lassila and Birnbaum [68] suggested that the mechanism of intergranular hydrogen embrittlement of nickel is the deformation and fracture of relatively soft region at grain boundaries saturated by hydrogen by diffusive segregation. The segregation can occur by

means of lattice diffusion, grain boundary diffusion or dislocation transport.

The experimental study of Kimura and Birnbaum [74] suggests that the kinetics of intergranular hydrogen embrittlement of nickel under conditions in which the hydrogen is supplied at the external specimen surface is controlled by H-diffusion along GBs. The results and analyses of Kimura and Birnbaum do not support the enhancement of hydrogen diffusivity in nickel by dislocation transport on macroscopic distances.

Experiments of Robertson and Birnbaum [40] showed that the intergranular crack advances along the deformation zone that follows the contour of the boundary rather than along the boundary interface. It was also reported [40] that the advance of transgranular cracks, in both vacuum and hydrogen, occurs by the direct emission of dislocations from crack tip or by a process of void nucleation and growth ahead of the crack; the generation and the velocity of dislocations as well as the crack propagation rate were markedly increased by the presence of hydrogen. Robertson and Birnbaum concluded that the effect of hydrogen is to decrease the stress required for crack advance and to localize the deformation; macroscopically this confinement of the plastic deformation to a narrow zone gives the impression of a brittle type fracture.

Lassila and Birnbaum [70] found that slow straining of nickel with a relatively uniform distribution of hydrogen can allow appreciable amounts of diffusive segregation of hydrogen to GBs during testing, and it lead to an increase in the extent of intergranular fracture relative to that observed at fast strain rates.

Eastman et al. [75] investigated the effect of hydrogen on the plastic deformation in nickel with different carbon (C) content with the emphasis on the behaviour at very low strains and low strain rates (of the order of 10^{-5}-10^{-8}). According to their results, at very low C-concentration hydrogen results in solution hardening. However, at moderate C-concentration the addition of hydrogen results in solution softening during slow strain rate tests and at low plastic strains [75].

Consequences of H-dislocation interactions on contribution of hydrogen to the flow stress were reported by Girardin and Delafosse [76] who studied the hydrogen effect on nickel single crystals. In Figure 1.18, stress-strain curves for H-free and H-charged specimens are presented. One may see that the yield stress increases in the presence of hydrogen (this hardening effect is attributed to the viscous drag of H-solute atmospheres [76, 77]). In stage I, a unique slip system is active and a very low work hardening rate is observed.

In stage II, the introduction of hydrogen results in a significant increase of the work hardening corresponding to the activation of secondary slip systems [76, 77].

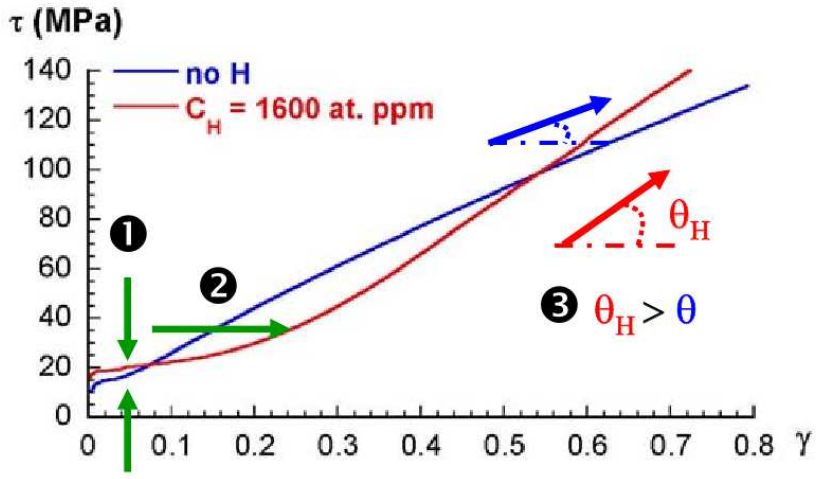

Figure 1.18: True stress-strain (normalised by the shear modulus, with $\mu = 75\ GPa$) curves of non-charged and hydrogen-charged nickel single crystals oriented for single slip [76].

The role of plasticity in establishing the conditions for hydrogen-induced crack initiation and propagation in the mode of intergranular fracture in nickel were discussed recently in the work of Martin and co-workers [78]. It was noted that in addition to the role in raising the local stress through work hardening, the deformation processes appear to contribute to forming significant hydrogen content at grain boundaries.

1.7 Summary

• The modelling of hydrogen embrittlement of metals requires the consideration of two aspects: (a) hydrogen transport in the metals to know solute distribution, and (b) hydrogen effect on the material behaviour which is mediated by its interaction with microstructural imperfections.

• The numerical simulations of hydrogen effect on material behaviour can be performed at different scales: scale of a vacancy, a dislocation, a crack in metal/hydrogen systems composed of several hundreds or thousands of atoms, or at the scale of laboratory tests (specimens with cracks or notches).

• The review of the data presented in the literature shows that to rationalize the apparent contradiction of material behaviour and to explain the discrepancies that can be observed in the magnitude of the hydrogen-induced changes in the material behaviour, the experimental conditions (hydrogen charging conditions, strain rate, temperature) and material structure (grains size, geometry of specimens, chemical composition, phase transformations) have to be carefully controlled.

Chapter 2

Simulation of hydrogen diffusion in polycrystals of 316L steel

2.1 Introduction

The process that precedes the embrittlement of a metal is the hydrogen transport. Hence, it is necessary to know the hydrogen distribution and its dependence on stresses and trapping for understanding and prediction of the material behaviour.

The numerical analyses of H-diffusion in which stresses and trapping have been taken into account simultaneously were developed in works of Sofronis and McMeeking [79, 80] and Krom et al. [81,82]. The hydrogen transport problem was studied in conjunction with large elasto-plastic deformations in the vicinity of a blunting crack tip in bcc material (impure iron). The effect of hydrostatic stress [79] and strain rate [81] on the H-diffusion were estimated. Considering the hydrogen distribution, two peaks were found on the concentration profile. The one is observed at the crack tip and corresponds to the maximum of plastic strain. The second peak of hydrogen concentration corresponds to the location of maximum hydrostatic stress ahead of the crack tip.

In the more recent work of Novak et al. [50], double- and single-notched bend testing clearly revealed that whereas ductile fracture in the H-free AISI 4340 steel (bcc) specimens is strain-controlled as the fracture initiated directly at the notch root where the local strains are highest, the local fracture event for the initiation of brittle fracture in the presence of hydrogen is stress-controlled as the fracture initiated ahead of the notch root,

near the elastic-plastic interface where the local tensile stresses attain maximum value.

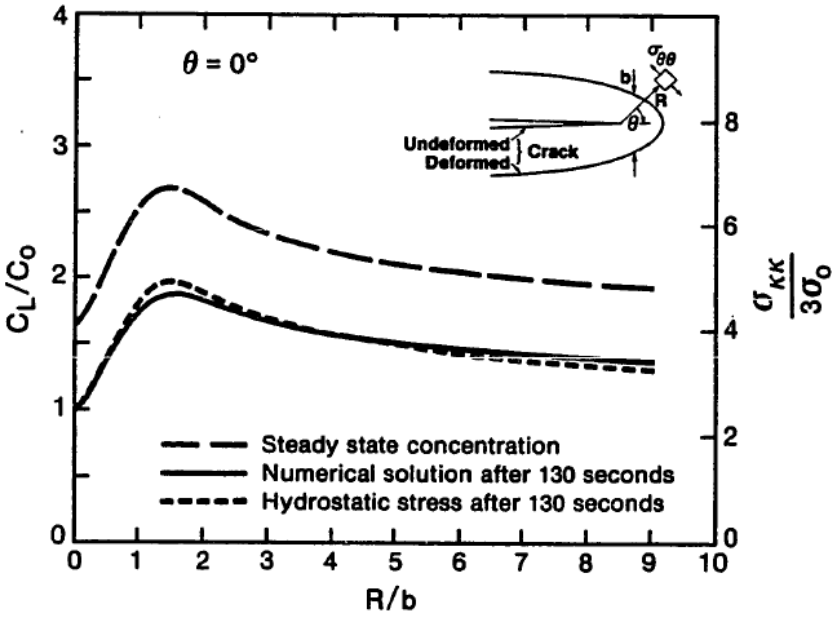

Figure 2.1: Plot of hydrogen concentration in normal lattice sites, hydrostatic stress and corresponding steady state concentration versus distance for impure iron after 130 seconds ($\sigma_0 = 250\ MPa$) [79].

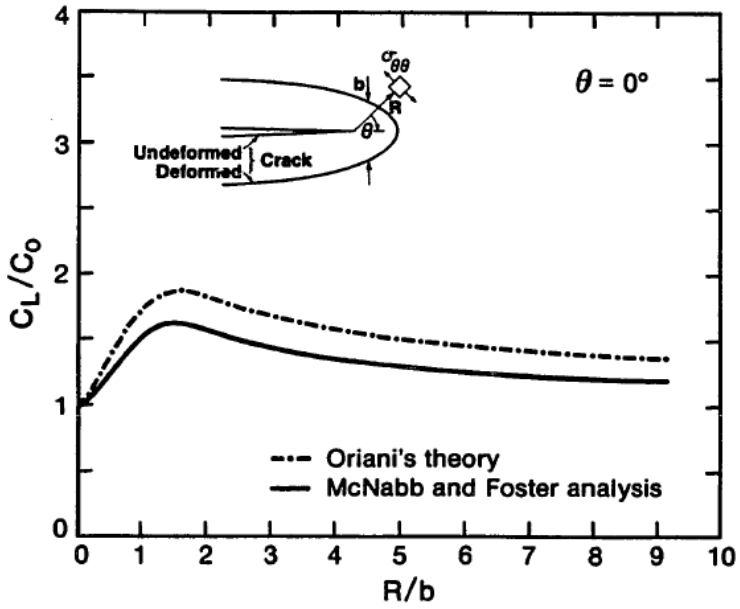

Figure 2.2: Plot of hydrogen concentration in normal lattice sites versus distance for impure iron after 130 seconds calculated using Oriani's equilibrium theory and McNabb and Foster approach [80].

The results of Sofronis and McMeeking and Krom et al. indicate that H-atoms in trapping sites determines the total hydrogen content in bcc iron. To describe hydrogen trapping, Sofronis and McMeeking [79] as well as Krom et al. [81] used the approach of Oriani [31] which is based on the local equilibrium of hydrogen in traps and in normal interstitial lattice sites. Sofronis demonstrated [80] that McNabb and Foster analysis of trapping [30] can be also used to compute hydrogen populations in a plastically deforming material. Concentrations in normal lattice sites were shown to develop in the same way as in Oriani's model (Figure 2.2). The difference was found to be attributed to the specific values of parameters utilized for describing trapping and untrapping rates. No effect of this parameters was found for the concentrations in trapping sites which were configured according to plastic straining of the material. However, it is necessary to note that the analysis of hydrogen transport in the vicinity of the crack tip carried out by Sofronis is valid only for low strain rates [82].

Due to elastic anisotropy, strong hydrostatic stress gradients are expected to be encounted in polycristalline materials under mechanical loading even without notch or crack. The resolution of an explicit polycrystalline microstructure computation can precise the stress-strain field and, hence, the hydrogen transport in the specimen during loading. A hydrogen diffusion analysis in which the material microstructure was taken into account was recently proposed by Reza et al. [83, 84]. Hydrogen heterogeneity was found mainly close to grain boundaries (Figure 2.3).

In the present chapter, the results of the study of the influence of stress field on the evolution of hydrogen in the context of microstructural mechanics by a one-way coupled analysis are presented. In our work, we adopted the crystal plasticity-hydrogen diffusion approach presented by Reza et al. A more simple way to solve the hydrogen diffusion problem was found, and a new numerical scheme proposed in [85] for the resolution of hyperbolic and parabolic equations was implemented. In-house diffusion code was developed in the framework of this PhD study and used for the computations on synthetic polycrystalline aggregates of stainless 316L steel. The results presented by Reza et al. were revisited and it was found that the finite element mesh used in the work of Reza et al. does not provide sufficient accuracy of diffusion computations in zones with high stress gradients. To obtain accurate results, we provide a carefully constructed mesh for each polycrystalline aggregate.

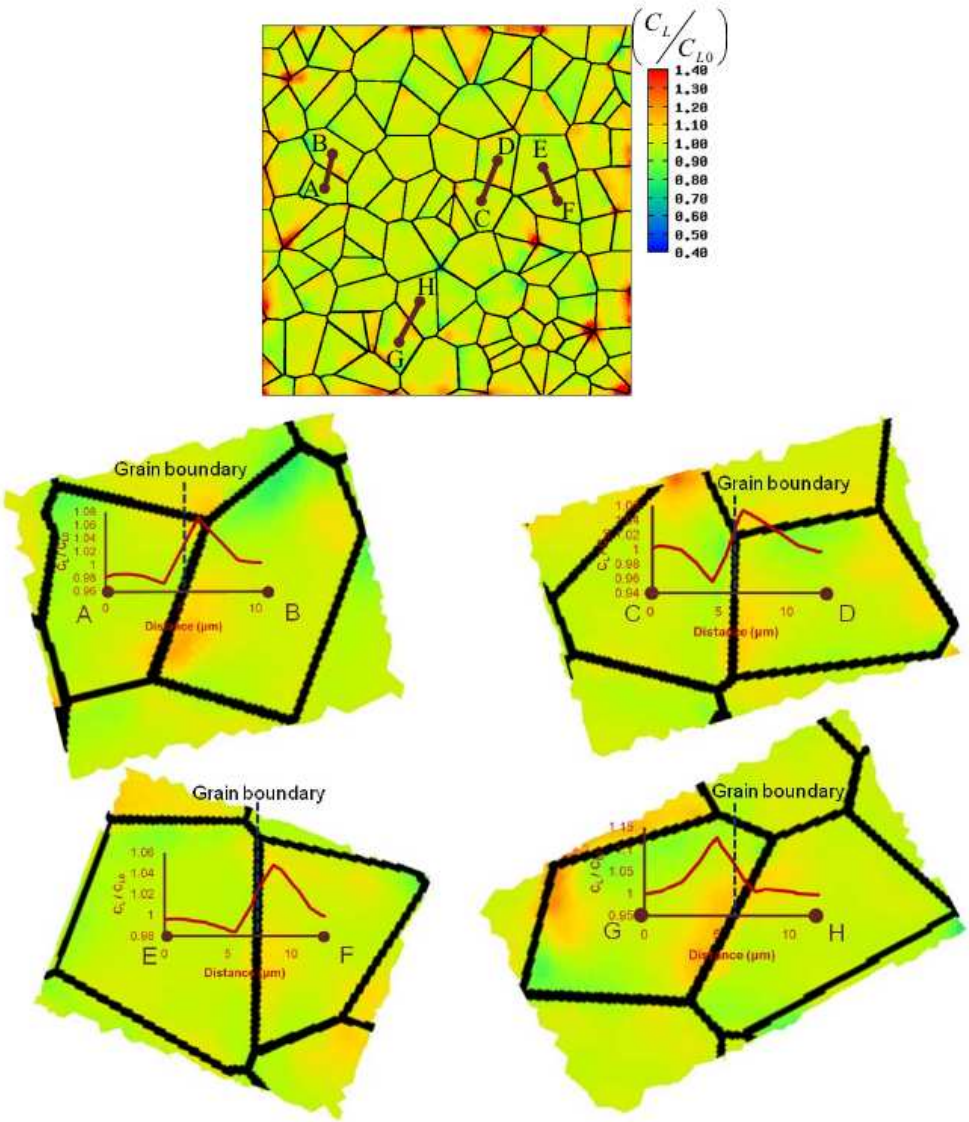

Figure 2.3: Contour of hydrogen concentration in normal interstitial lattice sites in polycrystalline 316L steel and its profiles along the indicated paths [83].

In the following sections, we first describe the hydrogen diffusion model and the numerical scheme used to solve hydrogen transport equations. Then, the formulation of crystal plasticity model is given. Grain geometry in polycrystals and finite element meshes used in the simulations are shown. The effect of microstructure-induced stress-strain heterogeneity on the evolution of hydrogen is studied considering several artificial polycrystalline aggregates of 316L steel with different grain geometries and crystal orientation sets.

2.2 Hydrogen transport in metals

2.2.1 Hydrogen transport model

According to the model used hydrogen atoms being adsorbed and absorbed into the metal specimen can reside at normal interstitial lattice sites (NILS) or saturable and reversible traps. Traps are assumed to be isolated, i.e. there is no interaction between occupied sites. Hydrogen is transported by lattice diffusion, dislocation transport is not considered. Oriani's equilibrium theory [31] is used to describe the relation between trapped and normal populations:

$$\frac{1-\theta_L}{\theta_L}\frac{\theta_T}{1-\theta_T} = K_T, \tag{2.1}$$

where θ_L is a hydrogen occupancy of NILS, θ_T denotes the hydrogen occupancy of trapping sites, K_T is an equilibrium constant such that $K_T = e^{-\Delta E_T/RT}$ with ΔE_T as a trap binding energy. This theory can be used if the time in which a change of C_L occurs by lattice diffusion in the normal population is sufficiently long to accomplish the change in trapped population which is usually the case.

The concentration in NILS can be expressed as

$$C_L = \theta_L N_L, \tag{2.2}$$

where N_L is a number of NILS per unit lattice volume and it is given by

$$N_L = \frac{N_A \beta \rho}{A_r}, \tag{2.3}$$

β is the number of interstitial lattice sites per solvent (metal) atom, N_A is Avogadro's number, ρ is the density of the metal and A_r is the atomic weight of the solvent atom.

The concentration in traps may be written

$$C_T = \theta_T N_T, \tag{2.4}$$

where N_T denotes the number of trapping sites per unit lattice volume. If only dislocation traps generated by plastic straining are considered then the trap density may be estimated by using the lattice parameter information. We consider fcc systems and assume one hydrogen trap per atomic plane threaded by a dislocation. Hence, the number of trapping sites can be expressed as

$$N_T = \frac{\rho_d}{d}, \tag{2.5}$$

where ρ_d - dislocation density, d is a distance between two (111) planes

$$d = \frac{a}{\sqrt{3}}, \tag{2.6}$$

a denotes the lattice parameter.

Considering a body volume V with surface S, using the mass conservation law we can write that the rate of change of total hydrogen concentration inside V is equal to the flux through S:

$$\frac{\partial}{\partial t}\int_V (C_L + C_T)dV + \int_S \vec{J}\cdot\vec{n}dS = 0 \tag{2.7}$$

where n is an outward-pointing unit normal vector and J denotes a hydrogen flux.

Chemical potential gradients constitute the driving force for the diffusion. If the concentration is low there is no interaction between the diffusing species, the rate of diffusion depends only on a hydrogen mobility [86]. Then the hydrogen flux can be related to the chemical potential gradient as:

$$J = -\frac{D_L C_L}{RT}\nabla\mu \tag{2.8}$$

where D_L is a lattice diffusion constant that is assumed to be independent of stress, R - gas constant, T - absolute temperature. The chemical potential for a system under external stress at a constant pressure and temperature can be written as

$$\mu = \mu_0 + RT\ln\frac{C_L}{N_L} + \mu_\sigma \tag{2.9}$$

where μ_0 is the chemical potential at a reference state and μ_σ is a stress dependent part of μ. A strain field caused by hydrogen in metal is assumed to be dilatational only [87]. Then

$$\mu_\sigma = -\sigma_h V_H \tag{2.10}$$

where σ_h denotes the hydrostatic stress and V_H is a partial molar volume of hydrogen

Substitution (2.9) and (2.10) into (2.8) results in

$$J = -D_L\nabla C_L + \frac{D_L C_L V_H}{RT}\nabla\sigma_h. \tag{2.11}$$

After substituting (2.11) into (2.7) and applying the divergence theorem for an arbitrary volume, we obtain the hydrogen transport equation with a drift term:

$$\frac{\partial C_L}{\partial t} + \frac{\partial C_T}{\partial t} - D_L\Delta C_L + \nabla\cdot(C_L\frac{D_L V_H}{RT}\nabla\sigma_h) = 0 \tag{2.12}$$

If we consider only very low C_L, $\theta_L << 1$, Oriani's equilibrium formulation may be written as

$$\frac{1}{\theta_L}\frac{\theta_T}{1-\theta_T} = K_T. \tag{2.13}$$

Using (2.2) and (2.4) we can express explicitly the H-concentration in traps in terms of C_L and N_T

$$C_T = \frac{C_L N_T K_T}{C_L K_T + N_L} \tag{2.14}$$

The required information for N_T can be obtained experimentally. The system of equation (2.12) and (2.14) is solved numerically by the finite element method. The numerical scheme is described in the following section.

2.2.2 Numerical scheme for the hydrogen transport equation

In the present work the equation (2.12) was descretized by using Galerkin methods for the first three terms and the N-scheme for the advection term [85].

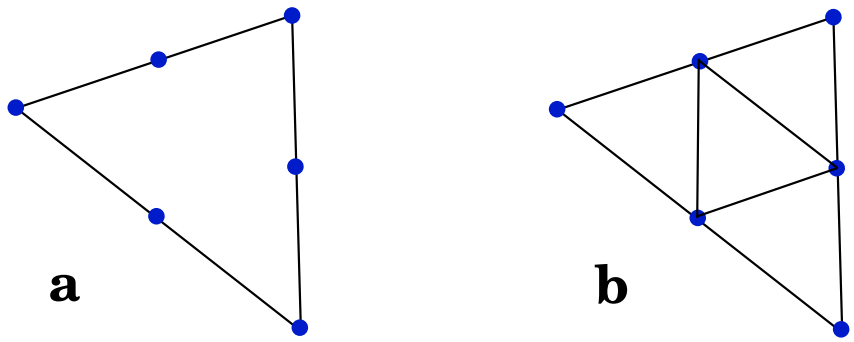

Figure 2.4: Triangle elements used in the finite element calculations. (a) Six-node triangles used in the FE computations of stresses and strains. (b) Three-node triangles constructed from the six-node elements were used for linear approximations in the diffusion computations.

Two finite element meshes are used. The first (original) mesh consists of six-node triangles and it is used for the quadratic approximation of stress. The second one consists of three-node triangular elements, each element is constructed from the original six-node triangle by connecting middle nodes of the triangle and it is implemented for the linear approximation of concentration on sub-elements (Figure 2.4).

The discretized diffusion equations (2.12) and (2.14) are written as follows:

$$|A_i|\frac{C_L^{i,n+1}-C_L^{i,n}}{t^{i,n+1}-t^{i,n}}+|A_i|\frac{C_T^{i,n+1}-C_T^{i,n}}{t^{i,n+1}-t^{i,n}}+D_L\sum_{K:i\in K}|K|\nabla N_K^i\cdot\nabla C_L^n+\sum_{K:i\in K}\Phi_K^{i,*}=0, \quad (2.15)$$

$$C_T^{i,n+1}=\frac{C_L^{i,n+1}N_T^{i,n+1}K_T}{C_L^{i,n+1}K_T+N_L},\ C_T^{i,n}=\frac{C_L^{i,n}N_T^{i,n}K_T}{C_L^{i,n}K_T+N_L} \quad (2.16)$$

where $C_L^{i,n+1}$ and $C_L^{i,n}$ denote NILS concentrations in the nodes with a number i at times $t^{i,n+1}$ and $t^{i,n}$ respectively, $C_T^{i,n+1}$ and $C_T^{i,n}$ denotes the trap concentration, $|K|$ is an area of the triangle containing the node with the number i, $|A_i|$ defines an "area of the node" which is equal to the sum of the areas of all the triangles containing the node i divided by 3 (the volume of the pyramid with unit height in other words):

$$|A_i|=\sum_{K:i\in K}\frac{|K|}{3}. \quad (2.17)$$

N_K^i denotes a linear shape function (basis function) on the element K that is equal to one in the node i and zero in the other two vertices of the triangle. $\Phi_K^{i,n}$ denotes a component of the divergence of hydrogen flux to the node i from the element K and it is calculated by using N-scheme:

$$\Phi_K^i=\langle k_i\rangle(C_L^i-\tilde{C}),\ \langle k_i\rangle=Max(k_i,0),\ k_i=-\frac{1}{2}\vec{v}\cdot\vec{n}_i \quad (2.18)$$

where $\vec{n}_i$ is an outward scaled normal to the opposite side of i in K, $\vec{v}$ denotes the average velocity on the element:

$$\vec{v}=\frac{1}{3}(\vec{v_1}+\vec{v_2}+\vec{v_3}) \quad (2.19)$$

$\vec{v}_1$, $\vec{v}_2$, $\vec{v}_3$ are velocities (stress gradient) in the nodes of element K:

$$\vec{v}_j=\frac{D_L V_H}{RT}\nabla\sigma_h^j. \quad (2.20)$$

Finally,

$$\tilde{C}=\left(\sum_j\langle k_j\rangle C_L^j-\Phi_K^{tot}\right)/\sum_j\langle k_j\rangle,\ \Phi_K^{tot}=\int_K div\left(\frac{D_L V_H}{RT}\nabla\sigma_h\right) \quad (2.21)$$

where quadratic (six-node) shape functions are used to approximate σ_h.

2.3 Crystal plasticity model

In the present work, we consider only the case where the plastic deformation is the result of dislocation slip. Twinning and vacancy diffusion are not considered (as well as the grain boundary mechanism). The model is written in the framework of viscoplasticity.

In the "micro-macro" approach to model the tensile or cyclic behaviour of a polycrystalline aggregate, the constitutive equations are introduced at the microscopical level which is the slip system. In this work, a fully anisotropic elasticity tensor is considered for modelling the elastic response of the polycrystal. To simulate the corresponding plastic behaviour, a crystal plasticity model is implemented.

The kinematic used in the field of crystal plasticity [88] conforms to the classical multiplicative decomposition of the deformation gradient

$$F = F_e F_p, \tag{2.22}$$

whose elastic part F_e comprises a small lattice deformation and possibly a large rigid body rotation. The elastic part, F_p, is assumed to be solely related to the slip deformation occurring in discrete crystallographic slip systems, s, characterized by unit vectors lying along the slip direction, l^s, and the normal to the slip plane, n^s. The evolution of the plastic deformation can be expressed as the superposition of all crystallographic slip rates, $\dot{\gamma^s}$, as follows:

$$\dot{F_p} = L_p F_p, \;\; L_p = \sum_{s=1}^{N} \dot{\gamma}^s l^s (n^s)^T. \tag{2.23}$$

The following variables are used:

- the elastic strain tensor, ε^e , associated with the macroscopic stress tensor, σ ,
- a vector of kinematic state variables, $\{\alpha^s\}_{s=1}^N$, associated with a vector, $\{x^s\}_{s=1}^N$,
- a vector of isotropic state variables, $\{q^s\}_{s=1}^N$.

The macroscopic strain, ε, is divided into an elastic and viscoplastic part:

$$\varepsilon = \varepsilon^e + \varepsilon^v \tag{2.24}$$

The shear strain rate or "slip rate", $\dot{\gamma^s}$, is related to the macroscopic viscoplastic strain rate, $\dot{\varepsilon^v}$, by

$$\dot{\varepsilon^v} = \sum_{s=1}^{N} m^s \dot{\gamma}^s, \;\; \dot{\varepsilon^v_{ij}} = \sum_{s=1}^{N} m^s_{ij} \dot{\gamma}^s. \tag{2.25}$$

The driving force for the plastic slip is based on the Schmid law:

$$\tau^s = m^s : \sigma = \sum_{i=1}^{3}\sum_{j=1}^{3} m_{ij}^s \sigma_{ij}, \tag{2.26}$$

where

$$m_{ij}^s = \frac{1}{2}(n_i^s l_j^s + n_j^s l_i^s),\ s = 1, ..., N\ ,$$

where τ^s is the resolved shear stress, which is computed for each slip system, $N = 12$ for fcc metals considered in the present work.

The slip rate depends on the resolved shear stress of the slip system, as well as on the kinematic and isotropic hardening, which, in turn, depends on all slip systems. The constitutive equations have to relate $\dot{\gamma^s}$ to τ^s. Two phenomenological isotropic and kinematic hardening variables are introduced at the micro-scale. They represent the mechanical effect of the microstructural state. The kinematic hardening is linked to the long range internal stresses due to the formation of dislocation cell structures or dislocation pile-ups. Dislocation pile-ups take place mainly at precipitates and grain boundaries. Short range interaction of dislocations are described by the isotropic hardening variables, r^s , which take into account the interaction with forest dislocations or cross-slip.

To calculate the shear stress on one slip system properly, the mobile and fixed dislocations have to be taken into account. The kinematic long range stress field, x^s, lowers the applied shear stress calculated by the Schmid law. The mobile dislocations are under an effective stress field, τ_{eff}^s, which is the superposition of the kinematic hardening, x^s, and the applied stress, τ^s:

$$\tau_{eff}^s = \tau^s - x^s. \tag{2.27}$$

If the effective shear stress is bigger than the threshold, the system enters the plastic regime.

Using a rate dependent flow rule, the crystallographic slip rate is expressed as a power law function of the slip system resolved shear stress, τ^s, as follows:

$$\dot{\gamma}^s = sign(\tau^s - x^s)\left\langle \frac{|\tau^s - x^s| - r^s}{k} \right\rangle^n, \tag{2.28}$$

$$\langle arg \rangle = Max(arg, 0) \text{ and } sign(arg) = \begin{cases} -1, & \text{if } arg < 0 \\ 0, & \text{if } arg = 0 \\ 1, & \text{if } arg > 0 \end{cases}$$

where k and n are viscosity parameters, and r^s is:

$$r^s = r_0 + q \sum_{r=1}^{N} h^{sr}(1 - exp(-b\nu^r)), \tag{2.29}$$

where r_0 is the critical resolved shear stress, and h^{sr} is a hardening matrix accounting for self ($r = s$) and latent ($r \neq s$) hardening, q and b are phenomenological constants.

By integrating the positive slip rate $\dot{\nu}^r$ in which $\dot{\nu}^r = |\dot{\gamma}^r|$, the accumulated slip can be calculated. The cumulative slip of one system can be quantified independently of the slip direction (which can change during the deformation mode) as follows:

$$\nu^r(t) = \int_0^t |\dot{\gamma}^r(u)| du. \tag{2.30}$$

x^s is the force associated with the kinematic state variable α^s which can be written in the form of vector. The kinematic hardening can be written as a nonlinear evolution of x^s as follows:

$$x^s = c\alpha^s, \tag{2.31}$$

$$\dot{\alpha}^s = \dot{\gamma}^s - d\dot{\nu}^s \alpha^s, \tag{2.32}$$

where c and d are material constants.

2.4 Modelling on a polycrystalline aggregate

To investigate the influence of stress field on the evolution of hydrogen in the context of microstructural mechanics, an uncoupled analysis has been established. Synthetic 2D microstructures containing about 110 grains were obtained by using the tools of microstructure generation GMICRO [89]. In the present work we did not take into account specific properties of grain boundaries: GBs are simply geometrical lines separating neighbouring grains. Each aggregate contains about 20,000 linear triangular elements and 40,000 nodes. The structural analysis was performed using the code ZeBuLoN [90]. Random crystal orientation sets were used: distribution of disorientation angle for each aggregate is close to Mackenzie distribution (the details are given in Appendix).

The uncoupled analysis was carried out on the artificial polycrystalline structure of austenitic stainless steel 316L taking into account the negligible effect of hydrogen on the local softening of this type of steel caused by very low H-diffusivity in this type of steel.

First we carried out the crystal plasticity analysis using the code ZeBuLoN. After completion of the structural analysis, the in-house diffusion code was implemented. Displacements, strains and stresses were transferred step by step from the results of structural analysis to the diffusion code.

2.4.1 Numerical simulation: initial and boundary conditions

The polycrystalline aggregate is located in the hydrogen chamber. This system can be useful in the case of boundary value problem in which the Dirichlet boundary conditions are imposed (for example, constant concentration can not be imposed on the boundary of the polycrystal since the solution for the problem of diffusion in the aggregate under mechanical loading does not exist in this case).

The geometry is shown in Figure 2.5. The size of the aggregate is 0.1 by 0.1 mm (0.2 by 0.2 mm with the hydrogen chamber).

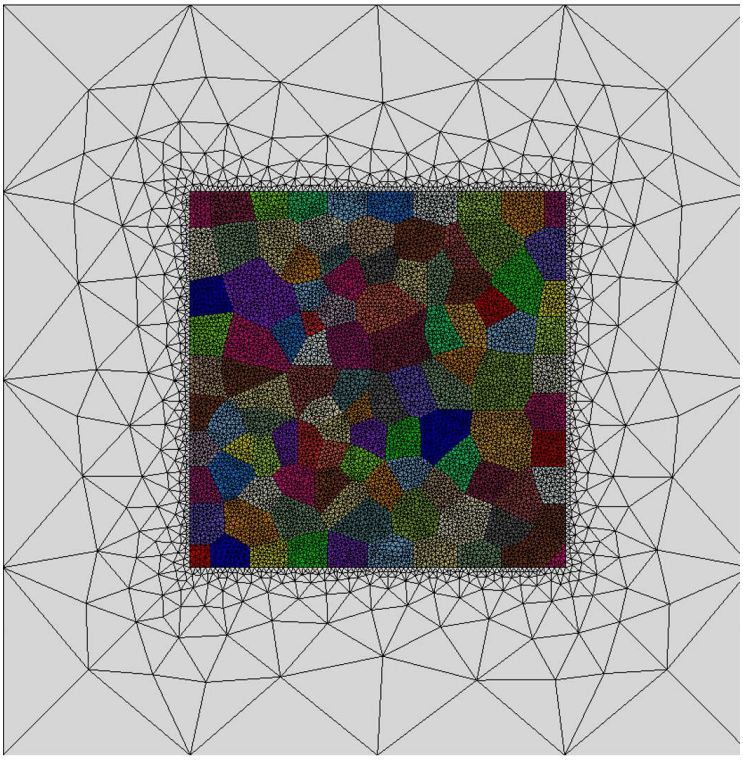

Figure 2.5: Geometry and mesh for one of the aggregates.

The uniform hydrogen concentration in the chamber and in the aggregate as dictated by Sievert's law at a pressure of $p = 20MPa$ and a temperature of $T = 300K$ was used as initial conditions:

$$C = \alpha\sqrt{\frac{p}{p_0}}exp\left(-\frac{\Delta H_S}{RT}\right) \tag{2.33}$$

where C is a total concentration of dissolved hydrogen in equilibrium with gaseous hydrogen at pressure p, α is a constant, $p_0 = 0.1MPa$ (atmospheric pressure) and ΔH_S denotes the relative partial molar heat of solution. When the solution is dilute, ΔH_S is nearly independent of temperature, hydrogen concentration and pressure. R denotes the gas constant and T is the absolute temperature. According to Mine et al. [91], under the assumed conditions applying (2.33) for the steel 316L, $\Delta H_S = 6,860J/mol$, the maximum total hydrogen content C is 5 mass ppm (i.e. $C = 2.313 \times 10^{25} atom/m^3$). At the beginning, the trap density is assumed to be equal to zero (in the absence of plastic deformation). Hence, as initial conditions for the diffusion problem one may choose:

$$C_{L0} = 2.313 \times 10^{25} atom/m^3,\ C_{T0} = 0 \tag{2.34}$$

and as a boundary condition (on the edge of the hydrogen chamber):

$$C_L = 2.313 \times 10^{25} atom/m^3,\ C_T = 0,\ \vec{J} \cdot \vec{n} = 0 \tag{2.35}$$

where J - hydrogen flux and n is the outward unit normal vector.

For the crystal plasticity problem, the boundary conditions consist of prescribed displacements on the bottom and top edges of the aggregate. The specimen is subjected to tensile loading up to 2.2% total strain.

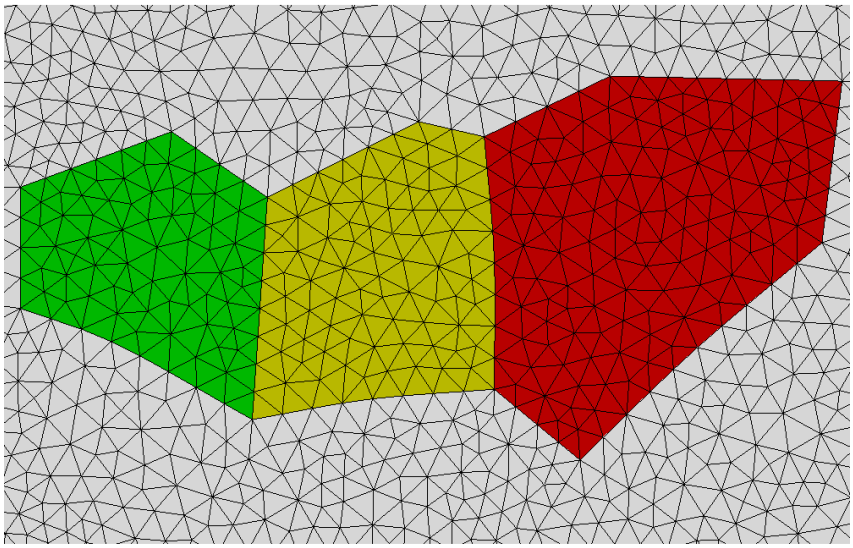

Figure 2.6: Grain shapes and mesh used in the modelling of H-diffusion in polycrystalline aggregates.

The finite element mesh consists of 19874 quadratic six-node (39748 linear three-node for the diffusion computation) triangular elements (79536 global degrees of freedom). 2000 time steps with automatic stepping in case of divergence have been used in the structural analysis. For numerical accuracy and stability, smaller steps are required in the diffusion analysis in which 50 sub-steps for each time step of structural analysis were added.

Parameters needed in the crystal plasticity analysis are collected in Table 2.1. An anisotropic model was considered for modelling the elastic response of the polycrystal in which non-zero components are: $E_{1111} = 206GPa$, $E_{1122} = 133GPa$, $E_{1212} = 119GPa$ (cubic elasticity tensor). Table 2.2 tabulates the parameters for the analysis of hydrogen evolution in 316L steel.

Table 2.1: Material parameters for crystal plasticity modelling.

Viscosity parameter, k	50 $MPa \cdot s^{(1/n)}$
Viscosity parameter, n	25
Critical shear stress, r_0	75 MPa
Phenomenological constant, q	125 MPa
Phenomenological constant, b	2
Hardening matrix components, h^{sr}	1

Table 2.2: Parameters for hydrogen diffusion analysis in case of steel 316L

Lattice diffusivity, D_L	$2.8 \times 10^{-16}\ m^2 \cdot s^{-1}$
Gas constant, R	$8.3144\ J \cdot mol^{-1} \cdot K^{-1}$
Temperature, T	$300\ K$
Partial molar volume of hydrogen, V_H	$1.65 \times 10^{-6}\ m^3 \cdot mol^{-1}$
Lattice sites per unit volume, N_L	$1.69 \times 10^{29}\ m^{-3}$
Trap binding energy, ΔE_T	$-13.5 \times 10^3\ J \cdot mol^{-1}$
Lattice parameter, a	$(3.597 \pm 0.003) \times 10^{-10}\ m$
Material density, ρ	$7.89 \times 10^3\ Kg \cdot m^{-3}$
Avogadro's number, N_A	$6.0232 \times 10^{23}\ mol^{-1}$
Atomic weight of the solvent atom, A_r	$56.3 \times 10^{-3}\ kg \cdot mol^{-1}$
Number of NILS per solvent atom, β	2

Using Eq. 2.5, the number of trapping sites is computed on the base of dislocation density of 316L at different amounts of equivalent plastic strains calculated from experimental data by Feaugas [92]. Data points are collected in Table 2.3. In this study, to establish the relationship between the number of traps and the equivalent plastic strain, the cubic spline interpolation was implemented (to avoid the Runge's phenomenon occurring).

Table 2.3: Data points for ρ_d with respect to the amount of equivalent plastic strain

Equivalent plastic strain, ε_p	Dislocation density, ρ_d
3.0×10^{-5}	10^{10}
3.5×10^{-3}	3.55×10^{13}
8.4×10^{-3}	7.01×10^{13}
1.4×10^{-2}	1.04×10^{14}
3.0×10^{-2}	2.23×10^{14}
6.4×10^{-2}	6.43×10^{14}
1.7×10^{-1}	1.11×10^{15}
3.6×10^{-1}	8.86×10^{14}

2.5 Results

First, the analysis carried out by Reza et al. [83] has been reproduced on the same polycrystalline aggregate but using the explicit residual distribution scheme for the discretization of hydrogen transport equation [85]. Our results are in a good agreement with results presented by Reza et al.: hydrogen diffuses mainly in the vicinity of grain boundaries at strain rates of the order of 10^{-5} and 10^{-6} s^{-1}.

To study the effect observed, three artificial polycrystals (three different grain geometries) with different grain orientation sets were tested.

2.5.1 Hydrogen in trapping sites

In Figure 2.7, temporal evolution of macroscopic tensile stress is shown. It is seen that longer than 90% of time the polycrystalline aggregate is subjected to plastic deformation. It means that dislocation trap sites are available during most of time of diffusion. However, the estimation of hydrogen content in trapping sites after the loading shows that H-concentration in traps is less than 1% of total concentration:

$$\frac{\int_V C_T dV}{\int_V (C_L + C_T) dV} < 0.01, \tag{2.36}$$

i.e. the effect of hydrogen trapping on the evolution of total concentration is small.

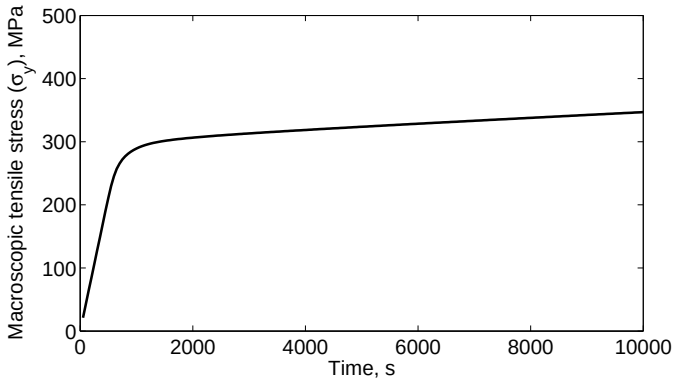

Figure 2.7: Temporal evolution of macroscopic tensile stress. Strain rate: $2.2 \cdot 10^{-6}$ s^{-1}.

Table 2.4 collects maximum values of normalised hydrogen concentration in traps for all the aggregates studied.

Table 2.4: Maximum values of C_T/C_{L0} in the bulk region.

Aggregate-Set	$max(C_T/C_{L0})$
1	0.0128
2	0.0132
3	0.0147
4	0.0121
5	0.0146
6	0.0114
7	0.0110
8	0.0135
9	0.0133

Figure 2.8a displays the H-concentration in trapping sites calculated for the aggregate shown in Figure 2.5. It can be seen that the regions of maximum concentration correspond to the bands of maximum plastic deformation (Figure 2.8b).

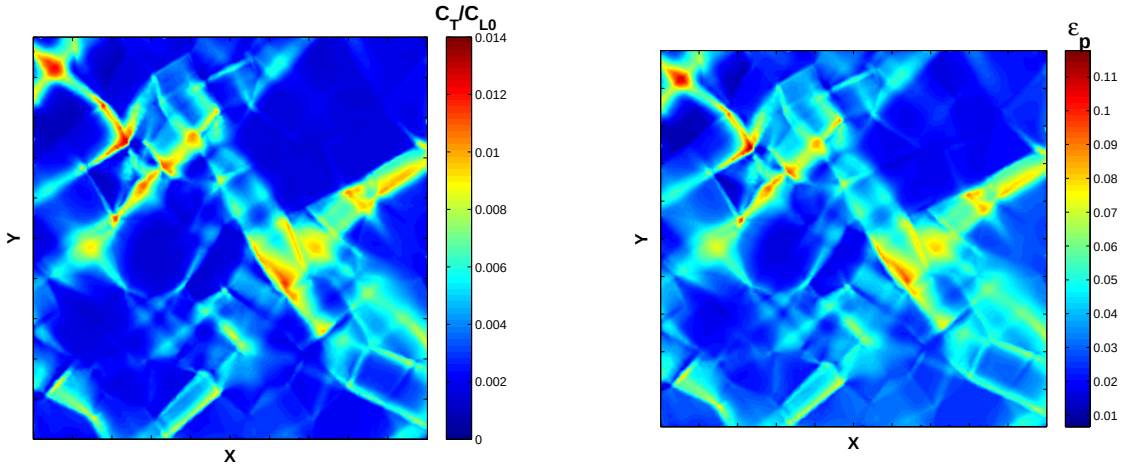

a) b)

Figure 2.8: (a) Normalised concentration of hydrogen in trapping sites and (b) the von Mises equivalent strain calculated for the aggregate shown in Figure 2.5. Total strain: 2.2%.

2.5.2 Hydrogen in normal lattice sites

Table 2.5 presents the maximum values of hydrogen concentration in NILS found for the aggregates investigated. Steady state concentrations are computed using the analytical solution derived for the steady state problem in the case of insulated system:

$$C_L(x,y) = \frac{\int_V C_{L0}dV - \int_V C_T(x,y)dV}{\int_V exp(\frac{V_H\sigma_h(x,y)}{RT})dV} \cdot exp(\frac{V_H\sigma_h(x,y)}{RT}). \tag{2.37}$$

Table 2.5: Maximum and minimum values of C_L/C_{L0} in the bulk region.

Aggregate-Set	Transient solution		Steady state
	$max(C_L/C_{L0})$	$min(C_L/C_{L0})$	$max(C_L/C_{L0})$
1	1.2655	0.8479	1.3123
2	1.1499	0.8223	1.2525
3	1.1965	0.8419	1.3504
4	1.2250	0.7351	1.2723
5	1.2793	0.8350	1.3266
6	1.2923	0.8307	1.3210
7	1.3016	0.8029	1.3444
8	1.1793	0.7649	1.3746
9	1.2585	0.8031	1.3292

Figure 2.9 displays the temporal evolution of hydrogen in normal interstitial sites for the aggregates shown in Figure 2.5. For the same aggregate, the cumulative distribution functions of the hydrogen concentration at all the nodes of FE model are plotted in Figure 2.10. Such a representation allows to describe statistically hydrogen redistribution during loading. The increases of H-concentration spread with deformation show the evolution of hydrogen heterogeneity and, hence, the progressive establishment of H-enriched/depleted zones within the microstructure. Similar cumulative distribution functions are found for all the computed aggregates.

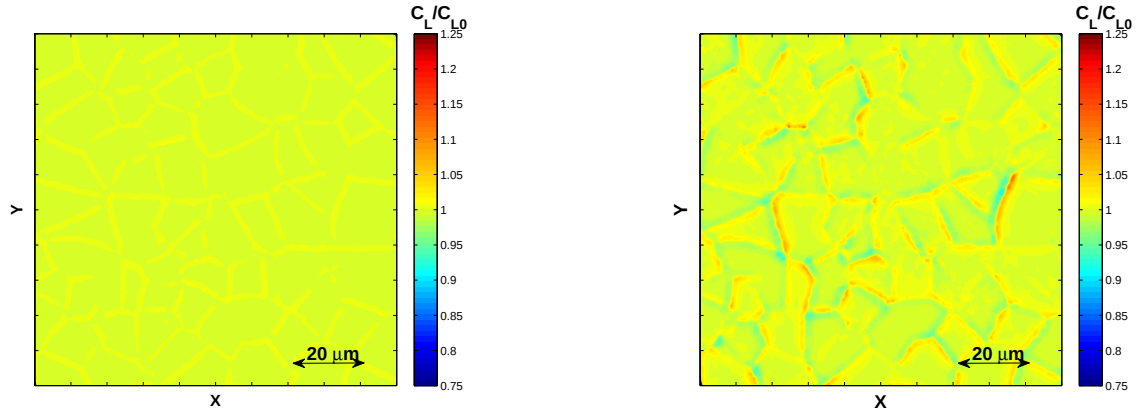

a) time: 500 s, strain: 0.11%

b) time: 2906 s, strain: 0.64%

c) time: 6738 s, strain: 1.48%

d) time: 10 000 s, strain: 2.2%

Figure 2.9: Temporal evolution of hydrogen in NILS. Color maps of C_L/C_{L0} are plotted.

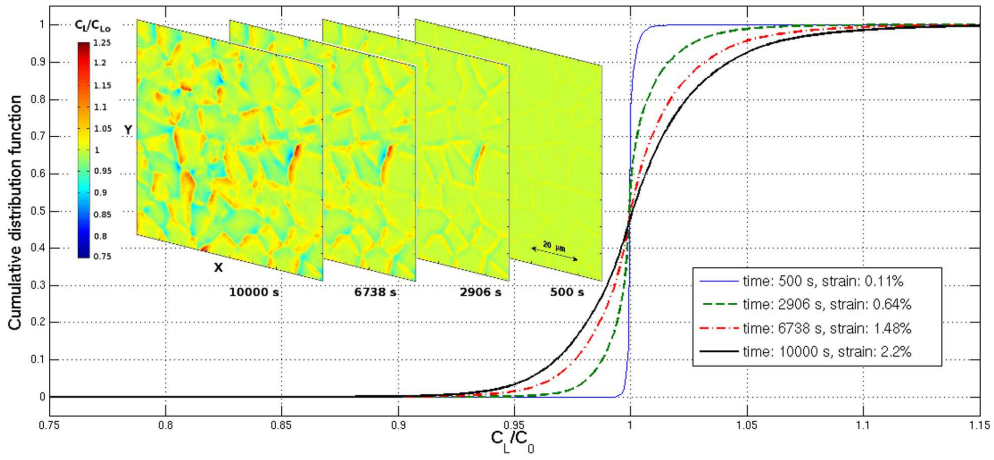

Figure 2.10: Hydrogen concentration cumulative distribution functions and maps at time 500 s, 2906 s, 6738 s and 10 000 s. Strain rate: $2.2 \cdot 10^{-6}\ s^{-1}$.

Figure 2.11 shows the hydrostatic stress field computed in the aggregate (corresponding to Figures 2.5) and the associated H-concentration maps obtained at different strain rates. The hydrostatic stress field (Figure 2.11a) is strongly heterogeneous and much higher stress gradients are observed nearby GBs compared to the bulk of grains. For the strain rates 2.2×10^{-5} s^{-1} (Figure 2.11b) and 2.2×10^{-6} s^{-1} (Figure 2.11c) the H-redistributions are observed mostly close to GBs since the diffusivity is low. The analysis of the temporal evolution of H-concentration reveals that hydrostatic stress gradients nearby GBs initiate the migration of H-atoms from one grain to the other. Hydrogen diffuses trough the GB to the grain where hydrostatic stress is higher. As a result H-depletion on one side of the GBs and H-enrichment on the other side occur.

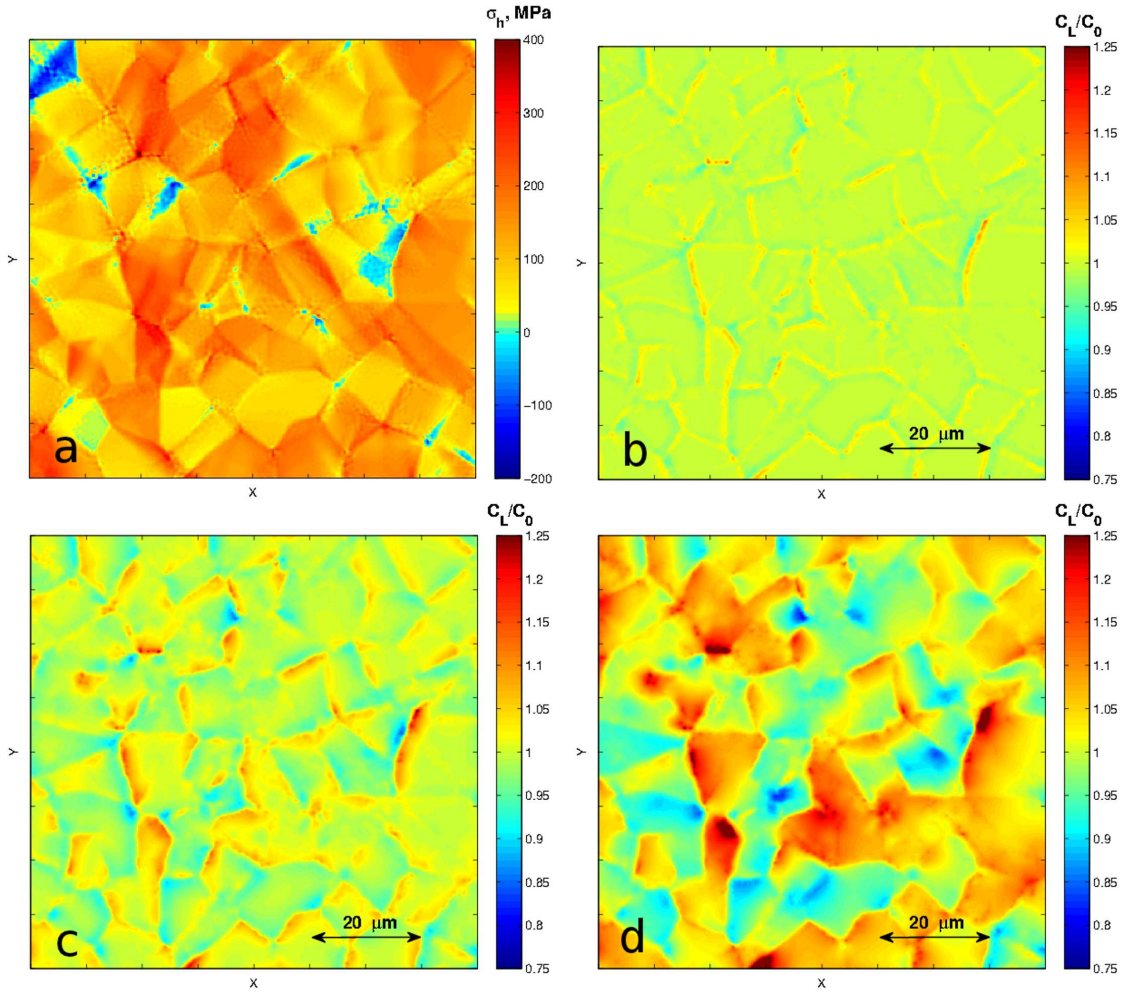

Figure 2.11: Results of mechanical (a) hydrostatic stress field and diffusion computations (H-distribution) at 2.2 % total strain at different strain rates, b) $2.2 \cdot 10^{-5}$ s^{-1}, c) $2.2 \cdot 10^{-6}$ s^{-1} and d) $2.2 \cdot 10^{-7}$ s^{-1}.

The time for the diffusion at strain rates $2.2\times10^{-5}\ s^{-1}$, $2.2\times10^{-6}\ s^{-1}$ and $2.2\times10^{-7}\ s^{-1}$ is 1,000 s, 10,000 s and 100,000 s respectively. At strain rate $2.2 \times 10^{-7}\ s^{-1}$ hydrogen has much more time to diffuse (Figure 2.11d). At this strain rate, the contrast of H-concentration in the microstructure is the highest and is observed at the grain scale as well as at the mesoscopic scale (group of neighbouring grains). This result is consistent with the known effect of the strain rate on the occurrence of hydrogen embrittlement (Chapter 1).

In Figure 2.12, the nine aggregates studied are shown after binarization of the grain average concentration maps (see Figure A.1 and Appendix A) corresponding to the strain rate of $2.2 \cdot 10^{-7}\ s^{-1}$. In this figure, each row corresponds to the same grain geometry, knowing that orientation sets are all different for the nine aggregates. Black grains correspond to an average normalised concentration higher than 1.0 (average enrichment of the grain) and white grains are depleted ones. The fraction of saturated grains is statistically a half of the total number of grains in the aggregates. The isolated enriched/depleted grains are occasional. Both the geometry and orientation set vary the clustering of grains enriches/depleted is observed. Therefore, the observed trend of clustering is characteristic for the aggregates without texture. Hydrogen - plasticity interactions will be the highest in the saturated clusters.

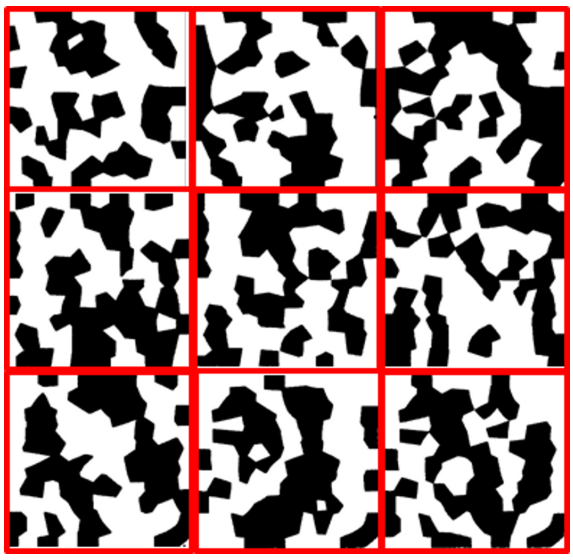

Figure 2.12: Binarized images of the grain average normalised H-concentration on the nine aggregates studied. The H-enriched grains are black. Strain rate: $2.2 \cdot 10^{-7}\ s^{-1}$. Total strain: 2.2 %.

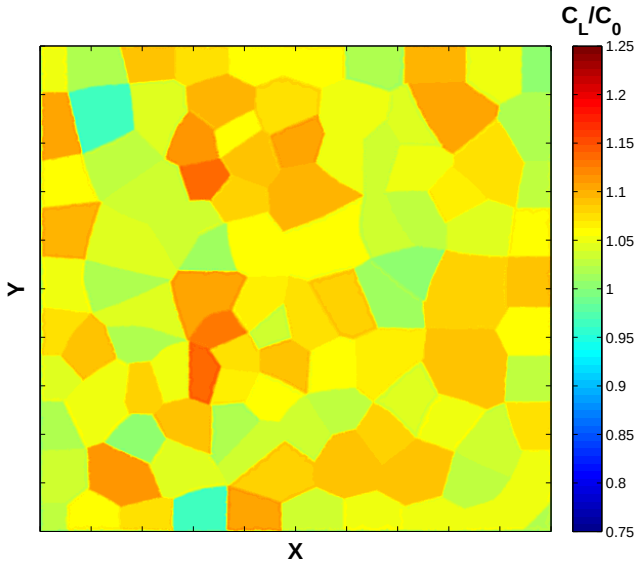

Figure 2.13: Aggregate-1, orientation set-1. Grain average concentration of hydrogen in NILS corresponding to the strain rate of $2.2 \cdot 10^{-7}$ s^{-1} and total strain of 2.2 %.

2.6 Discussion

The first thing which is noted to be different in the results of the simulations presented in this chapter from the results of the calculation reported by Sofronis and McMeeking [79] and by Krom [81] is the negligible fraction of trapped hydrogen in the total amount of H-solutes in 316L steel. According to Sofronis and McMeeking and Krom the concentration in trapping sites (namely, dislocation traps) determines the distribution of hydrogen near the blunting crack tip in the sample of impure iron. In contrast with this finding, the present study demonstrates that trapping of hydrogen by dislocations does not affect noticeably the distribution of hydrogen in the polycrystals of fcc 316L steel. The amount of hydrogen in traps is less than 1%, and the total concentration is determined by hydrogen in normal interstitial lattice sites.

Estimating the maximum value of a number of trapping sites from the experimental data given by Feaugas [92] as $N_T^{max} = 5.34495 \times 10^{24}$ and considering saturable traps, we can obtain the following assessment ($C_{L0} = 2.313 \times 10^{25} atom/m^3$):

$$\frac{C_T}{C_{L0}} = \frac{\theta_T N_T}{C_{L0}} \leq \frac{N_T}{C_{L0}} \leq \frac{5.34495 \times 10^{24}}{2.313 \times 10^{25}} \approx 0.23 \tag{2.38}$$

The estimation of the maximum hydrogen concentration in trapping sites for the iron specimen with blunting crack tip considered by Sofronis and McMeeking [79] is given below. The initial concentration ($C_{L0} = 2.084 \times 10^{21}\ atom/m^3$) and the maximum number of traps ($N_T^{max} = 3.162 \times 10^{23}\ atom/m^3$) are adopted from the work of Sofronis and McMeeking:

$$\frac{C_T}{C_{L0}} = \frac{\theta_T N_T}{C_{L0}} \leq \frac{N_T}{C_{L0}} \leq \frac{3.162 \times 10^{23}}{2.084 \times 10^{21}} \approx 151.74 \tag{2.39}$$

This assessment shows that, in contrast with bcc metals, it is the H-concentration in the normal interstitial lattice sites that determines the total concentration in fcc 316L stainless steel.

It is worth mentioning that in the present work the effect of trapping by dislocations was modelled assuming one trap site per plane threaded by dislocation (similar to the assumption of Sofronis and McMeeking and Krom). Assuming, for example, five or ten trap sites per plane, the amount of hydrogen in trapping sites will be higher by a factor of five or ten, respectively. In addition, higher magnitudes of trap binding energy, ΔE_T, will result in an increase of hydrogen population in traps (the equilibrium constant K_T

will increase). However, the latter can results also in some effect of trapping kinetics, and the assumption of local equilibrium may not be valid. This will be discussed in following chapters considering the impact of grain boundary trapping which is not taken into account here.

Since the distribution of hydrogen in polycrystals of 316L steel is determined by the concentration in normal interstitial lattice sites, the hydrostatic stress field plays the crucial role in the evolution of hydrogen in this material. In turn, the hydrostatic stress heterogeneity is determined by the crystal orientation set. Different orientations of crystals in the polycrystalline aggregate result in the inhomogeneous stress field from both elastic (due to elastic anisotropy) and plastic (due to different orientations of slip systems) deformations. It can be expected that the presence of texture in the material will affect the results observed for polycrystals with random orientation sets studied in this chapter. However, the preliminary analysis of texture effect (see Appendix) shows that it is not remarkable and does not change significantly the degree of hydrostatic stress heterogeneity (and, as a result, the extent of hydrogen redistribution). At the same time, it was noticed that the texture affects equivalent plastic strain field in polycrystalline 316L steel which, in turn, determines hydrogen trapping. The amount of hydrogen in traps is negligible in comparison with the normal lattice population in this material. However, the effect of texture can be significant in bcc metals where the effect of trapping is higher.

2.7 Summary

• The approach used in this chapter allows to take into account stress-strain heterogeneities at the microscopic scale and to describe hydrogen evolution in polycrystals under mechanical loading.

• The analysis was carried out with different crystal orientation sets and grain geometries of the polycrystalline aggregates. The results show that H-concentration in trapping sites is negligible in 316L stainless steel in comparison with hydrogen content in NILS. For low strain rate, hydrogen redistribution in the vicinity of GBs finally leads to the hydrogen segregation in clusters of grains with high hydrostatic stresses.

• The modelling and numerical scheme used in the present work are suitable for contributing to the prediction of the hydrogen effect on fcc materials.

Chapter 3

Hydrogen diffusion across grain boundaries

In Chapter 2, the results of hydrogen diffusion simulation in the austenitic polycrystalline 316L steel suggest that H-interstitials redistribute in the microstructure under mechanical loading due to the presence of stress-strain heterogeneities. The effect of hydrogen trapping was shown to be negligible compared to the quantity of H-solutes in normal interstitial lattice sites, and the stress-driven flux determines the diffusion in fcc polycrystalline aggregates. The analysis of hydrostatic stress distributions and concentration evolution in the polycrystals indicate that H-atoms redistribute locally between neighbouring grains. H-interstitials moving from one grain to the other where hydrostatic stress is higher have to cross the interface between grains. It is known that grain boundaries have specific structures, properties different from the bulk and can affect diffusion. Most of the studies of diffusion at grain boundaries and their impact on the effective diffusivity in polycrystalline materials usually focus on the effect of fast transport along boundaries, so called *short circuit paths*. Fewer works were devoted to the problem of the diffusion across interfaces. Since the width of boundaries is very small (about 0.5 nm), it is still unclear to what extent they can influence H-transport in polycrystals and what is the grain size dependence. In the first part of the present chapter, we review the data presented in the literature which support the necessity to study the effect of grain boundary transverse diffusion. In the second part, employing the one-dimensional atomic layer model, the impact of boundaries is analysed locally on nickel bicrystals and globally by

considering the diffusion in a nickel membrane in which several interfaces are parallel to the surface.

3.1 Introduction

3.1.1 Segregation to grain boundaries

Grain boundary (GB) segregation is of great importance since it generally affects the structure and chemistry of interfaces and influences many of physical properties of materials. This phenomenon has been the subject of research over decades [93–95].

An intensive study of GB segregation started in the 1970s and was reinforced by the development of surface analysis techniques, in particular Auger electron spectroscopy (AES). Since that time, considerable progress has been achieved in understanding this phenomenon. It is now well recognized that solute or impurity segregation substantially affects the basic properties of grain boundaries: energetics, kinetics, cohesion, mobility and electrochemical behaviour, and that in turn results in a change of many related materials properties such as creep embrittlement, recrystallization, diffusion creep, temper brittleness, hydrogen and liquid metal embrittlement, intergranular corrosion, stress corrosion cracking and sintering [94].

Since the 1970s the solute segregations were measured mainly in polycrystalline materials. The results of these measurements provide good estimation of segregation behaviour and thermodynamic parameters. However, all the data obtained from experiments with the polycrystals represent some average value over all the grain boundaries in these samples [94] and, hence, depend on crystal orientation set. The development of analysis techniques in the 1980s enabled the study of the segregation parameters of individual GBs in bicrystals [96]. Later, other techniques such as Atom-Probe Field Ion Microscopy (AP-FIM), high resolution Transmission Electron Microscopy (TEM) and more recently Atom Probe Tomography [97, 98] made possible to investigate the solute segregation at individual sites of selected GBs.

For the measurement of segregation characteristics using direct Auger electron spectroscopy analysis, the sample need to be fractured *in situ* along a grain boundary. However, this procedure limits the application only to intrinsically brittle materials, such as ceramics and some intermetallic compounds, and are practically impossible in most pure metals [99], [100]. In addition, the sensitivity of the Auger analysis is limited and a considerable fraction of a monolayer of segregated solute is required for detection.

In general, solute segregation can be considered as the result of an interaction between a "chemical" defect (foreign atom in an homogeneous bulk) and a structural defect of a material [94]. The driving force for this process is defined as the difference of the free energy between two states:

(I) a foreign atom dissolved in the bulk, and

(II) the foreign atom in a structural defect.

A general theory of segregation to interfaces was developed by Guttmann in the 1970s on the basis of thermodynamic description of distribution of different types of species between two phases, i.e. bulk and interface [94]. Considering interactions between all possible combinations of atoms and assuming that all species occupy the same area in the boundary, Guttmann theory can be expressed in a generalized form for a multicomponent system by

$$\frac{X_I^{\Phi}}{X^{0\Phi} - \sum_J^{M-1} X_J^{\Phi}} = \frac{X_I}{1 - \sum_J^{M-1} X_J} \exp\left(-\frac{\Delta F_{seg}}{kT}\right), \tag{3.1}$$

where X_I^{Φ} and X_I are the mole fractions of element I at the interface Φ and in the bulk respectively, and $X^{0\Phi}$ is the total ratio of all sites available at the interface. The free energy of segregation, ΔF_{seg}, is

$$\Delta F_{seg} = \Delta H_I^0 - T\Delta S_I^0 - 2\alpha_{MI}(X_I^{\Phi} - X_I) + \sum_{J\neq I}^{M-1} \alpha_{MIJ}(X_J^{\Phi} - X_J), \tag{3.2}$$

where ΔH_I^0 and ΔS_I^0 are the standard molar enthalpy and entropy of segregation in a dilute binary $M-I$ system in which no interaction exists, α_{MI} and α_{MIJ} are the parameters for binary interaction between atoms I in the matrix M, and for ternary interaction between atoms I and J in the same matrix respectively. All the parameters which appear in Eq.(3.2) depend on the type of the interface. The entropy of segregation depends on the temperature. The interaction parameters, α_{MI} and α_{MIJ}, alter with temperature and additional solutes in the system [94]. This multiple parametric dependence reflects the complexity of the equilibrium segregation to GBs.

An assumption of a binary $M-I$ system without interaction simplifies Equations (3.1) and (3.2) to the well-known form of Langmuir-McLean segregation equation:

$$\frac{X_I^{\Phi}}{X^{0\Phi} - X_I^{\Phi}} = \frac{X_I}{1 - X_J} \exp\left(-\frac{\Delta F_{seg}}{kT}\right) \tag{3.3}$$

with

$$\Delta F_{seg} = \Delta H_I^0 - T\Delta S_I^0. \tag{3.4}$$

This equation represents an analogy to the Langmuir gas adsorption isotherm and is the most frequently used segregation equation for binary systems. This approach ignores any interaction of solute atoms, and the energy of segregation, ΔF_{seg}, is assumed to be constant over the grain boundary and independent of the interface coverage below one monolayer.

3.1.2 Grain boundary trapping kinetics

In material science, thermodynamics is the study of equilibrium states in which state variables do not change with time, and kinetics is the study of the rates at which systems that are out of equilibrium change under the influence of various forces [93]. The thermodynamic description of segregation (trapping) to grain boundaries provides valuable information about the final equilibrium state of a system. As it was already mentioned in Chapter 1, the assumption of local equilibrium is mostly used for describing the hydrogen trapping in metals. Kinetic processes of hydrogen trapping are rapid, and the equilibrium is usually assumed to be nearly satisfied locally [31, 50, 79]. However, it is unclear how the trapping kinetics can affect the evolution of concentrations of H-solutes in the case of an interface acting as a trapping wall.

Concerning the aspect of segregation kinetics, some works are worth to be mentioned [94]. The kinetics of GB trapping (segregation) was first described by McLean by applying the Fick's laws for the diffusion from two semi-infinite half crystals taking into account a constant enrichment factor $s = c_{gb}(\infty)/c_g$ with the volume concentration c_g and the boundary concentration c_{gb} at time $t \to \infty$. With $c_{gb}(0)$ at $t = 0$ the model gives for $c_{gb}(t)$

$$\frac{c_{gb}(t) - c_{gb}(0)}{c_{gb}(\infty) - c_{gb}(0)} = 1 - \exp\left(\frac{4D_g t}{s^2\delta^2}\right)\left[1 - erf\left(\frac{4D_g t}{s^2\delta^2}\right)^{1/2}\right], \tag{3.5}$$

where D_g is the diffusivity in the bulk (grain) and δ is the GB width.

Since the segregation kinetics are similar for both the grain boundaries and the free surfaces the McLean solution can be applied for the former. In general, however, the approach to equilibrium after the McLean model is too slow due to the oversimplified assumption $s = c_{gb}(\infty)/c_g$ is constant and impede the interpretation of the surface segregation data measured [94, 101].

To explain the experimental results of surface segregation of Sn on Cu [101], for example, Hofmann and Erlewein used the atomic layer model [102]. For the sufficiently high free energy of segregation, ΔF_{seg}, the solution is given by [94]

$$\frac{c_{gb}(t) - c_{gb}(0)}{c_{gb}(\infty) - c_{gb}(0)} = c_{bulk}\left[1 + \frac{2}{\delta}\left(\frac{D_g t}{\pi}\right)^{1/2}\right]. \tag{3.6}$$

Figure 3.1 shows the time dependence of the surface enrichment and subsurface composition distribution of Sn on Cu which perfectly reproduces the experimental data [101,102].

There are many examples of successful use of Eq. 3.6 in the literature [94].

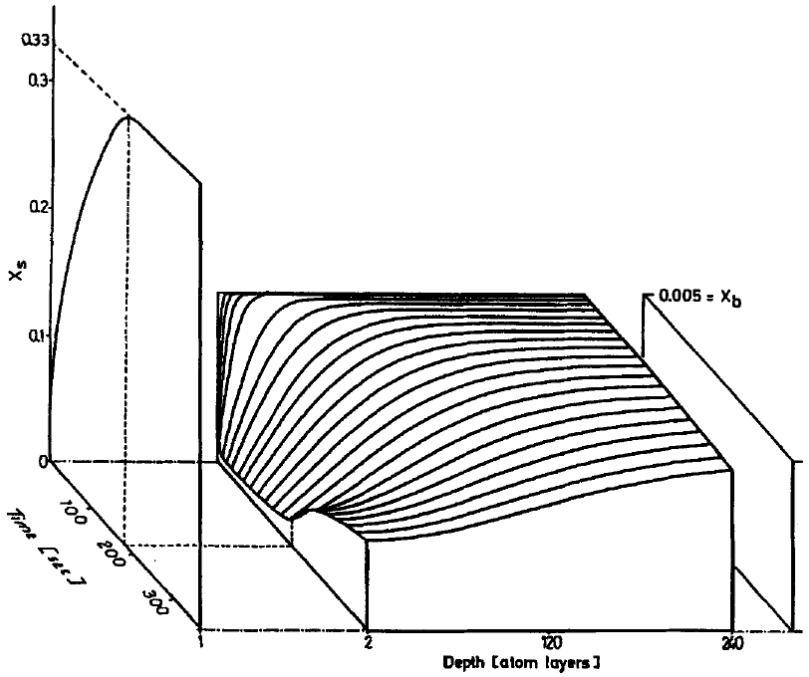

Figure 3.1: Time dependence of the surface enrichment and subsurface composition distribution of Sn on Cu [102].

In principle, the segregation process to free surfaces is similar to enrichment of grain boundaries [94]. Hence, the atomic layer approach, used by Hofmann and Erlewein [102] in the modelling of surface enrichment, can be practically useful in the study of grain boundary diffusion and segregation.

3.1.3 Anisotropy of grain boundary diffusion

The rate of grain boundary diffusion strongly depends on the detailed atomic structure of the interface. It is known that diffusivity along grain boundaries varies from small to high-angle boundaries [93]. This concerns the rate of diffusion both along and across GB. Most of the studies of diffusion at GBs and their impact on the effective diffusivity in polycrystalline materials usually focus on the effect of fast transport along boundaries. However, this property is valid for substitutional diffusion and is questionable in the case of H-interstitial diffusion.

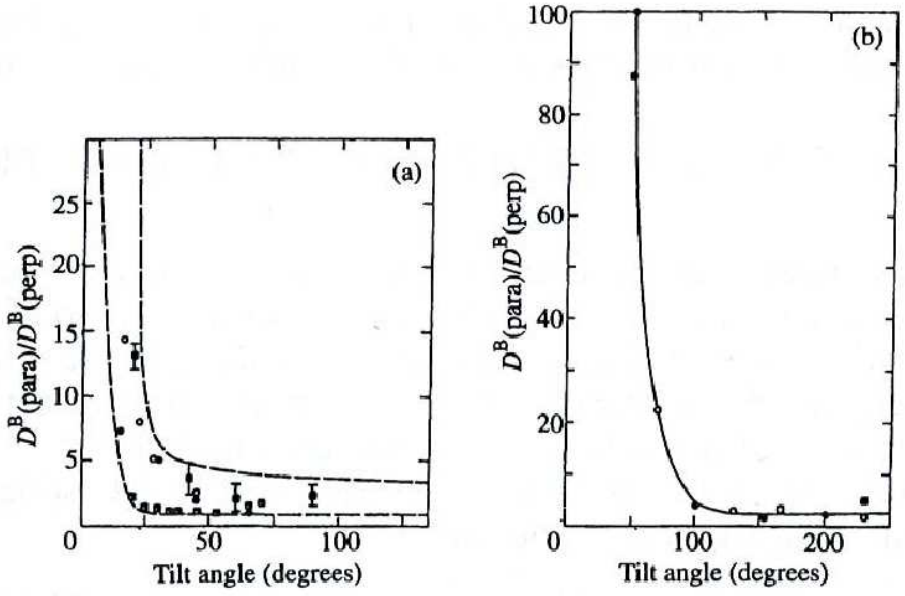

Figure 3.2: Ratio of boundary diffusion parallel to the tilt axis, D^B(para), and perpendicular to the tilt axis, D^B(perp), for $\langle 001 \rangle$ symmetric tilt boundaries as a function of tilt angle, θ. (a) Values for metal systems. Open circles, Ag^{110} tracer in Ag; filled circles, Al^{28} tracer in Al; filled squares, Zn^{63} tracer in Al; half-filled squares, Ag^{110} tracer in Cu. (b) Values for ionic systems. Open circles, Cr^{51} tracer in Al_2O_3; filled circles, Cr^{51} tracer in MgO; filled squares, Cr^{51} tracer in $MgAl_2O_4$; open squares, Cr^{51} tracer in MgO plus 0.45 at % Cr [103].

If the diffusivity of hydrogen at GBs is low, the effect of anisotropy is important since the diffusion rate across GB can affect the transport of solutes significantly and should be distinguished from the diffusion rate along GB.

Grain boundary diffusion anisotropy was detected first by Hoffman [104] who investi-

gated self diffusion at [011] tilt grain boundaries in silver and found that for small-angle misorientations between grains the anisotropy was especially strong being a factor of 15 faster along grain boundary than across it.

In both metallic and ionic systems, the measurements of grain boundary diffusion parallel and perpendicular to the tilt axis in [001] symmetric tilt boundaries were conducted by Stubican [103]. In Figure 3.2, it is seen that the diffusivity perpendicular to the tilt axis is less than parallel to the tilt axis, and the ratio $D^B(para)/D^B(perp)$ increases with decreasing the tilt angle.

The diffusion rate of Na ions through polycrystalline specimens (ion conductors) was found to be markedly reduced by the presence of grain boundaries which act as barriers to the normally rapid lattice diffusion [93,105]. Therefore, it is important to take into account the diffusion anisotropy (and trapping, as it was discussed in the previous sections) at interfaces to properly describe an evolution of diffusing atoms in a polycrystalline material.

Atomistic computer simulations also predict a significant anisotropy of grain boundary diffusion in metals and its dependence on the boundary structure [6, 106].

Pedersen and Jonsson [6] studied three different grain boundaries in aluminium $\Sigma5$ twist, $\Sigma5$ tilt and general, twist + tilt by using an adaptive kinetic Monte Carlo method. They found that these interfaces do not significantly enhance hydrogen diffusion. On the contrary, in some cases, they impede the diffusion quite significantly. In the case of diffusion perpendicular to the $\Sigma5$ twist boundary, the hydrogen transport is blocked by the grain boundary at room temperature due to high diffusion migration barriers (Figure 3.3). Pedersen and Jonsson found that the tilt and twist + tilt grain boundaries cause trapping within the boundary layer, the diffusion does not occur by hops between trapping sites within the interface, but rather when the hydrogen atom exits the grain boundary into one of the crystal grains. In the case of the twist + tilt grain boundary, the trapping is so strong that the H-atom spends about 99 % of the total simulated time in the grain boundary region. According to the estimation of Pedersen and Jonsson, the tilt and twist+tilt boundaries reduce the diffusivity respectively by a half and by an order of magnitude of the value for a perfect crystal.

Du et al. [7] investigated the interaction of H-interstitials with grain boundaries in α- and γ-Fe. Using the density-functional theory, they analysed the interface structure of $\Sigma3[1\bar{1}0](112)$ and $\Sigma5[001](310)$ grain boundaries in the ferromagnetic bcc α-iron and

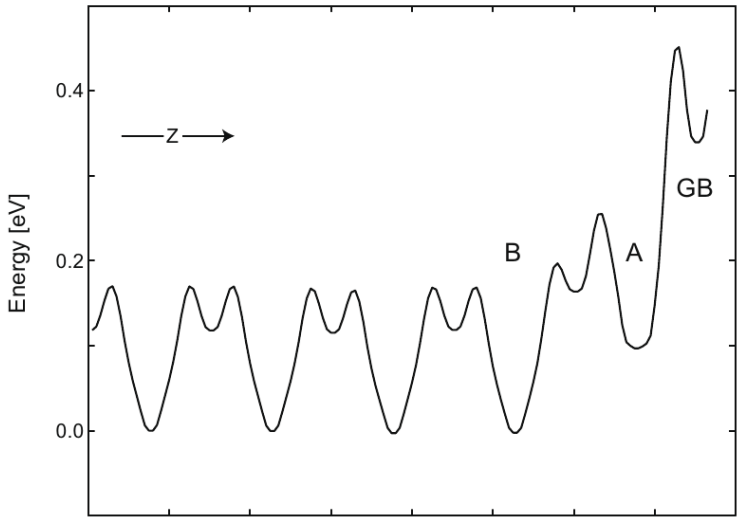

Figure 3.3: Minimum energy path for H-atom diffusion perpendicular to the plane of the Σ5 twist GB in aluminium. The feature is the large increase in energy close to the GB. This explains why the diffusion trajectory does not cross the GB during the simulation [6].

$\Sigma3[1\bar{1}0](111)$ and $\Sigma11[1\bar{1}0](113)$ boundaries for the nonmagnetic fcc γ-iron. In both α- and γ-Fe, Σ3 grain boundaries represent a low energy dense structure boundaries. In contrast, Σ5 and Σ11 boundaries are much more open structures (Figure 3.4).

Employing the nudged-elastic band method, Du et al. determined the energetic barriers for diffusion jumps between different sites in the grain boundary regions. For all the investigated interfaces, it was found that none provides a fast diffusion channel for H-atoms (in the low H-concentration limit). The close-packed Σ3 structures do not promote hydrogen diffusion and represent two-dimensional barriers. For Σ3 boundary in bcc Fe, the hydrogen migration barrier within interface is about 0.6 eV, which is much higher than the migration barrier in the bulk (≈0.1 eV). Thus, if a H-atom is trapped at the Σ3 boundary in bcc Fe, it becomes immobile. For the Σ3 grain boundary in fcc Fe, it was found that it is repulsive to hydrogen, that is similar to the interaction of hydrogen with the Σ5 twist boundary in aluminium reported in [6]. In the open Σ5 and Σ11 grain boundaries, H-atoms are still mobile since the diffusion paths exist with barriers (≈0.25 eV for Σ5 in bcc Fe and 0.7 eV for Σ11 in fcc Fe) comparable to the bulk values (≈0.1 eV in bcc and 0.6 eV in fcc Fe). However, the large barriers for hydrogen atoms to escape from the interfaces to the bulk region were found as for Σ5 in bcc so for Σ11 in fcc (≈0.57 eV and 0.9 eV, respectively).

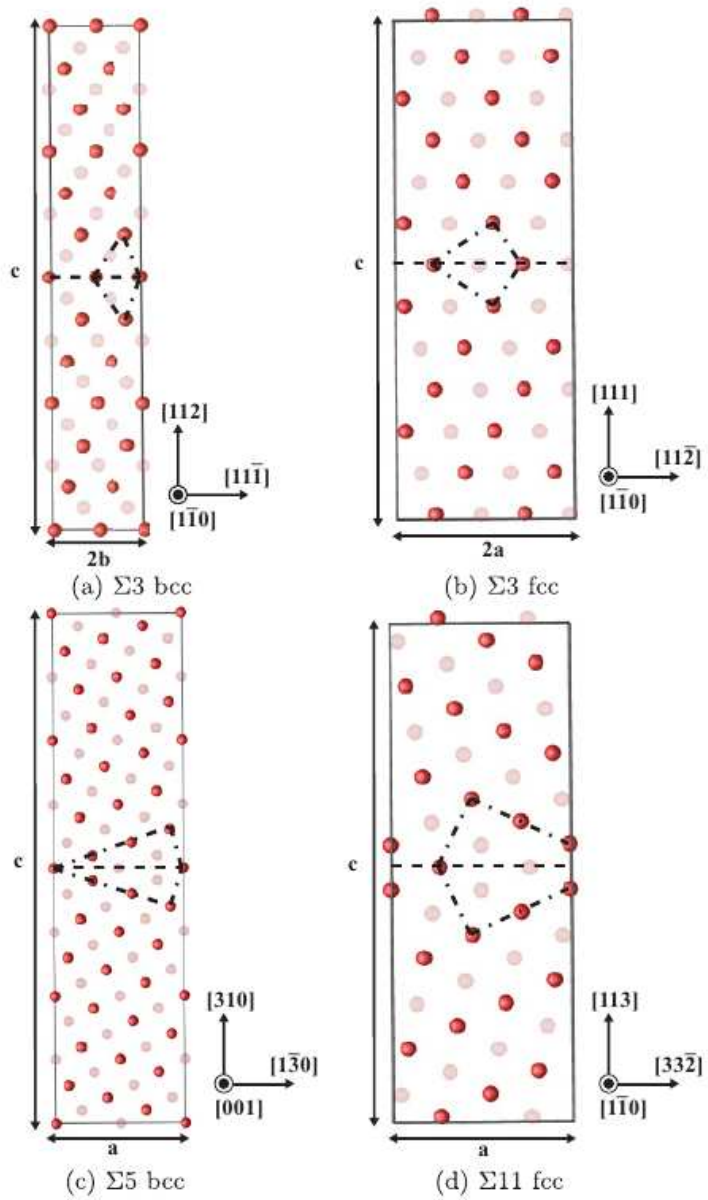

Figure 3.4: Supercells for the grain boudanries computed in [7]. The structures of the Σ3 boundaries in bcc and fcc iron are shown in (a) and (b), respectively. The more open interface structures of the Σ5 in bcc and Σ11 in fcc iron are shown in (c) and (d). The dashed-dotted lines indicate available free space at the respective interfaces.

Using the data about available interstitial sites, diffusion barriers and solution energies obtained from first-principle calculations in [7], Du et al. presented the results of the study of H-diffusion within different microstructures in bcc iron employing kinetic Monte Carlo simulations in [106]. The diffusion constant was calculated as the time-weighted average

of the diffusion constants for each segment, i, of kinetic Monte Carlo trajectory [106]:

$$D_{kk} = \sum_i D_{kk,i} \Delta t_i / t, \tag{3.7}$$

where Δt_i is a time length of segment i, and the diffusion constant $D_{kk,i}$ is computed from the mean square displacement of hydrogen atoms:

$$D_{kk,i} = \langle [r_k(t_i) - r_k(t_{i-1})]^2 \rangle / 2\Delta t_i. \tag{3.8}$$

Here $r_k(t_i)$ is a position of H-atom in k direction (with $k = x, y, z$) at time moment t_i, and the angle brackets denote the average over all particles.

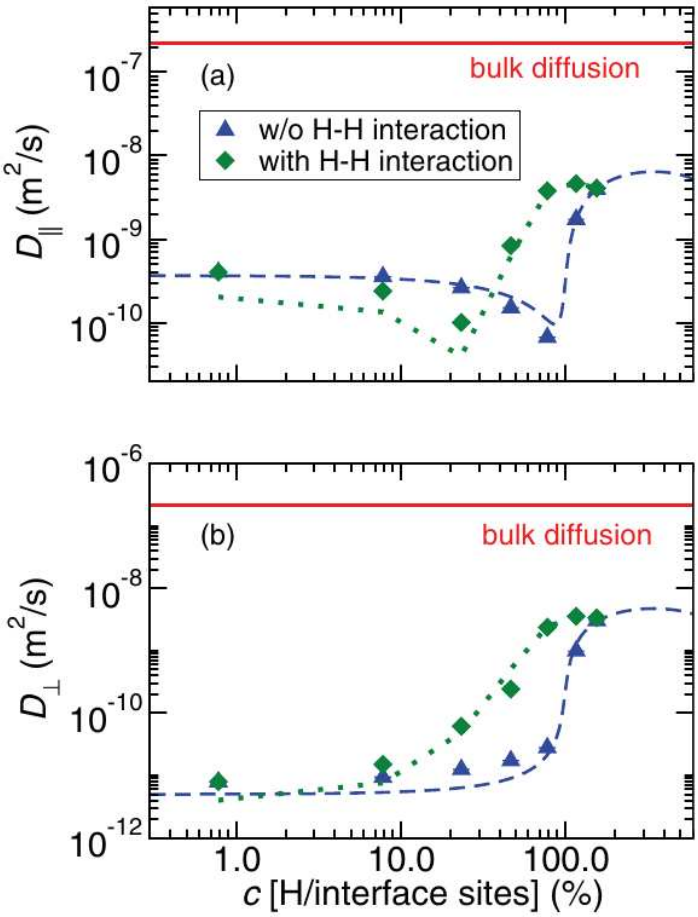

Figure 3.5: Diffusion constants as a function of H-concentration at 600 K temperature calculated for an idealized layered structure using the kinetic Monte Carlo simulation [106]. The diffusivities along ($D_{\parallel}$) and across ($D_{\perp}$) the interface layers are shown in (a) and (b), respectively.

Du et al. found that the diffusion rates of H-transport both across and along $\Sigma 5[001](310)$ grain boundary are several orders of magnitude less than the bulk diffusivity (Figure 3.5). It was also noted that the diffusivity increases with site occupancy but does not exceed the bulk one.

The data found in the literature suggest that the hydrogen diffusivity both perpendicular and parallel to interfaces can be lower than the diffusion rate in the bulk. Moreover, some boundaries can act as the two-dimensional diffusion barriers [6, 106]. For the interfaces across which H-transport is obstructed, it is unclear to what extent this can affect globally the evolution of hydrogen content in the material (i.e. the effective diffusivity). To answer this question, in the next part of the present chapter, we focus on the study of the diffusion across grain boundaries and investigate the dilatory effect of boundaries on the hydrogen diffusion in a nickel bicrystal membrane and in a nickel bamboo type membrane in which the interfaces are parallel to the surface.

We first describe the atomistic plane by plane (atomic layer) model [102, 107] used in the diffusion simulation. Physics of the diffusion process is given by the frequency of atomic hops between planes. As a first approach, the grain boundary is modelled by a layer fully composed of trap sites. The boundary value problem with constant source condition at the entry side and both with reflecting surface (i.e. the desorption is neglected) and sink type conditions (fast desorption) at the exit side of the membrane is considered. The effect of GB segregation-barrier is analysed in the aggregates initially free of hydrogen or pre-charged. H-redistribution in the presence of stress heterogeneities is simulated in the bicrystal.

3.2 Numerical simulation of hydrogen diffusion across grain boundaries

3.2.1 Atomic layer diffusion model

This section describes the formulation of the atomic layer model for the specific case of interstitial diffusion. The derivation is inspired from the works of Hofmann and Erlewein [102] and Martin [107].

We consider a bicrystal containing $2N + 1$ atomic planes with the axis X as the normal direction. The planes with numbers from $-N$ to -1 correspond to one grain, the planes with numbers from 1 to N correspond to the other grain, and the middle plane is supposed to represent the GB. It is assumed that each plane contains Ω interstitial sites. The configuration $\mathbf{C}$ of the system is defined by the set $\{n_{-N}; ...n_\alpha; ...n_N\}$, where n_α is the number of occupied interstitial sites in the plane α. The corresponding concentration can be written as $c_\alpha = n_\alpha/\Omega$. The concentration profile is given by $c(x)$ with $x = (\alpha - 1)h$, where h is the interplanar distance in X direction.

For a given configuration, there are $\frac{\Omega!}{n_\alpha!(\Omega-n_\alpha)!}$ arrangements of the n_α diffusing atoms among Ω positions in each plane α. If Ω is large, the ideal configurational entropy is:

$$S(\mathbf{C}) = -\Omega k \sum_{\alpha=-N}^{N} [c_\alpha \ln c_\alpha + (1 - c_\alpha) \ln(1 - c_\alpha)], \tag{3.9}$$

where k is the Boltzmann constant.

Assuming a negligible interaction between diffusing atoms apart from exclusion on a single interstitial site, the internal energy can be written as follows:

$$E(\mathbf{C}) = E_{metal} + \sum_{\alpha=-N}^{N} n_\alpha E_\alpha, \tag{3.10}$$

with E_α the solution energy of diffusing atoms and E_{metal} the reference energy of the metal without solutes.

Then, the Helmholtz free energy functional, $F(\mathbf{C})$, is:

$$F(\mathbf{C}) = E(\mathbf{C}) - TS(\mathbf{C}), \tag{3.11}$$

where T is the temperature, constant in this work.

After substituting (3.9) and (3.10) into (3.11), one obtains:

$$F(\mathbf{C}) \;=\; E_{metal} \;+\; \sum_{\alpha=-N}^{N} n_\alpha E_\alpha \;+\; \Omega kT \sum_{\alpha=-N}^{N} [c_\alpha \ln c_\alpha \;+\; (1 \;-\; c_\alpha)\ln(1 \;-\; c_\alpha)]. \quad (3.12)$$

The chemical potential, μ_a, of the diffusing atoms in the plane α is

$$\mu_\alpha = \frac{\partial F(\mathbf{C})}{\partial n_\alpha} = \frac{1}{\Omega}\frac{\partial F(\mathbf{C})}{\partial c_\alpha}. \quad (3.13)$$

By substituting the expression (3.12) into (3.13) finally we have:

$$\mu_\alpha = E_\alpha + kT \ln \frac{c_\alpha}{1 - c_\alpha}. \quad (3.14)$$

If the system is in equilibrium, μ_α is uniform, we can write $\mu_\alpha = \mu_\beta$ with μ_β the chemical potential in the neighbouring plane β, or using (3.14):

$$E_\alpha + kT \ln \frac{c_\alpha}{1 - c_\alpha} = E_\beta + kT \ln \frac{c_\beta}{1 - c_\beta}. \quad (3.15)$$

If the plane β is the GB (i.e. $\beta = N + 1$), noting the corresponding immersion energy in the GB $E_\beta = E_{gb}$, we can write

$$E_\alpha + kT \ln \frac{c_\alpha}{1 - c_\alpha} = E_{gb} + kT \ln \frac{c_{gb}}{1 - c_{gb}}, \quad (3.16)$$

and the equilibrium equation for the concentration in the interface plane is

$$\frac{c_{gb}}{1 - c_{gb}} = \frac{c_\alpha}{1 - c_\alpha} \exp\left(-\frac{\Delta E_{seg}}{kT}\right), \quad (3.17)$$

where the segregation energy $\Delta E_{seg} = E_{gb} - E_\alpha$.

In addition, to describe the kinetics of diffusing atoms in the system, the frequency, $\Gamma_{\alpha\beta}$, for an atom to jump from the plane α into the plane β is introduced. The concentration $c_\alpha = c_\alpha(t)$ is considered as the probability that an interstitial site in the plane α is occupied by a diffusing atom at time moment t. The probability that a site in the plane β is empty, i.e. free to receive an atom jumping from the plane α, is $(1 - c_\beta)$. The net flux $J_{\alpha\beta}$ of diffusing atoms from the plane α to β is

$$J_{\alpha\beta} = n_\alpha(1 - c_\beta)\Gamma_{\alpha\beta} - n_\beta(1 - c_\alpha)\Gamma_{\beta\alpha}. \quad (3.18)$$

Any change in the concentration at the node α in the GB is given by the difference between inward and outward fluxes which can be written as

$$\frac{\partial c_\alpha}{\partial t} = \sum_{\alpha\sim\beta}(\Gamma_{\beta\alpha}(1 - c_\alpha)c_\beta - \Gamma_{\alpha\beta}(1 - c_\beta)c_\alpha), \quad (3.19)$$

where $\alpha \sim \beta$ means that nodes with indices α and β are neighbours.

At equilibrium $J_{\alpha\beta} = 0$, then:

$$\frac{c_\alpha(1-c_\beta)}{c_\beta(1-c_\alpha)} = \frac{\Gamma_{\beta\alpha}}{\Gamma_{\alpha\beta}}. \tag{3.20}$$

This condition should coincide with the "statistic" equilibrium (3.15)-(3.17). $\Gamma_{\alpha\beta}$ is therefore defined by the equation:

$$\Gamma_{\alpha\beta} = z\nu \exp\left(-\frac{E_{\alpha\beta}}{kT}\right), \tag{3.21}$$

where z is a number of nearest neighbouring interstitial lattice sites in plane β for each site in plane α, $E_{\alpha\beta}$ is an activation barrier for the hydrogen atom to jump from the plane α into the plane β (Figure 3.6), ν is an attempt frequency. By doing so, diffusion is considered as a stochastic Poisson process, and the jump frequencies can incorporate quantum effects [5].

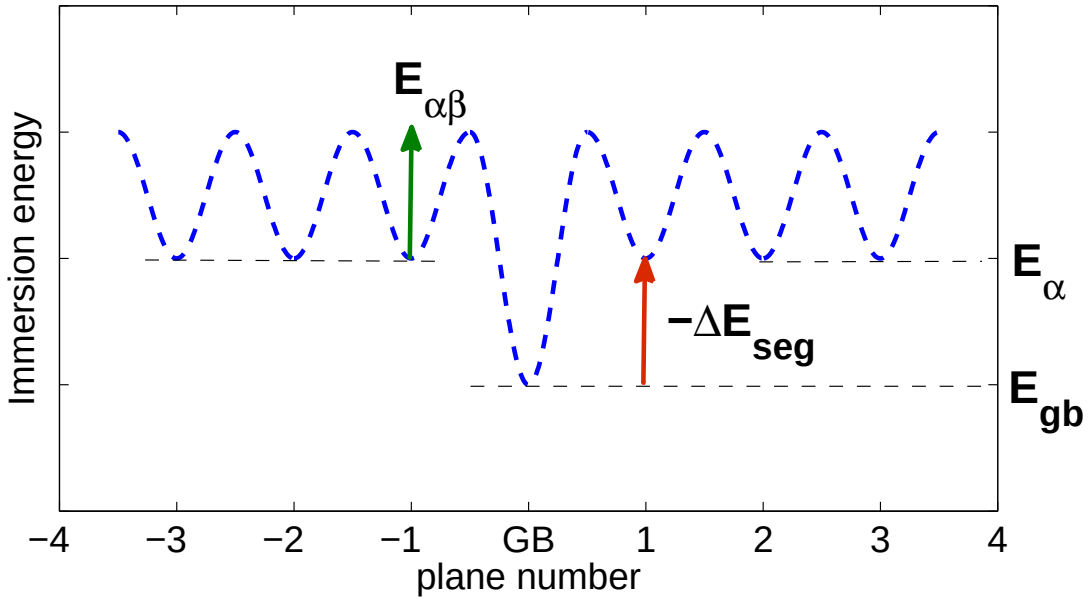

Figure 3.6: Immersion energy profile for atomic jumps across the grain boundary. The points of minimum energy correspond to the planes in the atomic layers model.

For the single crystal diffusion $\Gamma_{\alpha\beta} = \Gamma_{\beta\alpha} = \Gamma$ (forward and backward hops occur with the same jump rate), we can write:

$$J_{\alpha\beta} = \Gamma(n_\alpha(1-c_\beta) - n_\beta(1-c_\alpha)). \tag{3.22}$$

Substituting $c_\alpha = n_\alpha/\Omega$ into (3.22) we have:

$$J_{\alpha\beta} = \Gamma(n_\alpha - n_\beta). \tag{3.23}$$

By relating n_α and n_β to the volume concentration $c_\alpha^V(x,t)$

$$c_\alpha^V = \frac{n_\alpha}{h},\ c_\beta^V = \frac{n_\beta}{h}, \tag{3.24}$$

we find the volume flux J^V for the single crystal diffusion

$$J^V = \Gamma h(c_\alpha^V - c_\beta^V). \tag{3.25}$$

In diffusion studies the concentration field $c^V(x,t)$ varies slowly with respect to the distance x and in a Taylor expansion of the concentration-distance function we can keep only the first term [8]:

$$J^V = -\Gamma h^2 \frac{\partial c^V}{\partial x}. \tag{3.26}$$

By comparison with Fick's law we obtain the following expression for the lattice diffusion coefficient:

$$D_g = \Gamma h^2. \tag{3.27}$$

3.2.2 Modelling of one-dimensional H-diffusion on a nickel bicrystal

To investigate the segregation-barrier effect on the hydrogen transport across grain boundary, the atomic layer model was used for the one dimensional diffusion simulation on a nickel bicrystal (Figure 3.7).

Figure 3.7: Bicrystal type membrane considered in the simulation of 1D diffusion across the grain boundary.

The set of planes models two grains. The middle plane $p = 0$ corresponds to the GB. The mean values of the energy of hydrogen segregation for symmetric tilt grain boundaries were calculated by Shiga et al. by using embedded atom method [3]. All the energies reported by Shiga et al. are listed in Table 3.1. According to this data the average segregation energies are in the range of -0.21 eV and -0.36 eV, the individual energies for the corresponding GB sites are in the range of -0.02 eV and -0.46 eV. It is necessary to note that the segregation energies given in [3] can not be considered as the effective segregation energies, since almost all of them is simply the arithmetic mean of segregation energies of different sites within a given interface, excepting the $\Sigma 11(113)[1\bar{1}0]$ and $\Sigma 19(331)[1\bar{1}0]$ boundaries which contains the interstitial sites of one type. As the first approach in the present work, we use the average values from [3] in the diffusion simulations by the atomic layer model.

The parameters required for the computation of the jump frequencies, $\Gamma_{\alpha\beta}$, are listed in Table 3.2. The frequency for H-atom to leave the interface, $\Gamma_{gb\to 1}$ (or $\Gamma_{gb\to -1}$), is:

$$\Gamma_{gb\to 1} = z\nu \exp\left(-\frac{E_{gb\to 1}}{kT}\right), \tag{3.28}$$

where $E_{gb\to 1}$ is the activation barrier for hydrogen atom to jump from the grain boundary plane into the neighbouring bulk layer. The diffusion barrier for H-atom to jump into the GB layer is the same as for the bulk diffusion jump ($E_{\alpha\beta} = 0.4\ eV$).

Table 3.1: Segregation energies ΔE_{seg} of hydrogen atom for symmetrical tilt grain boundaries in nickel calculated by using embedded-atom method (from [3]). The binding energies for different sites on a given GB are listed in the third column.

GB type	$\Delta E_{seg}, eV$	E^i_{seg}, eV
$\Sigma3(121)[1\bar{1}1]$	-0.26	-0.32, -0.20
$\Sigma5(012)[100]$	-0.27	-0.29, -0.24
$\Sigma5(013)[100]$	-0.30	-0.35, -0.32, -0.23
$\Sigma5(132)[1\bar{1}1]$	-0.31	-0.37, -0.32, -0.23
$\Sigma9(221)[1\bar{1}0]$	-0.21	-0.37, -0.24, -0.02
$\Sigma11(332)[1\bar{1}0]$	-0.29	-0.46, -0.31, -0.32, -0.08
$\Sigma11(113)[1\bar{1}0]$	-0.29	-0.29
$\Sigma17(410)[001]$	-0.34	-0.42, -0.37, -0.31, -0.24
$\Sigma19(331)[1\bar{1}0]$	-0.36	-0.36
$\Sigma27(115)[1\bar{1}0]$	-0.33	-0.36, -0.30
$\Sigma35(531)[1\bar{2}1]$	-0.22	-0.39, -0.23, -0.05
average	-0.29	

Table 3.2: Parameters for the atomic layer model used in the simulation of hydrogen diffusion in the bicrystal.

Parameter	Value
z	4
ν	$10^{13}\ s^{-1}$
$E_{\alpha\beta}$	$0.4\ eV$
k	$8.617 \cdot 10^{-5}\ eV$
T	$300\ K$

First, the effect of GB segregation-barrier was analysed on the bicrystal with nano-grains: the total number of atomic layers is 2001, the corresponding grain size is about

176 nm (the distance between planes $h = a/2$, where a is the lattice parameter for nickel: $a = 3.524 \cdot 10^{-10}\ m$). Then, the larger bicrystal composed of 11351 atomic planes (the corresponding grain size is 1 μm) was used in the diffusion simulation.

The hydrogen diffusion was modelled imposing the boundary conditions of constant source at the left (entry) side and reflecting free surface (i.e. the desorption is neglected) or constant concentration at the right (exit) side. Two cases of initial conditions were considered: H-free and pre-charged bicrystal. All the cases of boundary-initial conditions used for the modelling of H-diffusion in the present section are collected in Table 3.3. If the concentration at the left edge plane is only given, it means that the right edge plane is considered as the reflecting surface.

Table 3.3: Boundary-initial conditions for 1D H-diffusion problems

	Grain size	Initial conditions	Boundary conditions
Problem 1a	176.2 nm	$c_\alpha = 0$	$c_{-N} = 0.000134$
Problem 1b	176.2 nm	$c_\alpha = 0.000134$	$c_{-N} = 0.00134$
Problem 2a	1 μm	$c_\alpha = 0$	$c_{-N} = 0.000134$
Problem 2b	1 μm	$c_\alpha = 0$	$c_{-N} = 0.000134, c_N = 0$
Problem 2c	1 μm	$c_\alpha = 0.000134$	$c_{-N} = 0.00134, c_N = 0.000134$

Problem 1a. The bicrystal is considered to be H-free initially. The boundary conditions of constant source for the left side and reflecting free surface (i.e. the desorption is neglected) for the right side are imposed. The problem is described by the following system of equations:

$$\begin{cases} \frac{\partial c_\alpha}{\partial t} = \sum_{\alpha\sim\beta}(\Gamma_{\beta\alpha}(1-c_\alpha)c_\beta - \Gamma_{\alpha\beta}(1-c_\beta)c_\alpha), \\ c_\alpha(0) = 0, \quad \alpha = -N+1, .., N, \\ c_{-N}(t) = 0.000134. \end{cases} \tag{3.29}$$

First, we consider the bicrystal with GB segregation energy $\Delta E_{seg} = -0.36\ eV$. H-distributions at different time moments are presented in Figure 3.2.2. In Figure 3.2.2a, the blue line corresponds to the H-distribution after 0.002 s of diffusion: the concentration profile is not affected by the interface since the characteristic diffusion length is less than the grain size. At time moment $t = 0.007\ s$, the peak of the concentration is observed at the grain boundary.

The segregation-barrier effect of the boundary is well pronounced for later times as it is seen in Figure 3.2.2 b. At time moments $t = 0.1\ s$ and $t = 0.5\ s$, the concentration profile is linear in the left grain with the peak at the boundary ($c_{gb} \approx 0.08$, $c_{gb} \approx 0.486$, respectively) where the diffusion is blocked due to the high activation barrier for H-atoms to jump from the interface layer into the crystal. When the grain boundary is saturated ($c_{gb} \approx 0.96$ and $c_{gb} \approx 0.993$ after 1 s and 1.5 s of diffusion, respectively), hydrogen diffuses more freely and H-content in the bicrystal increases rapidly during the time interval between $t = 1\ s$ and $t = 1.5\ s$.

H-diffusion in the bicrystal were simulated for all the mean values of GB segregation energy listed in Table 3.1. The results are shown in Figure 3.2.2 for the time moment $t = 0.5\ s$. It is seen that the effect of blocking increases when the segregation energy decreases (segregation energy is negative). The linear concentration profile in the left grain is observed for all the energy values considered.

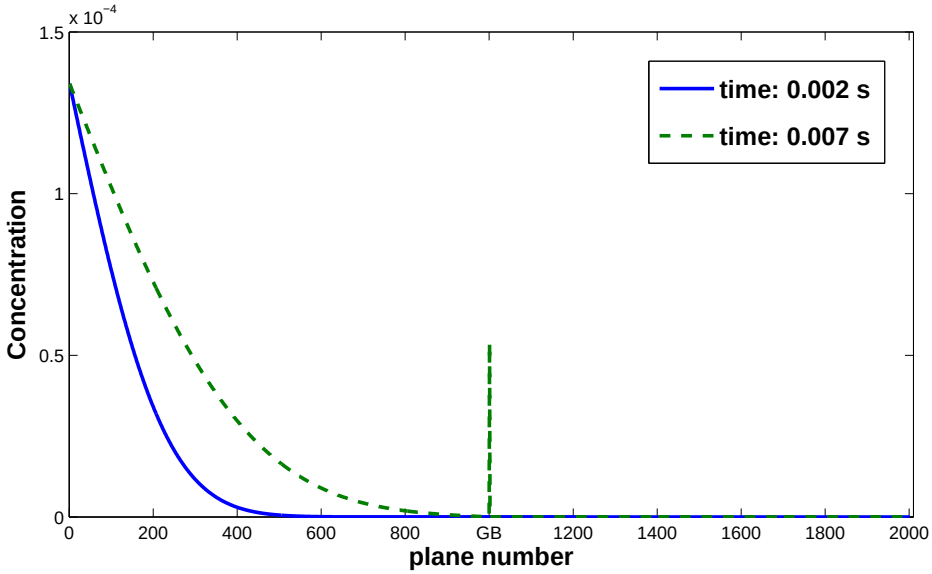

a) GB concentration: $c_{gb}(0.001) = 0$, $c_{gb}(0.007) \approx 0.0000538$

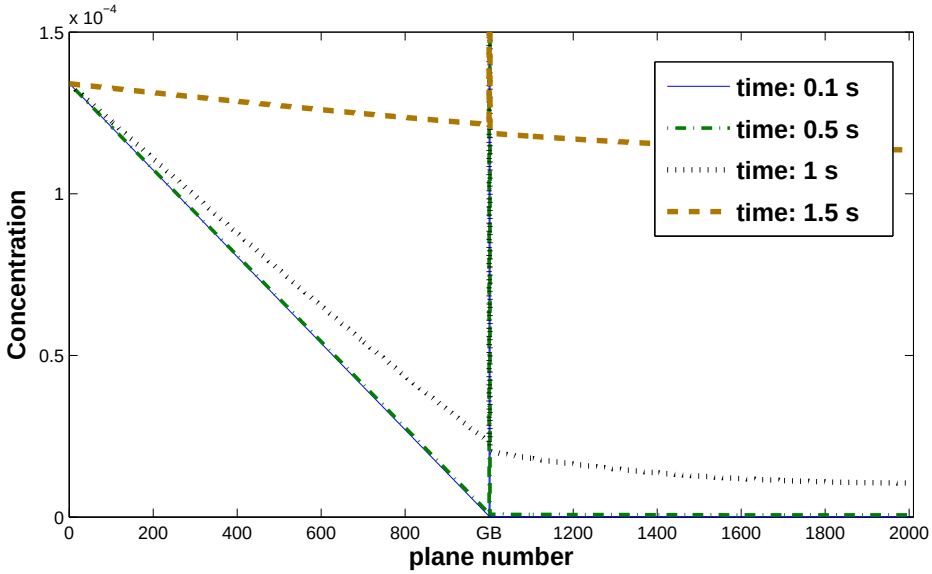

b) GB concentration: $c_{gb}(0.1) \approx 0.08$, $c_{gb}(0.5) \approx 0.486$, $c_{gb}(1.0) \approx 0.96$, $c_{gb}(1.5) \approx 0.993$

Figure 3.8: Time evolution of hydrogen concentration in the initially H-free nickel bicrystal. The grain boundary segregation energy $\Delta E_{seg} = -0.36\ eV$. The reflecting surface condition is imposed on the right edge plane.

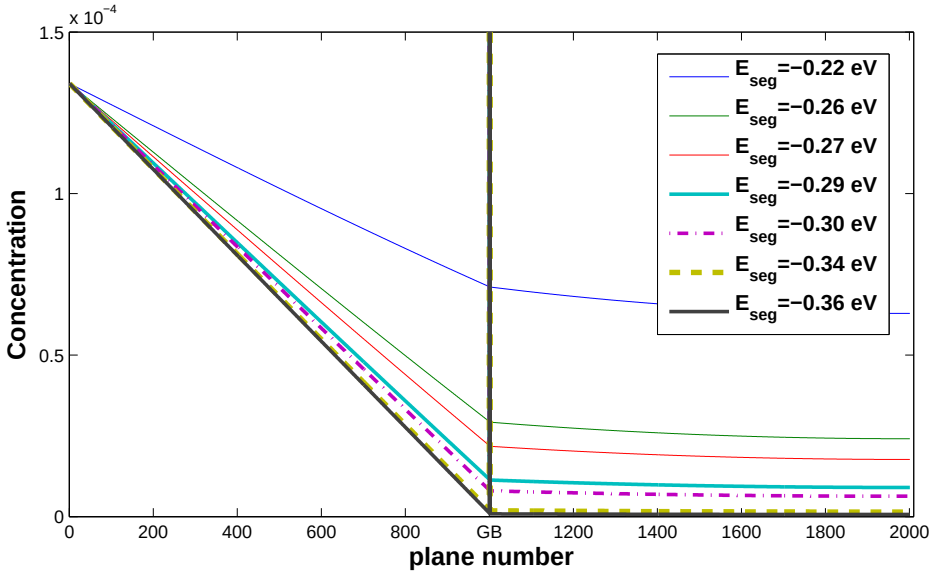

Figure 3.9: H-concentration profiles for different grain boundary segregation energies at time moment $t = 0.5\ s$. The reflecting surface condition is imposed on the right edge plane.

Problem 1b. Hydrogen atoms are supposed to be homogeneously distributed in the bicrystal. The concentration in the left edge plane is maintained constant. The initial GB concentration, c_{gb}, is given by Eq. (3.17). The diffusion problem is described by the equations:

$$\begin{cases} \frac{\partial c_\alpha}{\partial t} = \sum_{\alpha\sim\beta}(\Gamma_{\beta\alpha}(1-c_\alpha)c_\beta - \Gamma_{\alpha\beta}(1-c_\beta)c_\alpha), \\ c_{gb}(0) = \left(1 + \frac{1-c_\alpha(0)}{c_\alpha(0)}\exp\left(\frac{\Delta E_{seg}}{kT}\right)\right)^{-1} \\ c_\alpha(0) = 0.000134, \quad \alpha = -N+1, .., -1, 1, .., N, \\ c_{-N}(t) = 0.00134. \end{cases} \tag{3.30}$$

The results of the diffusion simulation for the segregation energies $\Delta E_{seg} = -0.36\ eV$ and $\Delta E_{seg} = 0.29\ eV$ are plotted in Figure 3.2.2. H-concentration profile calculated without taking into account the interface is shown for the comparison. In the case of the pre-charged bicrystal, as the interface is almost saturated initially ($c_{gb} \approx 0.993$ and $c_{gb} \approx 0.91$ for $\Delta E_{seg} = -0.36\ eV$ and $\Delta E_{seg} = 0.29\ eV$, respectively), the effect of high migration energy barrier across the boundary is determinative. However, in the case of the boundary with $\Delta E_{seg} = -0.29\ eV$, the effect of segregation can be remarked: the green line in Figure 3.2.2 is placed lower than the curve corresponding to the single crystal diffusion. In the case of the boundary with $\Delta E_{seg} = -0.36\ eV$, the concentrations in the left grain are higher than the ones calculated for the single crystal diffusion and lower in the right grain due to blocking of H-atoms at the boundary.

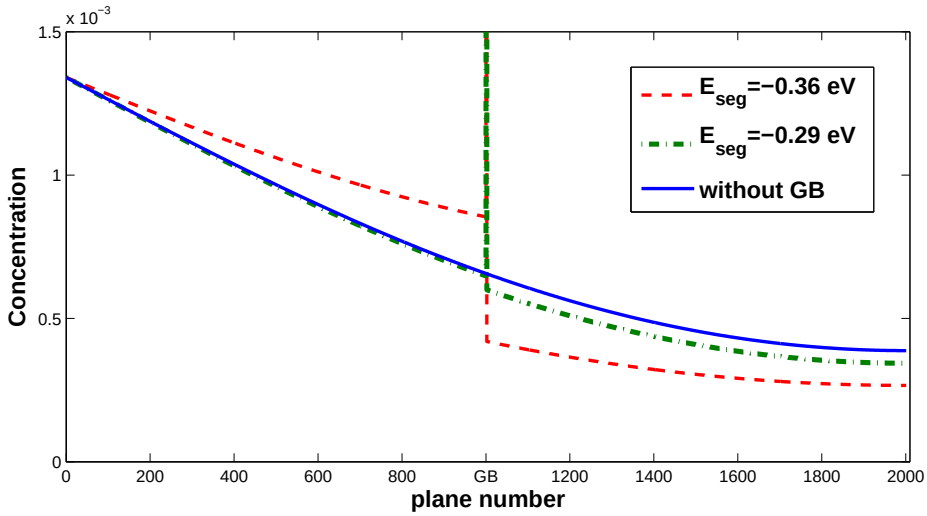

Figure 3.10: H-concentration profiles in the pre-charged (the initial concentration $c_0 = 0.000134$) nickel bicrystal at time moment $t = 0.1\ s$. The reflecting surface condition is imposed on the right edge plane.

Problem 2a. Conditions are analogous to the ones described in Problem 1 a. Grain size is about 1 μm (the total number of planes is 11351).

The diffusion was simulated for the case of the grain boundary for which the segregation energy $\Delta E_{seg} = -0.36\ eV$. The results are presented in Figure 3.11 in comparison with the concentration profile calculated without taking into account the interface.

The H-concentration profiles computed with and without considering the GB properties at time moment $t = 0.2\ s$ match as it is seen in Figure 3.11 a. The little difference between H-distribution in grains can be noted in the vicinity of the interface after 0.4 s (Figure 3.11 b). For the later time moments, $t = 4\ s$ and $t = 8\ s$, the retarding effect of the boundary on the diffusion is highlighted (Figure 3.11 c-d).

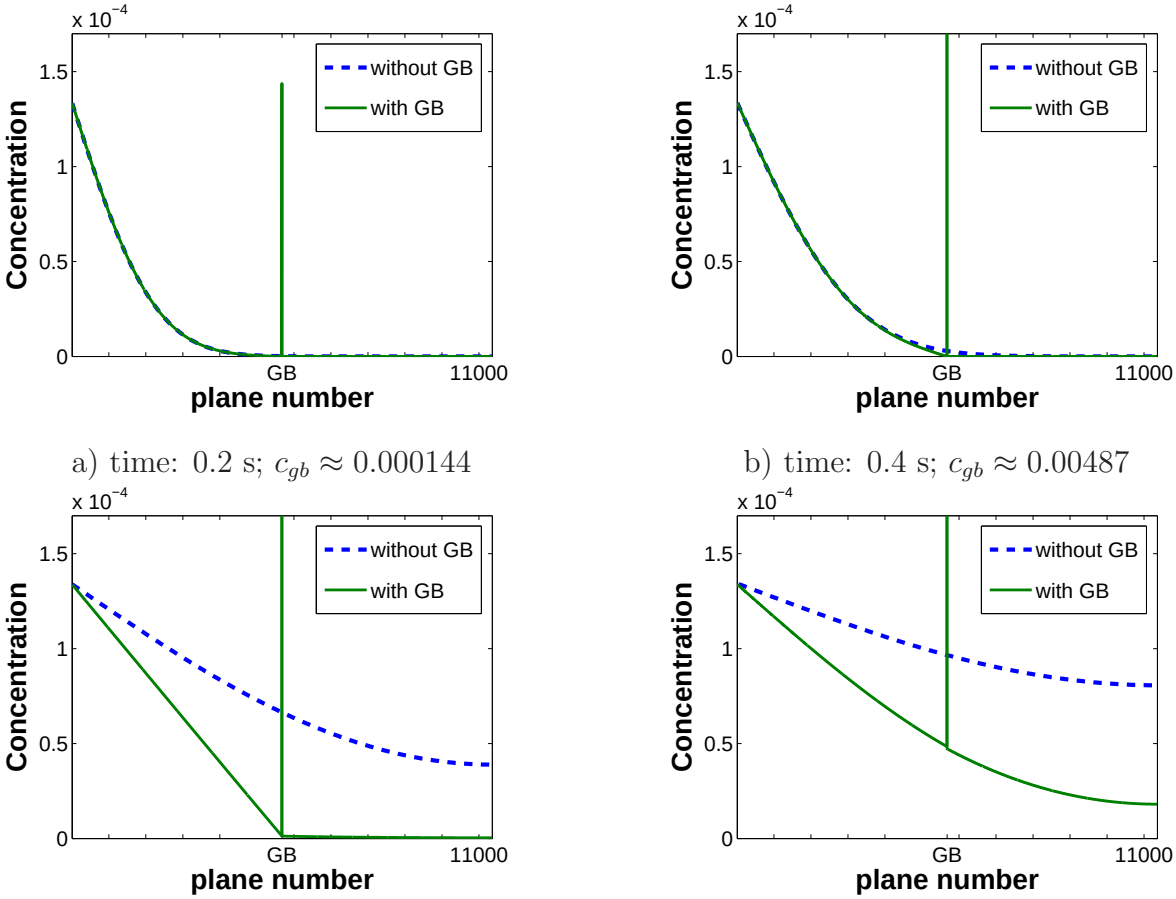

a) time: 0.2 s; $c_{gb} \approx 0.000144$

b) time: 0.4 s; $c_{gb} \approx 0.00487$

c) time: 4 s; $c_{gb} \approx 0.585$

d) time: 8 s; $c_{gb} \approx 0.982$

Figure 3.11: Time evolution of hydrogen concentration in the initially H-free nickel membrane without and with grain boundary. GB segregation energy: $\Delta E_{seg} = -0.36\ eV$. The reflecting surface condition is imposed on the right edge plane.

Problem 2b. The bicrystal is H-free initially. Dirichlet boundary conditions are used for both entry and exit sides. The problem is described by the following system of equations:

$$\begin{cases} \frac{\partial c_\alpha}{\partial t} = \sum_{\alpha\sim\beta}(\Gamma_{\beta\alpha}(1-c_\alpha)c_\beta - \Gamma_{\alpha\beta}(1-c_\beta)c_\alpha), \\ c_\alpha(0) = 0, \quad \alpha = -N+1, .., N-1, \\ c_{-N}(t) = 0.000134, \\ c_N(t) = 0 \end{cases} \tag{3.31}$$

The results of the diffusion simulation are presented in Figure 3.12. The time evolution of the concentration profile in the bicrystal with grains of 1 μm shows that the effect of the interface on the diffusion can be remarkable not only in nano-crystalline materials considered before.

In Figure 3.12 a, the curves of H-distribution in the bicrystal and in the single crystal at time moment $t = 0.2\ s$ match. At time moment $t = 0.4\ s$ (Figure 3.12 b), the little difference between the H-concentration profiles appears. For both time moments $t = 0.2\ s$ and $t = 0.4\ s$ the H-distribution is identical to one obtained with the reflecting boundary conditions considered in Problem 2a. The discrepancy increases with time and the retarding effect of the boundary is well pronounced after 2 s (Figure 3.12 c) and 4 s (Figure 3.12 d). At time moment $t = 4\ s$, while in the single crystal the steady state is already reached, the concentrations in the right grain of the bicrystal are still close to zero, and the linear profile is observed in the left grain.

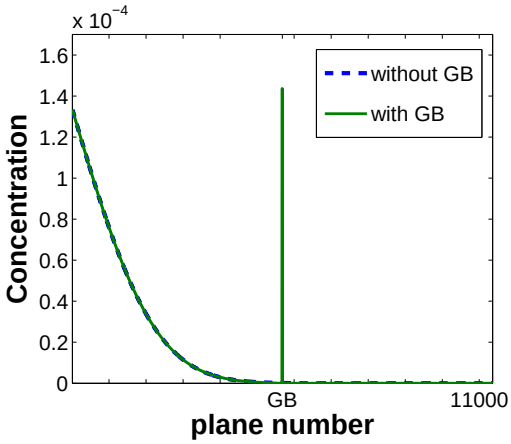

a) time: 0.2 s; $c_{gb} \approx 0.000144$

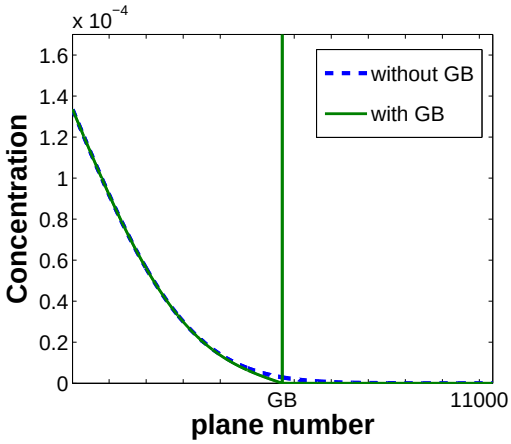

b) time: 0.4 s; $c_{gb} \approx 0.00487$

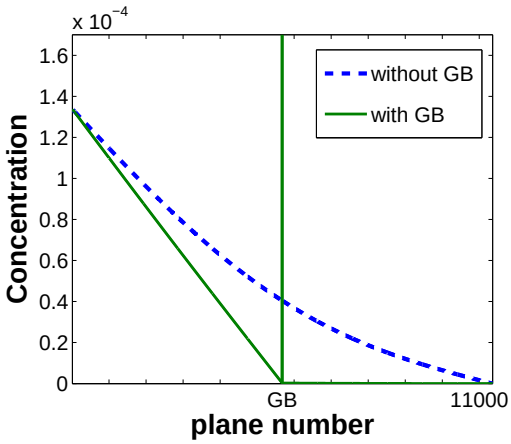

c) time: 2 s; $c_{gb} \approx 0.233$

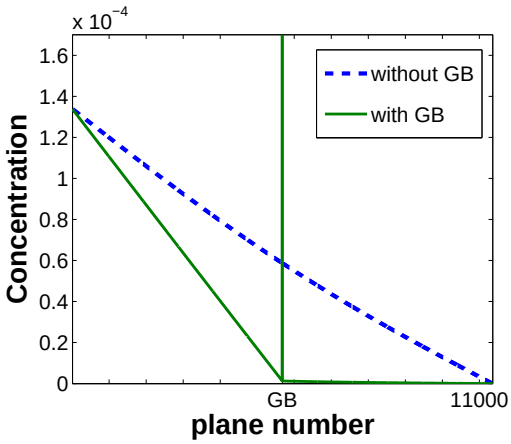

d) time: 4 s; $c_{gb} \approx 0.585$

Figure 3.12: Time evolution of hydrogen concentration in the initially H-free nickel membrane without and with grain boundary. GB segregation energy: $\Delta E_{seg} = -0.36\ eV$.

Problem 2c. Hydrogen atoms are supposed to be homogeneously distributed in the bicrystal at the beginning. The start concentration at the interface, c_{gb}, is given by Eq. (3.17). The concentrations in the left and right edge planes are maintained constant. The diffusion problem is described by the equations:

$$\begin{cases} \frac{\partial c_\alpha}{\partial t} = \sum_{\alpha\sim\beta}(\Gamma_{\beta\alpha}(1-c_\alpha)c_\beta - \Gamma_{\alpha\beta}(1-c_\beta)c_\alpha), \\ c_{gb}(0) = \left(1 + \frac{1-c_\alpha(0)}{c_\alpha(0)} \exp\left(\frac{\Delta E_{seg}}{kT}\right)\right)^{-1} \\ c_\alpha(0) = 0.000134, \quad \alpha = -N+1, .., -1, 1, .., N-1, \\ c_{-N}(t) = 0.00134, \\ c_N(t) = 0.000134. \end{cases} \tag{3.32}$$

The H-concentration profiles were calculated for the case of the interface with segregation energy $\Delta E_{seg} = -0.36\ eV$. The corresponding initial concentration at the grain boundary $c_{gb} \approx 0.993$, i.e. the interface is saturated and the contribution from the diffusion migration barrier to leave the GB is determinative.

The results are shown in Figure 3.13. It is seen that the retarding effect of the boundary is less pronounced in comparison with the diffusion in the initially H-free bicrystal.

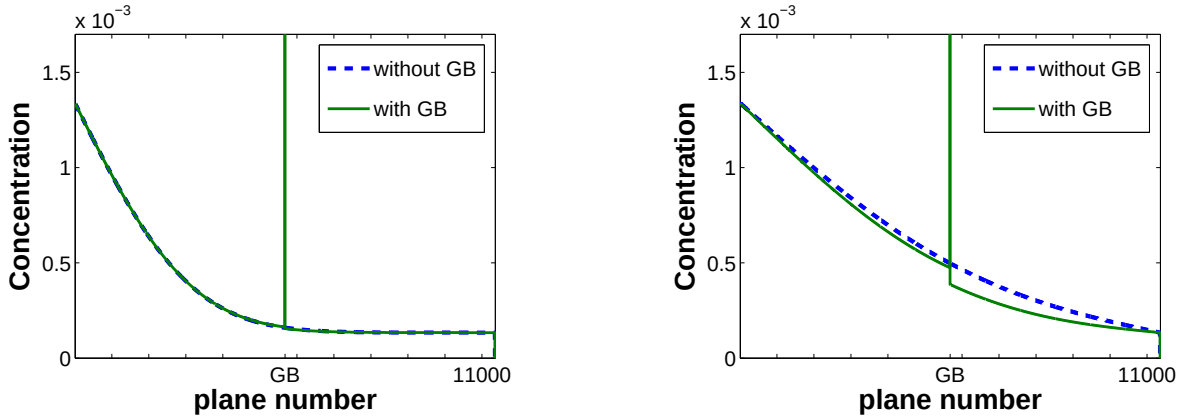

a) time: 0.4 s b) time: 2 s

Figure 3.13: Time evolution of hydrogen concentration in the pre-charged nickel membrane without and with grain boundary. GB segregation energy: $\Delta E_{seg} = -0.36\ eV$.

3.2.3 Steady state in the bicrystal

For the bicrystal, the GB effect on the hydrogen distribution in the bicrystal was analysed under steady state with Dirihlet boundary condition. The diffusion equations (**??**) formulated for the transient state can be rewritten for the steady state problem assuming the partial derivative with respect to time is equal to zero. Denoting the hydrogen flux from the plane $p-1$ to the neighbouring plane p as $J_{p-1\to p}$ and the flux from the plane p to the neighbouring plane $p+1$ as $J_{p\to p+1}$, the steady state problem can be written as:

$$\begin{aligned} J_{p-1\to p} &= J_{p\to p+1}, \quad p=-N+1,..,N-1 \\ c_{-N} &= C_a, \\ c_N &= C_b, \end{aligned} \tag{3.33}$$

where C_a and C_b are the concentrations prescribed for the left and right edge planes, respectively.

The system (3.33) was solved analytically. The solution for the left grain of the bicrystal is

$$c_p = C_a + \frac{Q}{\Gamma}(p+N), \quad p=-N,..,-1, \tag{3.34}$$

and for the right grain

$$c_p = C_b - \frac{Q}{\Gamma}(p-N), \quad p=1,..,N, \tag{3.35}$$

where Γ is the jump frequency for hydrogen atom hops in the nickel crystal, and Q is given as follows:

$$Q = \frac{\tilde{\Gamma}\Gamma(C_a - C_b)}{2N\tilde{\Gamma} + (C_a + C_b)(\Gamma - \tilde{\Gamma})}, \tag{3.36}$$

$\tilde{\Gamma}$ is the jump frequency for H-atom to leave the GB plane, and it is given by:

$$\Gamma = z\nu \exp\left(-\frac{E_{gb\to 1}}{kT}\right), \tag{3.37}$$

the migration energy barrier $E_{gb\to 1}$ is illustrated in Figure 3.6 and computed as

$$E_{gb\to 1} = E_{1\to gb} - E_{seg}, \tag{3.38}$$

where $E_{1\to gb}$ is equal to the diffusion migration barrier in the nickel crystal (0.4 eV). The grain boundary concentration is

$$c_{gb} = \frac{Q + \Gamma c_1}{\tilde{\Gamma}(1-c_1) + \Gamma c_1}. \tag{3.39}$$

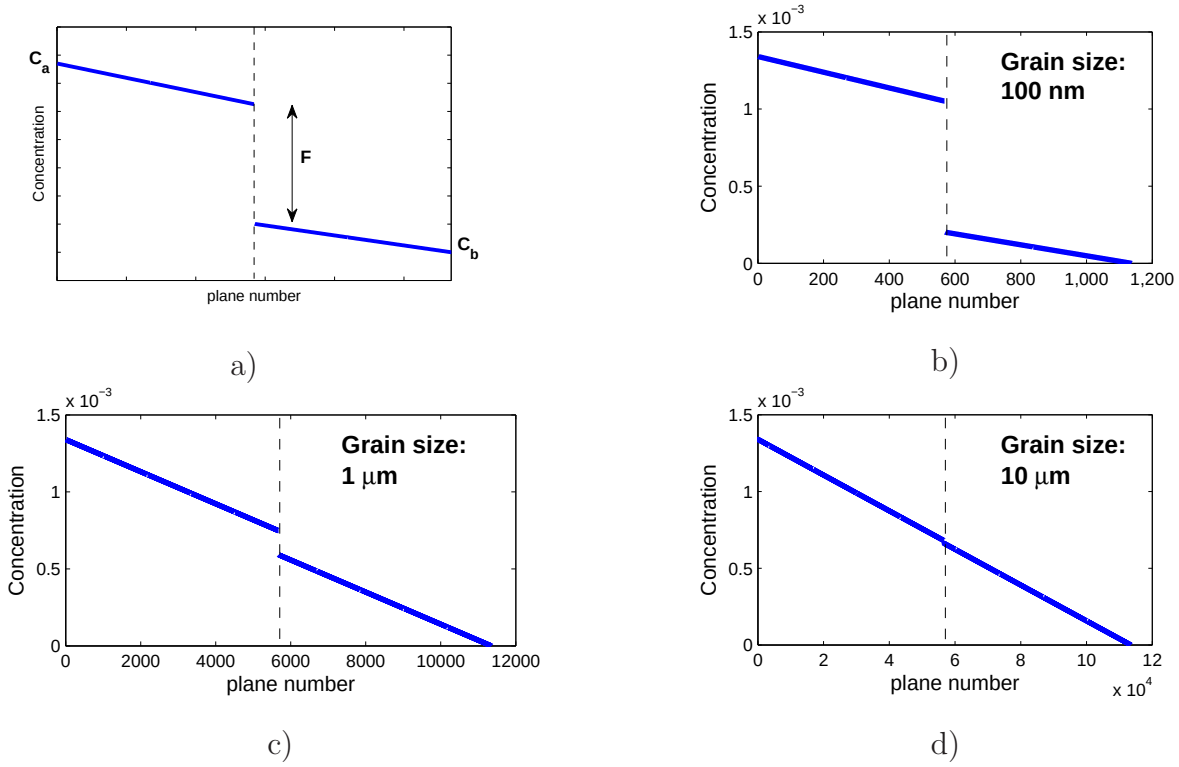

Figure 3.14: Steady state H-distribution in the bicrystal in the case of the GB segregation energy $\Delta E_{seg} = -0.36\ eV$. (a) The pattern of the analytical solution and the concentration profiles calculated for three grain sizes: (b) 100 nm, (c) 1 μm, (d)10 μm.

The pattern of the solution is given in Figure 3.14a. The concentration profiles computed for the bicrystals with different grain sizes (100 nm, 1 μm and 10 μm) are presented in Figure 3.14 b-d. All the results were obtained for the case of low GB segregation energy ($\Delta E_{seg} = -0.36\ eV$), and the edge concentrations $C_a = 0.00134$ and $C_b = 0$.

The characteristic concentration fall observed at the interface (Figure 3.14a) is given by the expression

$$F = c_{-1} - c_1 = C_a - C_b - \frac{2(N-1)\tilde{\Gamma}(C_a - C_b)}{2N\tilde{\Gamma} + (C_a + C_b)(\Gamma - \tilde{\Gamma})}, \tag{3.40}$$

It is seen that F depends on the boundary conditions (C_a, C_b), number of planes (in other words, grain size), N, and the GB segregation energy, ΔE_{seg}. The concentration fall is observed in all the cases and it varies with grain size. It can be noted that

$$\lim_{N\to\infty} F = 0.$$

The dependence of the fall, F, on the grain size for the GB segregation energies $\Delta E_{seg} = -0.29\ eV$ and $\Delta E_{seg} = -0.36\ eV$ and the edge concentrations $C_a = 0.00134$ ($C_b = 0$) and

$C_a = 0.000134$ ($C_b = 0$) is plotted in Figure 3.15. It is seen that the effect of the interface on the steady state concentration profile is higher in the bicrystal with nano-grains and it increases with the concentration prescribed on the entry side.

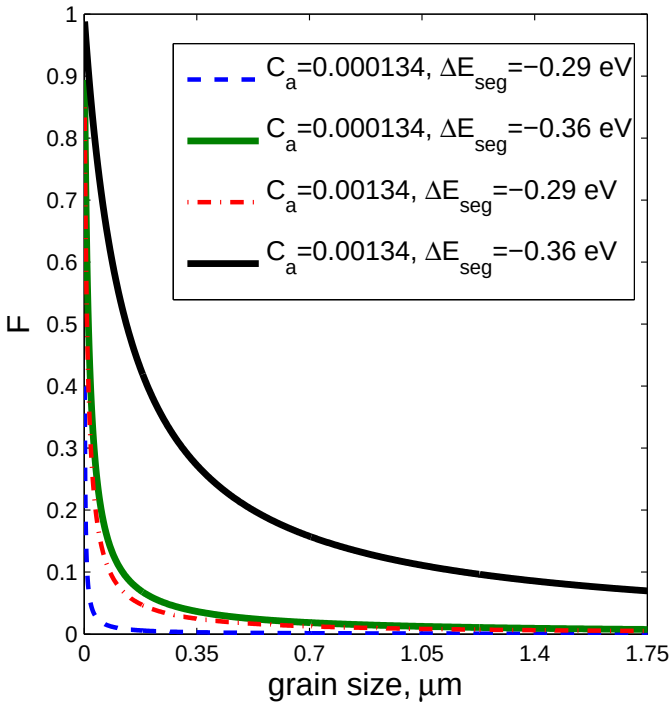

Figure 3.15: The dependence of the concentration fall on the grain size found for the steady state H-distribution in the bicrystal.

3.2.4 Simulation of hydrogen diffusion in a bamboo type membrane

The study of the GB segregation-barrier effect on the diffusion in the bicrystal revealed that the interface retards the H-transport through the membrane. The effect increases with decreasing the grain size and less in the initially charged material. In the present section, the hydrogen diffusion was studied in the nickel bamboo type membrane (Figure 3.16) composed of 50 grains (and 49 grain boundaries, respectively).

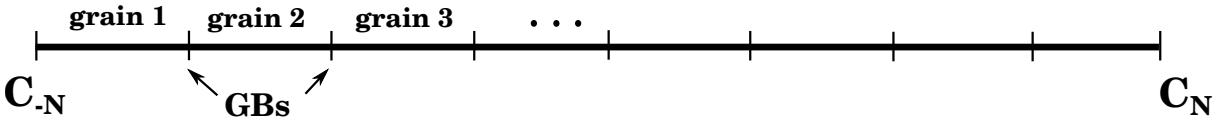

Figure 3.16: Bamboo type membrane considered in the simulation of one dimensional diffusion across the grain boundaries.

In the atomic layer model, the total number of planes is 57,000, the corresponding grain size is about 200 nm. The grain boundary segregation energy was chosen $\Delta E_{seg} = -0.36\ eV$ for all the interfaces.

Two types of boundary-initial conditions were considered as limiting cases. First, the initially H-free material with the constant concentrations at the entry and exit sides was analysed. In the second case, the bamboo type membrane is supposed to be initially uniformly charged ($c_0 = 0.000134$) and all the grain boundaries are almost saturated ($c_{gb} \approx 0.993$) according to the equilibrium condition (Eq. 3.17); constant concentrations at the edge planes were assumed as the boundary condition. All the cases of boundary-initial conditions used for the modelling of H-diffusion in the bamboo type membrane are collected in Table 3.4.

Table 3.4: Boundary-initial conditions for 1D H-diffusion in the bamboo type membrane

	Grain size	Initial conditions	Boundary conditions
Problem 1	200 nm	$c_\alpha = 0$	$c_{-N} = 0.000134, c_N = 0$
Problem 2	200 nm	$c_\alpha = 0.000134$	$c_{-N} = 0.00134, c_N = 0.000134$

Problem 1.

In Figure 3.17, the H-profile is presented in the case of the initially H-free membrane for time moments $t = 10\ s$ and $t = 30\ s$. It can be seen that the H-transport in the bamboo membrane is retarded significantly in comparison with the diffusion in the single crystal membrane. Analysing Figure 3.17a, the H-penetration depth in the bamboo membrane can be estimated $\approx 1.2\ \mu m$ (according to the sixth concentration peak observed at the interfaces). However, the concentrations in the 5th and in the 6th grains are negligible compared to the surface concentration, and the diffusion length can be approximated by taking into account only four first grains in the bamboo membrane ($\approx 0.8\ \mu m$). The diffusion length for the single crystal membrane is greater by a factor of ≈ 7.

The linear concentration profiles (already observed in the case of H-diffusion in the bicrystal) in grains are characteristic for the nano-crystalline bamboo type membrane and observed in Figure 3.17 for both time moments $t = 10\ s$ and $t = 30\ s$.

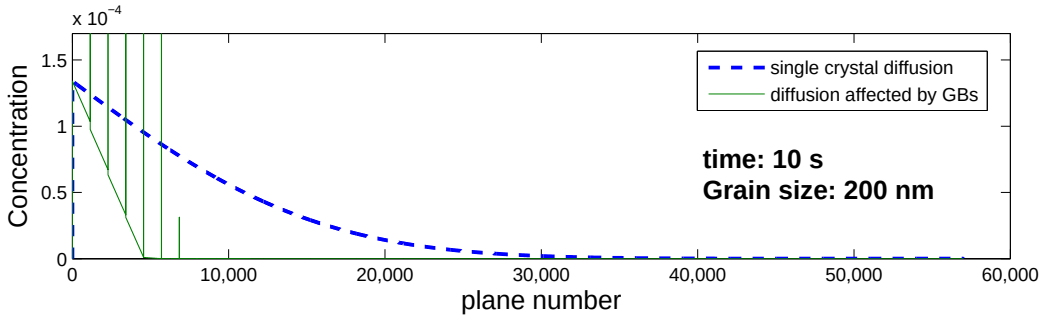

a)

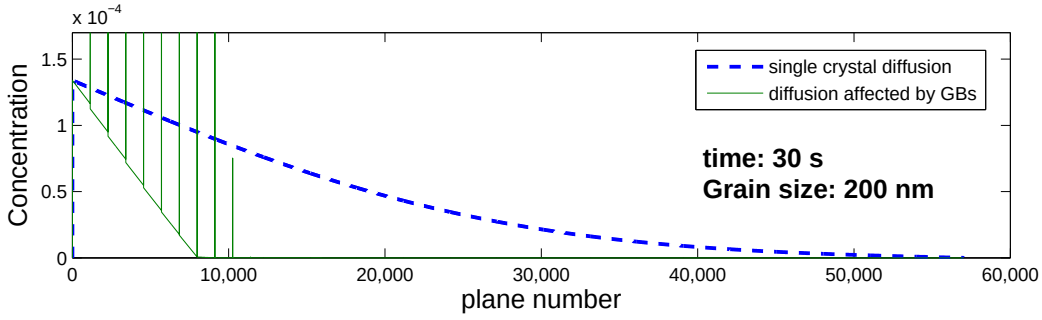

b)

Figure 3.17: H-concentration profile in the initially H-free nickel membrane at time moments (a) $t = 10\ s$ and (b) $t = 30\ s$. The blue dashed curves correspond to the H-diffusion profiles calculated without taking into account grain boundaries. The green curves show the H-distribution in the bamboo membrane, the characteristic concentration peaks (vertical lines) are due to the segregation to interfaces.

Problem 2.

In Figure 3.18, the results of the simulation for times $t = 10\ s$ and $t = 30\ s$ are presented for the initially pre-charged membrane. The difference between single crystal diffusion and H-profile for the pre-charged bamboo membrane is less than for the initially H-free system.

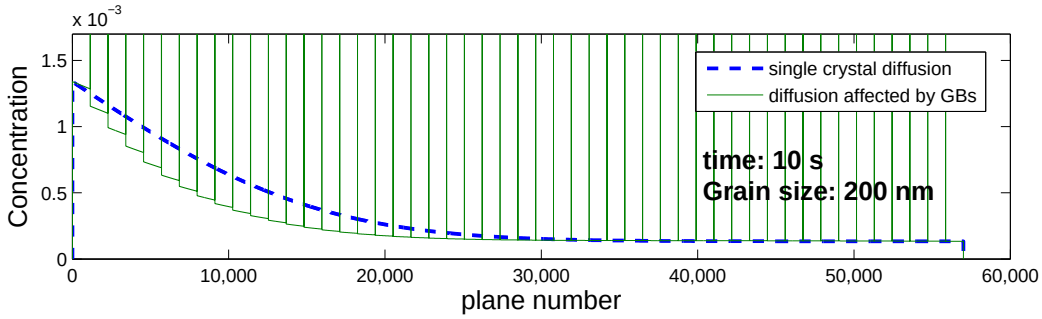

a) duration: 10 s

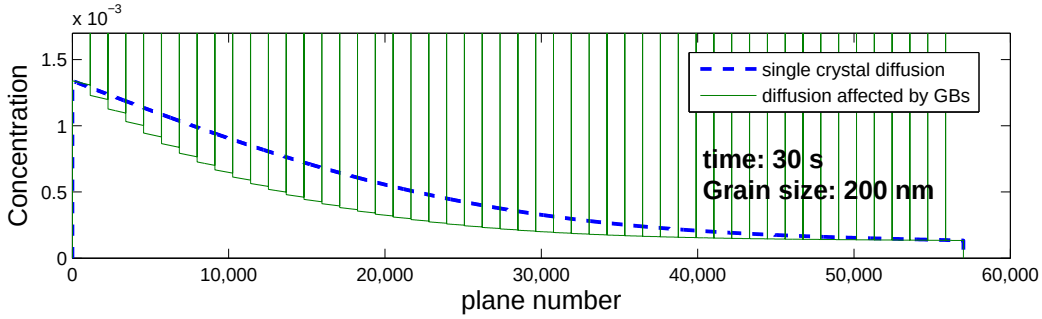

b) duration: 30 s

Figure 3.18: H-concentration profiles in the pre-charged (the initial concentration $c_0 = 0.000134$) nickel bamboo membrane at time moments (a) $t = 10\ s$ and (b) $t = 30\ s$. The blue dashed curves correspond to the H-diffusion profiles calculated without taking into account grain boundaries. The green curves show the H-distribution in the bamboo membrane, the characteristic concentration peaks (vertical lines) are due to the segregation to interfaces.

3.2.5 The effect of stress heterogeneities: cyclic loading

The effect of cyclic loading on the hydrogen redistribution was investigated on a nickel bicrystal. The system is composed of 20 000 atomic planes, the corresponding grain size is about 1.76 μm. As the initial condition, H-concentration is supposed to be uniform. The system is assumed to be isolated, that is the H-flux at the edge planes is equal to zero.

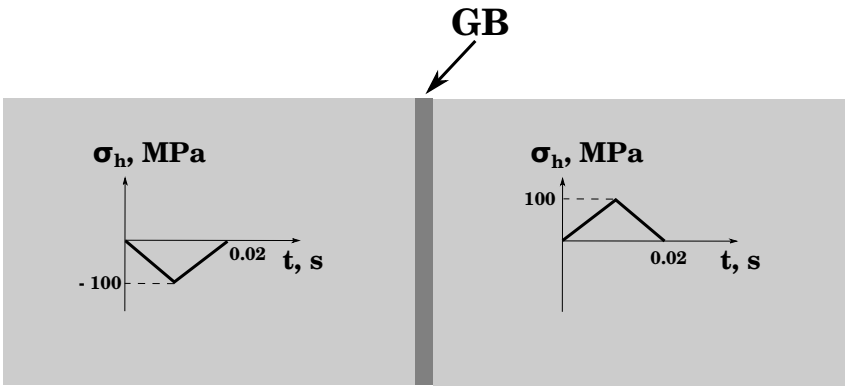

Figure 3.19: Evolution of hydrostatic stresses modelled in the bicrystal. One cycle of loading. Frequency: 50 Hz.

To model the H-redistribution induced by stress gradients at the interface (or, in other words, stress heterogeneities in the bicrystal), the stresses are supposed to change linearly in loading and unloading modes as follows:

Loading mode:
- from 0 to 100 MPa in the right grain,
- from 0 to -100 MPa in the left grain,
- duration: 0.01 s

Unloading mode:
- from 100 to 0 MPa in the right grain,
- from -100 to 0 MPa in the left grain,
- duration: 0.01 s

The hydrostatic stress field is imposed to be homogeneous in each grain.

For the sake of simplicity, we assume that stresses do not affect the diffusivity in the grains. Any change, $\Delta\mu_\sigma$, of the energy profile describing the atomic jump process is estimated as:

$$\Delta\mu_\sigma = -\sigma_h V_H, \tag{3.41}$$

where σ_h is a hydrostatic stress, and V_H is a partial molar volume of hydrogen in nickel ($V_H = 1.7 \cdot 10^{-6}\ m^3 \cdot mol^{-1}$).

The GB segregation energy $\Delta E_{seg} = -0.36\ eV$ is assumed. For the bicrystal before applying stresses, the diffusion barrier for H-atom to jump into the GB layer is the same as for the bulk diffusion jump ($E_{\alpha\beta} = 0.4\ eV$), the barrier to escape from the GB is $E_{\alpha\beta} - \Delta E_{seg} = 0.76\ eV$. After applying stresses, the immersion energy profile at the GB is recomputed as follows. If $\Delta\mu_\sigma^{-1}$ is a shift of energy level in plane $i = -1$, and $\Delta\mu_\sigma^{1}$ is the one in plane $i = 1$, then in the GB plane it is calculated as follows:

$$\Delta\mu_\sigma^{gb} = \frac{1}{2}(\Delta\mu_\sigma^{-1} + \Delta\mu_\sigma^{1}), \tag{3.42}$$

and shifts in positions $i = -1/2$ and $i = 1/2$, respectively:

$$\Delta\mu_\sigma^{-1/2} = \frac{1}{2}(\Delta\mu_\sigma^{-1} + \Delta\mu_\sigma^{gb}), \tag{3.43}$$

$$\Delta\mu_\sigma^{1/2} = \frac{1}{2}(\Delta\mu_\sigma^{gb} + \Delta\mu_\sigma^{1}), \tag{3.44}$$

First, H-distribution in the bicrystal was calculated without considering the specific segregation-barrier properties of the interface. The results for one cycle of loading (time: 0.02 s) are presented in Figure 3.20. The characteristic effect of stress heterogeneities on the hydrogen redistribution is observed: hydrogen diffuses from one grain to the other in which the hydrostatic stress is higher, the zones of depletion and saturation are observed (blue dashed line in Figure 3.20). After unloading, the residual hydrogen concentration heterogeneities are present in the vicinity of GB. The extremums of concentration are reduced and shifted towards the interior of the grains (to the left and to the right in the left grain and in the right one, respectively) due to the relaxation. The same calculation for one cycle of loading was performed with accounting for the specific GB segregation-barrier properties assuming for the interface: $\Delta E_{seg} = -0.36\ eV$. The results of the simulation are shown in Figure 3.21. The concentration peak at the boundary is observed due to the segregation effect. The residual H-heterogeneities are present in the bicrystal after one cycle of loading as in the simulation without considering the interface.

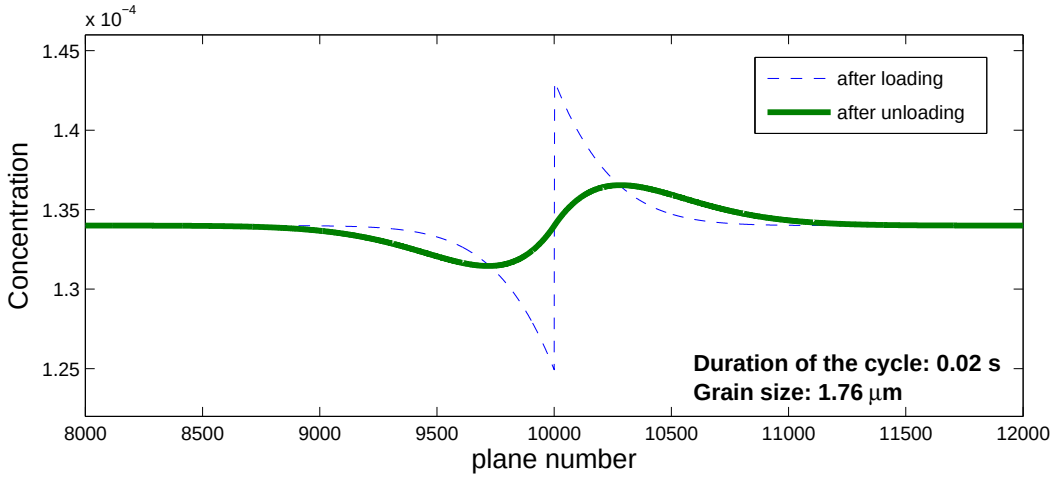

Figure 3.20: Hydrogen distribution in the bicrystal for one cycle of loading without taking into account GB segregation-barrier properties. Hydrogen concentration profiles in the vicinity (4001 atomic planes are shown) of the GB after loading (blue dashed line) and unloading (green line) modes are plotted.

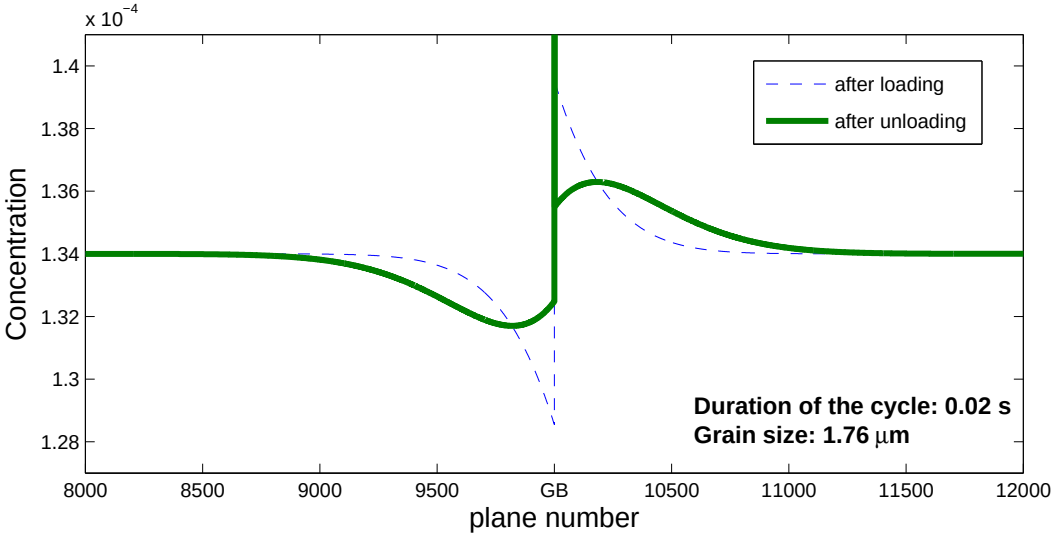

Figure 3.21: Hydrogen distribution in the bicrystal for one cycle of loading. Hydrogen concentration profiles in the vicinity (4001 atomic planes are shown) of the GB after loading (blue dashed line) and unloading (green line) modes are plotted.

For the comparison, the maximum values of the concentration in the enriched grain after loading are $\approx$ 1.43 and $\approx$ 1.39 without and with taking into account the GB segregation-barrier properties, respectively.

The effect of the interface on the H-diffusion in the presence of stresses can be estimated considering the ratio of the residual hydrogen to the hydrogen quantity involved into the

redistribution:

$$\Delta = \frac{C_{resid}}{C_{redistr}}, \tag{3.45}$$

where C_{resid} is the summary quantity of the residual hydrogen heterogeneities in the enriched zone (right grain) after one cycle of loading (Figure 3.22b), $C_{redistr}$ is the total additional quantity of hydrogen in the enriched grain after a half-cycle (Figure 3.22a). It was found that $\Delta \approx 0.83$ in the case of the diffusion simulation without considering GB segregation-barrier properties and $\Delta \approx 0.997$ for the nickel bicrystal in which the specific GB diffusion properties are taken into account.

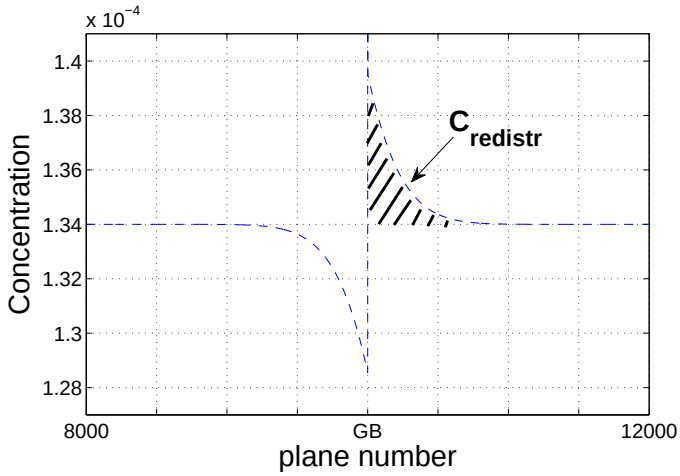

a)

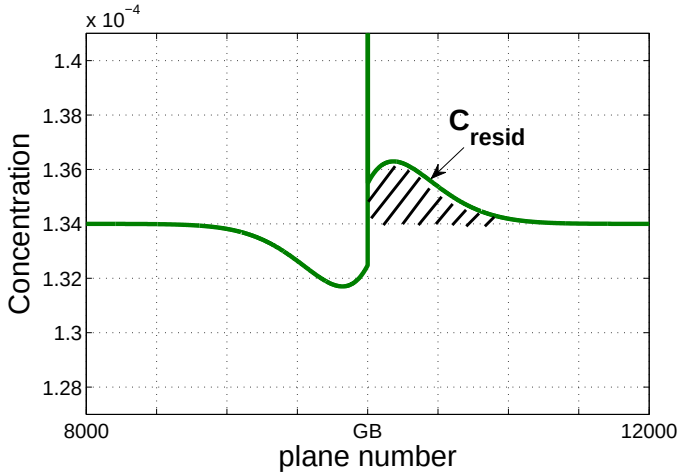

b)

Figure 3.22: (a) The additional hydrogen content due to the stress induced redistribution (after loading) and (b) the residual hydrogen heterogeneity (after unloading) in the enriched grain are shaded.

Figure 3.23 represents the H-distribution after 50 cycles (diffusion duration: 1 s) in the whole bicrystal. It is seen that hydrogen atoms accumulate in the grain with higher hydrostatic stress.

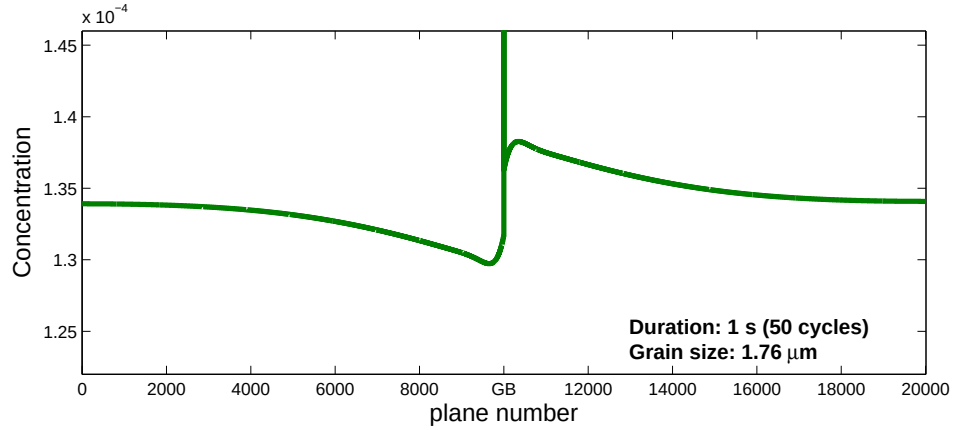

Figure 3.23: Hydrogen distribution in the entire (20 001 atomic planes) bicrystal after 50 cycles of loading.

H-distribution computed for different frequencies (5 Hz, 50 Hz and 500 Hz) of cyclic loading are presented in Figure 3.24 for comparison. It is seen that the concentration peak is located farther from the interface for lower frequencies since the time for relaxation during unloading is longer for these frequencies.

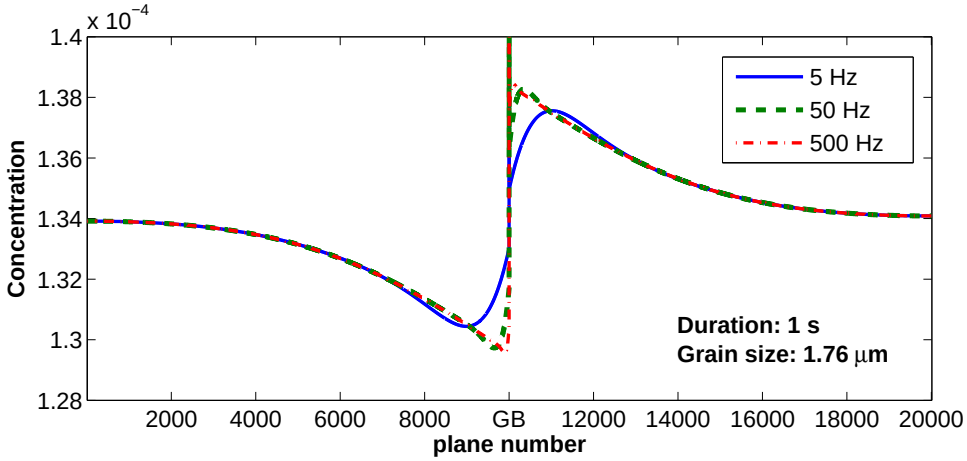

Figure 3.24: Hydrogen distribution in the bicrystal after 1 s of cyclic loading with different frequencies: 5 Hz, 50 Hz and 500 Hz.

3.2.6 Discussion

There is a number of simplifications in the model that we used. We start this summary with a list of them keeping in mind that most of them could be lifted in the future.

The jump probabilities which appear in the expression of flux in the atomic layer model are discussed in the paper of Hofmann and Erlewein [102]. In the case of the of surface segregation [101], the most probable expression is found to be:

$$J_{\alpha\beta} = c_\alpha \left(1 - \frac{c_\beta}{c_\beta^m}\right)^{c_\beta^m} \Gamma_{\alpha\beta} - c_\beta \left(1 - \frac{c_\alpha}{c_\alpha^m}\right)^{c_\alpha^m} \Gamma_{\beta\alpha}, \tag{3.46}$$

where c_α^m and c_β^m is the maximum coverage of layers α and β, respectively. In our simulations, it was assumed that $c_\alpha^m = 1$ as a first approach.

Hydrogen segregation energies used in the present work for the simulation on the bamboo structure membrane are rather high in absolute value and the chosen bulk concentrations correspond to almost H-filled GBs. At high H-concentrations, repulsive H-H interactions can affect H-diffusivity in the vicinity of GBs blocking H-atoms. The effects of volume expansion and formation of hydride phase at very high concentration are expected to be observed [3, 109]. For other types of GBs, the segregation energies and activation barriers might be lower [3], and the hydrogen diffusion could be less affected. In addition, the GBs are supposed to consist only of trapping sites, and each site in the bulk planes $p = -1$ and $p = 1$ has four nearest neighbouring sites in the GB plane ($p = 0$). A more realistic GB structure should be introduced with multiple sites.

Despite the number of simplifications, the results of calculations show that in the initially H-free bamboo membrane grain boundaries act as sinks and barriers retarding H-transport through the membrane. In the case of the pre-charged membrane, the effect of blocking of H-atoms by the boundaries is less since GBs are already saturated. In the framework of the model used, it means that H-atoms can pass more freely across the boundaries. However, the diffusion is impeded by the high GB activation energy barrier, $E_{gb\to1}$, for H-solutes to leave the interface.

In the presence of stresses, hydrogen redistribution in the loading mode is not affected significantly since the bicrystal is considered to be pre-charged and the GB is almost saturated. Nevertheless, the blocking effect of the interface is remarkable on the stage of unloading (Sec. 3.2.5).

3.2.7 Summary

The main conclusions of the present chapter are listed below.

• Linear H-concentration distribution in grains is characteristic effect of grain boundaries acting as sinks/barriers in the considered aggregates with grain size from 176 nm up to 1 μm.

• Comparison of the results of diffusion simulation on the initially H-free and on the pre-charged bicrystals reveals the concentration dependence of H-diffusivity. The retarding effect of the interface is lower in the case of the pre-charged membrane.

• Concentration fall at the interface is observed in the steady state solute distribution for the problem with ideal sink condition at the exit side of the membrane. The fall is greater for higher magnitudes of GB segregation energy (in absolute value) and decreases with increasing the grain size.

• Hydrogen accumulation in the grain with higher hydrostatic stresses was observed in the simulation of H-evolution in bicrystal under cyclic loading. In the unloading mode, the grain boundary was found to impede the relaxing of solute heterogeneities produced on the loading stage.

Chapter 4

Multi-scale method for the simulation of grain boundary diffusion

The specific properties of grain boundaries were discussed in the previous chapter. It was shown that H-segregation to interfaces and H-diffusivities, different from the bulk, can play important role, such as retarding the transport of H-atoms through a nickel bamboo type membrane with boundaries parallel to the surface.

Grain boundary segregation and diffusion of hydrogen in solids is of great interest in relation to hydrogen embrittlement and intergranular stress corrosion cracking. In this chapter, we review the classical grain boundary diffusion models and elaborate a multi-scale method that can be used to investigate the influence of GB diffusion-segregation in polycrystalline materials with any structure. The method describes the effect of grain boundary segregation explicitly by considering the kinetic processes, instead of assuming a local equilibrium. Examples of hydrogen diffusion and segregation in a nickel bicrystal with longitudinal, transverse and inclined grain boundary configurations as well as the H-diffusion in three grains junction are considered.

4.1 Introduction

4.1.1 Diffusion along grain boundaries

The fact that grain boundaries can act as fast diffusion channels is known since 20-30s of the past century. The rate of grain boundary diffusion strongly depends on the detailed atomic structure of the boundary. In particular, it is known that diffusivity along grain boundaries varies from small to high-angle boundaries [93]. This behaviour can be explained on the basis of the dislocation pipes model [110]. Small-angle GBs are usually described as fast diffusion "pipes" embedded in a relatively low diffusivity material. Large-angle GBs have a considerably more disarranged structure and provide high diffusion paths [93,104]. This mechanism is based on the decreased density of atoms and as a results a high vacancy concentration or vacancy like defects in the core of grain boundaries. This structure provides the enhanced transport along the interfaces for substitutional diffusion. However, hydrogen diffuses in metals by interstitial mechanism and does not require vacancies, which are low energy sites and can trap H-atoms retarding diffusion [111, 112].

For the grain boundary diffusion of hydrogen atoms, a wide range of experimental results has been obtained. These data is rather contradictory. Some results indicate that hydrogen diffusion is higher in grain boundaries than in the bulk, whereas others show the opposite effect.

We first review the experimental data obtained for the diffusion of hydrogen in polycrystalline materials as well as in bicrystals. Then, classical grain boundary diffusion models are formulated and the results of numerical simulations found in the literature are analysed.

Calder et al. [113] studied the diffusion of tritium in 304 and 316 austenitic steels. Tritium was injected through transmutation of a surface blanket of ^{6}LiF. To establish the diffusion gradient, specimens were heated isothermally. Measurements of the tritium activity in specimen layers (removed with a lathe and/or electro-polishing) were conducted. Analyzing the tritium concentration profiles, Calder and co-workers found that the diffusion coefficient at grain boundaries is eight orders of magnitude higher than in the bulk in 304 and 316 austenitic steels.

Tsuru and Latanision [114] performed hydrogen charging of polycrystalline Ni by ele-

crochemical method and analyzed a permeation rate. The permeation flux increased over a period of several hours depending on the specimen thickness (from 0.15 to 0.006 mm) and then reached steady state after more than ten hours. In the early stages of permeation, a very small incremental increase in the exit current occurred after a few minutes and reached a steady state current wuthin 10 to 20 minutes. In the analysis of Tsuru and Latanision, this increment was presumed to correspond to the grain boundary diffusion flux. It was found that $D_{gb}/D_g \approx 60$. The data obtained by the ion microprobe analysis are compatible with the rapid diffusion of hydrogen along grain boundaries and show the increased hydrogen concentration at grain boundaries (Figure 4.1).

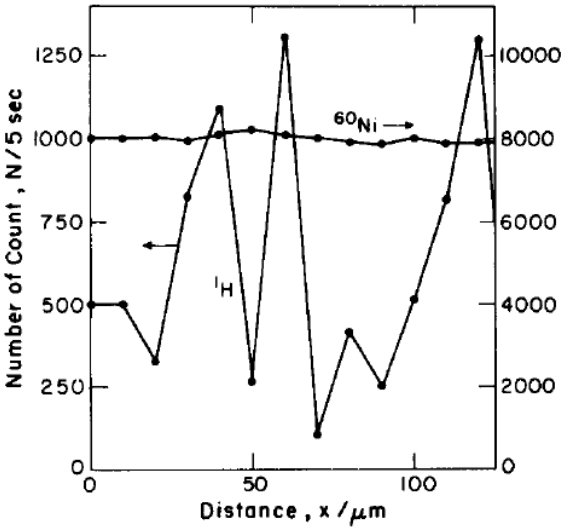

a) IMA data

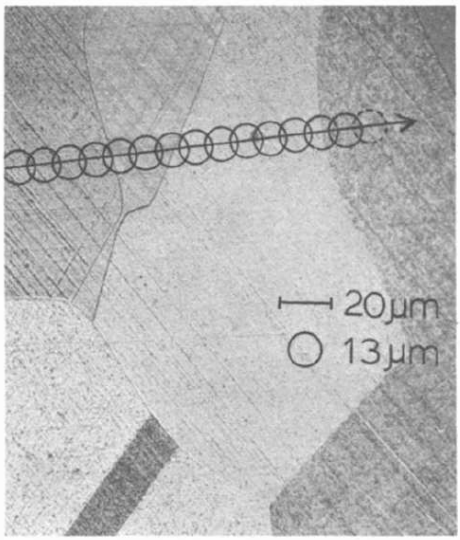

b) IMA scannig direction

Figure 4.1: The results of ion microprobe analysis (IMA) performed by Tsuru and Latanision [114] on a nickel polycrystalline specimen cathodically charged. The hydrogen concentration peaks in Fig. (a) correspond to the intersections of grain boundaries and scanning direction shown in Fig. (b).

Ladna and Birnbaum [115] studied the deuterium distribution at the surface and at grain boundaries of cathodically charged (current densities: 20 and 2 mA/cm^2, temperature: 295 K) nickel bicrystals. Using Secondary Ion Mass Spectrometry (SIMS) with the sample cooled to 140 K, they measured $D_{gb}/D_g \approx 8-17$ for $\Sigma 9[110]$ symmetric tilt grain boundary but did not find any evidence of fast diffusion along $\Sigma 11[110]$.

The acceleration of H-diffusion by grain boundaries was reported by Kimura and

Birnbaum [72]. Using the extent of intergranular fracture as a measure of the hydrogen penetration depth, they concluded that the kinetics of intergranular embrittlement of Ni from an external hydrogen source are controlled by grain boundary diffusion of hydrogen. Kimura and Birnbaum estimated $D_{gb}/D_g \approx 2$. However, Yao and Cahoon [116] reviewed the derivation of Kimura and Birnbaum and found that their conclusion may not be justified. Using the data reported by Kimura and Birnbaum, Yao and Cahoon calculated $D_{gb}/D_g \approx 13000 - 150000$ depending on the time of hydrogen charging.

Harris and Latanision [117] performed permeation tests (current density: in a range of 1 and 35 mA/cm^2) on fine-grained foils of nickel as well as on the annealed material (Figure 4.2a). The evolution of hydrogen flux at the exit side of the membrane with lower grain size obtained after electrodeposition was measured to be faster than in the annealed specimens. The grain boundary diffusivity was estimated: $D_{gb}/D_g \approx 40$ (at temperature of 30^{o}C).

Accelerated diffusion of hydrogen was observed by Brass and Chanfreau [118] at room temperature in polycrystalline nickel using the electrochemical permeation (20 mA/cm^2) technique. A larger hydrogen flux was measured in annealed samples with 25 μm grain size whereas faster hydrogen diffusion was observed at the early stage of the permeation process in samples with a larger grain size (150 μm) (Figure 4.2b). The grain boundary diffusivity was estimated to be 2-7 times greater than the lattice one.

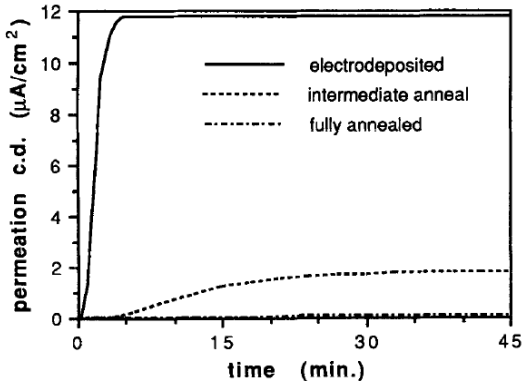

a)

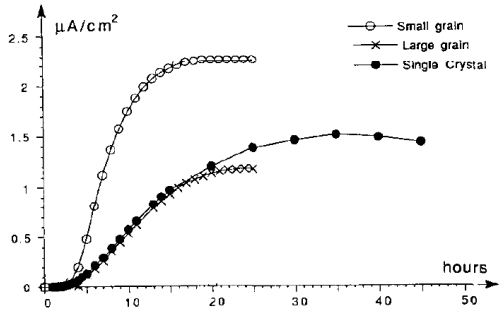

b)

Figure 4.2: Permeation transients for nickel in (a) the electrodeposited (grain size: 0.1 μm – 2 μm) and different heat-treated materials (average grain size is 1.3 μm after intermediate annealing and 45 μm for fully annealed material) reported in [117] and (b) samples with 25 μm and 150 μm grains in comparison with single crystal diffusion found in [118]

Mütschele and Kirchheim [119] measured the diffusion coefficient of hydrogen in cathodically charged nano-crystalline palladium (average grain size: 5 nm) at temperature of 293 K. They detected that diffusivity is lower than single-crystalline value at low H-concentrations and increases with H-content. It was also noted that the solute-solute interaction affects the diffusion coefficient for high hydrogen concentrations in the material (Figure 4.3).

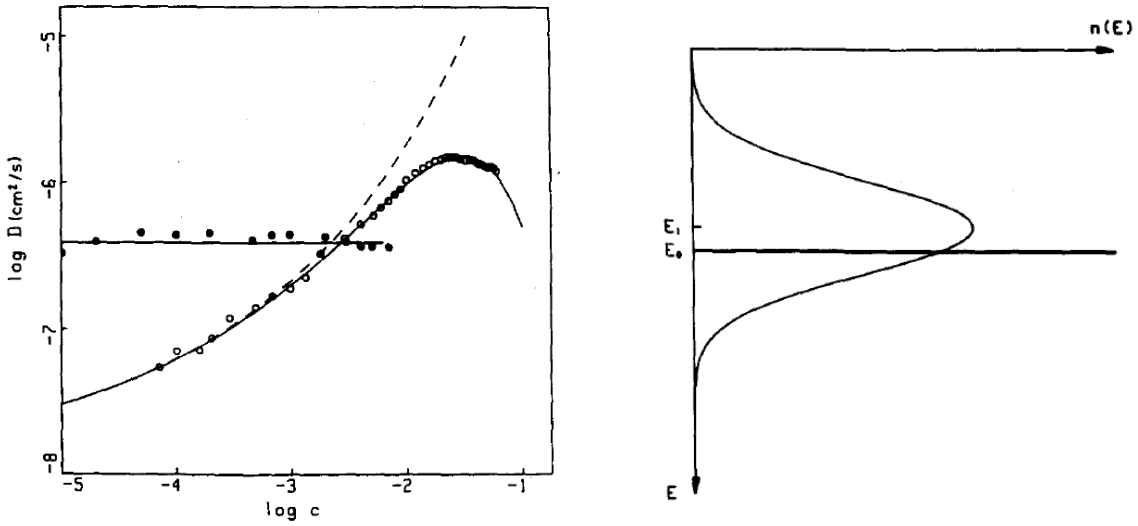

a) b)

Figure 4.3: (a) Diffusion coefficient of hydrogen at 293 K as a function of concentration in single-crystalline Pd (closed circles) and nano-crystalline Pd (open circles) reported in [119]. Calculations were made with (solid line) and without (dashed line) solute-solute interaction. The curves were calculated by assuming the Gaussian distribution of site energies shown in Fig. (b) where $E_0 = 3.9\ kJ/mol$ corresponds to sites within the grains whereas the line at $E = E_1$ represents sites in the boundaries. The experimental results were explained with values $E_1 - E_0 = 5.3\ kJ/mol$ ($\approx 0.05\ eV$) and width of the Gaussian $\sigma = 15\ kJ/mol$ ($\approx 0.15\ eV$) [119].

Using electrochemical permeation (current density: 1 mA/cm^2, temperature: 293 K) and silver decoration tests performed in polycrystalline nickel (two grain sizes: 10 and 150), Yao and Cahoon [120] found that the diffusion of hydrogen along grain boundaries in nickel is concentration dependent and emphasized that, when the hydrogen concentration is extremely low, grain boundary diffusion is virtually stopped.

More recently, Teus et al. [112] studied the role of grain boundaries in the diffusion of interstitial and substitutional atoms in α-iron using autoradiography measurements

and the sectioning method as well as molecular dynamics simulations. The experimental data for carbon atoms, which diffuse by interstitial mechanism like hydrogen, reveal that GBs act as traps and do not accelerate the transport of such atoms in α-iron. Molecular dynamic simulations of hydrogen and carbon diffusion in bicrystals of α-iron demonstrate a retarding effect of the interface. The results of hydrogen permeation simulation performed by Teus et al. are shown in Figure 4.4. Authors [112] proposed that high values of effective diffusion coefficient typically measured in experiments can be attributed to the microcracks initiation.

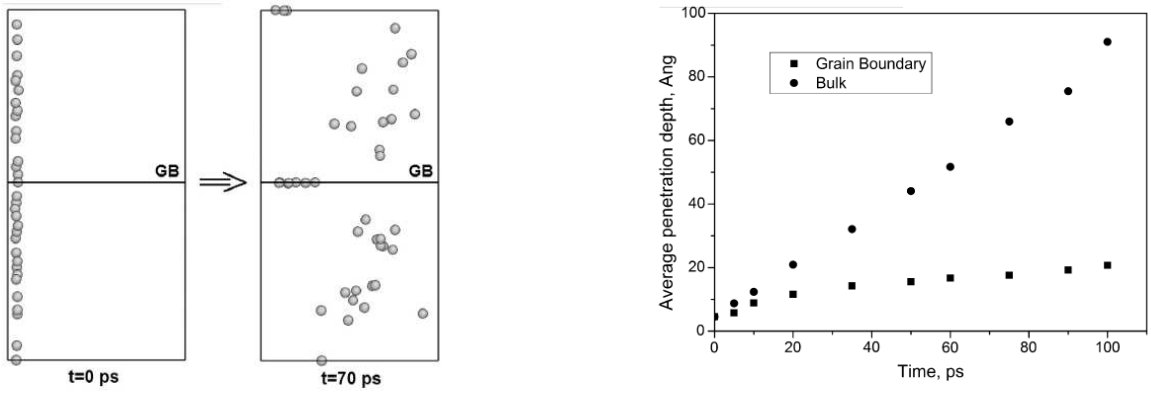

a) hydrogen atom redistribution

b) permeation depth

Figure 4.4: Molecular dynamics simulation of hydrogen diffusion in the α-iron bicrystal $\Sigma5(310)[001]$ GB [112]. Initially, H-atoms were homogeneously distributed on one side of the box as shown in (a). Crystal size is $90 \times 180 \times 85$ A^3. The effect of hydrogen trapping by the interface is shown at time moment $t = 70$ ps. As it can be seen in (b), the average penetration depth in the GB is less than in the bulk.

The effect of grain size on H-diffusion in nickel was studied by Oudriss et al. [121] (Figure 4.5b) by using the permeation (current density: 20 mA/cm^2, temperature: 298 K) technique. Non-monotonic dependence of effective diffusivity of hydrogen on grain size was found both in sorption and desorption stages (Figure 4.5). Oudriss et al. propose [121] that these results can be explained by the competitive effects of hydrogen diffusion acceleration at "random" type grain boundaries, which are considered as "amorphous phases" and provide high diffusion paths, and hydrogen trapping by "special" type boundaries, at which the crystallographic misorientation of grains is accommodated by a set of dislocation network and vacancies.

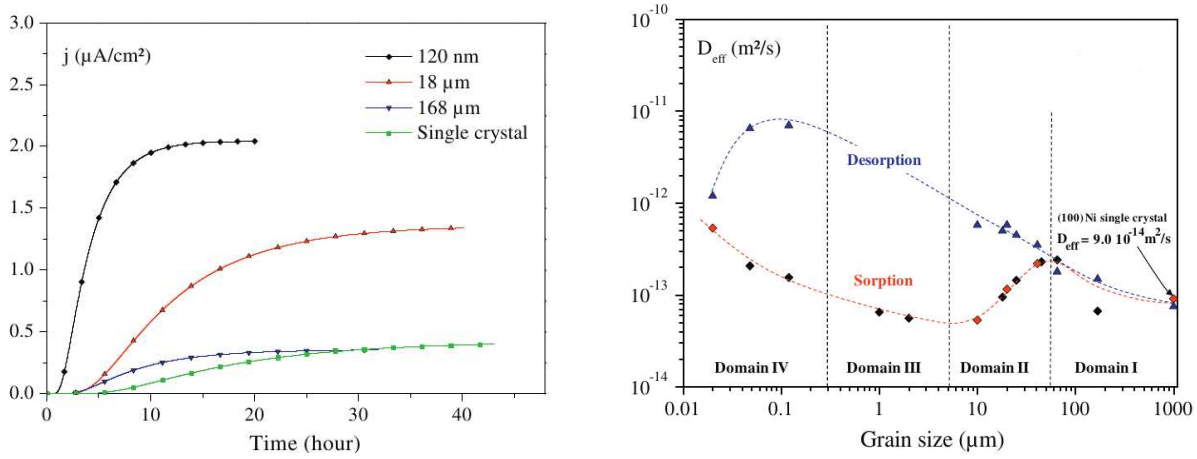

Figure 4.5: (a) Results of hydrogen permeation on nickel specimens: (a) permeation current density with respect to time measured on samples of different grain sizes and (b) dependence of hydrogen diffusion rate on grain size in sorption and desorption stages reported in [121].

It is necessary to notice that hydrogen diffusion acceleration along grain boundaries is reported in the experimental works where the value of applied current density during cathodic charging is high (typically 20 mA/cm^2) and may results in the formation of microcracks affecting the results [112]. In the case of the relatively low current density of $1-2$ mA/cm^2 (low concentrations and low concentration gradients), the grain boundary diffusion acceleration was not observed.

4.2 Classical grain boundary diffusion models

4.2.1 Formulation of the models

Mathematical treatments of GB diffusion are mostly based on the model proposed by Fisher [122]. In Fisher's formulation, it is supposed that grain boundary has a constant thickness δ and $D_{gb} \gg D_g$, i.e. interface diffusion is dominant (B and C regimes in Harrison's classification [123] shown in Figure 4.6). The diffusivity is supposed to be isotropic. Since the GB width is very small ($\delta \approx 0.5\ nm$), any concentration variation across the interface is considered to be negligible.

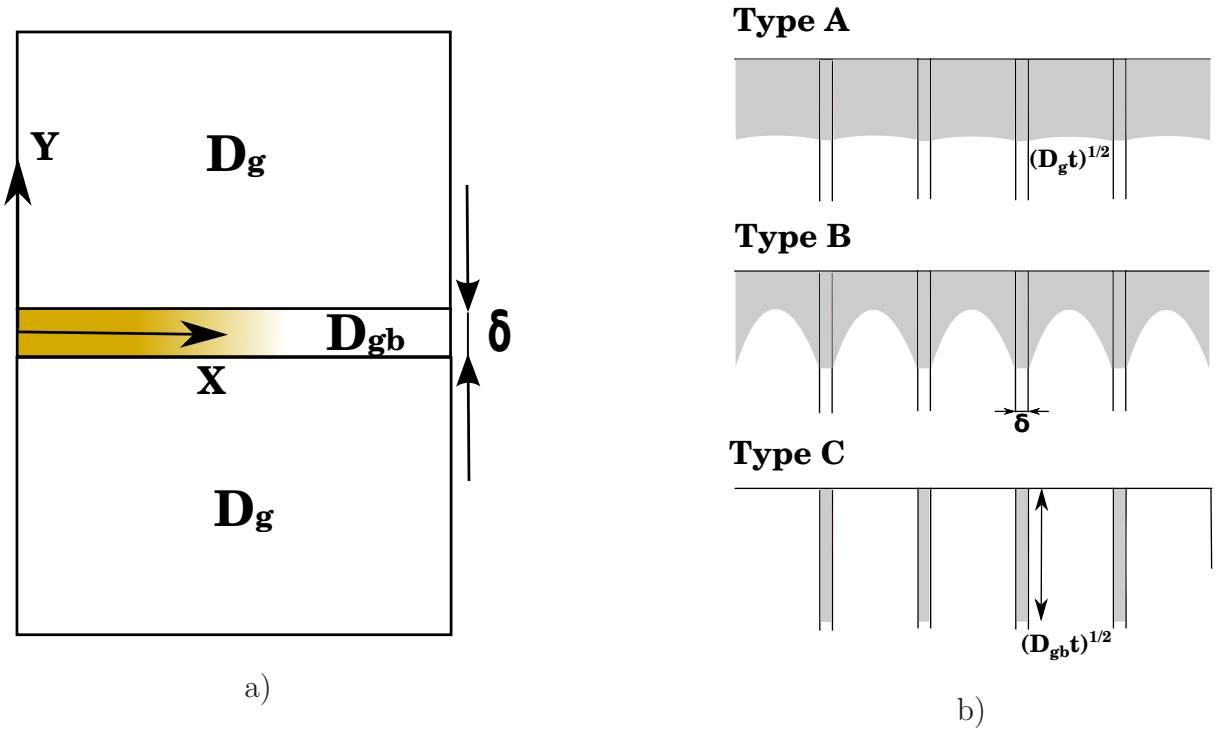

Figure 4.6: (a) Grain boundary enhanced diffusion corresponding to the regime C in (b) Harrison's A-B-C classification [123].

Fisher's GB diffusion equations can be obtained from a continuum 2D diffusion model. The derivation can be found in [124]. The continuum 2D model is composed of the mass transport equations describing the diffusion in the bulk and in the GB, and of the

continuity conditions:

$$\begin{cases} \frac{\partial c}{\partial t} = \boldsymbol{\nabla}^T \mathbf{D} \boldsymbol{\nabla} c, \\ \frac{\partial c_{gb}}{\partial t} = \boldsymbol{\nabla}^T \mathbf{D_{gb}} \boldsymbol{\nabla} \mathbf{c_{gb}}, \\ c(x, \pm\delta/2, t) = c_{gb}(x, \pm\delta/2, t), \\ J(x, \pm\delta/2, t) = J_{gb}(x, \pm\delta/2, t), \end{cases} \tag{4.1}$$

where $c \equiv c(\mathbf{x}, t)$ is a concentration of diffusing elements in the point $\mathbf{x} = (x, y)$ at the moment of time t, the symbol $\boldsymbol{\nabla} = (\frac{\partial}{\partial x_1}, \frac{\partial}{\partial x_2})^T$ denotes the gradient with transpose ^{T} and the 2×2 matrix $\mathbf{D}$ is a symmetric diffusivity tensor in the grain G ($|y| \geq \delta/2$):

$$\mathbf{D} = \begin{pmatrix} D_g & 0 \\ 0 & D_g \end{pmatrix} \tag{4.2}$$

and

$$\mathbf{D_{gb}} = \begin{pmatrix} D_{gb}^{\parallel} & 0 \\ 0 & D_{gb}^{\perp} \end{pmatrix} \tag{4.3}$$

is the diffusivity tensor in the grain boundary domain I ($|y| \leq \delta/2$).

To derive GB diffusion equations which appear in Fisher's formulation, we first assume:

$$D_{gb}^{\parallel} = D_{gb}^{\perp} = D_{gb}, \tag{4.4}$$

Fisher's system of GB diffusion equations can obtained by considering the Taylor expansion of GB concentration function, c_{gb}:

$$c_{gb}(x, y, t) = c_{gb}(x, y, t)|_{y=0} + y \frac{\partial c_{gb}(x, y, t)}{\partial y}|_{y=0} + \frac{y^2}{2} \frac{\partial^2 c_{gb}(x, y, t)}{\partial y^2}|_{y=0} + ... \tag{4.5}$$

Since X is the axe of symmetry, the odd derivatives in (4.5) give zero, and it reduces to:

$$c_{gb}(x, y, t) = c_{gb}(x, y, t)|_{y=0} + \frac{y^2}{2} \frac{\partial^2 c_{gb}(x, y, t)}{\partial y^2}|_{y=0} + \frac{y^4}{4!} \frac{\partial^4 c_{gb}(x, y, t)}{\partial y^4}|_{y=0} + ... \tag{4.6}$$

Substituting Eq. (4.6) into the second equation in the system (4.1) and neglecting the terms of order δ^2 and higher, we obtain

$$\frac{\partial c_{gb}(x, 0, t)}{\partial t} = D_{gb} \frac{\partial^2 c_{gb}(x, 0, t)}{\partial x^2} + D_{gb} \frac{\partial^2 c_{gb}(x, y, t)}{\partial y^2}|_{y=0}. \tag{4.7}$$

The last simplification is based on the assumption of Fisher model, in which it is supposed that the width of GB, δ, is so small that concentration variations across boundary is negligible [124].

The analogous substitution of Eq. (4.6) into the joining conditions in (4.1) gives (neglecting the terms of order δ^2 and higher):

$$c(x, \pm\delta/2, t) = c_{gb}(x, 0, t), \tag{4.8}$$

$$D_g \frac{\partial c(x, \pm\delta/2, t)}{\partial y} = D_{gb} \frac{\delta}{2} \frac{\partial^2 c_{gb}(x, y, t)}{\partial y^2}|_{y=0}. \tag{4.9}$$

Finally, we obtain the following system of equations (Fisher's model):

$$\begin{cases} \frac{\partial c}{\partial t} = D_g \nabla c, & |y| \geq \delta/2; \\ \frac{\partial c_{gb}}{\partial t} = D_{gb} \frac{\partial^2 c_{gb}}{\partial^2 x} + \frac{2}{\delta} D_g \frac{\partial c}{\partial y}|_{|y|=\delta/2}, & |y| \leq \delta/2, \\ c(x, \pm\delta/2, t) = c_{gb}(x, t), \end{cases} \tag{4.10}$$

where the second term in the right-hand side of the GB diffusion equation takes into account a leakage of diffusing atoms from the interface to the bulk.

4.2.2 Analytical solution of Fisher GB diffusion equations

The Fisher system can be solved analytically. For the constant concentration source on a surface,

$$\begin{cases} c(0, y, t) = C_0 H(t), \\ c(x, y, 0) = 0, \quad x > 0, \\ c(\infty, y, t) = 0, \end{cases} \tag{4.11}$$

where $H(t)$ is the Heaviside step function

$$H(t) = \begin{cases} 1, & \text{if } t \geq 0 \\ 0, & \text{if } t < 0 \end{cases} \tag{4.12}$$

the solution was obtained by Whipple [125] by means of the Fourier-Laplace transform. It can be written as

$$c(\xi, \eta, \beta) = c_1(\eta) + c_2(\xi, \eta, \beta), \tag{4.13}$$

where

$$c_1(\eta) = C_0 \left(\frac{\eta}{2}\right) \tag{4.14}$$

describes the contribution from the volume diffusion, and

$$c_2(\xi, \eta, \beta) = \frac{C_0 \eta}{2\pi^{1/2}} \int_1^{\Delta} \frac{\exp(-\eta^2/4\sigma)}{\sigma^{3/2}} \left[\frac{1}{2} \left(\frac{\Delta - 1}{\Delta - \sigma}\right) \left(\frac{\sigma - 1}{\beta} + \xi\right)\right] d\sigma \tag{4.15}$$

corresponds to the impact of grain boundary transport. The variables ξ and η are dimensionless coordinates:

$$\xi = \frac{|y| - \delta/2}{\sqrt{D_g t}}, \quad |y| \geq \delta/2 \tag{4.16}$$

$$\eta = \frac{x}{\sqrt{D_g t}}, \tag{4.17}$$

and

$$\beta = \frac{(\Delta - 1)\delta}{2\sqrt{D_g t}}, \tag{4.18}$$

where

$$\Delta = D_{gb}/D_g. \tag{4.19}$$

Suzuoka [126] obtained the analytical solution of the Fisher system for the instantaneous source condition

Papers devoted to the analysis and applications of analytical solutions of the Fisher system (4.10) for constant [125] as well as for the instantaneous sources obtained by Suzuoka [126] can be found in the literature [127–132]. Review paper devoted to the diffusion along grain boundaries can be found in the literature as well (for example, the works of [95, 99, 133]).

4.2.3 Simulations of grain boundary diffusion

In the work of Yazdipour et al. [134], hydrogen permeation in polycrystalline X70 steel was simulated using the Fisher GB diffusion model formulated in the two-dimensional form. The Cellular Automation technique combined with the finite difference method were used for the numerical solution. Grain boundaries were considered as fast diffusion paths, and the effect of grain size was studied. However, the influence of GB trapping was not taken into account, and the discrepancy between the modelling results experimental data obtained from permeability studies was found (Figure 4.7).

Rimoli and Ortiz carried out three dimensional finite element calculation of hydrogen-assisted intergranular crack initiation and propogation in AISI 4340 steel [53]. They specifically focused on type C kinetics [99], i.e. when the bulk diffusion is nearly locked and diffusion takes place almost exclusively at the GBs, without any essential leakage to the neighbouring grains.

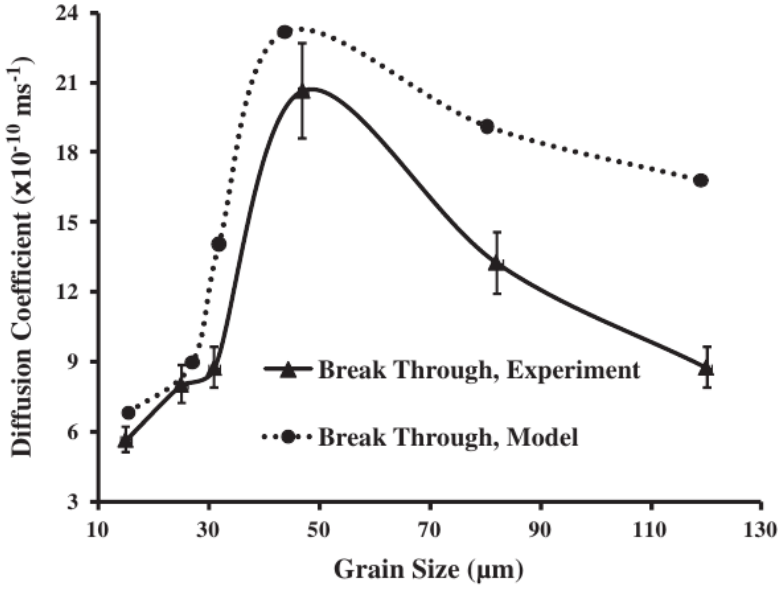

Figure 4.7: The effect of average grain size on the diffusion coefficient in X70 steel, experimental results from permeability studies and results of the computation based on Fisher model for the grain boundary diffusion [134].

As an example of the application of Fisher model, the work of Gryaznov et al. [135,136] is worth to be mentioned. The situation in which the fast core pathway is sandwiched between between blocking space charge layers (SCLs) in ionic material was modelled using the finite element method. It was found that the diffusion in nano-crystalline ZrO_2 is retarded significantly due to the blocking spaces at grain boundaries and extremely long times are required for diffusing atoms to fill the grains.

Legrand et al. [137] studied the influence of scale effects and microstructure on H-transport in polycrystalline aggregates by using the classical Fick's equations for the modelling of both bulk and accelerated GB diffusion.

In the present work, both systems (4.1) and (4.10) were solved numerically by the finite element method and compared with the multi-scale approach (the details are given in Appendix).

4.3 Multi-scale/multi-scheme approach

In this part, the multi-scale model of GB diffusion is presented. First, we consider a two dimensional domain which consists of two parts. The diffusion in one part, G, is calculated by using the finite element (FE) method. The diffusion in the other part, I, is computed by applying the Finite Difference-Atomic Layer (FDAL) scheme. The method of coupling of FE and FDAL diffusion equations is described.

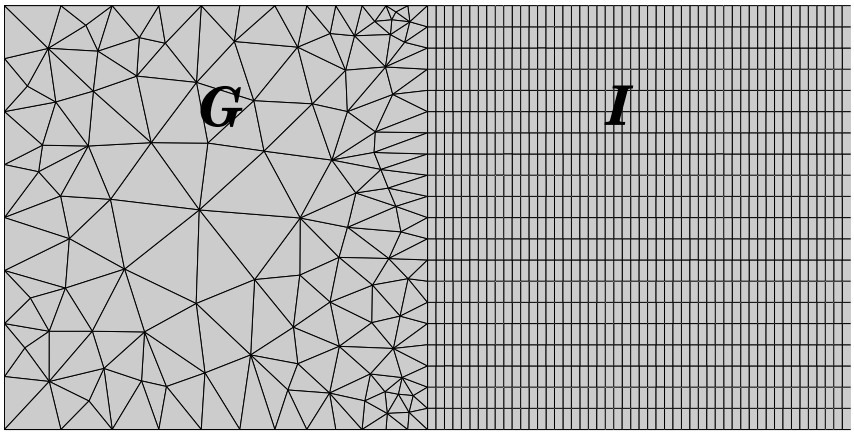

Figure 4.8: The diffusion domain consisting of two parts, G and I. The domain G is meshed by triangles used in the finite element method. The finite difference grid is utilized in the domain I.

Diffusion process in the first part, G, is supposed to be described by the classical Fick's diffusion law, i.e. continuum 2D model:

$$\frac{\partial c}{\partial t} = \boldsymbol{\nabla}^T \mathbf{D} \boldsymbol{\nabla} c. \tag{4.20}$$

Equation (4.20) can be solved numerically by the finite element method. Let φ_α, $\alpha \in \mathcal{G}$, be the set of basis functions for the finite element method. The notation for atomic planes, α and β, are adopted from the previous section and used to describe the 2D numerical network (set of nodes) considered in the multi-scheme method (Figure 4.9). Support of each φ_α belongs to G, and supports of all φ_α cover G. As in the standard finite element method, we suppose that the concentration function $c(\mathbf{x}, t)$ for $\mathbf{x} \in G$ is a sum of basis functions $\varphi_\alpha(\mathbf{x})$ with coefficients $c_\alpha \equiv c_\alpha(t)$

$$c = \sum_{\alpha \in \mathcal{G}} c_\alpha \varphi_\alpha. \tag{4.21}$$

Substituting (4.21) into (4.20), multiplying by φ_β, $\beta \in \mathcal{G}$ and taking the integral over G with applying integration by parts and corresponding boundary conditions we obtain the following set of linear equations

$$\sum_{\alpha\in\mathcal{G}} \frac{\partial c_\alpha}{\partial t} \int_G \varphi_\alpha \varphi_\beta d\mathbf{x} = -\sum_{\alpha\in\mathcal{G}} c_\alpha \int_G \boldsymbol{\nabla}\varphi_\beta \cdot \mathbf{D}\boldsymbol{\nabla}\varphi_\alpha d\mathbf{x} + \sum_{\alpha\in\mathcal{G}} c_\alpha \int_{\partial G} \varphi_\beta \mathbf{e}^T \mathbf{D}\boldsymbol{\nabla}\varphi_\alpha \tag{4.22}$$

where ∂G is a boundary of G and $\mathbf{e} = \mathbf{e}(\mathbf{x})$ is a unit normal vector to ∂G. The equation (4.22) can be rewritten in the matrix form

$$\frac{\partial}{\partial t}(c_\alpha) = (\Phi_{\alpha\beta})(c_\beta), \tag{4.23}$$

where the matrix

$$(\Phi_{\alpha\beta}) = (\Phi_{1,\alpha\beta'})^{-1}(\Phi_{2,\beta'\beta}) \tag{4.24}$$

with

$$(\Phi_{1,\alpha\beta'}) = \left(\int_G \varphi_\alpha \varphi_{\beta'} d\mathbf{x}\right), \quad (\Phi_{2,\beta'\beta}) = \tag{4.25}$$

$$-\left(\int_G \boldsymbol{\nabla}\varphi_{\beta'} \cdot \boldsymbol{\nabla}\varphi_\beta d\mathbf{x}\right) + \left(\int_{\partial G} \varphi_{\beta'} \mathbf{e}^T \mathbf{D}\boldsymbol{\nabla}\varphi_\beta\right). \tag{4.26}$$

Diffusion in the second part, I, of the considered domain is described by the combination of 1D diffusion equations discretized by FD method and discrete AL model. The AL model presented in the previous section is used to take into account segregation and diffusivity across the grain boundary. To account for the transport along the grain boundary, the FD scheme is implemented. In fact, we extend the formulation of the one dimensional AL model to the two dimensional case by writing the FD scheme in terms of jump frequencies $\Gamma_{\alpha\beta}$. Any change in the concentration at the node α in the GB is given by the difference between inward and outward fluxes which can be written as

$$\frac{\partial c_\alpha}{\partial t} = \sum_{\alpha\sim\beta} (\Gamma_{\alpha\beta}(1 - c_\alpha)c_\beta - \Gamma_{\beta\alpha}(1 - c_\beta)c_\alpha), \tag{4.27}$$

where $\alpha \sim \beta$ means that nodes with indices α and β are neighbours; $\alpha, \beta \in \mathcal{I}$, and the set $\mathcal{I}$ consists of indices of nodes which belong to the GB, I.

For the terms corresponding to the diffusion along the GB, we use the identities (see Sec. 3.2.1)

$$\Gamma_{\alpha\beta} = \Gamma_{\beta\alpha} = D_{\mathrm{gb}}^{\parallel}/s^2, \tag{4.28}$$

where s is a mesh step of the FD scheme shown in Figure 4.9.

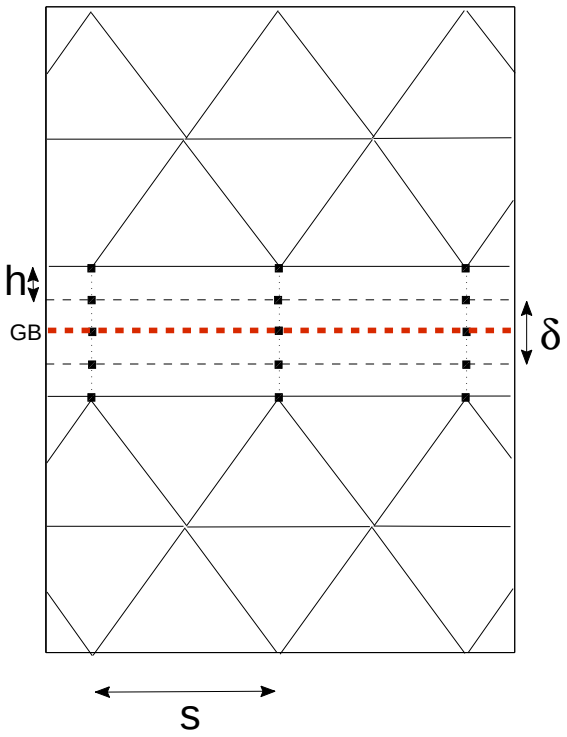

Figure 4.9: Network of the FEFDAL method used for modelling diffusion at the grain boundary. In the middle, the grid for the Finite Difference - Atomic Layer Model is shown by the dashed lines connecting the neighbouring nodes. The top and bottom domains (grains) are meshed by finite elements (triangles). The distance between atomic layers, h, the GB thickness, δ, and mesh step along the GB, s, are shown.

It is easy to see that the substitution of (4.28) into (4.27) gives the second order derivative discretized by FD method and corresponding to the gradient of flux along the interface. For the diffusion across the interface the coefficients $\Gamma_{\alpha\beta}$ can be different ($\Gamma_{\alpha\beta} \neq \Gamma_{\beta\alpha}$) and are calculated from (3.21) according to the immersion energy profile (Figure 3.6).

Finally, replacing the time derivative for both identities (4.23) and (4.27) with

$$\frac{\partial c_\alpha}{\partial t} = \frac{c_\alpha(t_{n+1}) - c_\alpha(t_n)}{\Delta t}, \qquad \Delta t = t_{n+1} - t_n, \quad n = 0, .., N \tag{4.29}$$

and choosing initial conditions $c = c_0$ for $t = 0$, we can successively solve our system of equations (4.23) and (4.27) to find all the concentrations $c_\alpha(t)$ at the moment $t = t_N$.

The multi-scale model was validated on a single crystal divided in two domains: in one of which hydrogen concentration was calculated by FE method and, in the second one, the combination of FD scheme and AL model was used. The results obtained using the multi-scale model match the ones computed by the uniform FE scheme.

Next, the FEFDAL method is applied for the simulation of the diffusion in a bicrystal. The network for the numerical solution is plotted in Figure 4.9. For modelling the diffusion at the GB, three rows of nodes are inserted between two grains of the bicrystal. The middle plane corresponds to the grain boundary plane, and two others are used for joining the FE and FDAL schemes. Thereby the thickness of the GB region treated by FDAL method is $4h$, and the effective thickness accounting for the GB properties is $2h$ (noted as δ in Figure 4.9).

It was checked that the solution obtained by applying the uniform FE scheme matches the one calculated by using the multi-scale method without accounting for specific GB properties. In the following section, we apply the multi-scale FEFDAL method to study some fundamental aspects of intergranular diffusion in the case of a bicrystal and the junction of three grains including enhanced GB diffusion, GB trapping kinetics, barrier effect and stress heterogeneity in neighbouring grains.

4.4 Grain boundary diffusion

4.4.1 Nickel bicrystal

In the present work, hydrogen nickel is chosen as a model system to investigate the impact of the physical properties of the GB core on diffusion profiles by applying the multi-scale method described in Sec. 4.3.

Hydrogen lattice diffusivity in Ni used in the simulation $D_g = \Gamma h^2$. The coefficient Γ is calculated from (3.21) where $E_{\alpha\beta} = 0.4\ eV$, $k = 8.617 \cdot 10^{-5}\ eV$, $T = 300\ K$, $\nu = 10^{13}\ s^{-1}$, $z = 4$. The distance between atomic planes, h, is equal to the half of the lattice parameter for Ni ($h = 1.762 \cdot 10^{-10}\ m$).

In the calculation, the system is considered to be initially hydrogen free. The constant source surface condition (site occupancy $c(0, y, t) = c_0 = 0.000134$) was used for the entry side, and the hydrogen flux is supposed to be equal to zero on the exit side of the bicrystal.

Different geometrical configurations of the grain boundary in the bicrystal were considered. First, the H-diffusion along the grain boundary considered as a short circuit path is modelled by the multi-scale FEFDAL method and compared with the results obtained by the Fisher (4.10) and 2D continuum (4.1) approaches (Sec. 4.4.2). Then, the GB trapping effect alone was investigated considering the same configuration of bicrystal (Sec. 4.4.3) but with no acceleration assumed (Kirchheim's A2 regime [111]). The effect of transverse diffusivity on the evolution of solutes was studied by employing the multi-scale method on the bicrystal with the GB parallel to the entry and exit sides (Sec. 4.4.4). The case of the three grains junction was also studied in Sec. 4.4.5. Finally, the hydrogen redistribution in a pre-charged bicrystal in the presence of stress gradients is computed in Sec. 4.4.6.

4.4.2 Diffusion in a bicrystal: short circuit path along the GB

Figure 4.10 shows the hydrogen distribution along the interface of a bicrystal calculated by the FE method using Fisher's model (4.10), the 2D continuum approach (4.1) and the multi-scale method. The ratio $D_{gb}/D_g = 1000$ is assumed ($E_{\alpha\beta} \approx 0.22\ eV$ at the GB). It is seen that the concentrations calculated by the multi-scale method are higher than the ones obtained by the 2D continuum approach (4.1) but lower than the values computed by using the Fisher model (4.10).

It is worth mentioning that with reducing the ratio D_{gb}/D_g from 1000 to 100 and 10 the discrepancy between concentration profiles computed by the continuum and multi-scale models decreases, and the solutions are in agreement for $D_{gb}/D_g = 1$.

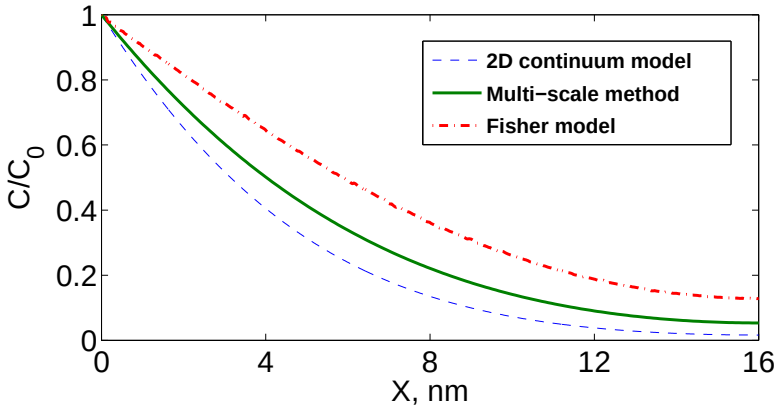

Figure 4.10: Hydrogen concentration profiles along the grain boundary in the nickel bicrystal calculated by different methods in the case of a fast diffusion in the GB core without trapping. $D_g = 2.37 \cdot 10^{-13}\ m^2 \cdot s^{-1}$. $D_{gb}/D_g = 1000$. Duration: 1000 ns.

4.4.3 Diffusion in a bicrystal: impact of trapping

The multi-scale method was employed for the simulation of hydrogen diffusion along an interface accounting for the GB trapping kinetics alone. The segregation energy, ΔE_{seg}, was chosen to be equal to $-0.36\ eV$ [3]. The barrier to jump into the GB layer is the same as for the bulk diffusion jump (i.e. $E_{\alpha\beta} = 0.4\ eV$), the barrier to escape from the GB is $E_{\alpha\beta} - \Delta E_{seg} = 0.76\ eV$. The diffusivity along the grain boundary is assumed to be the same as in the bulk $D_{gb}^{\parallel} = D_g$.

H-distribution in the nickel bicrystal after 1 s and 3 s of diffusion annealing is shown in Figure 4.11. The concentration maps presented in Figures 4.11a-b demonstrate the effect of trapping kinetics of the grain boundary acting as a sink and how the interface can retard the diffusion by trapping diffusing atoms from the near bulk. This regime of GB diffusion was proposed intuitively by Kirchheim [111] but is simulated for the first time here by the multi-scale method.

It can be noticed in Figures 4.11c-d that the GB diffusion profile is smooth in comparison to the atomic scale, while the transverse profile exhibits a discontinuity (Figure 4.12a) at the GB plane.

The dependence of the impact of the value of the segregation energy is shown in Figure 4.12. In Figure 4.12a, the concentration profiles along the section perpendicular to the GB at the distance of characteristic diffusion length, $2\sqrt{D_g t}$, at time moment $t = 1\ s$ are displayed. In Figure 4.12b, the difference between Fick's concentration on the edge of bicrystal, C_E, (no influence of the segregation) and the concentration in the atomic plane neighbouring to the GB, C_G, are shown for different values of segregation energy. It is seen that the effect of GB is the highest for segregation energies lower than $-0.3\ eV$ and reduces rapidly with increasing the energy value to $-0.2\ eV$ for which the retarding effect of GB is negligible. It means that only GBs with deep traps will retard the diffusion significantly.

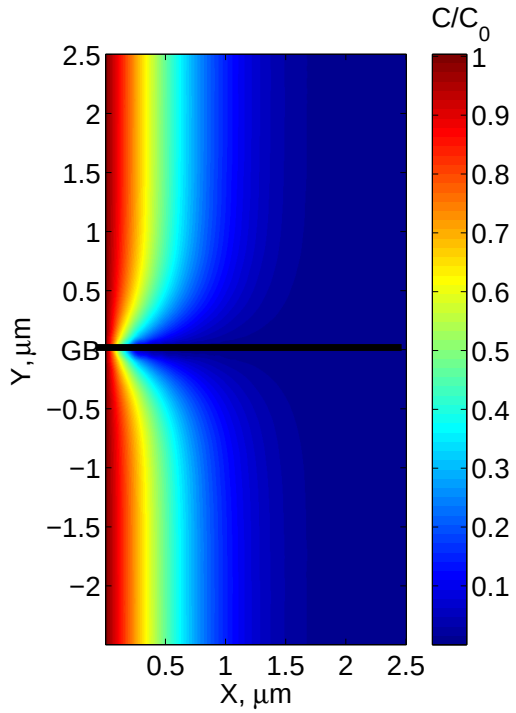

a) Bulk concentrations, t=1 s

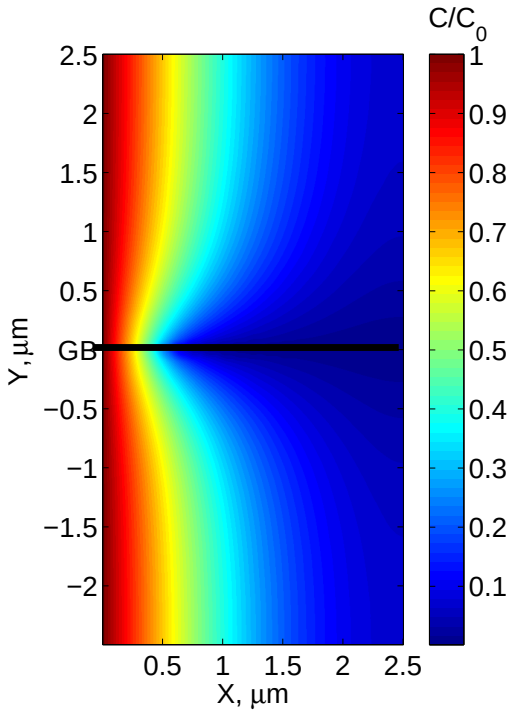

b) Bulk concentrations, t=3 s

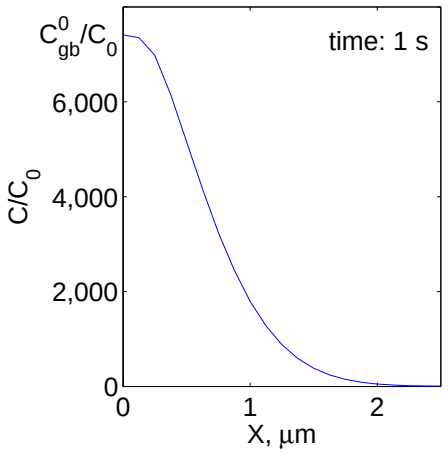

c) GB concentrations, t=1 s

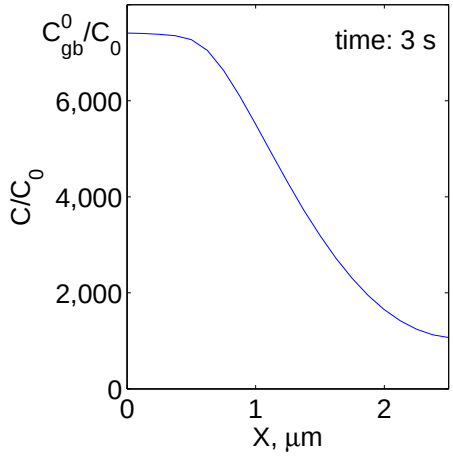

d) GB concentrations, t=3 s

Figure 4.11: Time evolution of the H-concentration in a nickel bicrystal with a grain boundary perpendicular to the surface grain boundary (shown as the black line in a-b). The effect of grain boundary segregation on the H-distribution in the bulk is shown at times (a) $t = 1\ s$ and (b) $t = 3\ s$; the corresponding GB concentration profiles are presented in (c) for $t = 1\ s$ and (d) for $t = 3\ s$. The thickness of the membrane is 2.5 μm. Grain boundary segregation energies $\Delta E_{seg} = -0.36\ eV$. The diffusivity along the interface is assumed to be equal to the volume one: $D_{gb}^{\parallel} = D_g$.

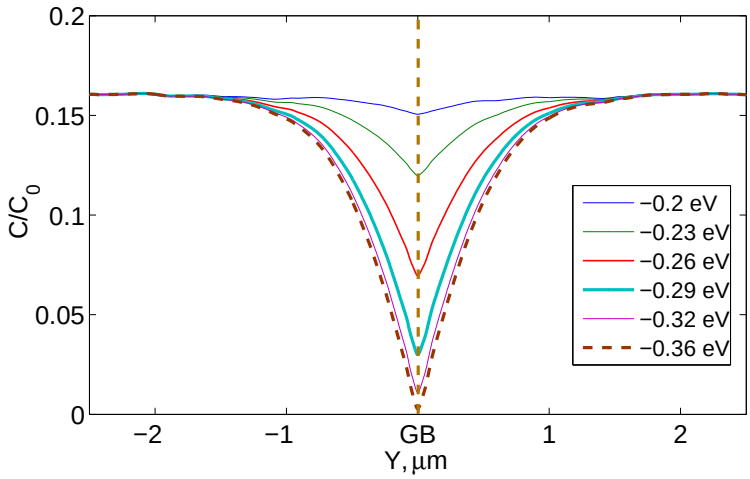

a)

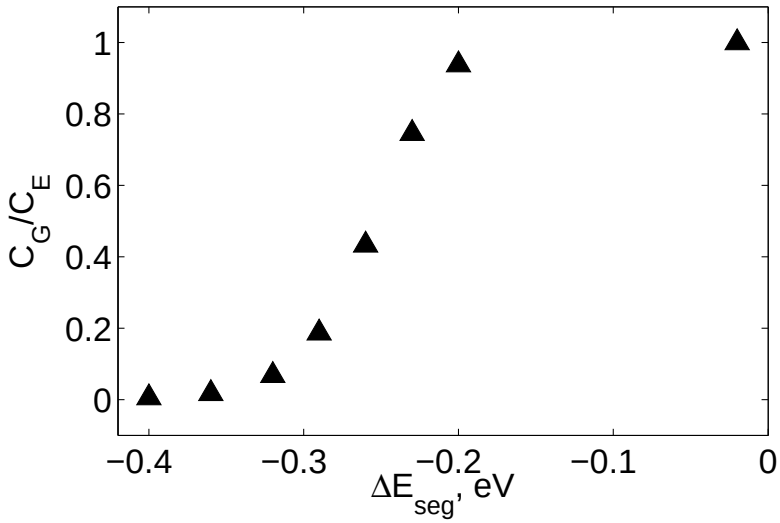

b)

Figure 4.12: Impact of the value of the segregation energy on the transverse diffusion profile taken at a distance of the characteristic diffusion front propagation, $2\sqrt{D_g t}$, at time $t = 1\ s$. (a) Concentration profiles across GB and (b) the ratio of Fick's concentration, C_E, (no effect of the segregation) and the concentration in the atomic plane neighbouring to the GB, C_G, are shown for different values of energy.

4.4.4 Transverse diffusion: barrier-trapping effect

Another phenomenon that can be studied using the multi-scale approach is the barrier effect of GBs. We employed the multi-scale FEFDAL method in the simulation of H-diffusion in the bicrystal membrane in which H-solutes are forced to diffuse across the grain boundary. The segregation energy, the barriers to jump into the GB layer and to escape are the same as used in the previous section. The membrane thickness is 2 μm.

The concentration at time moment $t = 3\ s$ is shown in Figure 4.13. It is seen that the distribution of solute atoms is strongly affected by the presence of GB. At time moment $t = 3\ s$, the concentrations in the second (right) grain are close to zero due to the blocking effect of the boundary. The concentration profile in the first (left) grain is linear due to the strong segregation to the GB that acts as an absorbing layer in the first moments.

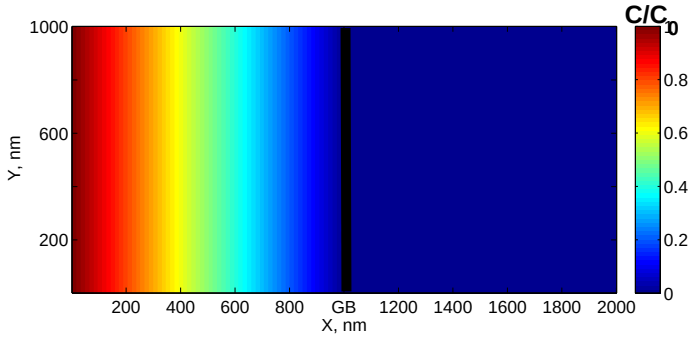

a)

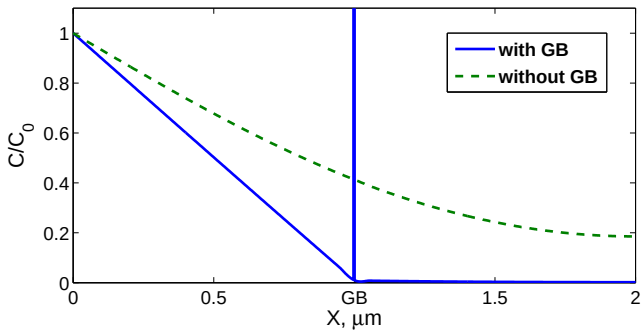

b)

Figure 4.13: Effect of the grain boundary barrier and trapping on the hydrogen diffusion in the bicrystal with a grain boundary parallel to the surface. (a) H-distribtuion in the nickel bicrystal at time moment $t = 3\ s$ is shown. (b) The concentration profile along X direction is presented in comparison with the H-distribution calculated without accounting for the GB. The characteristic concentration peak at the boundary is observed due to the segregation: $C_{gb}/C_0 \approx 3057$.

4.4.5 Diffusion through a three grains junction

Finally, after validating the multi-scale method on the bicrystal, we study diffusion at the vicinity of the junction between three grains, since it combines the effect of barrier and trapping due to the inclination of the GBs with respect to the H-charging surface.

According to the results of microstructure analysis reported by Oudriss et al. [121], the fraction of triple junctions of $\Sigma-\Sigma-\Sigma$ and $\Sigma-\Sigma-R$ type (where R notes the random type GB) is about 20%. The most frequently observed special GBs are of type $\Sigma3$, $\Sigma9$ and $\Sigma27$ [121]. Segregation energies $\Delta E_{seg} = -0.26\ eV$ for all three grain boundaries were chosen for the sake of simplicity. This mean value of segregation energy corresponds to the $\Sigma3$ type GB [3].

The size of the aggregate is $1 \times 1\ \mu m$. The initial and boundary conditions are identical to those which were used for the bicrystal membranes. The duration of diffusion is 3 s.

In Figure 4.14, the hydrogen concentrations in the homogeneous (without GBs) membrane and in the three grains junction are plotted for comparison. The retarding effect of GBs is observed.

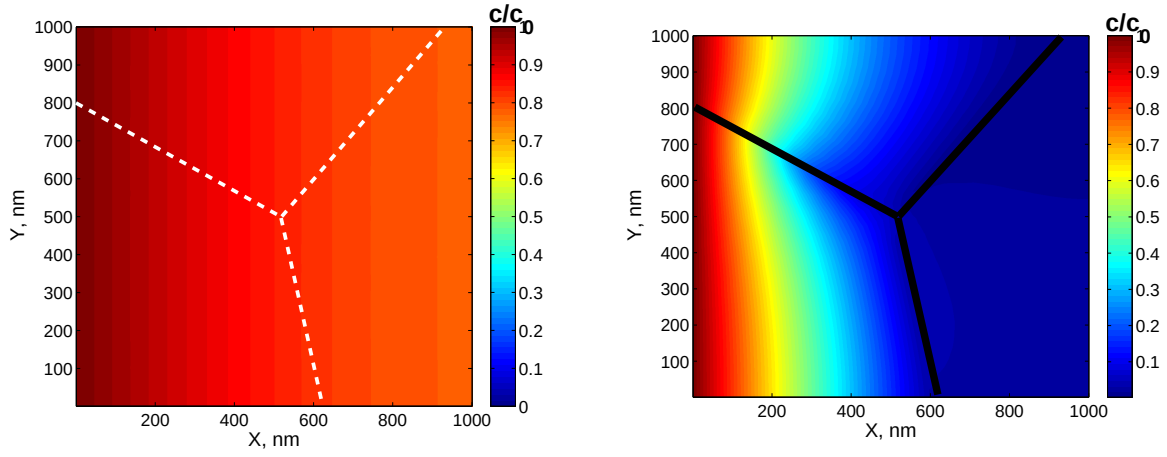

Figure 4.14: H-distribution in an initially H-free three grains junction in nickel at time $t = 1\ s$ (a) without and (b) with accounting for the GB ($\Delta E_{seg} = -0.26\ eV$) trapping properties. The black lines correspond to the grain boundaries.

4.4.6 Diffusion in the presence of stress heterogeneities

Finally, the multi-scale FEFDAL method was used to simulate hydrogen diffusion affected by hydrostatic stress gradients at the GB in the bicrystal. High stress gradients are usually present at GBs in polycrystalline materials under mechanical loading due to heterogeneous mechanicals properties of neighbouring grains. They cause the redistribution and segregation of hydrogen in grains with higher hydrostatic stresses [138]. These singularities present at GBs have to be treated carefully in numerical simulations of H-diffusion in polycrystals to provide the accuracy of computations.

For the sake of simplicity, we assume that stresses do not affect the diffusivity in the bulk. Applying of stresses affects the energy profile (Figure 3.6) describing the atomic jump process. Any change of the profile, $\Delta\mu_\sigma$, is calculated as:

$$\Delta\mu_\sigma = -\sigma_h V_H, \tag{4.30}$$

where σ_h is a hydrostatic stress, and V_H is the partial molar volume of hydrogen in nickel ($V_H = 1.7 \cdot 10^{-6} m^3 \cdot mol^{-1}$).

Hydrostatic stresses are assumed to appear in the bicrystal from the time moment $t = 0$: $\sigma_h = -100\ MPa$ in the left grain and $\sigma_h = 100\ MPa$ in the right one (Figure 4.15). The corresponding shift in the left grain $\Delta\mu_\sigma \approx 0.00176\ eV$ and is the same and negative in the right grain.

After applying stresses, the immersion energy profile at the GB is recomputed as it is described in Sec. 3.2.5 of Chapter 3.

The hydrogen concentration is supposed to be uniform initially ($c(x, y, 0) = c_0 = 0.000134$). The system is considered to be insulated, i.e. the boundary condition imposes a zero normal flux on the edges of bicrystal.

In Figure 4.15, the hydrogen distribution in (a) grains and (b) concentration profile across the GB are shown at time moment $t = 0.3\ s$. The enrichment in the grain with tensile hydrostatic stresses and the depletion in the grain with compression hydrostatic stresses are observed. It is seen that the concentration profile is symmetric which means that high stress gradients are treated accurately by the multi-scale method. The discontinuity and the characteristic concentration peak are observed at the GB.

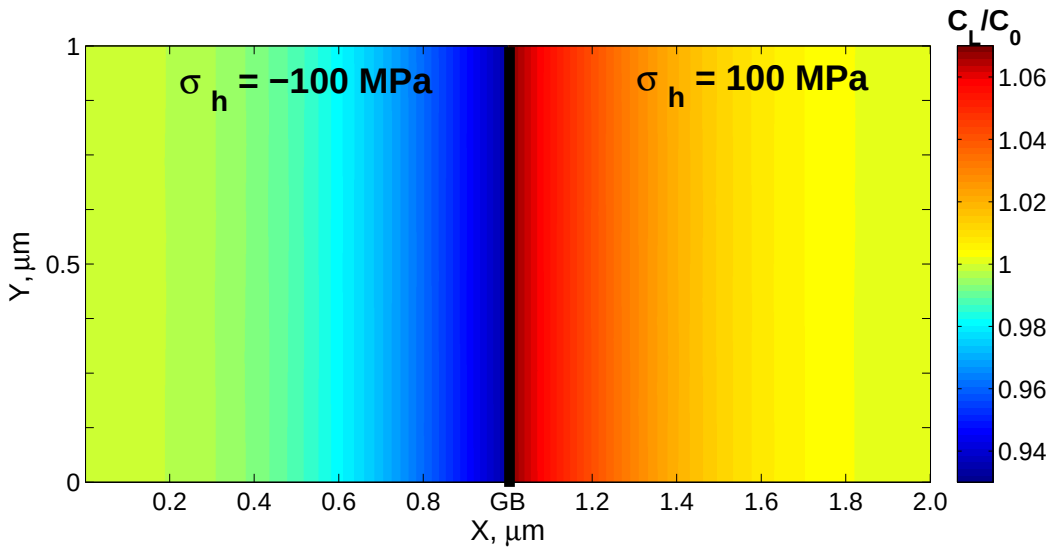

a) Concentration map

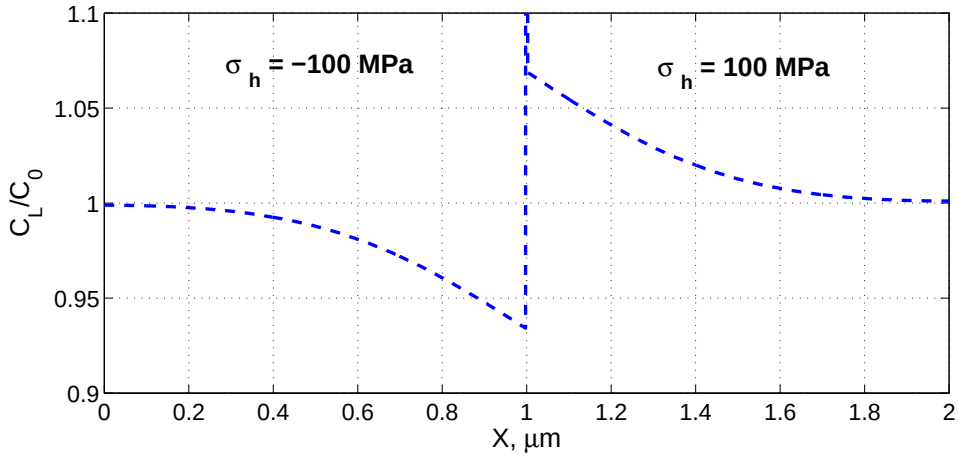

b) Section along X direction

Figure 4.15: Hydrogen redistribution due to the presence of a hydrostatic stress gradient in the initially uniformly H-charged Ni bicrystal. Hydrostatic stresses are supposed to appear instantaneously at $t = 0$: $\sigma_h = -100\ MPa$ in the left grain and $\sigma_h = 100\ MPa$ in the right one; the segregation energy is $-0.26\ eV$. (a) H-distribution in the bicrystal is shown at time $t = 0.3\ s$. H-enrichment is observed in the grain with higher hydrostatic stresses. (b) The corresponding transverse concentration profile.

4.5 Discussion

In Sec. 4.4.2, the results of fast diffusion along the interface of bicrystal were compared for the different models. It was shown that the concentration profiles calculated by using the classical GB diffusion models and the multi-scale method differ. This discrepancy can be explained by the different mathematical treatment of the leakage of diffusing atoms from the interface to the volume.

The difference between the results obtained by multi-scale and 2D continuum approaches can be understood noticing that only 3 atomic planes correspond to the interface in the FEFDAL (multi-scale) approach. The equations of AL diffusion model are equivalent to the continuum ones descretized by the FD scheme. Hence, this model can be considered as a "rough discretization" from the viewpoint of the numerical treatment inside the GB where only three atomic planes (four space steps in the finite difference grid) are inserted (Figure 4.9).

In the Fisher model,

$$\frac{\partial c_{gb}}{\partial t} = D_{gb}\frac{\partial^2 c_{gb}}{\partial^2 x} + \frac{2}{\delta}D_g\frac{\partial c}{\partial y}|_{|y|=\delta/2}, \quad |y| \leq \delta/2, \tag{4.31}$$

the term $\frac{2}{\delta}D_g\frac{\partial c}{\partial y}$ describing the leakage from the interface replaces the second order concentration derivative, $D_{gb}\frac{\partial^2 c_{gb}}{\partial^2 y}$, corresponding to the gradient of flux across the interface in the 2D continuum model

$$\frac{\partial c_{gb}}{\partial t} = D_{gb}\frac{\partial^2 c_{gb}}{\partial^2 x} + D_{gb}\frac{\partial^2 c_{gb}}{\partial^2 y}, \quad |y| \leq \delta/2. \tag{4.32}$$

It can be noted that this assumption can be oversimplified or satisfactory depending on the GB structure and the corresponding migration energy barrier. Thus, in the case of a fast self-diffusion (i.e. without segregation effect) at grain boundaries, the effect of leakage from an interface towards the grains can be more or less pronounced, thereby defining whether the diffusion process is in the framework of Fisher's assumptions or not. In turn, for the impurity diffusion, the leakage of solute atoms to the bulk is less due to the segregation-barrier effect, and, hence, the assumptions of Fisher's approach seem to be rather valid for the boundaries with low segregation energies. However, in the mathematical treatment of segregation effect, the local equilibrium is usually assumed instead of considering the kinetics, and the diffusion coefficient appeared in the Fisher

GB diffusion equation (4.31) in the leakage term corresponds to the volume diffusivity but not to the diffusion energy barrier for solute atoms to leave the boundary. Therefore, the classical approach may not be able to describe the effects of segregation and diffusion barrier properties of GBs reported in the literature [6, 7, 106, 112, 120].

One may notice that the discrepancy between GB diffusion profiles computed by the multi-scale, 2D continuum and Fisher approaches can be accounted to explain the difference between hydrogen diffusion rates from modelling and experimental results found by Yazdipour et al. [134] for X70 steel (mentioned in Sec. 4.2.3 in this chapter).

In Fisher's approach (4.10), the effect of segregation can be taken into account supposing the joining condition which is known as Henry isotherm:

$$c_{gb}(x,t) = sc(x, \pm\delta/2, t), \tag{4.33}$$

where s is an equilibrium segregation factor. In the case of strong segregation, a non-linear dependence of the volume concentration on the GB occupancy is usually accounted by using McLean's isotherm:

$$c_{gb} = \frac{sc}{1 + (s-1)c}, \tag{4.34}$$

where s is supposed to depend only on temperature $s = s_0 exp(-\Delta E_{seg}/kT)$.

In the models of Henry and McLean, the local equilibrium is assumed and trapping by the GB does not affect the distribution of solutes in grains. In contrast to these approaches, the multi-scale FEFDAL model takes into account the kinetics of segregation and transverse diffusion and demonstrates the impact of GBs on the evolution of concentrations in grains. The characteristics of the methods analysed in this chapter are summarized in Table 4.1.

Table 4.1: Characteristics of GB diffusion calculation methods

Method	Features		
	Segregation kinetics	Diffusion anisotropy	Concentration dependence
Multi-scale	yes	yes	yes
2D continuum	no	yes	yes
Fisher	no	no	more or less

The aspect of segregation kinetics was considered in Sec. 3.1.2 of Chapter 3. As it was noted, the approach to equilibrium after the McLean model is too slow due to the oversimplified assumption of constant segregation factor and impede the interpretation of the surface segregation data.

The results presented in Sec. 4.4.3 (namely, in Figure 4.11b) is in agreement with the GB diffusion regime proposed intuitively by Kirchheim [111], excepting that in the present work the diffusivity along the GB is assumed to be equal to the one in grains, and Kirchheim discussed the case when the GB diffusivity is very slow compared to the bulk ($D_{gb} \ll D_g$). The last remarks means that the retarding impact of GB on the distribution of diffusing atoms in grains is only due to trapping by the GB. The low diffusivity along the GB will contribute additionally to this dilatory effect.

The simplifications used in the multi-scale model presented in this chapter are the same as discussed in Chapter 3 for the atomic layer approach. Hydrogen segregation energies are rather high and corresponds to the almost H-filled GBs for the chosen bulk concentrations. At high H-concentrations, the repulsive H-H interaction can strongly affect the H-diffusivity in the vicinity of GBs blocking H-atoms. The effects of volume expansion and forming the hydride phase are expected to be present. For the other types of GBs, the segregation energies and activation barriers are lower [3], and the hydrogen diffusion can be less affected. The data about GB structure is required to precise the analysis presented.

From the physical point of view, AL model formulated in terms of jump frequencies can precise a stress driven flux across GB which can be present in polycrystalline materials under mechanical loading [138]. At the same time, it was demonstrated that the approach used in the multi-scale method provides an accurate numerical treatment of stress gradients at interfaces.

At the macroscopic scale, the diffusion in polycrystals is usually described by a classical Fick's law as for a homogeneous medium with some effective diffusion coefficient, D_{eff}, which accounts for the lattice and grain boundary diffusivity. However, in these models the effective diffusivity is computed assuming the constant diffusion rate both in the bulk and in the GBs as well as a constant GB segregation factor. The experimental and theoretical studies reviewed in the first part of this chapter show that these assumptions are not valid in any conditions (such as high solute concentrations and concentration gradients) and

can impede the correct interpretation of experimental observations (see also [139, 140]). The dependence of GB diffusivity on concentration and GB trapping kinetics should be accounted. The multi-scale FEFDAL method allows to treat successfully these situations and can be easily modified to model correctly the effects of GB diffusion in polycrystalline materials.

4.6 Summary

• The developed FEFDAL multi-scale approach allows to quantitatively describe the diffusion taking into account the effects of 1) trapping kinetics, 2) anisotropy and 3) dependence of the transverse diffusivity at interfaces on the concentration evolution in the bulk.

• The FEFDAL method was tested on the bicrystal membranes with GBs parallel and perpendicular to the surface as well as on the three grains junction. It was demonstrated that the method ensures convergence in the case of high concentration gradients which are present at interfaces due to the segregation effect.

• The FEFDAL multi-scale method provides successful numerical treatment of stress gradients appearing at GBs and triple junctions due to the external load. Therefore, the scheme presented in this chapter is applicable for the computations of mass transport in polycrystalline materials both without stresses and under mechanical loading.

• The discrepancy between the results obtained using the classical GB diffusion models and the FEFDAL multi-scale method was found for the problem of fast GB diffusion, that can be explained by different treatment of the leakage from the interface into the grains.

• Taking into account GB trapping kinetics instead assuming a local equilibrium allowed to demonstrate the retarding effect of the boundary acting as a sink and to model the corresponding regime of GB diffusion which was not reported in other works. In addition, the effect of the diffusion barrier across the GB was shown.

Chapter 5

Conclusions and perspectives

5.1 Conclusions

In the present work, the hydrogen transport was studied at the scale of a polycrystalline aggregate as well as on bicrystals and in the vicinity of a three grains junction. The austenitic stainless steel 316L was considered in the simulation performed on polycrystals. The pure nickel was chosen for the investigations carried out on bicrystals and junction of three grains.

The simulation of hydrogen diffusion presented in Chapter 2 shows how hydrogen can evolute in the polycrystalline 316L steel subjected to the mechanical loading. The effect of hydrogen trapping by dislocations in this material has been found to be negligible that is consistent with experimental data. It was demonstrated that microstructure induced stress-strain heterogeneities in the steel during deformation causes the redistribution and, finally, the localization of hydrogen in zones where hydrostatic stresses are higher. The extent of H-redistribution depends on the deformation level and is higher for greater strains. The degree of redistribution varies also with strain rate (which is related to the time of diffusion). The extent of hydrogen concentration heterogeneity is higher for lower strain rates, and clusters of hydrogen enriched/depleted grains appear. This result can be related to the known effect of strain rate on the occurrence of hydrogen embrittlement. In the groups of H-enriched grains, the effect of hydrogen on the plasticity behaviour is expected to be higher than in hydrogen depleted grains. In addition, in clusters of H-saturated grains hydrogen segregation to grain boundaries (GBs) can contribute to the

intergranular decohesion.

The analysis of the mechanism of hydrogen redistribution in the polycrystals reveals that hydrogen transport during mechanical loading is governed by stress gradients across GBs. The effect of specific diffusion properties of GBs was not considered in the modelling on polycrystalline aggregates (Chapter 2). This aspect was considered in Chapter 3 and Chapter 4.

In Chapter 3, the effect of trapping and low diffusivity across GB was investigated by performing the numerical simulations of hydrogen permeation through the bicrystal and bamboo membranes in which GBs are parallel to the surface. The one-dimensional diffusion problem was solved by using the atomic layer model, and both transient and steady state solutions were analysed. It was shown that the hydrogen concentration profile cannot be calculated by using the error function solution of classical Fick's equation since the trapping effect of GBs appears to influence significantly the distribution of H-solutes in the membrane.

For transient H-distribution in the membranes (both bicrystal and bamboo type) with prescribed constant concentration on one side, the linear concentration profile was observed for all grain sizes (from 176 nm up to 1 μm) investigated in the case of GB segregation energy of $-0.36\ eV$. This finding demonstrates the trapping effect of the interface acting as the absorbing layer (sink). The impact of GB on hydrogen diffusion decreases with reducing the magnitude (absolute value) of GB segregation energy and increasing the grain size. The extent of GB influence also depends on initial H-concentrations. The GB effect in hydrogen pre-charged membranes is lower compared to the initially H-free aggregates since in the pre-charged aggregates GBs are saturated at the beginning. The same dependence on the initial conditions was observed in the simulations of diffusion in bamboo type membranes.

To study the effect of stress, the redistribution of hydrogen in the pre-charged bicrystal was modelled for the case of a cyclic loading assuming heterogeneous stress field. It was found that the relaxation of hydrogen concentration heterogeneity formed during loading is impeded by the grain boundary in the stage of unloading and, finally, this contributes to the accumulation of hydrogen in the grain with higher stress.

To extend the one dimensional model of GB trapping and barrier effect to the two-dimensional case the multi-scale Finite Element-Finite Difference-Atomic Layer (FEF-

DAL) method has been developed in Chapter 4. This approach was used to study the fundamental aspects of intergranular diffusion in the case of nickel bicrystal and junction of three grains considering enhanced GB diffusion without trapping, GB trapping kinetics, barrier effect and stress heterogeneity in neighbouring grains.

The enhanced GB diffusion without trapping has been computed by using the multi-scale method and compared with the results of obtained from the classical GB diffusion approaches. The GB concentration calculated by the multi-scale method are lower than ones obtained by using Fisher's approach but higher than ones computed by using the 2D continuum diffusion model. As it was shown in Chpater 4, this discrepancy is due to the different numerical treatment of solute leakage from the GB to the bulk of grains.

The multi-scale FEFDAL method allowed to reveal the retarding effect of GB trapping on the hydrogen evolution in the bulk for different orientations of bicrystal. The new grain boundary diffusion regime (regime of Kirchheim's type [111]) was modelled by accounting for the trapping kinetics. This results is remarkable and was not reported earlier in works dealing with the classical approaches in which the local equilibrium is assumed. The FEFDAL method was also used to model hydrogen transport through a three grains junction, and one of typical situations of hydrogen distribution that can be observed in polycrystalline aggregates was simulated. In addition, it was demonstrated that the multi-scale method, in which diffusion is modelled by using atomic jump frequencies, can provide the accurate computational results from the physical point of view as well as from the point of numerical treatment of high stress gradient across grain boundaries which govern hydrogen redistribution in polycrystals under mechanical loading. One may conclude that the developed multi-scale FEFDAL method can enrich and improve the crystal plasticity-hydrogen diffusion analysis.

The results of the present work are useful for understanding the mechanisms of hydrogen transport in polycrystalline materials and complex hydrogen interactions with microstructure induced heterogeneities. The methods developed can be utilized for analyses and controlling the behaviour of materials as well as for their design to provide safe and reliable systems for hydrogen transport and storage. For example, the following strategy can be proposed for the predictive analysis of hydrogen assisted cracking in the specimen with a notch under mechanical loading (Figure 5.1). This case was studied a lot by numerous authors and it was shown that brittle intergranular cracking in the presence of

hydrogen is stress controlled and the crack initiates ahead of the notch where hydrostatic stresses are the highest. At the first stage, the continuum approach for modelling the mechanical behaviour of the specimen can be used. FE method can be utilised to compute the distribution of hydrostatic stresses and plastic strains. On the second step, knowing the critical zone where the hydrostatic stress is the highest, the experimental investigation of this region can be carried out using Electron Backscatter Diffraction technique. This analysis provides the information about grain structure and crystallographic orientation set. Using these data, the grain boundaries can be characterized by the angle of disorientation (Appendix B). It allows to impose specific diffusion-segregation properties for each grain boundary. On the next step, the microstructural mechanical analysis can be performed which provides the data about the stress and strain field at the microscopic scale. This data in conjunction with the knowledge about the effect of deformation and the impact of grain boundaries on hydrogen diffusion will allow to predict critical zones (in particular, grain boundaries) for a crack initiation in the presence of hydrogen.

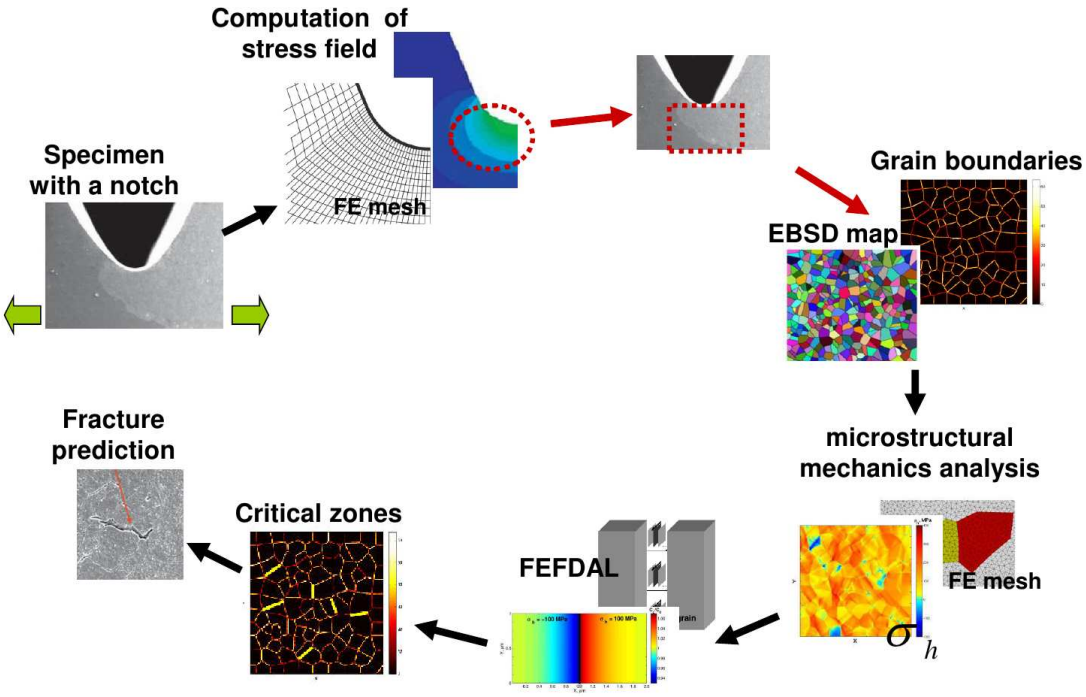

Figure 5.1: Strategy for the predictive analysis of hydrogen assisted cracking in the specimen with a notch (see the text for details).

5.2 Perspectives

The progress in modelling and numerical simulation of hydrogen diffusion was achieved in the present work and some fundamental aspects of hydrogen-microstructure interaction were investigated in the case of metals with fcc crystal lattice. The schemes developed in the present study are suitable for contributing to the prediction of hydrogen impact not only on fcc but also on bcc materials. The same crystal plasticity-hydrogen diffusion approach can be used for the simulation of hydrogen behaviour in bcc polycrystals, but some differences can be remarked and previewed, such as higher effects of trapping and smaller characteristic times of diffusion for bcc metals.

The multi-scale method developed in the present work and used for the simulations of hydrogen diffusion in the bicrystals and three grains junctions can be utilized for studies of hydrogen diffusion and grain boundary segregation in polycrystalline aggregates. The method can be generalised generalized on three dimensional (3D) case and used for the crystal plasticity-diffusion calculations in 3D polycrystals. In this case, tetrahedral elements have to be used for the finite element method and the multi-scale FEFDAL method should be modified using a 3D finite difference grid for grain boundary regions. The effect of triple junctions can be modelled in terms of atomic jump frequencies also. Grain boundaries in polycrystals have to be identified according to their misorientation angle (see Appendix) and the corresponding segregation energy should be imposed for each boundary.

In Chapter 2, the problem of H-evolution was studied in polycrystals pre-charged by hydrogen. Different H-charging conditions can be considered in the simulations. For example, the coupled crystal plasticity-hydrogen diffusion analysis can be performed for the polycrystal without pre-charging imposing boundary conditions on the edges of the aggregate. In this case, the stage of hydrogen adsorption can be treated in a way similar to one used in the multi-scale method. Moreover, the atomic layer model has been already successfully applied for the one dimensional problem of surface segregation (see also Appendix).

In the present work, the hydrogen diffusion was considered in the polycrystals subjected to uniaxial tensile loading. Various deformation modes and the impact of higher strains can be investigated. The deformation level of 2.2% considered in our study is

quite low. Some additional effect of trapping are expected to be observed in the case of higher levels of deformation (void growth, crack initiation etc.). Hydrostatic stress gradients, which increase with strain, will contribute additionally to the extent of hydrogen concentration heterogeneities.

A lot of works can be found in the literature in which the transport of hydrogen was studied in the vicinity of a blunting crack tip or a notch. In these studies, the effect of microstructure induced stress-strain heterogeneities was not taken into account. Taking into account this aspect can precise these analyses. In addition, the effect of deformation induced austenite-martensite transformations on hydrogen behaviour at the microscopic scale can be modelled in similar way of coupling the crystal plasticity and hydrogen diffusion analyses (Figure 5.2).

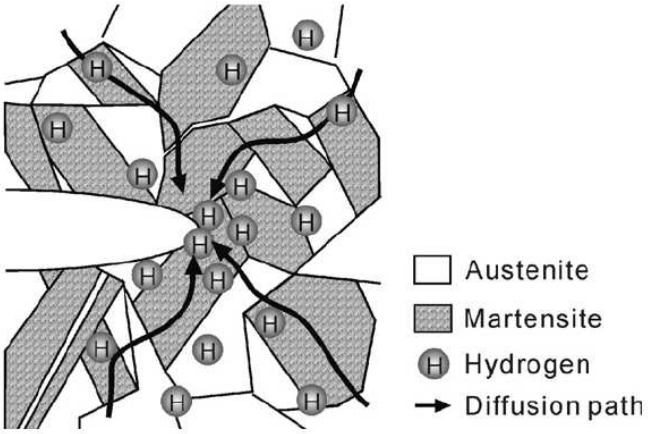

Figure 5.2: Schematic illustration of hydrogen diffusion path near a crack tip. The transformed martensite acts as a highway for hydrogen diffusion in the surrounding austenite [141].

In the case of the deformation induced austenite-martensite transformations the problem of high concentration gradients will be encountered due to distinguished solubilities in these phases. The possibility to treat high concentration gradients makes the multi-scale FEFDAL method a powerful instrument for diffusion simulation in materials with different phases or in any other systems with reduced dimensions (for example, multi-layers).

A problem of hydrogen diffusion in the presence of carbides is also interesting and important to be considered for the prediction of a decohesion at a carbid/matrix interface and in turn intergranular fracture (Figure 5.3) that can be observed, for example, in nickel base alloys.

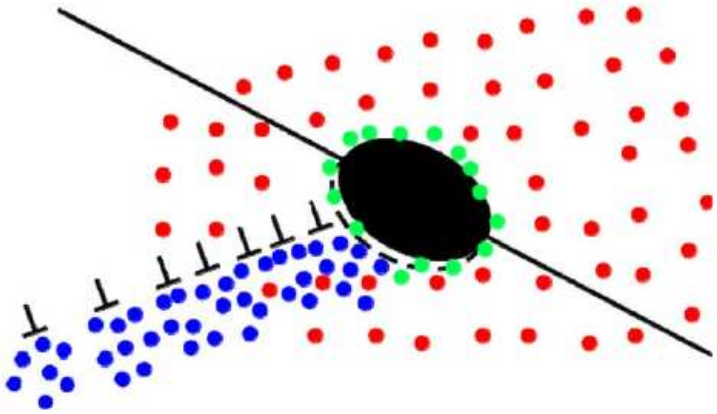

Figure 5.3: Schematic showing a dislocation pile-up impinging on a grain boundary carbide leading to decohesion at a carbide/matrix interface and in turn intergranular fracture [50].

Some modifications can be proposed to enrich the approaches presented in this dissertation.

In the present work, the transport of hydrogen by dislocations was not taken into account. In bcc metals, where the significant amount of hydrogen solutes locates in dislocation trap sites, the mechanism of hydrogen diffusion due to dragging of H-atoms by dislocations can be important and contribute to H-enrichment of grain boundaries.

As it is mentioned before in this section, the computation on polycrystals can be also enriched by considering the aspect of hydrogen segregation to grain boundaries and specific diffusion properties. The data about structure and segregation energies of grain boundaries can be obtained from atomistic calculations. At the same time, the atomistic models can provide some precisions about the evolution of stresses and strains in the vicinity of grain boundaries (Figure 5.4). The crystal plasticity analysis can be also improved considering the effect of grain boundaries on mechanical response of polycrystals [142–145].

In the present work, hydrogen diffusion is studied in the context of hydrogen embrittlement problem and the one way coupled crystal plasticity-hydrogen diffusion analysis was performed. The full coupling can be established on the next stage considering the hydrogen effect on mechanical properties of metal such as the effect on the yield stress and cohesion strength at interfaces. Finally, the hydrogen-assisted cracking in materials

can be modelled.

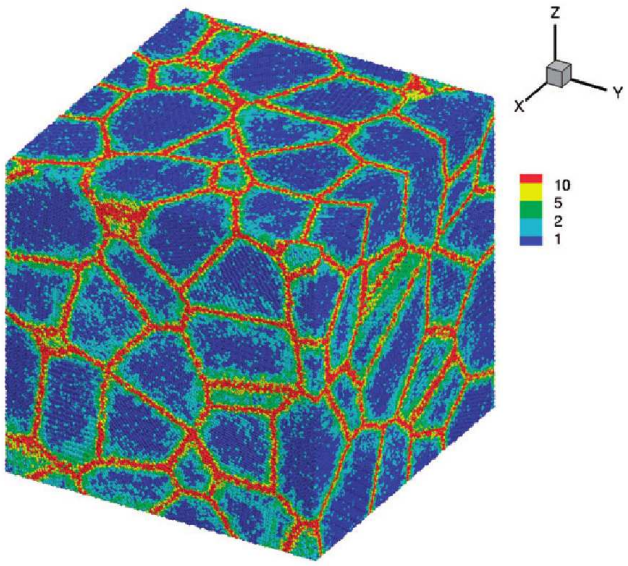

Figure 5.4: Spatial distribution of atomic residual stress in an equilibrated nanocrystalline Cu containing 50 grains with a mean grain size of 15.22 nm at temperature of 1 K calculated using molecular dynamics simulation [146].

Experimental evidences of hydrogen evolution at the microscopic scale can be obtained by using different techniques. Scanning Kelvin Probe Force Microscopy (KFM) is one of the tools allowing to study hydrogen distribution on the surface of metals by measuring a change in potential. An experimental set up was recently developed for *in situ* hydrogen permeation under Atomic Force/Kelvin Force Microscopy in the department DUMAS of I2M. Preliminary results have shown that this method is promising for detecting hydrogen distribution at the scale of the microstructure. Similar approach was used and some results were reported by Senöz et al. [147, 148].

Experimental measurements of GB diffusion and trapping properties are desirable and can be conducted on well characterized bicrystals with different orientations (diffusion across and along the interface). The multi-scale FEFDAL method can be used in these studies to relate experimental data with results of atomistic calculations of GB structures, diffusion barriers and segregation energies. This type of analyses can be used as a method to determine appropriate atomic layer configurations for the interfaces in FEFDAL computations.

Appendices

Appendix A

Grain average concentration maps

In this section, all the grain average concentration maps for the polycrystals considered in Chapter 2 are presented.

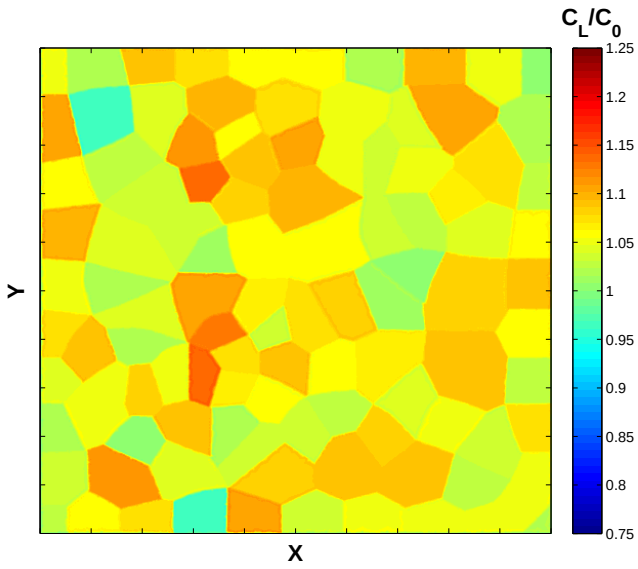

Figure A.1: Aggregate-1, orientation set-1. Grain average concentration of hydrogen in NILS corresponding to the strain rate of $2.2 \cdot 10^{-7}$ s^{-1} and total strain of 2.2 %.

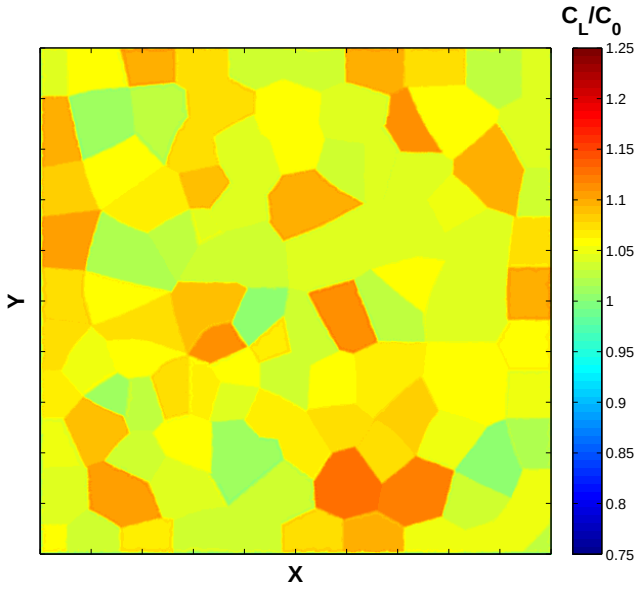

Figure A.2: Aggregate-1, orientation set-2. Grain average concentration of hydrogen in NILS corresponding to the strain rate of $2.2 \cdot 10^{-7}$ s^{-1} and total strain of 2.2 %.

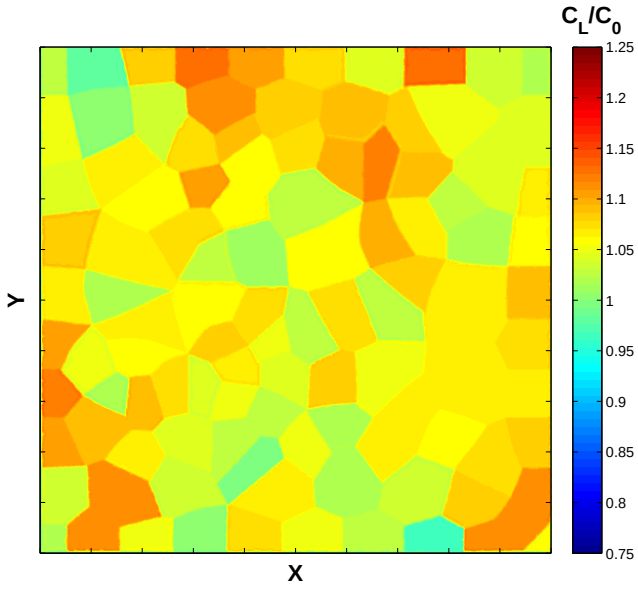

Figure A.3: Aggregate-1, orientation set-3. Grain average concentration of hydrogen in NILS corresponding to the strain rate of $2.2 \cdot 10^{-7}$ s^{-1} and total strain of 2.2 %.

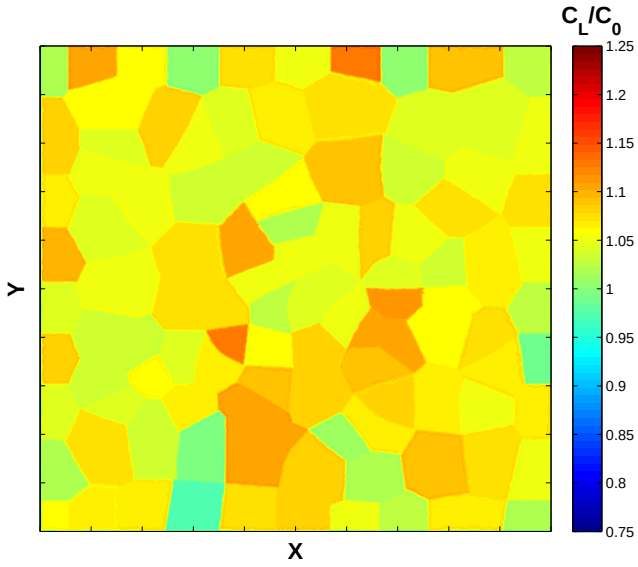

Figure A.4: Aggregate-2, orientation set-1. Grain average concentration of hydrogen in NILS corresponding to the strain rate of $2.2 \cdot 10^{-7}$ s^{-1} and total strain of 2.2 %.

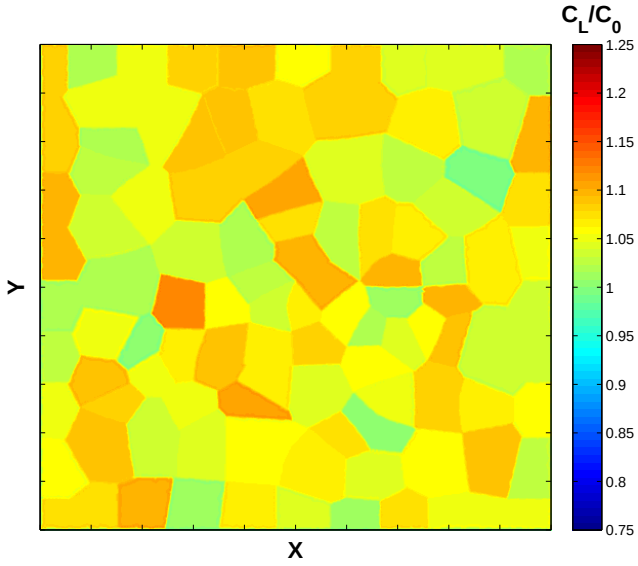

Figure A.5: Aggregate-2, orientation set-2. Grain average concentration of hydrogen in NILS corresponding to the strain rate of $2.2 \cdot 10^{-7}$ s^{-1} and total strain of 2.2 %.

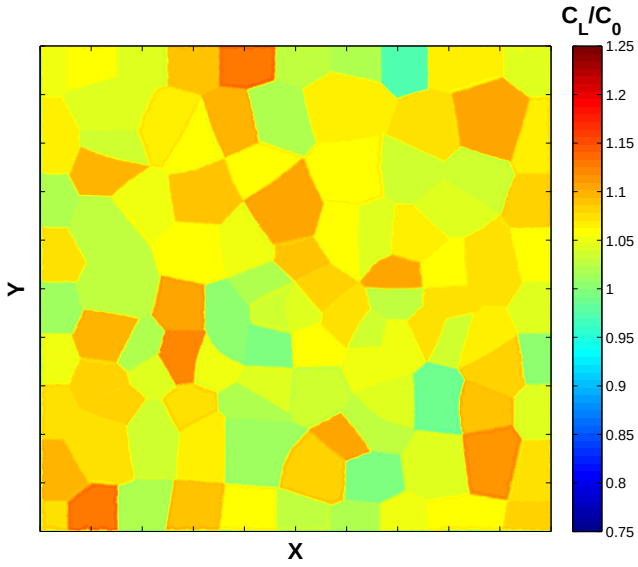

Figure A.6: Aggregate-2, orientation set-3. Grain average concentration of hydrogen in NILS corresponding to the strain rate of $2.2 \cdot 10^{-7}$ s^{-1} and total strain of 2.2 %.

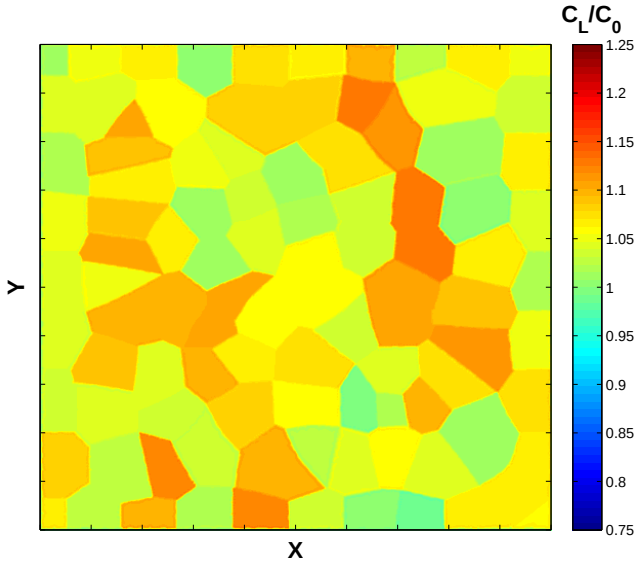

Figure A.7: Aggregate-3, orientation set-1. Grain average concentration of hydrogen in NILS corresponding to the strain rate of $2.2 \cdot 10^{-7}$ s^{-1} and total strain of 2.2 %.

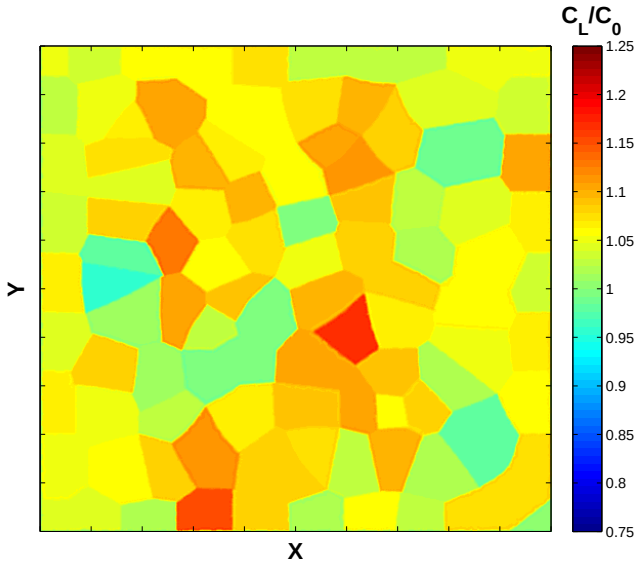

Figure A.8: Aggregate-3, orientation set-2. Grain average concentration of hydrogen in NILS corresponding to the strain rate of $2.2 \cdot 10^{-7}$ s^{-1} and total strain of 2.2 %.

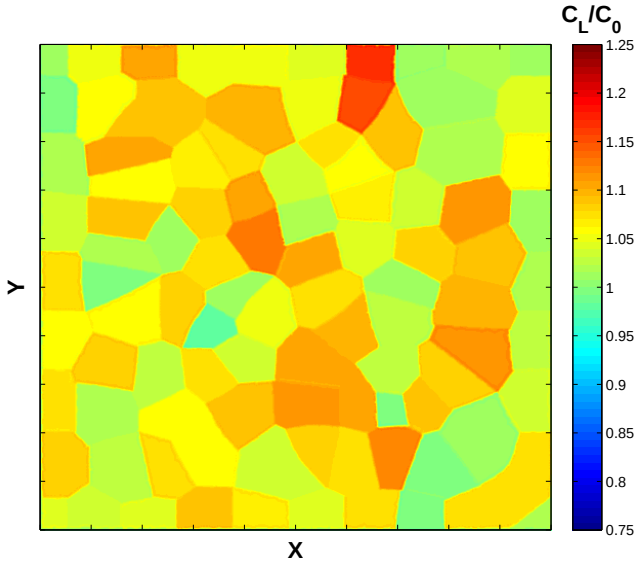

Figure A.9: Aggregate-3, orientation set-3. Grain average concentration of hydrogen in NILS corresponding to the strain rate of $2.2 \cdot 10^{-7}$ s^{-1} and total strain of 2.2 %.

Appendix B

Disorientation angle map of a polycrystalline aggregate

To describe a crystalline orientation in polycrystalline materials, three independent parameters Euler angles, ϕ_1, Φ, ϕ_2, defined by Bunge, are needed. The Euler angles are three rotations required to bring principle axes of the sample into coincidence with principle axes of the crystal.

According to Euler theorem, if a sphere is moved around its centre it is always possible to find a diameter whose direction in the displaced position is the same as in the initial position, i.e. any Cartesian coordinate systems with a common origin are related by a rotation about some fixed axis. Thus an orientation can also be described by the axis and the angle of rotation about this axis.

Similarly, Rodrigues vector defines the orientation by a rotation axis as in the axis-angle representation, but the vector has a magnitude, which is given by the tangent of the rotation angle divided by two. This representation is the most mathematically elegant and has received a lot of attention in recent years, but it is not used in the present work.

The misorientation angle is calculated in terms of axis-angle for a pair of grains supposing that orientations of the grains are described by the Euler angles.

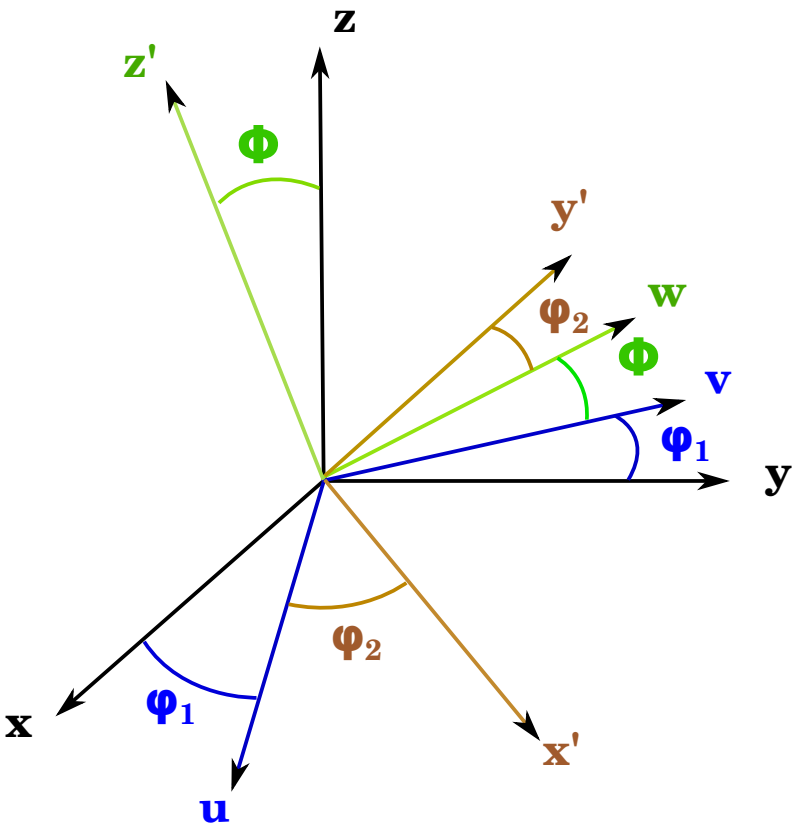

Figure B.1: Euler angles discribing the rotation coordinate system XYZ to X'Y'Z'

If the Euler angles, ϕ_1, Φ, ϕ_2, are known, the rotation matrix may be calculated:

$$\begin{bmatrix} C\phi_1 C\phi_2 - S\phi_1 S\phi_2 C\Phi & S\phi_1 C\phi_2 + C\phi_1 S\phi_2 C\Phi & S\phi_2 S\Phi \\ -C\phi_1 S\phi_2 - S\phi_1 C\phi_2 C\Phi & -S\phi_1 S\phi_2 - C\phi_1 C\phi_2 C\Phi & C\phi_2 S\Phi \\ S\phi_1 S\Phi & -C\phi_1 S\Phi & C\Phi \end{bmatrix} \tag{B.1}$$

where the notations C and S represent cosine and sine, respectively.

If the orientation of the grain A (Figure B.2) is described by the rotation matrix g_A (with respect to the sample axes) and its neighbour B is given by g_B, then the misorientation operator Δg_{AB} going from A to B can be defined as follows:

$$\Delta g_{AB} = g_B g_A^{-1}. \tag{B.2}$$

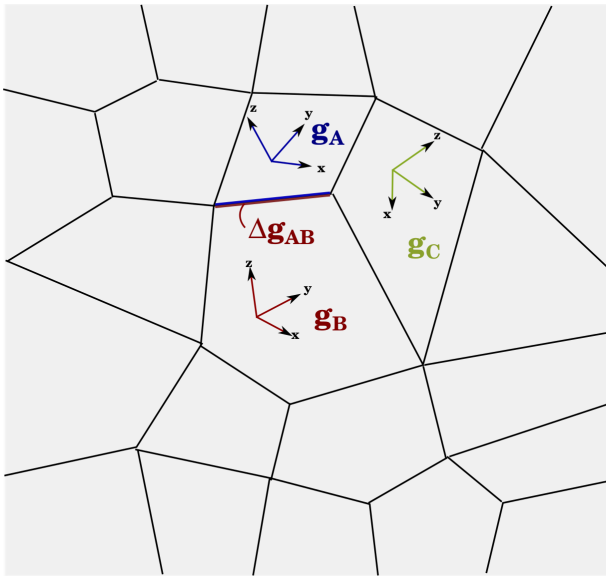

Figure B.2: Calculation of misorientation matrix for each paire of grains.

Due to the symmetry, a crystal in a given orientation cannot be distinguished from a crystal in a symmetric orientation. The group of symmetry operations on a cube with indistinguishable faces consists of 24 proper rotations:

a) the identity element or no rotation,

b) rotations of 180° about the three axes of references,

c) rotations of ±90° about the same axes,

d) rotations of 180° about axes parallel to the six face diagonals of the cube,

e) rotations of ±120° about axes parallel to the four diagonals of the cube.

On taking axes of reference parallel to the edges of the cube these 24 rotations can be represented by 3×3 orthogonal matrices. These matrices have only three non-zero elements which are either +1 or -1 and are arranged in all possible ways such that there is a non-zero element in each row and column and the determinant of the matrix is +1.

The matrices representing these proper symmetry rotations will be denoted by S_i $(i = 1, .., 24)$. The 3×3 orthogonal matrix, which represents an arbitrary proper rotation through an angle ψ about an axis in the direction $n = [n_1, n_2, n_3]$, is denoted by M here:

$$M = \begin{bmatrix} m_{11} & m_{12} & m_{13} \\ m_{21} & m_{22} & m_{23} \\ m_{31} & m_{32} & m_{33} \end{bmatrix} \tag{B.3}$$

If the rotation matrix M is known, the angle ψ and the axis n can be found:

$$cos\psi = \frac{1}{2}\left(Trace(M) - 1\right). \tag{B.4}$$

The vector n is an eigenvector of M corresponding to the eigenvalue $\lambda = 1$.

Thanks to the crystal symmetry, no two cubic lattices can be different by more than 62.8°. Taking into account the symmetry rotations, one may calculate a disorientation angle, ψ_d (minimum rotation angle between two lattices):

$$cos\psi_d = \frac{1}{2}\left(\max_i(MS_i) - 1\right) \tag{B.5}$$

An algorithm for finding neighbouring grains and boundary nodes from the data about mesh geometry (file .geof utilized in ZeBuLoN) was elaborated. The disorientation angle was calculated for each pair of grains by using Eq. B.5. In-house code was written. These computational tools can be used for modelling and analyses of the effects of specific grain boundary diffusion properties on hydrogen transport in polycrystalline aggregates. Figure B.3 and Figure B.4 presents the disorientation angle distribution and the disorientation angle map, respectively, for the polycrystal considered in Chapter 2. All the data were obtained using the in-house codes developed.

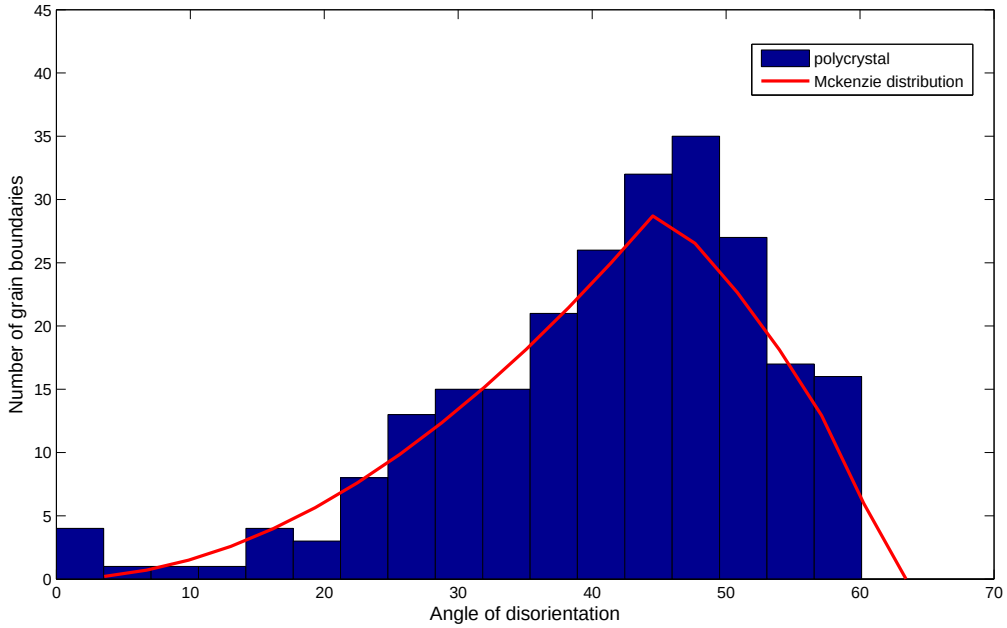

Figure B.3: Distribution of disorientation angle for the polycrystalline Aggregate-Set 1 considered in Chapter 2.

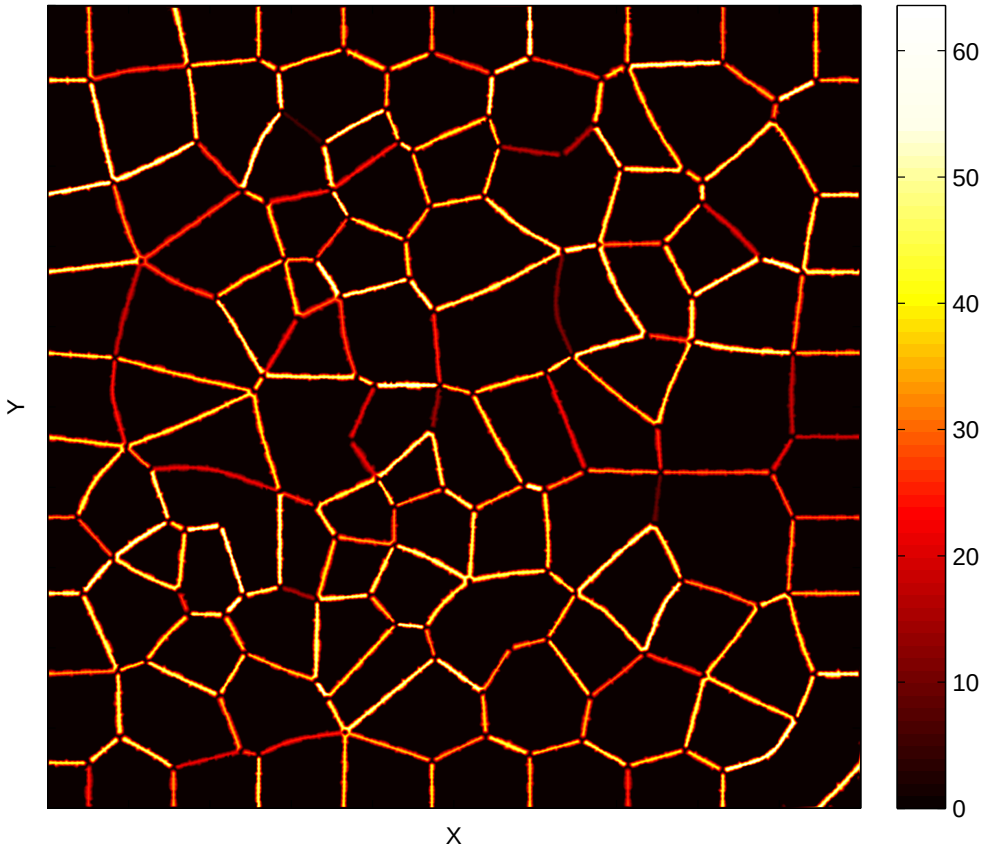

Figure B.4: Disorientation angle map of the polycrystalline Aggregate-Set 1. These data can be used for modelling the effects of grain boundary segregation and specific diffusivity on hydrogen diffusion in polycrystalline aggregates.

Appendix C

Texture effect

C.1 Polycrystalline aggregate with hexagonal grains

To study the effect of texture on the character and the extent of stress driven hydrogen redistribution at micro- and mesoscopic scale, a synthetic microstructure of stainless 316L steal with 314 hexagonal grains was generated (Figure C.7). This number is sufficient for considering a representative volume element [142, 149] to represent bulk polycrystalline material. Grain boundaries are simply geometrical lines separating neighbouring grains. Finite element mesh with six-node triangles used in the structural analysis is shown in Figure C.7. The aggregates contains about 64000 triangular elements and 128000 nodes. The size of the aggregate is 270×270 μm. The structural analysis was performed using the code ZeBuLoN.

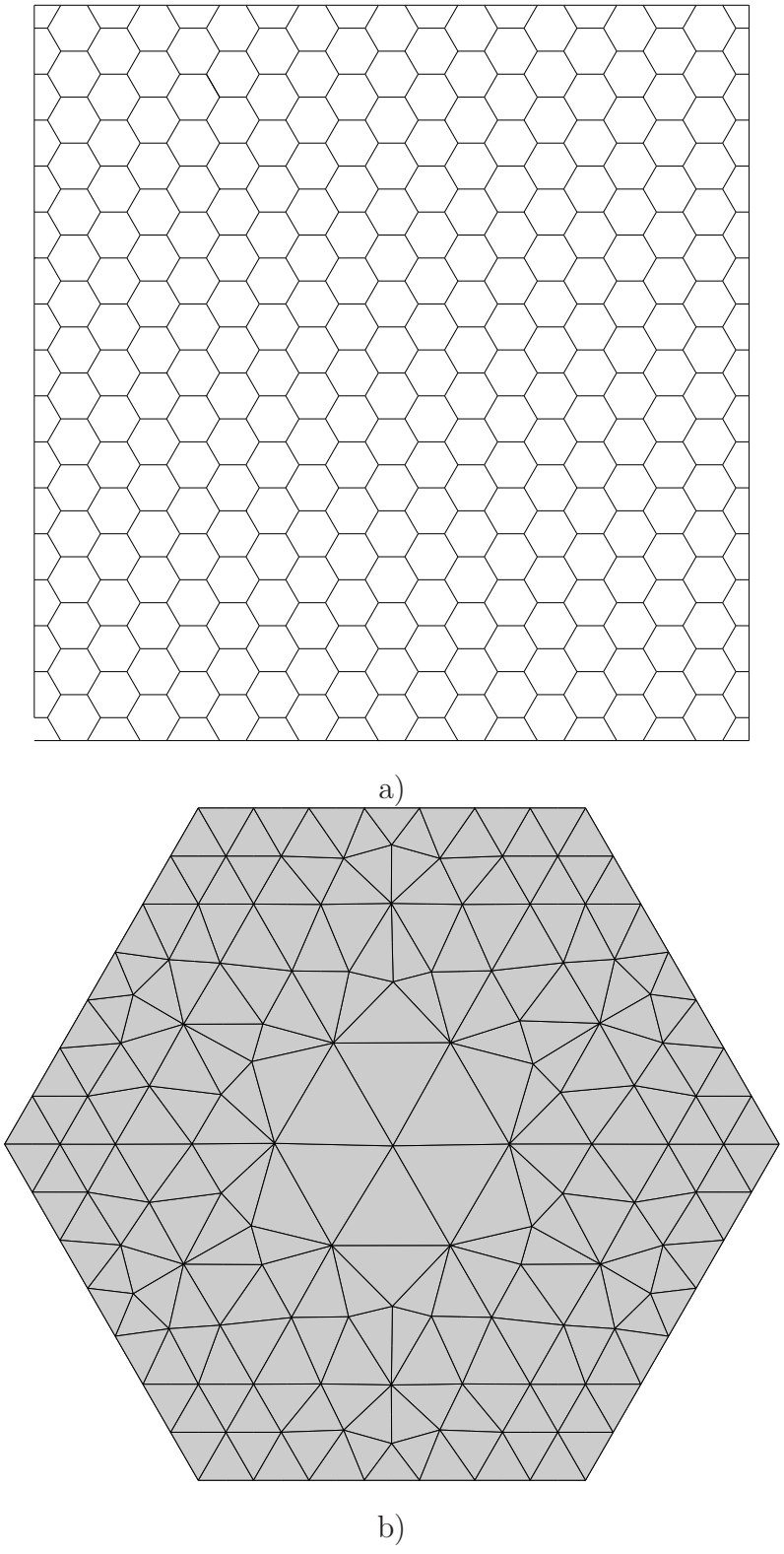

Figure C.1: (a) Artificial polycrystalline aggregate composed by 314 hexagonal grains and (b) finite element mesh (six-node triangles) used for the structural-diffusion analysis.

C.2 Textures used in the analysis

Three degrees of texture (40%, 80%, 200%) of the rolled steal were obtained from the set of 314 random crystal orientations by using VPSC code [150,151]. Corresponding pole figures are shown in Figure C.2.

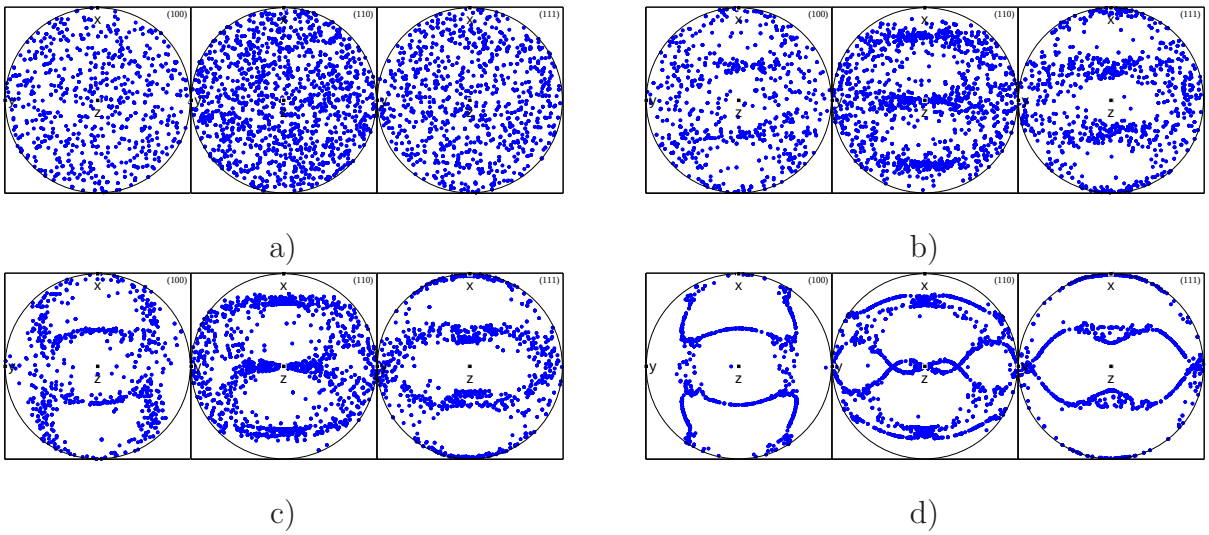

Figure C.2: Pole figures for the polycrystals with (a) random crystal orientation set and with (b) 40%, (c) 80% and (d) 200% textures.

C.3 Modelling: crystal plasticity-hydrogen diffusion analysis

An uncoupled analysis was carried out as described in Chapter 2. For the crystal plasticity analysis, boundary conditions consist in prescribed displacements on the bottom and top edges of the aggregate. The polycrystal is subjected to tensile loading up to 2% total strain. The initial conditions for hydrogen diffusion are adopted from Chapter 2. Zero flux boundary conditions are imposed on the edges of the aggregate.

C.4 Results

C.4.1 Steady state concentration maps

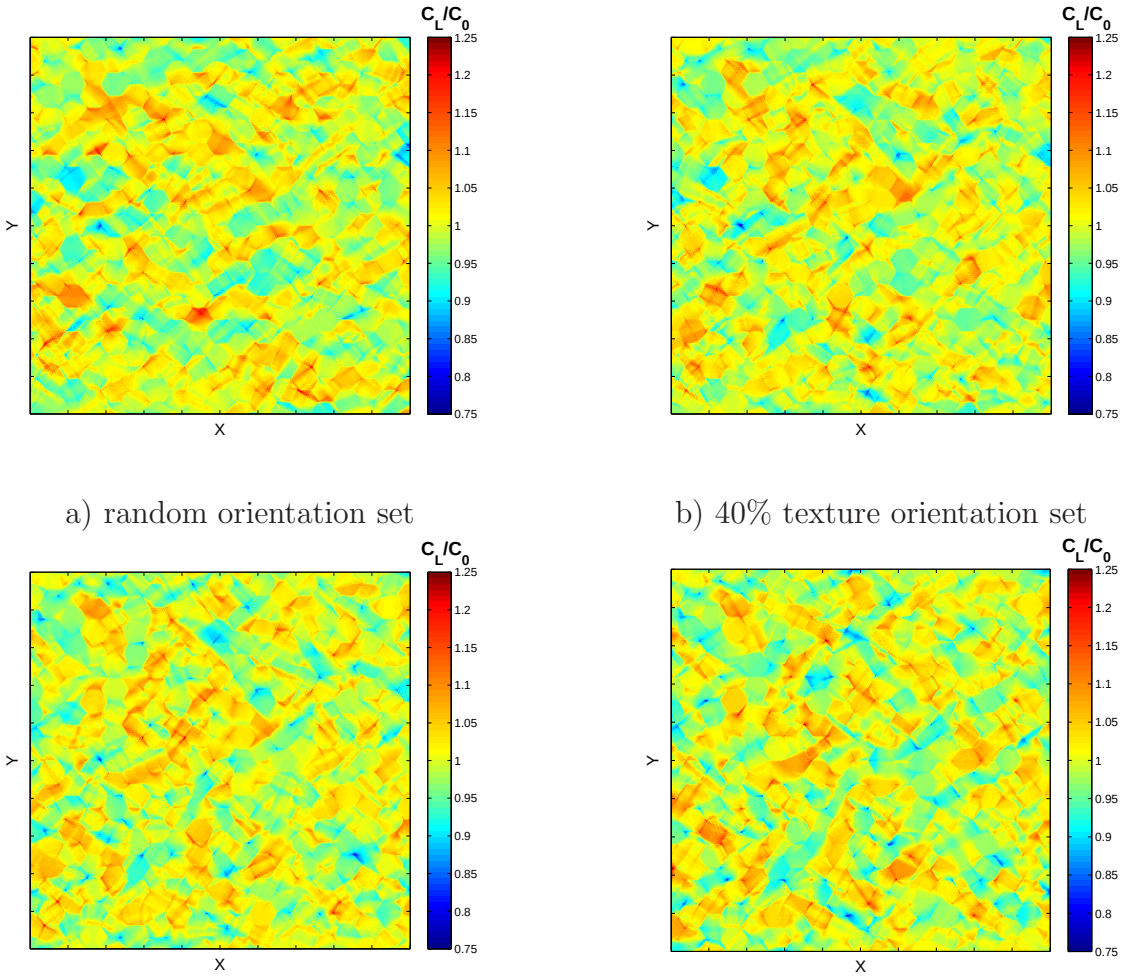

a) random orientation set

b) 40% texture orientation set

c) 80% texture orientation set

d) 200% texture orientation set

Figure C.3: Steady state concentration maps. Tension in X direction. Total strain: 2%.

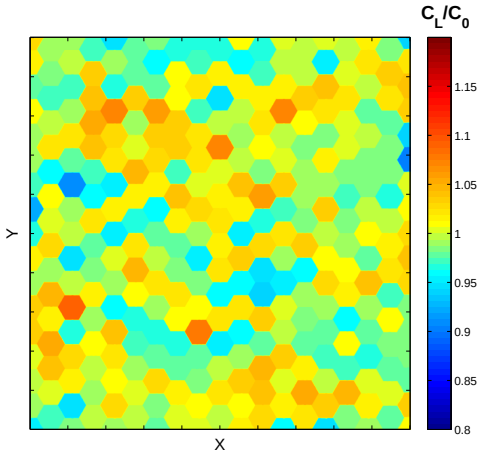

a) random orientation set

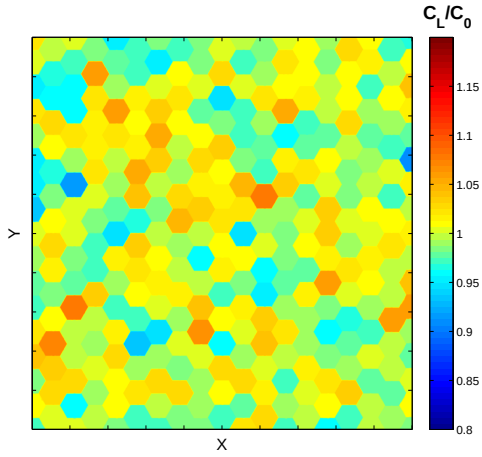

b) 40% texture orientation set

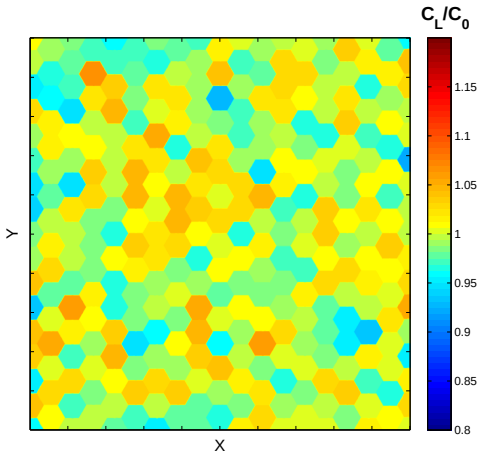

c) 80% texture orientation set

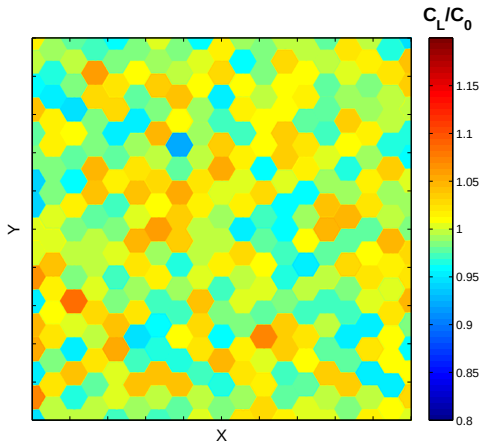

d) 200% texture orientation set

Figure C.4: Steady state average concentration maps. Tension in X direction. Total strain: 2%.

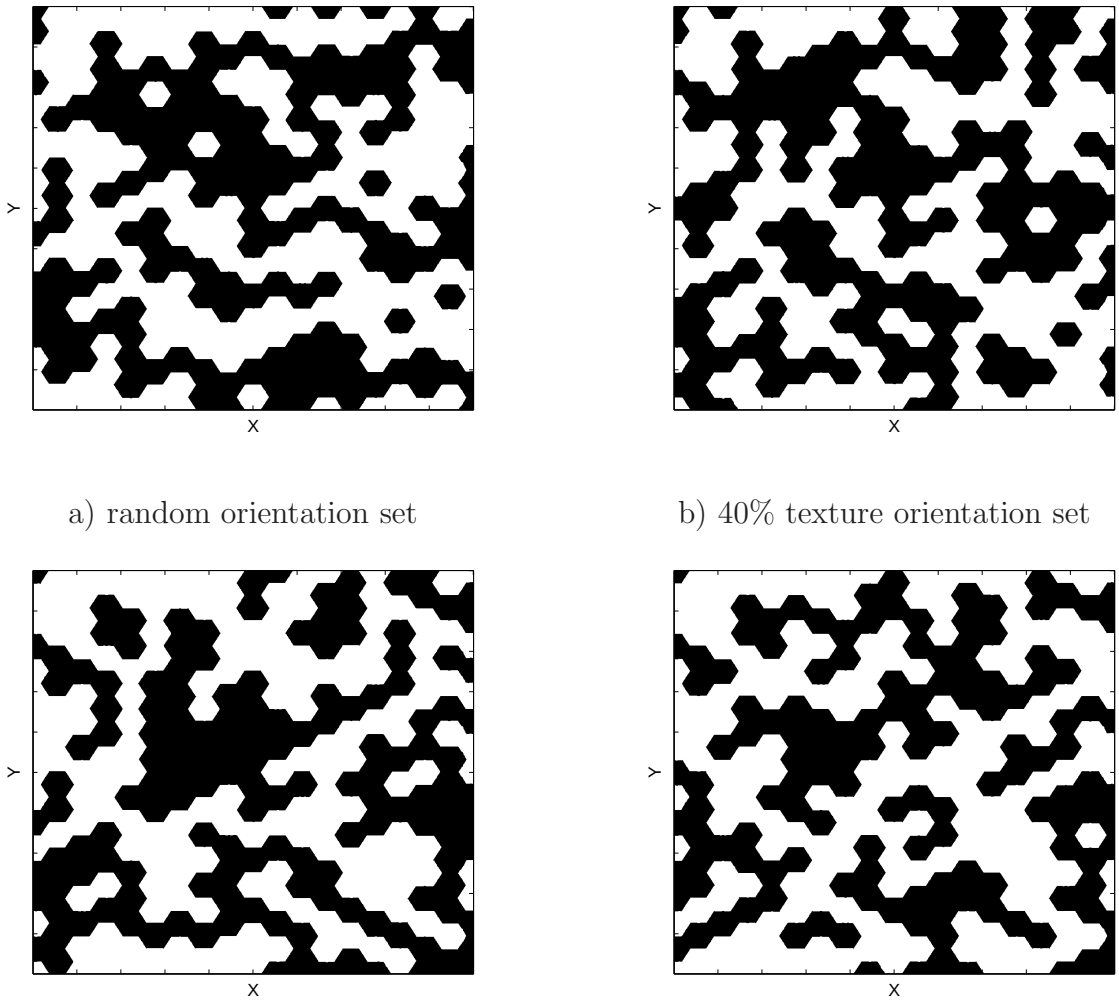

a) random orientation set

b) 40% texture orientation set

c) 80% texture orientation set

d) 200% texture orientation set

Figure C.5: Binarized images of the grain average normalised H-concentration in steady state. The H-enriched grains are black. Tension in X direction. Total strain: 2%.

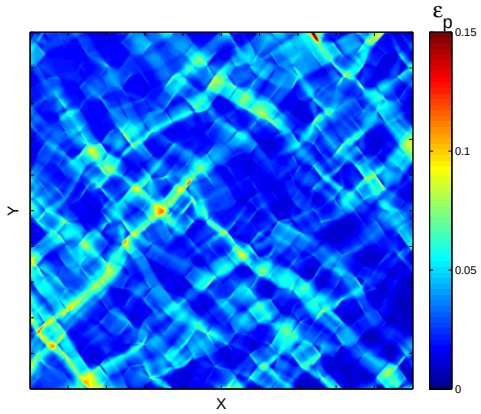

a) random orientation set

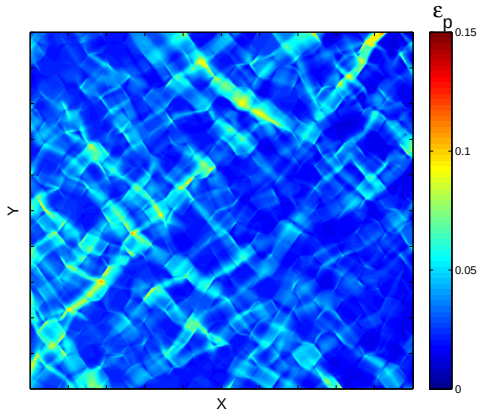

b) 40% texture orientation set

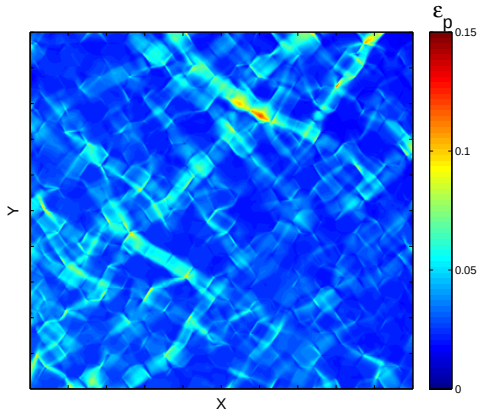

c) 80% texture orientation set

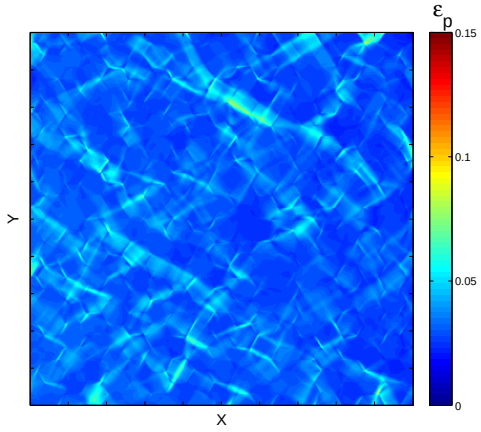

d) 200% texture orientation set

Figure C.6: Equivalent plastic strain. Tension in X direction. Total strain: 2%.

C.4.2 Transient H-diffusion analysis

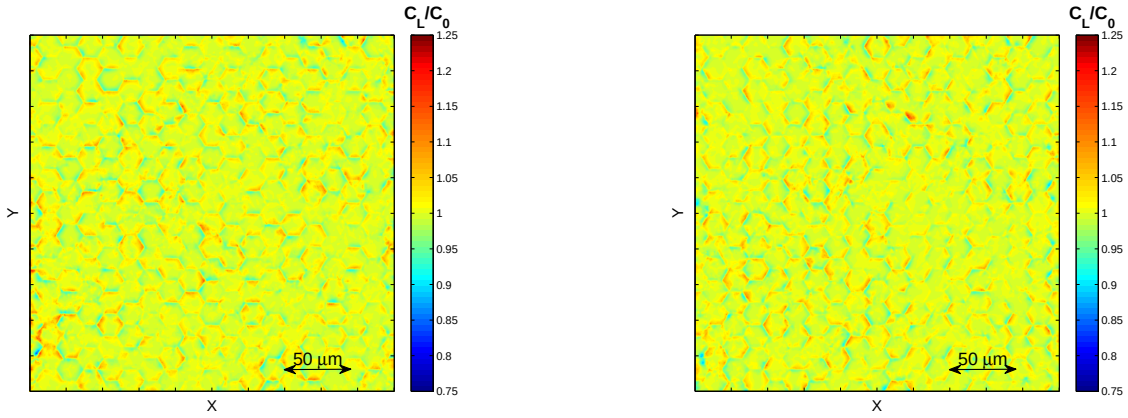

a) random orientation set b) 80% texture

Figure C.7: H-distribution in the polycrystal deformed at $2\times10^{-6}s^{-1}$ strain rate in X direction. Total strain: 2%. Time of diffusion: 10 000 s.

The results of the analysis show the negligible effect of texture on the extent of hydrogen redistribution (or, in other words, hydrostatic stress heterogeneity since H-concentration is proportional to the exponential function of stress according to Eq. 2.37 in Chapter 2). However, in Figure C.6, it is seen that the degree of heterogeneity of equivalent plastic strain in the material with texture decreases with increasing the texture degree. It allows to conclude that in bcc metals, where H-concentration in traps determines total H-distribution, the effect of texture could be remarkable.

Appendix D

Effect of anisotropy on H-diffusion in polycrystals

The influence of anisotropy on the concentration in NILS is shown in Figure D.1, Figure D.2 and Figure D.3. One may see that the usage of anisotropy model results in higher concentration in NILS in comparison with the hydrogen segregation obtained in case of isotropic elasticity. This is due to the fact that the anisotropy results in heterogeneous stress field from the stage of elastic deformation and, hence, hydrogen redistribution begins earlier (from the beginning) than in the case of isotropic elastic tensor.

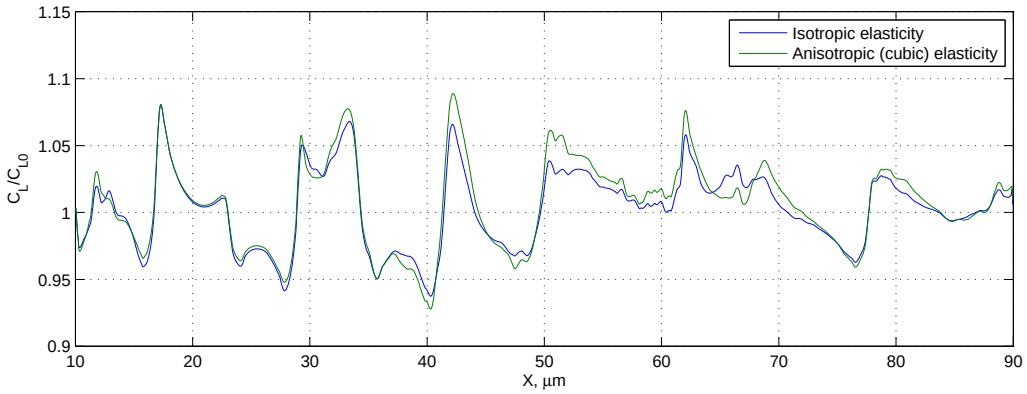

Figure D.1: Influence of anisotropy. C_L/C_{L0} is plotted along the section $y = 30\mu m$. Time: 10 000 s. Strain: 3%

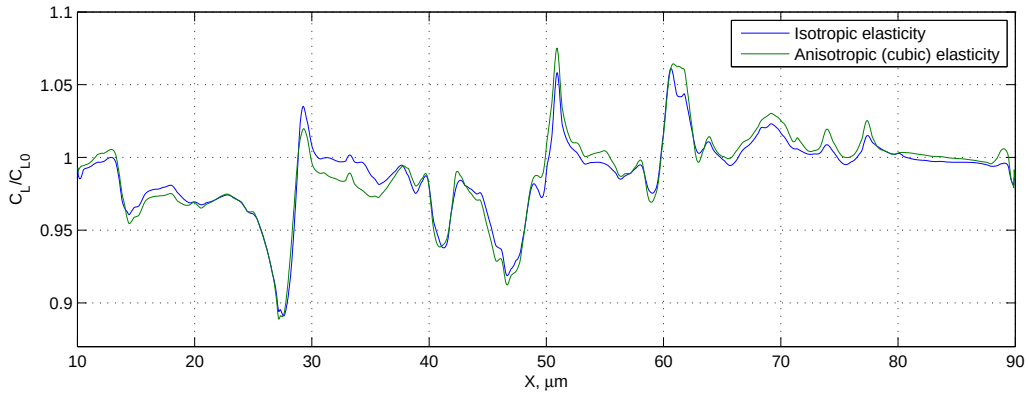

Figure D.2: Influence of anisotropy. C_L/C_{L0} is plotted along the section $y = 40\mu m$. Time: 10 000 s. Strain: 3%

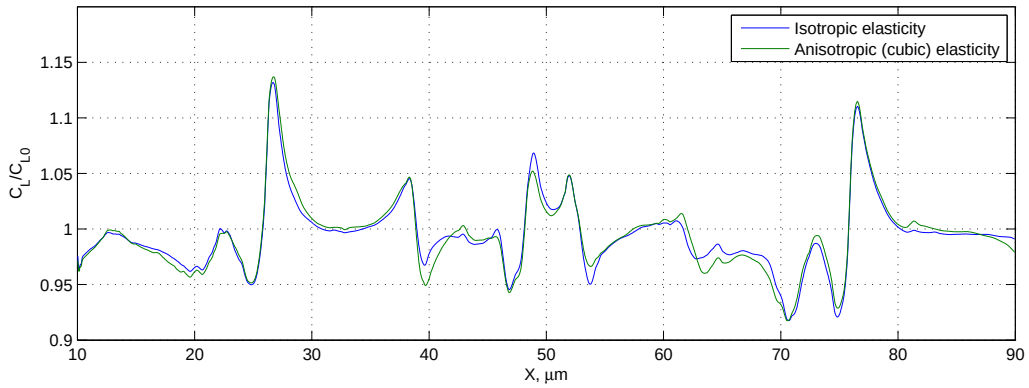

Figure D.3: Influence of anisotropy. C_L/C_{L0} is plotted along the section $y = 50\mu m$. Time: 10 000 s. Strain: 3%

Appendix E

Stationary case in a bicrystal

The extent of hydrogen heterogeneity induced by hydrostatic stress gradients can be estimated analytically by considering the diffusion in a bicrystal. We do not take into account trapping and assume that stress field is symmetric with respect to the Y-axis. In this formulation the diffusion problem reduces to one-dimensional case:

$$\frac{\partial C_L(x,t)}{\partial t} - \frac{\partial}{\partial x}\left[D_1(x)\frac{\partial C_L(x,t)}{\partial x} - D_1(x)C_L(x,t)e^{-x^2}\right] = 0 \tag{E.1}$$

where the exponent at the last term in brackets approximates the hydrostatic stress gradient (velocity field).

In steady state, one may write:

$$\frac{\partial}{\partial x}\left[D_1(x)\frac{\partial C_L(x)}{\partial x} - D_1(x)C_L(x)e^{-x^2}\right] = 0, \tag{E.2}$$

$$\frac{\partial C_L(x)}{\partial x} - C_L(x)e^{-x^2} = \frac{C_1}{D_1(x)}. \tag{E.3}$$

Searching the solution in the form

$$C_L(x) = A(x)e^{\Phi(x)} \tag{E.4}$$

where

$$\Phi(x) = \int e^{-x^2}dx, \tag{E.5}$$

we obtain:

$$C_L(x) = \left(\int e^{-\Phi(x)}\frac{C_1}{D_1(x)}dx + C_2\right)e^{\Phi(x)}, \tag{E.6}$$

C_1, C_2 - constants to find from boundary conditions.

In the case of the **insulated system**, the equation E.3 gives the first constant $C_1 = 0$ (since the flux is equal to zero on the boundary), the solution is:

$$C_L(x) = C_2\, e^{\Phi(x)} \tag{E.7}$$

and C_2 should be find from the condition that the total concentration in the system is constant. If C_0 is an initial concentration then:

$$\int_{-a}^{a} C_0\, dx = \int_{-a}^{a} C_2\, e^{\Phi(x)} dx, \tag{E.8}$$

$$C_2 = \frac{2aC_0}{\int_{-a}^{a} e^{\Phi(x)} dx}. \tag{E.9}$$

Now we can write the solution in case of insulated system:

$$C_L(x) = \frac{2aC_0}{\int_{-a}^{a} e^{\Phi(x)} dx}\, e^{\Phi(x)}, \tag{E.10}$$

where $\Phi(x)$ is given by Eq. E.5.

Appendix F

Hydrogen segregation to grain boundaries

The results of the analysis of hydrogen diffusion in polycrystals under mechanical loading (Chapter 2) showed that the deformation up to total strain of 2.2% can cause the 25-35% increase in hydrogen concentration in groups of grains with high hydrostatic stresses. In these H-enriched clusters the effect of hydrogen on mechanical properties of the material will be the highest. In addition, it is worth mentioning that the impact of stress driven hydrogen redistribution varies with charging conditions and initial hydrogen content.

In the present section, taking into account the segregation to grain boundaries, we demonstrate how the hydrogen redistribution in the bulk of a polycrystalline material can result in significant change in grain boundary concentrations.

The equilibrium (Langmuir-McLean) equation for the GB concentration (Eq. 3.17 in Chapter 3) is:

$$\frac{\theta_{gb}}{1-\theta_{gb}} = \frac{\theta_L}{1-\theta_L} \exp\left(\frac{\Delta E_{seg}}{kT}\right), \tag{F.1}$$

where θ_{gb} is the hydrogen grain boundary occupancy (fraction of occupied sites), θ_L hydrogen occupancy in the near bulk sites, E_{seg} is the grain boundary segregation energy and k and T are constants.

In the clusters of enriched grains the grain boundary saturation can be significant due to the exponential dependence in the Eq. F.1, and the degree of this saturation depends on the value of GB segregation energy.

In Figure F.1 the normalised grain boundary occupancy, θ_{gb}/θ_0, as a function of segregation energy is shown for some cases of hydrogen enrichment in the near bulk: $\theta_L/\theta_0 = 1$, $\theta_L/\theta_0 = 1.4$ and $\theta_L/\theta_0 = 2.0$. The occupancy of interstitial sites $\theta_0 = 0.000134$ is a solubility of hydrogen in Ni estimated at temperature 300 K and pressure of 20 MPa according to Sievert's law (Eq. 2.33 in Chapter 2). The spectrum of segregation energies was adopted from [3] reported in Chapter 3.

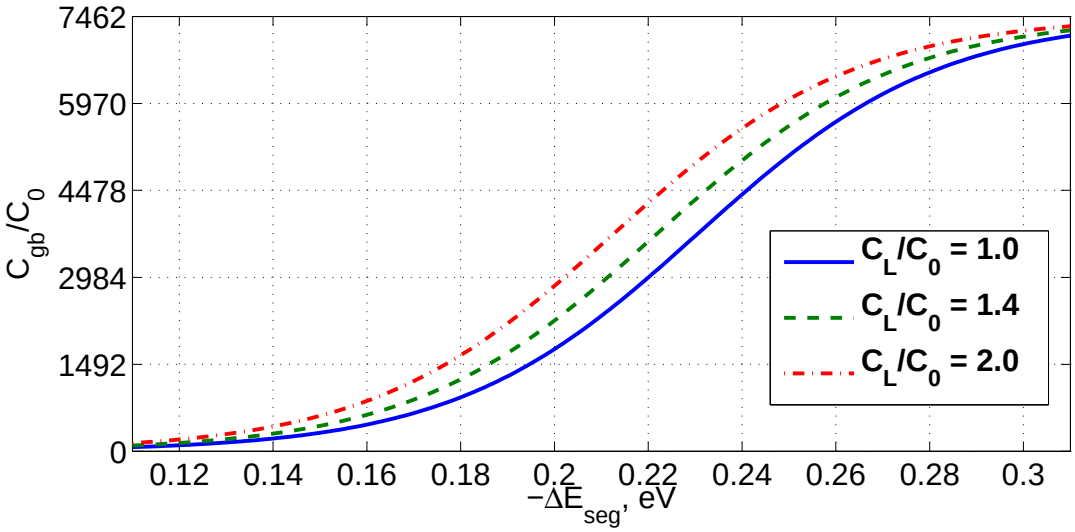

Figure F.1: GB normalised concentration with respect to the segregation energy for different normalised NILS concentrations. Initial occupancy $c_0 = 0.000134$.

It can be seen that the increase of hydrogen concentration in the bulk by a factor of 1.4 and 2 can cause the considerable raise of the hydrogen concentration at the grain boundary of segregation energy in the range between $-0.16\ eV$ and $-0.28\ eV$. In turn, this change may result in a decrease of cohesive strength at grain boundaries which should be taken into account in the simulations of hydrogen-assisted intergranular cracking.

Appendix G

Discussion on the problem of high stress gradients

Based on the consideration of stress gradients across grain boundaries at atomistic scale (Sec. 4.4.6), the rigorous formulation of H-transport problem in polycrystals is discussed in this section.

Stress driven diffusion of H-atoms in polycrystalline aggregates was studied in Chapter 1. The evolution of hydrostatic stress field was simulated using the crystal plasticity model implemented in the FEM code ZeBuLoN, and the redistribution of hydrogen solutes caused by stress heterogeneities was computed using the known hydrogen transport equation

$$\frac{\partial(C_L + C_T)}{\partial t} - D_L \Delta C_L + \nabla \cdot (C_L \frac{D_L V_H}{kT} \nabla \sigma_h) = 0, \tag{G.1}$$

in which the second term describes the mass transport resulted from gradients in concentration, and the third term takes into account the effect of heterogeneities in stress field, σ_h.

In Figure G.1, it is seen that the hydrostatic stress field in polycrystals has a jump like behaviour varying from grain to grain due to heterogeneous mechanical properties of neighbouring grains. As a results, the problem of treating of high stress gradients, $\nabla \sigma_h$, in Eq. (G.1) is encountered.

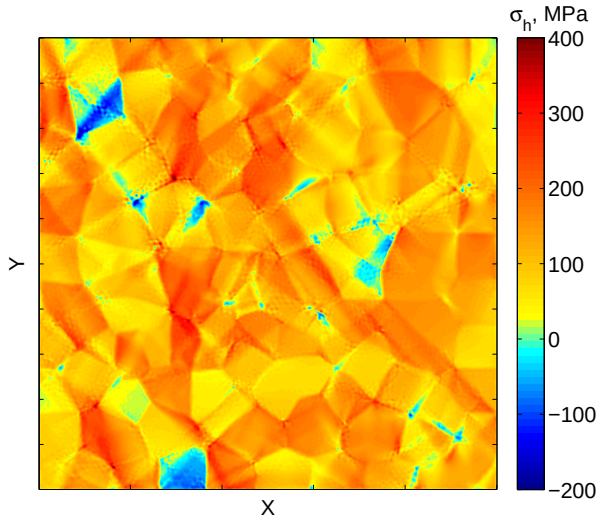

Figure G.1: Hydrostatic stress field in the polycrystalline aggregate of 316L steel calculated using the crystal plasticity model. Stress value varies from grain to grain, and high gradients across grain boundaries are present.

In the framework of the crystal plasticity approach used in the coupled analysis of plasticity-hydrogen diffusion interaction, stresses at grain boundary are interpolated values of stresses computed in grain nodes (or simply the mean values). Refining in mesh (Figure G.2) demonstrates that the curve of hydrostatic stress (section across a GB) in a bicrystal converges to the Heaviside type step function (see Figure G.3), and the corresponding stress gradient at the grain boundary increases.

In real polycrystals, the width of grain boundary is very small ($\approx 0.5\ nm$) and the stress distribution is close to the Heaviside type step function. However, the computation shows that the high stress gradients causes the lost in accuracy for transient concentration solution (Eq. G.1) and the divergence of the numerical scheme are observed with refining the mesh. Figure G.4 demonstrates hydrogen concentration profiles calculated using different meshes shown in Figure G.2. One may see that in the case of very fine meshes 3 and 4 the concentration profiles are asymmetric in contrast to the hydrogen distributions calculated using the meshes 1 and 2 (which are less refined), that indicates the lost in accuracy.

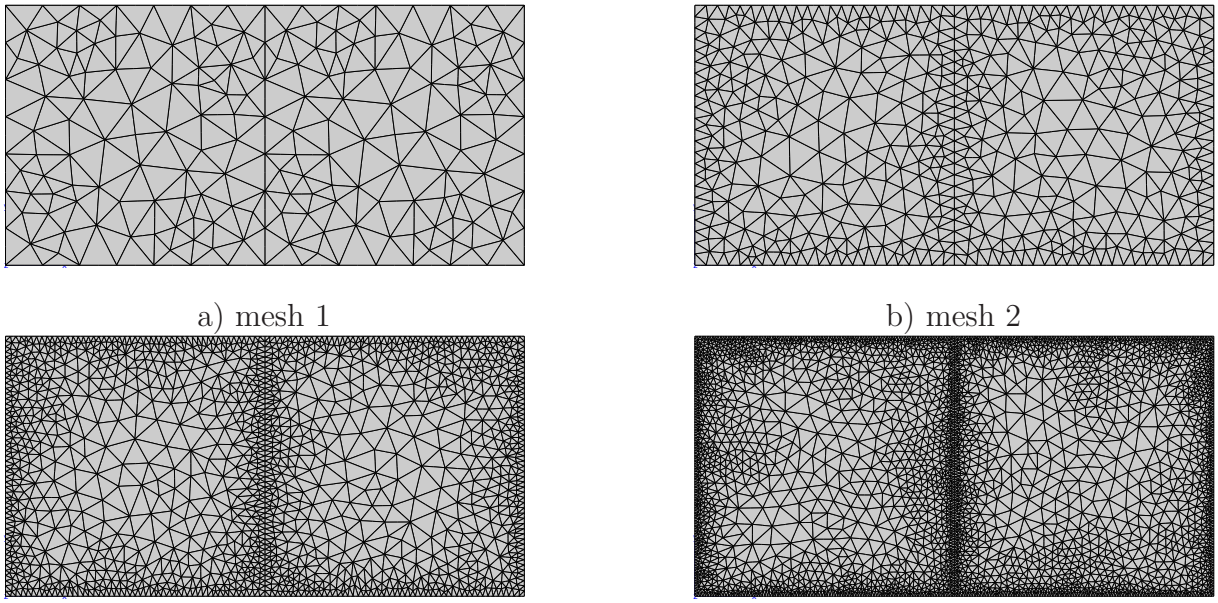

a) mesh 1 b) mesh 2

a) mesh 3 b) mesh 4

Figure G.2: Finite element mesh for crystal plasticity-hydrogen diffusion analysis performed on a bicrystal.

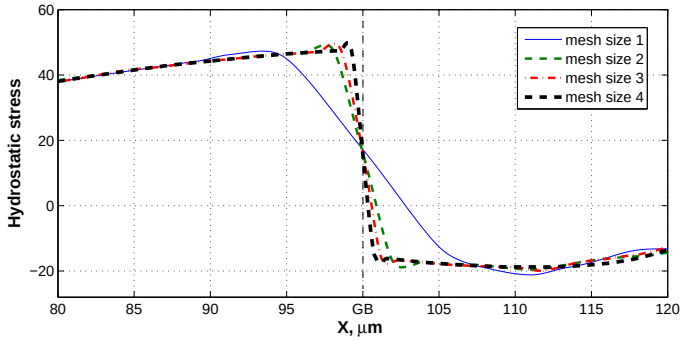

Figure G.3: Mesh size (Figure G.2) influence on the hydrostatic stress profile across the GB.

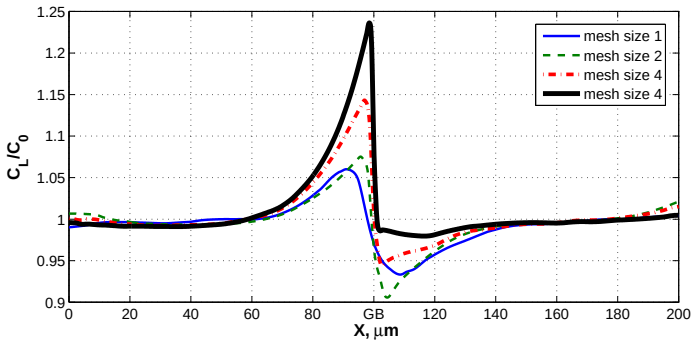

Figure G.4: Mesh size (Figure G.2) influence on the concentration profile across the GB.

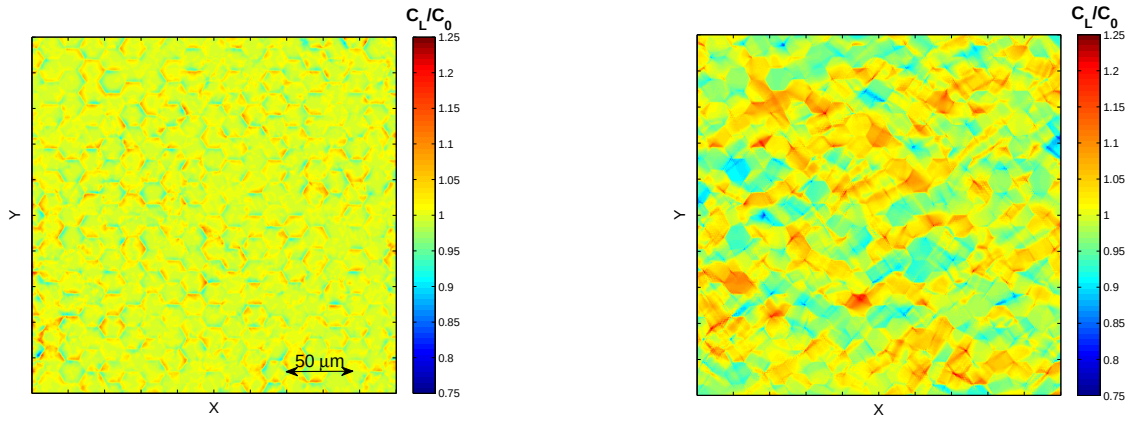

Figure G.5: Results of diffusion computations: H-distribution in the polycrystalline aggregate with hexagonal grains subjected to the uniaxial tensile loading up to 2% total strain at strain rate of $2 \times 10^{-6} s^{-1}$. (a) Transient H-distribution computed using the approach described in Chapter 2.(b) Steady state H-distribution (analytical solution given by Eq. 2.37).

The *long range diffusion* (i.e. the redistribution of solutes at mesoscale and the convergence of the transient solution to the steady state one) can not be considered without a rigorous mathematical formulation of the problem. To approach the situations with high hydrostatic stress gradients at GBs observed in real polycrystals, a careful numerical treatment is required.

Some methods of the mathematical treatment of stress gradients at grain boundaries can be found in the literature. As an example, the work of Sethian and Wilkening [152] is worth to be mentioned in which techniques from semigroup theory were used to represent the solution for the stress driven grain boundary diffusion. The specification of flux boundary conditions in the diffusion problem at grain boundaries is one of the approaches used by Sethian and Wilkening to solve the problem rigorously. Despite the fact that the stress driven grain boundary diffusion is a model of mass transport phenomena due to high current densities and gradients in normal stress *along* GBs, the similar rigorous mathematical formulation seems to be able to provide accuracy and convergence of the numerical solution in the case of high stress gradients *across* GBs.

In addition to the stress gradients, singularities present at grain boundaries, triple junctions and corners due to stress concentrations can influence the diffusion process. This aspect was considered in Chapter 3 and Chapter 4 assuming specific properties for

grain boundaries. It was shown, that in the case of strong segregation of solute atoms to grain boundaries, the diffusion is affected significantly. The multi-scale method proposed in Chapter 4 was shown to be able to account for this specific property of GBs and treat successfully singularities in hydrogen solubility and stress gradients from both numerical and physical point of view. However, to provide the accurate quantitative prediction of hydrogen evolution in polycrystalline aggregates, very small time steps are required in the multi-scale method to model the width of grain boundaries reported from experiments (about 0.5 nm). Hence, the optimisation of the method is desirable for simulating the long range diffusion and the diffusion in large systems.

The way to optimize the time of computation using the multi-scale method is to utilize larger time steps. In the atomic layer model, due to the small distance (of the order of lattice parameter) between atomic layers and the high atomic jump frequency, fine time stepping is required for the stability of the scheme. In the case of low effect of GB trapping kinetics on hydrogen evolution in the polycrystalline material, some approximations can be introduced. Namely, instead using explicitly the atomic layer model for simulations on polycrystals, the hydrogen flux at GBs can be computed knowing atomic jump frequencies corresponding to the hops of H-atoms between layers of neighbouring grains. In this case, the GB layer is neglected (low effect of trapping kinetics) and the atomic-informed diffusion computation with specified GB flux can be performed using a reasonable number of time steps.

Appendix H

Weak forms for grain boundary diffusion equations

H.0.3 2D continuum GB diffusion model

For the 2D continuum approach, the corresponding system of discretized equations can be obtained as it was described in Chapter 4:

$$\sum_{\alpha} \frac{\partial c_\alpha}{\partial t} \int_\Omega \varphi_\alpha \varphi_\beta d\mathbf{x} = -\sum_{\alpha} c_\alpha \int_\Omega \boldsymbol{\nabla}\varphi_\beta \cdot \mathbf{D}\boldsymbol{\nabla}\varphi_\alpha d\mathbf{x} + \sum_{\alpha} c_\alpha \int_{\partial\Omega} \varphi_\beta \mathbf{e}^T \cdot \mathbf{D}\boldsymbol{\nabla}\varphi_\alpha, \quad \text{(H.1)}$$

where the summation index, α, denotes all the nodes in the considered domain, $\Omega = G \cup I$ (i.e. grain and interface); the diffusivity tensor $\mathbf{D}$ should be replaced correspondingly by $\mathbf{D_{gb}}$ from (4.3) for the domain I; and the time derivative

$$\frac{\partial c_\alpha}{\partial t} = \frac{c_\alpha(t_{n+1}) - c_\alpha(t_n)}{\Delta t}, \quad \Delta t = t_{n+1} - t_n, \quad n = 0, .., N. \quad \text{(H.2)}$$

H.0.4 Fisher model

To obtain the weak form for the Fisher diffusion problem, we multiply the first equation in (4.10) on the test function, ϕ_β, and take integral over the domain G:

$$\int_G \frac{\partial c}{\partial t} \varphi_\beta d\mathbf{x} = \int_G \varphi_\beta \boldsymbol{\nabla}^{\boldsymbol{T}} \mathbf{D}\boldsymbol{\nabla} c d\mathbf{x} \quad \text{(H.3)}$$

Applying the divergence theorem results in:

$$\int_G \frac{\partial c}{\partial t} \varphi_\beta d\mathbf{x} = -\int_G \boldsymbol{\nabla}\varphi_\beta \cdot \mathbf{D}\boldsymbol{\nabla} c d\mathbf{x} + \int_{\partial G} \varphi_\beta \mathbf{e}^T \cdot \mathbf{D}\boldsymbol{\nabla} c. \quad \text{(H.4)}$$

Keeping only the integral over the part of ∂G which corresponds to the boundary between G and I and substituting $\mathbf{e}^T = (0, 1)$

$$\int_G \frac{\partial c}{\partial t}\varphi_\beta d\mathbf{x} = -\int_G \boldsymbol{\nabla}\varphi_\beta \cdot \mathbf{D}\boldsymbol{\nabla} c d\mathbf{x} - \int_0^l \varphi_\beta D_g \frac{\partial c}{\partial y} dx, \tag{H.5}$$

where l is a grain boundary length. Finally, we express the derivative $\partial c/\partial y$ from the second equation in (4.10) and substitute it into (H.5):

$$\int_G \frac{\partial c}{\partial t}\varphi_\beta d\mathbf{x} = -\int_G \boldsymbol{\nabla}\varphi_\beta \cdot \mathbf{D}\boldsymbol{\nabla} c d\mathbf{x} - \frac{\delta}{2}\int_0^l \varphi_\beta \frac{\partial c_{gb}}{\partial t} dx + \frac{\delta}{2}\int_0^l \varphi_\beta D_{gb} \frac{\partial^2 c_{gb}}{\partial^2 x} dx. \tag{H.6}$$

Applying the integration by parts for the last integral yields

$$\int_G \frac{\partial c}{\partial t}\varphi_\beta d\mathbf{x} = -\int_G \boldsymbol{\nabla}\varphi_\beta \cdot \mathbf{D}\boldsymbol{\nabla} c d\mathbf{x} - \frac{\delta}{2}\int_0^l \varphi_\beta \frac{\partial c_{gb}}{\partial t} dx - \frac{\delta}{2}\int_0^l D_{gb} \frac{\varphi_\beta}{\partial x}\frac{\partial c_{gb}}{\partial x} dx. \tag{H.7}$$

Using the joining condition $c(x, \pm\delta/2, t) = c_{gb}(x, t)$, Eq. (H.7) can be rewritten in the form:

$$\int_G \frac{\partial c}{\partial t}\varphi_\beta d\mathbf{x} + \frac{\delta}{2}\int_0^l \frac{\partial c}{\partial t}\varphi_\beta dx + \int_G \boldsymbol{\nabla}\varphi_\beta \cdot \mathbf{D}\boldsymbol{\nabla} c d\mathbf{x} + \frac{\delta}{2}\int_0^l D_{gb}\frac{\varphi_\beta}{\partial x}\frac{\partial c}{\partial x} dx = 0. \tag{H.8}$$

Finally, the discretized equations are

$$\sum_\alpha \frac{\partial c_\alpha}{\partial t}\left(\int_G \varphi_\alpha\varphi_\beta d\mathbf{x} + \frac{\delta}{2}\int_0^l \varphi_\alpha\varphi_\beta dx\right) +$$

$$+\sum_\alpha c_\alpha\left(\int_G \boldsymbol{\nabla}\varphi_\beta \cdot \mathbf{D}\boldsymbol{\nabla}\varphi_\alpha d\mathbf{x} + \frac{\delta}{2}D_{gb}\int_0^l \frac{\varphi_\alpha}{\partial x}\frac{\varphi_\beta}{\partial x} dx\right) = 0 \tag{H.9}$$

Appendix I

Hydrogen adsorption by a metal

The quantity of adsorbed gas at constant temperature is represented by the curved known as the isotherm of adsorption. The most frequently used isotherms are described by the equation of Temkin, Freundlich or Langmuir which are based on different assumptions about the dependence of the heat of adsorption on surface coverage by the adsorbate, θ:

$$\theta = N/N_0, \tag{I.1}$$

where N is a number of occupied sites on the surface, and N_0 is a total number number of sites.

According to Langmuir, the heat of adsorption is independent of coverage θ. For the physisorption, θ is given by the equation:

$$\theta = \frac{ap}{1+ap}, \tag{I.2}$$

where p is a pressure, and a is a constant given by:

$$a = A_0 \exp(\Delta H_{ph}/kT), \tag{I.3}$$

and ΔH_{ph} is an enthalpy of physisorption, A_0 is a constant, k - gas constant, T is an absolute temperature. For a diatomic gas dissociated during adsorption, the Langmuir isotherm takes the form:

$$\theta = \frac{(bp)^{1/2}}{1+(bp)^{1/2}}, \tag{I.4}$$

where the parameter b is determined by the relation between adsorption and desorption rates.

Freundlich proposed the following empirical relation for describing adsorption isotherm:

$$\theta = Wp^{1/n}, \text{or } \theta = Wp^{n'}, \tag{I.5}$$

where W is a constant at given temperature and it decreases with reducing of temperature ($K > 1$). Later, the Freundlich isotherm was proved theoretically and it was obtained

$$n = -kT \ln \frac{\theta}{q}. \tag{I.6}$$

According to Temkin, the heat of adsorption, q, depends linearly on θ:

$$q = q_0(1 - \alpha\theta), \tag{I.7}$$

where q_0 is a heat of adsorption for $\theta = 0$, α is constant. The Temkin isotherm is described by the relation:

$$\theta = \frac{kT}{q_0\alpha} \ln(A_0 p). \tag{I.8}$$

where

$$A_0 = a_0 \exp(q_0/kT), \tag{I.9}$$

α and a_0 are constants. The Temkin isotherm is valid for θ in a range between 0.2 and 0.8.

All mentioned isotherms were used for analysing the mechanisms of hydrogen embrittlement. It was noted that the isotherms of Freundlich and Temkin are more suitable than the adsorption isotherm of Langmuir [2].

The multi-scale FEFDAL method presented in Chapter 4 can be also used to model hydrogen adsorption in polycrystalline aggregates taking into account kinetics of adsorption processes. The energy profile similar to one assumed by Hofmann and Erlewein [102] in the model of kinetics of surface segregation of Sn in Cu can be used for hydrogen diffusion (Figure I).

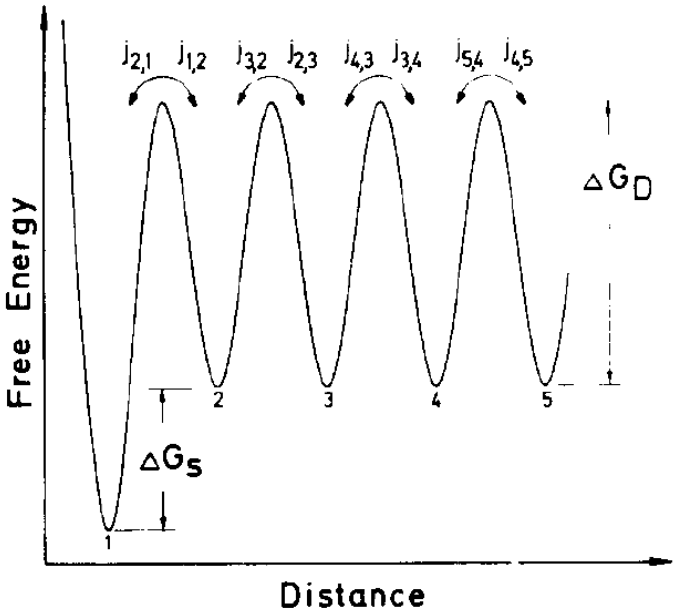

Figure I.1: Assumed energy profile for diffusing solutes at the surface and in the bulk [102].

Bibliography

[1] A.-M. Brass, J. Chêne. *Corrosion Sci.*, 48:3222, 2006.

[2] B. A. Kolachev. *Vodorodnaya hrupkost metallov*. Metallurgiya, 1985. *In Russian*

[3] M. Shiga, M. Yamaguchi, H. Kaburaki. *Phys. Rev. B*, 68:245402, 2003.

[4] D. E. Jiang, E. A. Carter. *Phys. Rev. B*, 70:64102, 2004.

[5] E. Wimmer, W. Wolf, J. Sticht, P. Saxe, C. Geller, R. Najafabadi, F. Young. *Phys. Rev. B*, 77:134305, 2008.

[6] A. Pedersen, H. Jónsson. *Acta Mater.*, 57:4036, 2009.

[7] Y. A. Du, L. Ismer, J. Rogal, T. Hickel, J. Neugebauer, R. Drautz. *Phys. Rev. B*, 84:144121, 2011.

[8] H. Mehrer. *Diffusion in Solids*. Springer, 2007.

[9] R. W. Balluffi, S. M. Allen, W. C. Carter. *Kinetics of materials*. Wiley, 2005.

[10] G. M. Pressouyre. *Metall. Trans. A*, 10A:1571, 1979.

[11] G. M. Pressouyre. *Metall. Trans. A*, 14A:1571, 1983.

[12] S. M. Myers, M. I. Baskes, H. K. Birnbaum, J. W. Corbett, G. G. DeLeo, S. K. Estreicher, E. E. Haller, P. Jena, N. M. Johnson, R. Kirchheim, S. J. Pearton, M. J. Stavola. *Rev. Mod. Phys.*, 64:559, 1992.

[13] Z. S. Dong, C. W. Zhao. *Physica B*, 405:171, 2010.

[14] J. P. Chateau, D. Delafosse, T. Magnin. *Acta Mater.*, 50:1507, 2002.

[15] P. Bastien, P. Azou. *C. R. Acad. Sci. Paris*, 232:1845, 1951.

[16] P. Bastien, P. Azou. In *First World Metallurgical Congress*, ASM, Cleveland, 1951.

[17] J. A. Donovan. *Metall. Trans. A*, 7A:1677, 1976.

[18] J. Chêne, A.-M. Brass. *Scripta Mat.*, 40(5):537, 1999.

[19] J. K. Tien, A. W. Thompson, I. M. Bernstein, R. J. Richards. *Metall. Trans. A*, 7:821, 1976.

[20] S. Taketomi, R. Matsumoto, N. Miyazaki. *Acta Mater.*, 56:3761, 2008.

[21] A. V. Fishgoyt, B. A. Kolachev. *Vzaimodeystviye defektov kristallicheskoy reshetki i svoistva metallov: Sbornik nauchnyh trudov*, page 3, 1984. *In Russian*

[22] G. Lu and E. Kaxiras. *Phys. Rev. Lett.*, 94:155501, 2005.

[23] O. Y. Vekilova, D. I. Bazhanov, S. I. Simak, and I. A. Abrikosov. *Phys. Rev. B*, 80:024101, 2009.

[24] Y. Tateyama, T. Ohno. *Phys. Rev. B*, 67:174105, 2003.

[25] R. Nazarov, T. Hickel, J. Neugebauer. *Phys. Rev. B*, 82:224104, 2010.

[26] P. Nordlander, J. K. Nörskov, F. Besenbacher, S. M. Myers. *Phys. Rev. B*, 40:1989, 1989.

[27] F. Besenbacher, S. M. Myers, P. Nordlander, J. K. Nörskov. *J. Appl. Phys.*, 61:1788, 1987.

[28] Y. Fukai and N. Okuma. *Phys. Rev. Lett.*, 73:1640, 1994.

[29] L. S. Darken, R. P. Smith. *Corrosion*, 5:1, 1949.

[30] A. McNabb, P. K. Foster. *Trans. Metall. Society AIME*, 227:618, 1963.

[31] R. A. Oriani. *Acta Metall.*, 18:147, 1970.

[32] J. B. Leblond, D. Dubois. *Acta Metall.*, 31:1459, 1983.

[33] A. R. Troiano. *Trans. ASM*, 52:54, 1960.

[34] C. D. Beachem. *Metall. Trans.*, 3:437, 1971.

[35] R. Kirchheim. *Scripta Mater.*, 62:67, 2010.

[36] A. Van der Ven, G. Ceder. *Acta Mater.*, 52:1223, 2004.

[37] D. E. Jiang, E. A. Carter. *Acta Mater.*, 52:4801, 2004.

[38] X. J. Shen, D. Tanguy, D. Connétable. *Phil. Mag.*, 94(20):2247, 2014.

[39] T. Tabata, H. K. Birnbaum. *Scripta Metall.*, 17:947, 1983.

[40] I. M. Robertson, H. K. Birnbaum. *Acta Metall.*, 34:353, 1986.

[41] P. Rozenak, I. M. Robertson, H. K. Birnbaum. *Acta Metall.*, 38:2031, 1990.

[42] P. J. Ferreira, I. M. Robertson, H. K. Birnbaum. *Acta Mater.*, 46(5):1749, 1998.

[43] P. Sofronis, H. K. Birnbaum. *J. Mech. Phys. Solids*, 43:49, 1995.

[44] J. P. Chateau, D. Delafosse, T. Magnin. *Acta Mater.*, 50:1523, 2002.

[45] S. Nedelcu, P. Kizler. *Phys. Status Solidi A, Appl. Res.*, 193:26, 2002.

[46] I. Telitchev, O. Vinogradov. *J. Mol. Model.*, 14:621, 2008.

[47] R. Matsumoto, S. Taketomi, S. Matsumoto, N. Miyazaki. *Int. J. Hydrogen Energy*, 34:9576, 2009.

[48] M. Wen, X.-J. Xu, Y. Omura, S. Fukuyama, K. Yokogawa. *Comput. Mater. Sci.*, 30:202, 2004.

[49] Y. Liang, P. Sofronis. *J. Mech. Phys. Solids*, 51:1509, 2003.

[50] P. Novak, Y. Yuan, B. P. Somerday, P. Sofronis, R. O. Ritchie. *J. Mech. Phys. Solids*, 58:206, 2010.

[51] A. Taha, P. Sofronis. *Eng. Fract. Mech.*, 68:803, 2001.

[52] S. Serebrinsky, E. A. Carter, M. Ortiz. *J. Mech. Phys. Solids*, 52:2403, 2004.

[53] J. J. Rimoli, M. Ortiz. *Philos. Mag.*, 90:2939, 2010.

[54] NASA. *Safety standard for hydrogen, hydrogen systems.* Washington, DC 20546, 1997.

[55] A. Valiente, L. Caballero, J. Ruiz. *Nuclear Eng. Design*, 188:203, 1999.

[56] J. Toribio, A. Valiente, R. Cortes, L. Caballero. *Fusion Eng. Design*, 29:442, 1995.

[57] E. Herms, J.-M. Olive, M. Puiggali. *Mater. Sci. Eng.*, A272:279, 1999.

[58] T. Matsuo, J. Yamabe, S. Matsuoka. *Int. J. Hydrogen Energy*, 39:3542, 2014.

[59] E. Minkovitz, D. Eliezer. *J.Mater. Sci.*, 16:2507, 1981.

[60] E. Minkovitz, D. Eliezer. *J.Mater. Sci.*, 17:3165, 1982.

[61] Y. Rosenthal, M. Mark-Markowitch and A. Stern. *Mater. Sci. Eng.*, 67:91, 1984.

[62] I. Aubert, J-M. Olive, N. Saintier. *Mater. Sci. Eng. A*, 527:5858, 2010.

[63] C. San Marchi, B. P. Somerday, X. Tang, G. H. Schiroky. *Int. J. Hydrogen Energy*, 33(2):889, 2008.

[64] T. Michler, Y. Lee, R. P. Gangloff, J. Naumann. *Int. J. Hydrogen Energy*, 34:3201, 2009.

[65] T. Boniszewski, G. C. Smith. *Acta Metall.*, 11:165, 1963.

[66] B. A. Wilcox, G. C. Smith. *Acta Metall.*, 13:331, 1965.

[67] R. M. Latanision, H. Oppenhauser. *Metall. Trans.*, 5:483, 1974.

[68] D. H. Lassila, H. K. Birnbaum. *Acta Metall.*, 34:1237, 1986.

[69] D. H. Lassila, H. K. Birnbaum. *Acta Metall.*, 35:1815, 1987.

[70] D. H. Lassila, H. K. Birnbaum. *Acta Metall.*, 36:2821, 1988.

[71] A. Kimura, H. K. Birnbaum. *Acta Metall.*, 35:1077, 1987.

[72] A. Kimura, H. K. Birnbaum. *Acta Metall.*, 36:757, 1988.

[73] S. Bechtle, M. Kumar, B. P. Somerday, M. E. Launey, R. O. Ritchie. *Acta Mater.*, 57:4148, 2009.

[74] A. Kimura, H. K. Birnbaum. *Scripta Metall.*, 21:219, 1987.

[75] J. Eastman, F. Heubaum, T. Matsumoto, H. K. Birnbaum. *Acta Metall.*, 30:1579, 1982.

[76] G. Girardin, D. Delafosse. *Mater. Sci. Eng. A*, 387-389:51, 2004.

[77] D. Delafosse, X. Feaugas, I. Aubert, N. Saintier, J.-M. Olive. In *Effects of Hydrogen on Materials*, page 78, Proceedings of the 2008 International Hydrogen Conference, 2009.

[78] M. L. Martin, B. P. Somerday, R. O. Ritchie, P. Sofronis, I. M. Robertson. *Acta Mater.*, 60:2739, 2012.

[79] P. Sofronis, R. M. McMeeking. *J. Mech. Phys. Solids*, 37:317, 1989.

[80] P. Sofronis. *Mechanics of hydrogen embrittlement.* PhD thesis, University of Illinois at Urbana-Champaign, USA, 1987.

[81] A. H. M. Krom, R. W. J Koers, A. Bakker. *J. Mech. Phys. Solids*, 47:971, 1978.

[82] A. H. M. Krom. *Numerical modelling of hydrogen transport in steel.* PhD thesis, Delft University, Netherlands, 1998.

[83] M. Reza, N. Saintier, H. Notsu, J.-M. Olive, H. Kanayama. *J. Comput. Sci. Technol.*, 4:105, 2010.

[84] M. Reza. *Finite element analysis of large elasto-plastic deformation in hydrogen related problems.* PhD thesis, Kyushu University, Japan, 2010.

[85] R. Abgrall. *Commun. Comput. Phys.*, 11:1043, 2012.

[86] P. Kedzierzawski. In *Hydrogen Degradation of Ferrous Alloys*, ed. by R. A. Oriani, J. P. Hirth, M. Smialowski. Noyes Publications, New Jersey, 1985.

[87] H. Peisl. *Appl. Phys.*, 28:53, 1978.

[88] G. Cailletaud, S. Forest, D. Jeulin, F. Feyel, I. Galliet, V. Mounoury, S. Quilici. *Comput. Mater. Sci.*, 27:351, 2003.

[89] C. Robert, N. Saintier, T. Palin-Luc, F. Morel. *Mech. Mater.*, 55:112, 2012.

[90] Z set package. *Available http://www.mat.ensmp.fr/Accueil/Telechargements/Zebulon/*, 10/09/2013.

[91] Y. Mine, C. Narazaki, T. Kanezaki, S. Matsuoka, Y. Murakami. Fatigue behavior of metallic materials exposed to high pressure hydrogen environment. In *Proceeding of ECF16*. Alexandroupolis, 2006.

[92] X. Feaugas. *Acta Mater.*, 47:3617, 1999.

[93] A. P. Sutton, R. W. Balluffi. *Interfaces in crystalline materials*. Oxford University Press, 1995.

[94] S. Hofmann, P. Lejček. *Interface Sci.*, 3:241, 1996.

[95] S. V. Divinski, F. Hisker, Y.-S. Kang, J.-S. Lee, Chr. Herzig. *Acta Mater.*, 52(3):631, 2004.

[96] M. Menyhard, M. Yan, V. Vitek. *Acta Metall. Mater.*, 42(8):2783, 1994.

[97] P. Stender, Z. Balogh, and G. Schmitz. *Phys. Rev. B*, 83:121407, 2011.

[98] M. Herbig, D. Raabe, Y. J. Li, P. Choi, S. Zaefferer, and S. Goto. *Phys. Rev. Lett.*, 112:126103, 2014.

[99] Yu. Mishin, Chr. Herzig. *Mater. Sci. Eng. A*, 260:55, 1999.

[100] Chr. Herzig, S. V. Divinski. *Mater. Trans.*, 44:14, 2003.

[101] S. Hofmann, J. Erlewein. *Scripta Metall.*, 10:857, 1976.

[102] S. Hofmann, J. Erlewein. *Surface Sci.*, 77:591, 1978.

[103] V. S. Stubican. In *Transport in nonstoichiometric compounds*, page 345, eds. V. S. Stubican G. Simkovich. Plenum Press, New York, 1985.

[104] R. E. Hoffman. *Acta Metall.*, 4:56, 1956.

[105] G. J. May, A. Hooper. *J. Mater. Sci.*, 13:1480, 1978.

[106] Y. A. Du, J. Rogal, R. Drautz. *Phys. Rev. B*, 86:174110, 2012.

[107] G. Martin. *Phys. Rev. B*, 41:2279, 1990.

[108] G. H. Vineyard. *J. Phys. Chem. Solids*, 3:121, 1957.

[109] J. von Pezold, L. Lymperakis, J. Neugebauer. *Acta Mater.*, 59:2969, 2011.

[110] D. Turnbull, R. E. Hoffman. *Acta Metall.*, 2:419, 1954.

[111] R. Kirchheim. In *Solid State Physics*, eds. H. Ehrenreich and F. Spaepen, 59:203. Elsevier, Amsterdam, 2004.

[112] S. M. Teus, V. F. Mazanko, J.-M. Olive, V. G. Gavriljuk. *Acta Mater.*, 69:105, 2014.

[113] R. D. Calder, T. S. Elleman, K. Verghese. *J. Nucl. Mater.*, 46:46, 1973.

[114] T. Tsuru, R. M. Latanision. *Scripta Metall.*, 16:575, 1982.

[115] B. Ladna, H. K. Birnbaum. *Acta Metall.*, 35:2537, 1987.

[116] J. Yao, J. R. Cahoon. *Scripta Metall.*, 22:1817, 1988.

[117] T. M. Harris, R. M. Latanision. *Metall. Trans. A*, 22:351, 1991.

[118] A. M. Brass, A. Chanfreau. *Acta Mater.*, 44(9):3823, 1996.

[119] T. Mütschele, R. Kirchheim. *Scripta Metal.*, 21:135, 1987.

[120] J. Yao, J. R. Cahoon. *Acta Metall. Mater.*, 39:119, 1991.

[121] A. Oudriss, J. Creus, J. Bouhattate, E. Conforto, C. Berziou, C. Savall, X. Feaugas. *Acta Mater.*, 60:6814, 2012.

[122] J. C. Fisher. *J. Appl. Phys.*, 22:74, 1951.

[123] L. G. Harrison. *Trans. Faraday Society*, 57:1191, 1961.

[124] I. Kaur, Y. Mishin, W. Gust. *Fundamentals of Grain, Interface Boundary Diffusion.* Wiley, 1995.

[125] R. T. P. Whipple. *Philos. Mag.*, 45:1225, 1954.

[126] T. Suzuoka. *Trans. Jap. Inst. Metals*, 2:25, 1961.

[127] H. S. Levine, C. J. MacCallum. *J. Appl. Phys.*, 31:595, 1960.

[128] A. D. Le Claire. *Brit. J. Appl. Phys.*, 14:351, 1963.

[129] Yu. M. Mishin. *Phys. Status Solidi A*, 133:259, 1992.

[130] Y-C. Chung, B. J. Wuensch. *J. Appl. Phys.*, 79:8323, 1996.

[131] J. W. Evans. *J. Appl. Phys.*, 82:628, 1997.

[132] D. Shaw, T. L. Shaw. *J. Appl. Phys.*, 84:3586, 1998.

[133] B. S. Bokstein. *Def. Diff. Forum Vols.*, 297-301:1267, 2010.

[134] N. Yazdipour, A. J. Haq, K. Muzaka, E. V. Pereloma. *Comput. Mater. Sci.*, 56:49, 2012.

[135] D. Gryaznov, J. Fleig, J. Maier. *Solid State Sci.*, 10:754, 2008.

[136] D. Gryaznov. *Simulation of diffusion in nanocrystalline materials: continuum approach*. PhD thesis, Stuttgart University, Germany, 2006.

[137] E. Legrand, J. Bouhattate, X. Feaugas, S. Touzain, H. Garmestani, M. Khaleel, D. S. Li. *Comput. Mater. Sci.*, 71:1, 2013.

[138] D. N. Ilin, N. Saintier, J-M. Olive, R. Abgrall, I. Aubert. *Int. J. Hydrogen Energy*, 39:2418, 2014.

[139] F. D. Fischer, G. Mori, J. Svoboda. Modelling the influence of trapping on hydrogen permeation in metals. *Corrosion Science*, 76(0):382 – 389, 2013.

[140] J. Svoboda, F. D. Fischer. *Acta Mater.*, 60:1211, 1987.

[141] Y. Murakami. Effect of hydrogen on metal fatigue. In *International hydrogen energy development forum*, Fukuoka, Japan, 2007.

[142] G. Cailletaud, O. Diard, F. Feyel, S. Forest. *Technische Mechanik*, 23:130, 2003.

[143] F. Roters, P. Eisenlohr, L. Hantcherli, D. D. Tjahjanto, T. R. Bieler, D. Raabe. *Acta Mater.*, 58:1152, 2010.

[144] A. Musienko, G. Cailletaud. *Acta Mater.*, 57:3840, 2009.

[145] A. Musienko. *Plasticite cristalline en presence de grandes deformation et d'endommagement.* PhD thesis, Ecole Nationale Superieure des Mines de Paris, 2005.

[146] Y.-B. Guo, T. Xu, M. Li. *Philos. Mag.*, page 1, 2012.

[147] C. Senöz, S. Evers, M. Stratmann, M. Rohwerder. *Electrochem. Commun.*, 13:1542, 2011.

[148] S. Evers, C. Senöz, M. Rohwerder. *Electrochimica Acta*, 110:534, 2013.

[149] F. Barbe. *Etude numerique de la plasticite d'agregats polycrystallins.* PhD thesis, Ecole Nationale Superieure des Mines de Paris, 2000.

[150] R. A. Lebensohn, C. N. Tomé. *Acta Metall. Mater.*, 41:2611, 1993.

[151] C. N. Tomé, R. A. Lebensohn. Manual for Code Visco-Plastic Self Consistent (VPSC), version 7a, Los Alamos National Laboratory, USA, 2006.

[152] J. A. Sethian, Jon Wilkening. *J. Comput. Phys.*, 193(1):275, 2004.